Stony Brook University

Transport Processes in High Temperature QCD Plasmas

A Dissertation Presented

by

Juhee Hong

to

The Graduate School

in Partial Fulfillment of the Requirements

for the Degree of

Doctor of Philosophy

in

Physics

Stony Brook University

August 2012

Stony Brook University

The Graduate School

Juhee Hong

We, the dissertation committee for the above candidate for the Doctor of Philosophy degree, hereby recommend acceptance of this dissertation.

Derek Teaney – Dissertation Advisor
Assistant Professor, Department of Physics and Astronomy

Matthew Dawber – Chairperson of Defense
Assistant Professor, Department of Physics and Astronomy

Thomas K. Hemmick
Distinguished Teaching Professor, Department of Physics and Astronomy

Peter Petreczky
RIKEN Fellow, Brookhaven National Laboratory

This dissertation is accepted by the Graduate School.

Charles Taber
Interim Dean of the Graduate School

Abstract of the Dissertation

Transport Processes in High Temperature QCD Plasmas

by

Juhee Hong

Doctor of Philosophy

in

Physics

Stony Brook University

2012

The transport properties of high temperature QCD plasmas can be described by kinetic theory based on the Boltzmann equation. In a leading-log approximation, the Boltzmann equation is reformulated as a Fokker-Planck equation. First, we compute the spectral densities of $T^{\mu\nu}$ and J^{μ} by perturbing the system with weak gravitational and electromagnetic fields. The spectral densities exhibit a smooth transition from free-streaming quasi-particles to hydrodynamics. This transition is analyzed with hydrodynamics and diffusion equation up to second order. We determine all of the first and second order transport coefficients which characterize the linear response in the hydrodynamic regime. Second, we simulate the wake of a heavy quark moving through the plasmas. At long distances, the energy density and flux distributions show sound waves and a diffusion wake. The kinetic theory calculations based on the Boltzmann equation at weak coupling are compared to the strong coupling results given by the AdS/CFT correspondence.

By using the hard-thermal-loop effective theory, we determine the photon emission rate at next-to-leading order (NLO), *i.e.*, at order $g^2 m_D/T$. There are three mechanisms which contribute to the leading-order photon emission: $2 \leftrightarrow 2$ elastic scatterings, $1 \leftrightarrow 2$ collinear bremsstrahlung, and $1 \leftrightarrow 1$ quark-photon conversions due to soft fermion exchange. At NLO, these three mechanisms are not completely independent. For instance, the $2 \leftrightarrow 2$ Compton process smoothly matches onto the $1 \leftrightarrow 2$ bremsstrahlung rate when the external gluon is soft. Similarly, bremsstrahlung reduces to quark-photon conversion process when the photon carries most of the incoming momentum. Therefore, the rates should be matched to determine the wide-angle NLO correction. Collinear bremsstrahlung can be accounted for by solving an integral equation which corresponds to summing ladder diagrams. With $\mathcal{O}(g)$ corrections in the collision kernel and the asymptotic mass of quarks, we determine the NLO correction from collinear processes.

Contents

List of Figures

List of Tables

Acknowledgements

I thank my advisor Derek Teaney for his guidance and patience during last five years. Thanks to him, I had a chance to work on good research projects and learned a lot of physics. I would also like to thank members of the nuclear theory group, especially Edward Shuryak and Dmitri Kharzeev for their help during my Ph.D.

I am grateful to my parents and my grandparents who have been always supporting me. Last but not least, I am indebted to my husband Hongjun An for encouraging me through tough times, as well as sharing valuable ideas.

Chapter 1

Introduction

1.1 High Temperature QCD Plasmas

The Relativistic Heavy Ion Collider (RHIC) and the Large Hadron Collider (LHC) produce high energy-density matter which is called the Quark-Gluon Plasma (QGP) [1, 2]. This phase of matter is similar to what is believed to exist in the early universe. At sufficiently high temperature (well above the phase transition temperature $T_c \approx 160\text{MeV}$), the description based on non-interacting quasi-particles can be a starting point to study thermodynamics and kinetics of the QGP. As it expands, the plasma cools down, and at T_c, experiences a phase transition from the QGP to hadronic gas. In the hadronic gas, quarks and gluons are no longer freely moving, and they are confined. One of the goals in heavy ion collisions is to create the "little bang" and study the properties and transition dynamics of the QCD matter. There has been much progress in investigating the matter, but it is not fully understood today.

The strong interaction of quarks and gluons can be described by quantum chromodynamics (QCD). The Lagrangian of QCD is given by[1] [3]

$$\mathcal{L} = -\sum_q \bar{\psi}_{q,i}(\gamma^\mu \partial_\mu \delta_{ij} - ig\gamma^\mu t^a_{ij} A^a_\mu + m_q \delta_{ij})\psi_{q,j} - \frac{1}{4} G^a_{\mu\nu} G^{a,\mu\nu}\,, \tag{1.1}$$

with the field tensor

$$G^a_{\mu\nu} = \partial_\mu A^a_\nu - \partial_\nu A^a_\mu - g f_{abc} A^b_\mu A^c_\nu\,. \tag{1.2}$$

Here $\psi_{q,i}$ is a spinor for a quark with mass m_q, a color index $i = 1, 2, 3$ for $N_c = 3$, A^a_μ corresponds to a gluon field, t^a_{ij} is a generator of the SU(3) group,

[1] There is an additional CP-violating term, $\theta \frac{\alpha_s}{8\pi} G^a_{\mu\nu} \tilde{G}^{a,\mu\nu}$, where $\tilde{G}^a_{\mu\nu} \equiv \frac{1}{2}\epsilon_{\mu\nu\sigma\rho} G^{a,\sigma\rho}$ is the dual of the gluon field tensor.

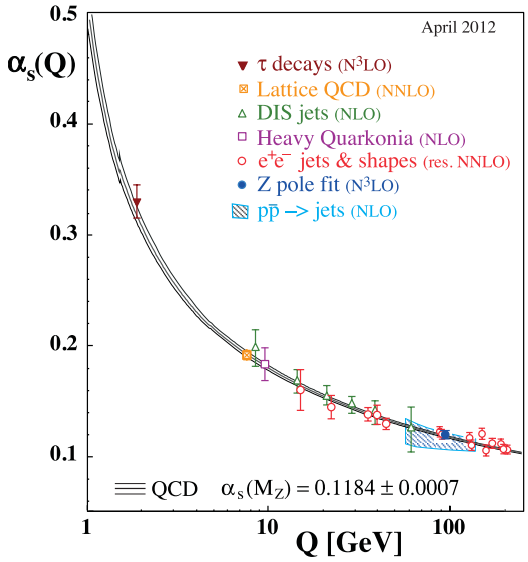

Figure 1.1: The QCD running coupling $\alpha_s = g^2/4\pi$. Due to the asymptotic freedom, the coupling decreases logarithmically at high energy. This plot is from Ref. [3].

and f_{abc} is the structure constant obeying $[t^a, t^b] = i f_{abc} t^c$.

Due to the asymptotic freedom, the QCD coupling constant g decreases logarithmically at high energy. Specifically, at one-loop g is running according to

$$\alpha_s(\mu^2) \equiv \frac{g^2(\mu^2)}{4\pi} = \frac{1}{\beta_0 \ln(\mu^2/\Lambda^2_{\rm QCD})} \,. \tag{1.3}$$

Here μ is a relevant energy scale, the QCD scale $\Lambda_{\rm QCD} \approx 200$MeV, and $\beta_0 = (11C_A - 4N_f T_F)/12\pi$ (where $C_A = N_c = 3$ and $T_F = 1/2$). At high temperature compared to $\Lambda_{\rm QCD}$, the coupling g is small (see Fig. 1.1). Therefore, perturbative calculations are applicable to describe the properties of weakly coupled plasmas.

In weakly coupled plasmas, there are momentum scales of T, gT, and g^2T [4, 5]. The first momentum scale $\sim T$ is called "hard", the second scale $\sim gT$ is called "soft", and the third scale $\sim g^2T$ is called "ultra-soft". The distance between hard particles is $\sim 1/T$, and the pressure (at zeroth order) due to hard particles is given by the free gas limit. The hard and soft scales can be studied by a perturbative setup, whereas the ultra-soft scale is non-perturbative. In particular, the soft sector of the Debye scale $\sim gT$ needs to be treated with special care. Bare perturbation theory breaks down at this order due to infrared divergences. However, in real plasmas there are no such divergences, since potential induced by the presence of charged particles is

screened at long distance $\sim 1/gT$.

Braaten and Pisarski proposed the hard-thermal-loop (HTL) resummation which takes account for the screening effect at the Debye scale [4, 6]. By using the HTL effective theory, there have been many achievements in perturbative gauge theories. For example, transport coefficients have been computed at leading order [7]. In ultra-relativistic plasmas where quarks and gluons are non-interacting, bremsstrahlung is as important as collisions to determine transport dynamics. Due to multiple scatterings, radiation is suppressed, which is known as the Landau-Pomeranchuk-Migdal (LPM) effect. Calculation of the leading order transport coefficients requires counting both hard scatterings and collinear bremsstrahlung involving the LPM effect.

To describe the properties of high temperature plasmas, we would like to compute physical quantities as a function of coupling g and temperature T. Among them, equilibrium quantities are under control and well-understood. By using the electrostatic QCD (EQCD) with dimensional regularization, pressure has been computed up to order of $g^6 \ln g$ [8]. The perturbative result is consistent with the lattice data at somewhat high temperature $\sim 5T_c$ [9]. On the other hand, real-time quantities such as transport coefficients are not well understood beyond leading order. The only dynamic quantity which has been computed at next-to-leading order is the heavy quark diffusion constant [10].

In heavy ion collisions, the temperature of the plasmas is rather low (as $T_{\rm HIC} \approx 300$MeV) than we discussed above [11]. Thus, $T_{\rm HIC}$ is not high enough compared to $\Lambda_{\rm QCD}$ so that perturbative expansions may or may not be applicable. Now an important question is that how much then we can trust perturbative calculations to explain collective phenomena in the QGP. To respond to this question, we will address the following points in this thesis:

- *Point I* - The evolution of heavy ion collisions can be characterized by viscous hydrodynamics [1, 2]. Hydrodynamics is valid when the time between collisions is short compared to the time during the Bjorken expansion, $\eta/sTv_{th}^2 \ll \tau$. With estimated experimental condition $\tau_o \approx 1$fm and $T_o \approx 300$MeV, we find that the hydrodynamic expansion is a good approximation for $\eta/s \lesssim 0.3$ [11]. For instance, the elliptic flow data can be described by the second order hydrodynamics. Fig. 1.2 shows simulation results for $v_2(p_T)$ which is the second coefficient in harmonic expansions of the particle distribution. By comparing the simulation to the non-flow corrected data, we can estimate the validity limit for the shear viscosity as $\eta/s \approx 0.08 \leftrightarrow 0.16$.
  In order to analyze the onset of the hydrodynamic limit, we consider the response of equilibrium plasmas to external perturbations. The transport properties of this high temperature plasma are described by kinetic

theory. By solving the Boltzmann equation, we study how the system evolves and equilibrates. At long wavelength limit, the solutions of the Boltzmann equation are consistent with hydrodynamic solutions. By comparing the kinetic theory results with hydrodynamics up to second order, we determine the validity regime for the macroscopic theory.

- *Point II* - In realistic plasmas, the coupling is not particularly small ($\alpha_s \approx 0.5$). It is not clear that the QGP is weakly coupled or strongly coupled. Therefore, we need to compare weakly coupled theories with strongly coupled theories. In order to find out the difference between kinetic theory at weak coupling and the AdS/CFT at strong coupling, we investigate the jet-medium interaction with a heavy quark probe in two theories.

- *Point III* - To see how well perturbative expansions work in heavy ion collisions, it is important to calculate transport coefficients. For example, we need to know the drag coefficient to understand the energy loss in jets. Plus, viscous hydrodynamic simulations require the value of the shear viscosity. The computation of the shear viscosity involves all the details of perturbation theories including screening and collinear bremsstrahlung.
  As a warm-up problem, we compute the photon emission rate at next-to-leading order (NLO). The computation of the photon emission rate has some, but not all, of the difficulties in computing the shear viscosity at NLO. In addition to the theoretical motivation, direct photons are measured at PHENIX (see Fig. 1.3 (a)) [13]. There are various sources of photons. Depending on the temperature scale, thermal photons are produced from hadronic gas and QGP. Also, there are prompt photons from p+p collisions. Roughly speaking, prompt photons are dominant at high transverse momentum $q_t > 3$GeV, fit with power-law function (see the green short-dashed line in Fig. 1.3 (b)). At low momentum $q_t < 2 - 3$GeV, thermal photons are dominant with exponential yield (see the blue long-dashed line and the red dashed-dotted line in Fig. 1.3 (b)). In particular, the leading order photon emission rate from the QGP, which was computed in Ref. [109] and shown as the red dashed-dotted line in Fig. 1.3 (b), is currently being used to compare with experimental data [14]. We compute the $\mathcal{O}(g)$ correction to this leading order result.

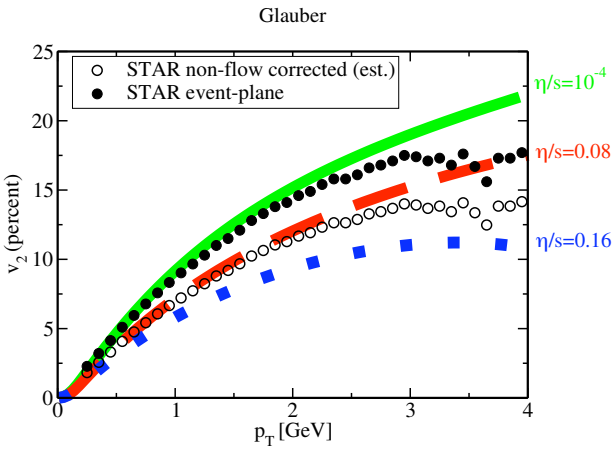

Figure 1.2: The elliptic flow depending on the shear viscosity. The simulation results should be compared to the non-flow corrected data. This plot is from Ref. [12].

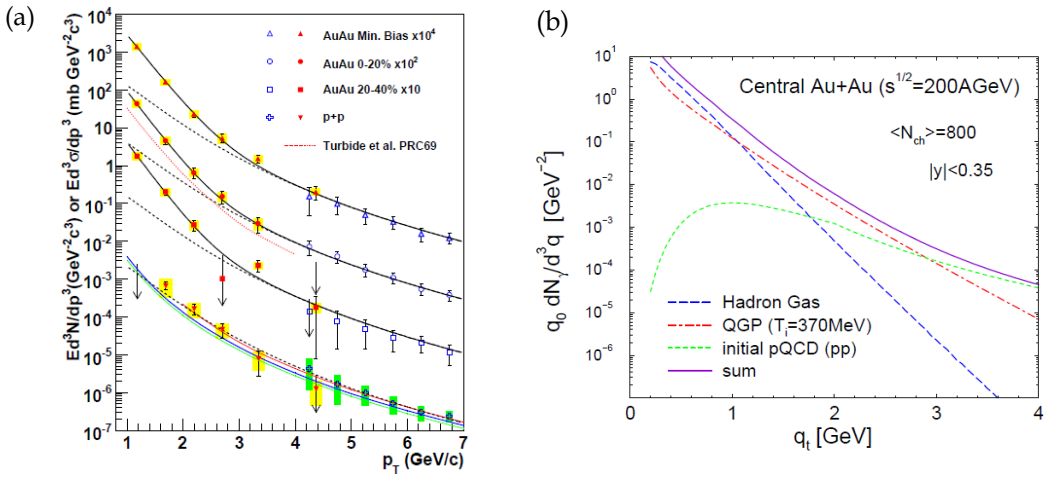

Figure 1.3: (a) Invariant yield of direct photons at PHENIX. The red dotted line is a theoretical calculation from Ref. [14]. This plot is from Ref. [13]. (b) Integrated photon emission spectra from central Au+Au collisions at RHIC. The blue long-dashed line indicates thermal hadron gas, the red dashed-dotted line indicates thermal QGP radiation computed in Ref. [109], the green short-dashed line indicates photons from primordial N+N collisions, and the purple solid line indicates the total direct photon yield. This plot is from Ref. [14].

1.2 Outline of This Thesis

To answer the three points mentioned in the last section, this thesis is organized as follows.

In chapter 2, we formulate the linearized Boltzmann equation at a leading-log approximation. We specify the appropriate boundary conditions (which are determined by collinear bremsstrahlung discussed above), and explain the physical significance of the boundary conditions. The formulation is mainly given for pure glue theory and is extended to including fermions. This Boltzmann equation is used in the following two chapters to compute spectral densities and investigate jet-medium interactions.

In chapter 3, we calculate the spectral densities of $T^{\mu\nu}$ and J^{μ} by perturbing the system with weak gravitational and electromagnetic fields. From the slope of spectral densities at $\omega = 0$, we extract all the first and second order transport coefficients. In particular, with the shear viscosity η and a second order hydrodynamic coefficient τ_π known, hydrodynamic solutions are determined up to second order in gradient expansions. By comparing kinetic theory results with hydrodynamic solutions, we analyze the hydrodynamic limit to answer the *Point I*.

In chapter 4, to answer the *Point II*, we simulate the wake of a heavy quark moving through plasmas with two different theories: kinetic theory based on the Boltzmann equation at weak coupling, and the AdS/CFT correspondence at strong coupling. A comparison between the kinetic theory results and the AdS/CFT results is given. At long distances, the energy density and flux distributions are compared with hydrodynamic solutions in both theories.

To respond to the *Point III*, in chapter 5 we compute the photon emission rate at next-to-leading order, *i.e.*, at order $g^2 m_D/T$. First, we summarize the leading order results on the photon emission rate. Then we discuss all the possible corrections of $\mathcal{O}(g)$ to the leading order results. The matching processes of the rates (among two particle elastic scattering, bremsstrahlung, and quark-photon conversion) are explained in detail.

Finally, in chapter 6 we conclude.

Chapter 2

Boltzmann Equation

2.1 Introduction

To describe the linear response in the gas of quarks and gluons, we use kinetic theory based on the Boltzmann equation. In this chapter, we will formulate the linearized Boltzmann equation at a leading-log approximation. As will be discussed in Section 2.2.1, the Boltzmann equation is not simple due to the particle number-changing process near $\boldsymbol{p} = 0$. This formulation will be used to compute spectral densities and simulate jet-medium interactions in the following two chapters.

At weak coupling, the kinetics of high temperature plasmas consists of several processes [15, 16]. First, random walks of hard particles causes momentum diffusion. Second, collisions affect the lifetimes of quasi-particle excitations. Finally, bremsstrahlung is important in the equilibration of high momentum modes. By using kinetic theory, we can study the dynamical properties of the plasmas. For instance, transport coefficients of high temperature plasmas can be computed [7, 17, 18], and equilibration in heavy ion collisions can be described [19, 20, 21, 22]. There has been considerable progress in understanding the dynamics of the soft background gauge fields out of equilibrium [23, 24, 25]. Ultimately, one can simulate heavy ion collisions and jet-medium interactions using the kinetic theory based on the Boltzmann equation.

The Boltzmann equation is a transport equation which describes statistical distributions of particles. In general, particles in plasmas are out of equilibrium. The distribution functions of particles depend on position and momentum, $f(t, \boldsymbol{x}, \boldsymbol{p})$. In the presence of weak perturbations, we can linearize the equation around equilibrium. Then the equation is reformulated as a Fokker-Planck equation to describe diffusion process. This analysis is limited to a leading-logarithmic order of the coupling constant g, where hard collisions

and collinear bremsstrahlung are neglected[1].

In this chapter, we discuss how to formulate the linearized Boltzmann equation in a leading-log approximation [26]. We start with a pure glue theory and extend to including fermions. For transport coefficients, the Boltzmann equation is usually solved as a variational problem [27]. However, when solving for the spectral functions described in Chapter 3, it is easier to discretize momentum space and solve the equation directly. The full numerical solutions capture the transition from Landau damping to hydrodynamics. In particular, we use an absorptive boundary condition at low momentum which reflects the flux of particles from the hard momentum scale $\sim T$ to the soft momentum scale $\sim gT$ [18]. Due to this boundary condition, the particle number changes during the evolution, whereas the energy and momentum are conserved.

Throughout, we will denote a four-dimensional vector with a capital letter P, and use $\boldsymbol{p}$ for three-dimensional vector, E_p for the energy component, and $p = |\boldsymbol{p}|$. Our metric convention is $\eta_{\mu\nu} = \mathrm{diag}(-1, +1, +1, +1)$, so that $u_\mu u^\mu = -1$. We use units of $c = \hbar = 1$.

2.2 Linearization with Pure Glue

In this section, we linearize the Boltzmann equation at a leading-log order. For simplicity, we consider the pure glue theory, where all the particles are gluons as in Fig. 2.1. The extension to including fermions will be discussed in Section 2.3.

The Boltzmann equation is given by[2]

$$\left(\frac{\partial}{\partial t} + \boldsymbol{v}_p \cdot \frac{\partial}{\partial \boldsymbol{x}}\right) f(t, \boldsymbol{x}, \boldsymbol{p}) = C[f, \boldsymbol{p}]\,, \tag{2.1}$$

where $\boldsymbol{v}_p = \hat{\boldsymbol{p}}$ for massless particles. We linearize the particle distribution function $f(t, \boldsymbol{x}, \boldsymbol{p})$ around equilibrium

$$f(t, \boldsymbol{x}, \boldsymbol{p}) = n_p^B + \delta f(t, \boldsymbol{x}, \boldsymbol{p})\,. \tag{2.2}$$

[1]Bremsstrahlung determines the boundary condition at low momentum, but otherwise can be neglected (see Section 2.2.1 for details).

[2]In general, there is a force term which is neglected here.

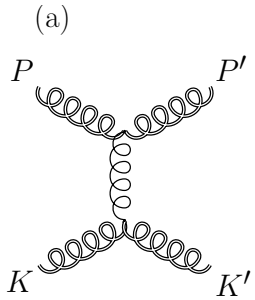

Figure 2.1: The pure glue t-channel $2 \leftrightarrow 2$ Feynman diagram which contributes at a leading-log order. External particles have momentum $\sim T$ and internal momentum is $\sim gT$. Double curly lines denote hard gluons and a single curly line denotes a soft gluon. Time runs from left to right.

Here the equilibrium distribution n_p^B is the Bose-Einstein statistics for gluons[3]

$$n_p^B \equiv \frac{1}{e^{E_p/T_o} - 1}\,, \tag{2.3}$$

where $E_p = p$ for massless particles and T_o is constant temperature. $C[f, \boldsymbol{p}]$ in Eq. (2.1) is the collision term which is given by[4]

$$C[f,\boldsymbol{p}] = -\int_{\boldsymbol{kp'k'}} \frac{1}{2}|M|^2(2\pi)^4\delta^4(P_{tot})\Big[f(\boldsymbol{p})f(\boldsymbol{k})[1+f(\boldsymbol{p'})][1+f(\boldsymbol{k'})] \\ - f(\boldsymbol{p'})f(\boldsymbol{k'})[1+f(\boldsymbol{p})][1+f(\boldsymbol{k})]\Big]\,. \tag{2.4}$$

Here, $|M|^2$ is the scattering amplitude of the process $P + K \to P' + K'$ and $\delta^4(P_{tot}) = \delta^4(P + K - P' - K')$. In a leading-log order, the only contribution is from t-channel $2 \leftrightarrow 2$ scatterings, where two external particles are hard with momentum $\sim T$ and the momentum exchange is soft $\sim gT$ (see Fig. 2.1). In order to simplify the collision kernel, we define

$$\delta f(t, \boldsymbol{x}, \boldsymbol{p}) \equiv n_p(1 + n_p)\chi(t, \boldsymbol{x}, \boldsymbol{p})\,. \tag{2.5}$$

At this order, the collision term is dominated by small angle scatterings, and

[3]We will drop the superscript B (or F) when the appropriate statistics is clear from context.

[4]Momentum space integrals are abbreviated as $\int_{\boldsymbol{p}} \equiv \int d^3\boldsymbol{p}/(2\pi)^3$.

the linearized Boltzmann equation can be written (see Appendix A for details)

$$\left(\frac{\partial}{\partial t}+\boldsymbol{v}_p\cdot\frac{\partial}{\partial \boldsymbol{x}}\right)\delta f = T\mu_A\frac{\partial}{\partial \boldsymbol{p}^i}\left[n_p(1+n_p)\frac{\partial\chi}{\partial \boldsymbol{p}^i}\right]+(\text{gain terms})\,. \tag{2.6}$$

Here μ_A and the Debye mass (for pure glue) are given by[5]

$$\mu_A \equiv \frac{g^2 C_A m_D^2}{8\pi}\ln\left(\frac{T}{m_D}\right), \tag{2.7}$$

$$m_D^2 = \frac{g^2 C_A}{d_A}\nu_g\int_{\boldsymbol{p}}\frac{n_p(1+n_p)}{T} = \frac{g^2T^2}{3}N_c\,. \tag{2.8}$$

Except the gain terms, Eq. (2.6) is a Fokker-Planck equation describing random walks of hard particles. As a result, particles lose their energy and momentum to plasmas. In this sense, we call the first term of the right-hand side in Eq. (2.6), the "loss" term. However, there are additional "gain" terms which compensate the lost energy and momentum. We discuss how the energy-momentum conservation works in the following.

Eq. (2.6) is a kind of diffusion equation. In this diffusion process, the momentum-space current is given by

$$\boldsymbol{j}_p = -T\mu_A n_p(1+n_p)\frac{\partial\chi}{\partial\boldsymbol{p}}\,. \tag{2.9}$$

Multiplying both sides of Eq. (2.6) by energy E_p and integrating over the phase space, the work on particles (per time, degree of freedom, and volume) can be found in terms of the current:

$$\frac{\mathrm{d}E}{\mathrm{d}t} \equiv \int_{\boldsymbol{p}}\hat{\boldsymbol{p}}\cdot\boldsymbol{j}_p\,. \tag{2.10}$$

Similarly, the momentum transfer (per time, degree of freedom, and volume) is

$$\frac{\mathrm{d}\boldsymbol{P}}{\mathrm{d}t} \equiv \int_{\boldsymbol{p}}\boldsymbol{j}_p\,. \tag{2.11}$$

If there were no gain terms in Eq. (2.6), particles lose their energy and momentum to the plasmas through the diffusion process. However, there are gain terms which are exactly given by the energy-momentum transfers (see

[5]The dimension and the Casimir of the adjoint representation are $d_A = N_c^2-1$ and $C_A = N_c$. For the fundamental representation, $d_F = N_c$ and $C_F = (N_c^2-1)/2N_c$. $\nu_g = 2d_A$ and $\nu_q = 2d_F$ count the spin and color degrees of freedom for gluons and quarks, respectively.

Appendix A for details):

$$(\text{gain terms}) = \frac{1}{\xi_B}\left[\frac{1}{p^2}\frac{\partial}{\partial p}p^2 n_p(1+n_p)\right]\frac{\mathrm{d}E}{\mathrm{d}t} + \frac{1}{\xi_B}\left[\frac{\partial}{\partial \boldsymbol{p}}n_p(1+n_p)\right]\cdot\frac{\mathrm{d}\boldsymbol{P}}{\mathrm{d}t}\,. \tag{2.12}$$

Here, we defined $\xi_B \equiv \int_{\boldsymbol{p}} n_p(1+n_p) = T^3/6$. Multiplying Eq. (2.6) by p^μ and integrating over the phase space, it is straightforward to verify that the total energy and momentum are conserved. With this formulation, however, the number of particles fluctuates, which will be discussed in the next section.

2.2.1 Boundary Conditions

The Boltzmann equation is an integro-differential equation. Without appropriate boundary conditions, they are not well-defined. In this section, we discuss physical boundary conditions at low and high momentum. Boundary conditions are non-trivial especially at $\boldsymbol{p} = 0$, where the particle number-changing process is present.

To determine an appropriate boundary condition at high momentum, we reexpress Eq. (2.6) as a Fokker-Planck equation (without gain terms)

$$\left(\frac{\partial}{\partial t} + \boldsymbol{v}_p\cdot\frac{\partial}{\partial \boldsymbol{x}}\right)\delta f = -\mu_A(1+2n_p)\hat{\boldsymbol{p}}\cdot\frac{\partial \delta f}{\partial \boldsymbol{p}} + T\mu_A\nabla_p^2\delta f\,. \tag{2.13}$$

Then the motion of the particle excess can be described by the Langevin equation:

$$\frac{d\boldsymbol{p}}{dt} = -\mu_A(1+2n_p)\hat{\boldsymbol{p}} + \boldsymbol{\xi}(t)\,, \tag{2.14}$$

where $\mu_A(1+2n_p) \simeq \mu_A$ is the drag coefficient of a high momentum gluon and $\boldsymbol{\xi}(t)$ is stochastic noise satisfying

$$\langle \xi^i(t)\xi^j(t')\rangle = 2T\mu_A\delta^{ij}\delta(t-t')\,. \tag{2.15}$$

At high momentum, drag is dominant, and the noise can be neglected in Eq. (2.13):

$$\left(\frac{\partial}{\partial t} + \boldsymbol{v}_p\cdot\frac{\partial}{\partial \boldsymbol{x}}\right)\delta f = -\mu_A\hat{\boldsymbol{p}}\cdot\frac{\partial \delta f}{\partial \boldsymbol{p}}\,. \tag{2.16}$$

This equation is first order in derivatives, and can be used as a boundary condition at high momentum.

In order to determine the appropriate boundary condition at low momentum, we consider the excess of soft gluons within a small ball of radius $\Delta p \sim gT$

centered at $\boldsymbol{p} = 0$:

$$\int_{p=0}^{p=\Delta p} \frac{\mathrm{d}^3\boldsymbol{p}}{(2\pi)^3} n_p(1+n_p)\chi(\boldsymbol{p}) \simeq \frac{T^2}{2\pi^2}\chi(\boldsymbol{0})\Delta p\,. \tag{2.17}$$

Since it is easy to emit a soft gluon, the excess should vanish, and it is intuitive to have the boundary condition [18]

$$\chi(\boldsymbol{p})\big|_{\boldsymbol{p}\to 0} = 0\,. \tag{2.18}$$

This absorptive boundary condition will be justified in the following.

At a leading-log approximation, bremsstrahlung and soft $1 \leftrightarrow 2$ scatterings can be neglected for momenta $\sim T$. However, near $\boldsymbol{p} \to 0$ limit inelastic processes are important for arbitrarily small coupling constant. Specifically, the total rate for hard particles to absorb (or emit) a gluon from the ball of radius $\Delta p \sim gT$ is [18]

$$\Gamma_{1\leftrightarrow 2} \sim g^4 T \int^{\Delta p} \frac{\mathrm{d}p}{p} f(p) \sim g^4 T^2 \int^{\Delta p} \frac{\mathrm{d}p}{p^2}\,, \tag{2.19}$$

where we used $f(p) \simeq T/p$ for $p \sim gT$. By using the thermal mass of gluon $m \sim gT$ as the infrared cutoff, the rate is given by

$$\Gamma_{1\leftrightarrow 2} \sim \frac{g^4T^2}{m} \sim g^3 T\,. \tag{2.20}$$

The time scale of the Fokker-Planck evolution is $T/\mu_A \sim 1/g^4 T\ln(1/g)$ which is large compared to the time scale of bremsstrahlung, $1/\Gamma_{1\leftrightarrow 2} \sim 1/g^3 T$. The ratio of these two scales gives the order of $\chi(p \sim gT)$ in the excess Eq. (2.17):

$$\chi(p \sim gT) \sim g\,. \tag{2.21}$$

The boundary condition in Eq. (2.18) is the leading result in the weak coupling limit $g \to 0$. Therefore, it is verified that we have the absorptive boundary condition at $\boldsymbol{p} = 0$. A consequence of this boundary condition is that gluon number is not conserved during the Fokker-Planck evolution. We will discuss this in the next section.

2.2.2 Evolution

We formulated the linearized Boltzmann equation and determined appropriate boundary conditions. To show how Boltzmann solutions evolve and

what the physical consequences are, we consider simple cases with arbitrary perturbations.

We solve the Boltzmann equation with some initial condition. Then the solution $\delta f(t, \boldsymbol{x}, \boldsymbol{p})$ will eventually reach the hydrodynamic form. Specifically, the form is described by a temperature excess $\delta T(t, \boldsymbol{x})$ (or equivalently the energy density fluctuation) and flow velocity $U^\mu = \big(1, \boldsymbol{u}(t, \boldsymbol{x})\big)$:

$$\begin{aligned} f_{eq}(t, \boldsymbol{x}, \boldsymbol{p}) &= \frac{1}{\exp\big[-P \cdot U(t, \boldsymbol{x})/[T_o + \delta T(t, \boldsymbol{x})]\big] - 1}, \\ &\simeq n_p + n_p(1 + n_p)\left[\frac{p\delta T(t, \boldsymbol{x})}{T_o^2} + \frac{\boldsymbol{p} \cdot \boldsymbol{u}(t, \boldsymbol{x})}{T_o}\right]. \end{aligned} \tag{2.22}$$

By using the definition Eq. (2.5), $\chi(t, \boldsymbol{x}, \boldsymbol{p})$ should approach to the equilibrium value at late times:

$$\chi_{eq}(t, \boldsymbol{x}, \boldsymbol{p}) = \frac{p\delta T(t, \boldsymbol{x})}{T_o^2} + \frac{\boldsymbol{p} \cdot \boldsymbol{u}(t, \boldsymbol{x})}{T_o}. \tag{2.23}$$

Here, the first and the second terms correspond to $l = 0$ and $l = 1$ partial waves, respectively.

As we discussed earlier, in this formulation, the total energy and momentum of the system are conserved during the Fokker-Planck evolution, whereas the particle number is not. Now, we examine how the total number of particles equilibrates. For simplicity, we ignore any spatial dependence of δf. The excess number of gluons is obtained by integrating $\delta f(t, \boldsymbol{p})$ over the phase space

$$\delta N_{FP} = \int_{\boldsymbol{p}} \delta f(t, \boldsymbol{p}). \tag{2.24}$$

By integrating both sides of Eq. (2.6), the rate of excess number is

$$\frac{\partial \delta N_{FP}}{\partial t} = \lim_{p \to 0} \frac{1}{(2\pi)^3} \int p^2 \mathrm{d}\boldsymbol{\Omega} \cdot \boldsymbol{j}_p + \frac{-T^2}{2\pi^2 \xi_B} \frac{\mathrm{d}E}{\mathrm{d}t}, \tag{2.25}$$

where $\boldsymbol{\Omega}_p$ is an outward-directed solid angle. The first term represents a diffusion flux of gluons with momentum $p \sim T$ to momentum $p \sim gT$. The second term gives the number of gluons disturbed from equilibrium per unit time by the random walk of the excess, δf. In general, these two terms have different rates and the number changes accordingly. In equilibrium, however, the two rates are equal and the excess number of gluons reach a constant. Specifically, by substituting the equilibrium distribution Eq. (2.22) to Eq. (2.25), we find that the net loss and gain of the excess gluons are same (with the opposite

sign):

$$\lim_{p\to 0}\frac{1}{(2\pi)^3}\int p^2 \mathrm{d}\boldsymbol{\Omega}\cdot\boldsymbol{j}_p\Big|_{eq} = -\frac{T\mu_A\delta T}{2\pi^2}\,, \qquad (\text{loss})\,, \tag{2.26}$$

$$\frac{-T^2}{2\pi^2\xi_B}\frac{\mathrm{d}E}{\mathrm{d}t}\Big|_{eq} = +\frac{T\mu_A\delta T}{2\pi^2}\,, \qquad (\text{gain})\,. \tag{2.27}$$

Thus, the particle number does not change at equilibrium.

The flux of particles can be obtained by taking the $\boldsymbol{p}\to 0$ limit of Eq. (2.6). At low momentum, $l=0$ and $l=1$ terms are dominant in a spherical harmonic expansion of χ:

$$\chi(t,\boldsymbol{p}) = \frac{\mathrm{d}\chi_{00}(t,\boldsymbol{p})}{\mathrm{d}p}\Big|_{\boldsymbol{p}=0} p + \frac{\mathrm{d}\boldsymbol{\chi}_{1m}(t,\boldsymbol{p})}{\mathrm{d}p}\Big|_{\boldsymbol{p}=0}\cdot\boldsymbol{p}\,. \tag{2.28}$$

Here we ignored the spatial dependence of χ for simplicity. By substituting this form into Eq. (2.6), the rate is

$$\frac{\partial\chi(t,\boldsymbol{p})}{\partial t} = -\frac{2T\hat{\boldsymbol{p}}}{p}\cdot\left(\mu_A\frac{\mathrm{d}\boldsymbol{\chi}_{1m}(t)}{\mathrm{d}p}\Big|_{\boldsymbol{p}=0} + \frac{1}{T\xi_B}\frac{\mathrm{d}\boldsymbol{P}}{\mathrm{d}t}\right)\,, \tag{2.29}$$

which is divergent as $\boldsymbol{p}\to 0$. Thus, the slope at $\boldsymbol{p}=0$ will satisfy the following condition to maintain the balance:

$$\frac{\mathrm{d}\boldsymbol{\chi}_{1m}(t)}{\mathrm{d}p}\Big|_{\boldsymbol{p}=0} = -\frac{1}{T\mu_A\xi_B}\frac{\mathrm{d}\boldsymbol{P}}{\mathrm{d}t}\,. \tag{2.30}$$

As a result, the flux $(p^2\boldsymbol{j}_p)$ at low momentum is determined by the momentum transfer to the hard particle by the bath. It is straightforward to verify that Eq. (2.23) satisfies this balance condition.

In order to demonstrate how the solutions of the Boltzmann equation approach to the equilibrium, we consider two simple cases:

$$\chi(t,\boldsymbol{p}) = \chi_{00}(t,p)H_{00}(\hat{\boldsymbol{p}})\,, \tag{2.31}$$

$$\chi(t,\boldsymbol{p}) = \chi_{10}(t,p)H_{10}(\hat{\boldsymbol{p}})\,. \tag{2.32}$$

Here $H_{00}(\hat{\boldsymbol{p}}) = 1/\sqrt{4\pi}$ and $H_{10}(\hat{\boldsymbol{p}}) = \sqrt{3/4\pi}\cos\theta$ are the $l=0$ and $l=1$ spherical harmonics. For the initial condition at time $t_0=0$, we take

$$\left.\begin{array}{l} p^2 n_p(1+n_p)\chi_{00}(p,t_0) \\ p^2 n_p(1+n_p)\chi_{10}(p,t_0) \end{array}\right\} \propto \sum_{s=\pm} s e^{-(p-sp_0)^2/2\sigma^2}, \tag{2.33}$$

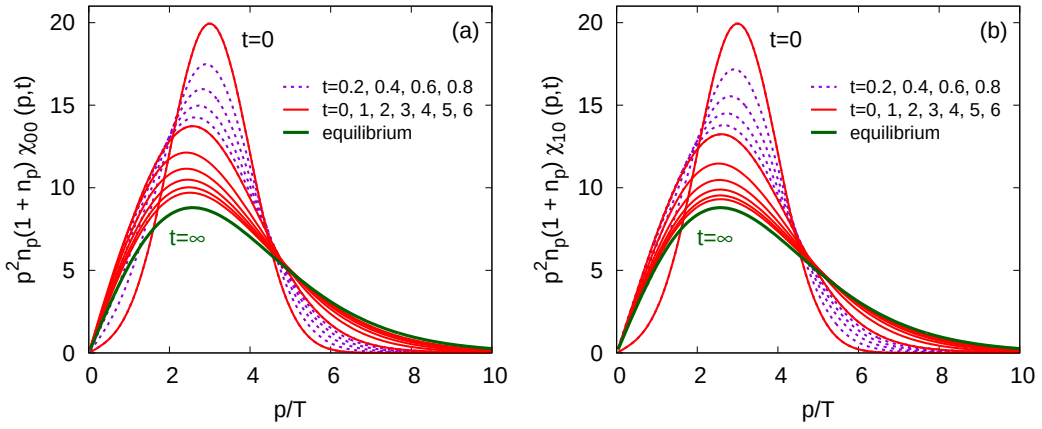

Figure 2.2: Evolution of an initial condition towards equilibrium in the linearized Boltzmann equation. (a) A spherically symmetric ($l = 0$) initial condition and (b) an initial condition proportional to the first spherical harmonic $H_{10}(\hat{\boldsymbol{p}})$ approaching to equilibrium. The solid lines show time steps in units of $1.0\,T/\mu_A$ and the dotted lines show time steps of $0.2\,T/\mu_A$, where $\mu_A = g^2 C_A m_D^2 \ln(T/m_D)/8\pi$.

with $p_0 = 3T_o$ and $\sigma^2 = T_o$. The numerical procedure for solving Eq. (2.6) for the l partial waves is as follows. The momentum space is discretized, and an implicit scheme is used to perform the update step. Then the equation is written as a matrix equation form. By using the conjugate gradient algorithm, we invert the matrix to solve the equation. Fig. 2.2 shows how the two initial conditions evolve as a function of time. Ultimately, the two solutions approach to the equilibrium distribution Eq. (2.23), where δT and $\boldsymbol{u}$ are determined by the total energy and momentum in the initial state:

$$\delta T = \frac{\nu_g T}{4e_o} \int_{\boldsymbol{p}} E_p n_p (1 + n_p) \chi(t_o, \boldsymbol{p})\,, \tag{2.34}$$

$$\boldsymbol{u} = \frac{\nu_g}{e_o + \mathcal{P}_o} \int_{\boldsymbol{p}} \boldsymbol{p} n_p (1 + n_p) \chi(t_o, \boldsymbol{p})\,. \tag{2.35}$$

Here $e_o = \int_{\boldsymbol{p}} E_p n_p$ is the equilibrium energy density and $\mathcal{P}_o = e_o/3$ is the pressure. We have verified that the total energy and momentum of the system are conserved during the evolution, whereas the particle number changes due to the boundary conditions.

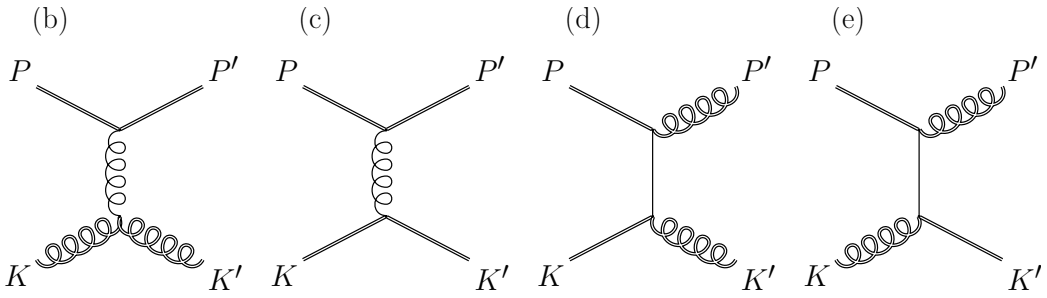

Figure 2.3: The rest t-channel $2 \leftrightarrow 2$ Feynman diagrams which contribute at a leading-log order, besides the pure glue diagram (a) in Fig. 2.1. External particles have momentum $\sim T$ and internal momentum is $\sim gT$. Double solid lines denote hard quarks, single solid lines denote soft quarks, double curly lines denote hard gluons, and single curly lines denote soft gluons. Time runs horizontally, either way.

2.3 Extension to Multi-component Plasmas

So far, we have discussed a pure glue theory. In QCD, quarks carry nearly half of the entropy, and it is important to extend the analysis to include quarks (see Fig. 2.3). The distribution function of fermions is[6]

$$n_p^F \equiv \frac{1}{e^{(E_p-\mu)/T_o}+1}\,. \tag{2.36}$$

For simplicity, we consider only zero chemical potential, $\mu = 0$. Similar to Eq. (2.5), each species is expanded as follows:

$$\delta f^a = n_p(1 \pm n_p)\chi^a(\boldsymbol{p})\,, \tag{2.37}$$

where $\pm$ corresponds to bosons and fermions, respectively.

In the presence of fermions, the collision operator is best expressed in terms of the sum of fermion and anti-fermion distribution functions, $\delta f^{q+\bar{q}} \equiv \delta f^q + \delta f^{\bar{q}}$, and the corresponding difference, $\delta f^{q-\bar{q}} \equiv \delta f^q - \delta f^{\bar{q}}$. To describe distribution functions of gluons and fermions in Fig. 2.1 and Fig. 2.3, we need the following collision terms (see Appendix A for details):

- The diagrams (a)-(c) in Fig. 2.1 and Fig. 2.3 contribute Fokker-Planck

[6]We define $\xi_F \equiv \int_{\boldsymbol{p}} n_p^F(1-n_p^F) = T^3/12$.

processes. The Fokker-Planck evolution loss term is given by

$$\mathcal{C}^a_{\text{FPloss}}[\chi, \boldsymbol{p}] = T\mu_a \frac{\partial}{\partial \boldsymbol{p}^i}\left(n_p(1+n_p)\frac{\partial}{\partial \boldsymbol{p}^i}\left[\frac{\delta f^a}{n_p(1+n_p)}\right]\right) . \tag{2.38}$$

Here the drag coefficient depends on species[7]

$$\frac{\mathrm{d}\boldsymbol{p}}{\mathrm{d}t} = -\mu_a \hat{\boldsymbol{p}} \qquad \text{with} \qquad \mu_a = \frac{g^2 C_{R_a} m_D^2}{8\pi} \ln\left(\frac{T}{m_D}\right) , \tag{2.39}$$

and the Debye mass is given by [29]

$$m_D^2 = \sum_a^{g\mathrm{f}\bar{\mathrm{f}}} \frac{g^2 C_{R_a}}{d_A} \nu_a \int_{\boldsymbol{p}} \frac{n_p^a(1 \pm n_p^a)}{T} = \frac{g^2 T^2}{3}\left(N_c + \frac{N_f}{2}\right) . \tag{2.40}$$

- The Fokker-Planck gain terms are

$$\mathcal{C}^a_{\text{FPgain}} = \frac{g^2 C_{R_a}}{T m_D^2 d_A}\left[\frac{1}{p^2}\frac{\partial}{\partial p} p^2 n_p(1+n_p)\right]\frac{\mathrm{d}E}{\mathrm{d}t} + \frac{g^2 C_{R_a}}{T m_D^2 d_A}\left[\frac{\partial}{\partial \boldsymbol{p}} n_p(1+n_p)\right]\cdot\frac{\mathrm{d}\boldsymbol{P}}{\mathrm{d}t} . \tag{2.41}$$

  Here $\mathrm{d}E/\mathrm{d}t$ and $\mathrm{d}\boldsymbol{P}/\mathrm{d}t$ are the total work and momentum transfer per volume on hard particles similar to Eqs. (2.10) and (2.11), except that the total diffusion current reads

$$\boldsymbol{j}_{\boldsymbol{p}} = -\sum_a \nu_a T \mu_a n_p^a (1 \pm n_p^a) \frac{\partial \chi^a(\boldsymbol{p})}{\partial \boldsymbol{p}} . \tag{2.42}$$

- The diagrams (d) and (e) in Fig. 2.3 contribute to the sum of fermion and anti-fermion distributions. The collision term is

$$\mathcal{C}^q_{qg} + \mathcal{C}^{\bar{q}}_{qg} = -2\gamma \frac{n_p^F(1+n_p^B)}{p}\left[\chi^q(\boldsymbol{p}) + \chi^{\bar{q}}(\boldsymbol{p}) - 2\chi^g(\boldsymbol{p})\right] , \tag{2.43}$$

  where we defined

$$\gamma \equiv \frac{g^4 C_F^2\, \xi_{BF}}{4\pi} \ln(T/m_D) , \qquad \xi_{BF} \equiv \int_{\boldsymbol{k}} \frac{n_k^F(1+n_k^B)}{k} = \frac{T^2}{16} . \tag{2.44}$$

[7] C_{R_a} is the Casimir of particle a.

The analogous gluon collision term is given by

$$\mathcal{C}^g_{qg} = -\sum_q^{\mathrm{f}} \frac{\nu_q}{\nu_g}(\mathcal{C}^q_{qg} + \mathcal{C}^{\bar{q}}_{qg})\,, \tag{2.45}$$

where the sum is over the light quark flavors.

- For the difference between fermion and anti-fermion, the collision term is (from diagrams (d) and (e) in Fig. 2.3)

$$\begin{aligned}(C^q_{qg} - C^{\bar{q}}_{qg}) = &-2\gamma \frac{n_p^F(1+n_p^B)}{p}\left[\chi^q(\boldsymbol{p}) - \chi^{\bar{q}}(\boldsymbol{p})\right] \\ &+ \frac{2\gamma}{\xi_{BF}} \frac{n_p^F(1+n_p^B)}{p} \int_{\boldsymbol{k}} \frac{n_k^F(1+n_k^B)}{k}\left[\chi^q(\boldsymbol{k}) - \chi^{\bar{q}}(\boldsymbol{k})\right]\,,\end{aligned} \tag{2.46}$$

where the first line is the loss term and the second line is the gain term.

With these collision operators, the distribution functions of gluon, the fermion sum, and the fermion difference are governed by

$$\left(\frac{\partial}{\partial t} + \boldsymbol{v}_p \cdot \frac{\partial}{\partial \boldsymbol{x}}\right) \delta f^g(t,\boldsymbol{x},\boldsymbol{p}) = \mathcal{C}^g_{\mathrm{FPloss}} + \mathcal{C}^g_{\mathrm{FPgain}} + \mathcal{C}^g_{qg}\,, \tag{2.47}$$

$$\begin{aligned}\left(\frac{\partial}{\partial t} + \boldsymbol{v}_p \cdot \frac{\partial}{\partial \boldsymbol{x}}\right) \delta f^{q+\bar{q}}(t,\boldsymbol{x},\boldsymbol{p}) = &(\mathcal{C}^q_{\mathrm{FPloss}} + \mathcal{C}^{\bar{q}}_{\mathrm{FPloss}}) \\ &+ (\mathcal{C}^q_{\mathrm{FPgain}} + \mathcal{C}^{\bar{q}}_{\mathrm{FPgain}}) + (\mathcal{C}^q_{qg} + \mathcal{C}^{\bar{q}}_{qg})\,,\end{aligned} \tag{2.48}$$

$$\left(\frac{\partial}{\partial t} + \boldsymbol{v}_p \cdot \frac{\partial}{\partial \boldsymbol{x}}\right) \delta f^{q-\bar{q}}(t,\boldsymbol{x},\boldsymbol{p}) = (\mathcal{C}^q_{\mathrm{FPloss}} - \mathcal{C}^{\bar{q}}_{\mathrm{FPloss}}) + (\mathcal{C}^{\mathrm{q}}_{qg} - \mathcal{C}^{\bar{q}}_{\bar{q}g})\,. \tag{2.49}$$

Here we note that for the fermion difference, the Fokker-Planck evolution is same as before, but the gain terms cancel.

2.4 Summary

We reformulated the leading-log Boltzmann equation as a Fokker-Planck equation. The work and momentum transfer during the diffusion process appear as additional gain terms which are essential to conserve energy and momentum. In a leading-log order, we have only t-channel $2 \leftrightarrow 2$ scatterings of hard particles, and bremsstrahlung does not contribute except the $\boldsymbol{p} \to 0$ limit. At low momentum, an absorptive boundary condition should be used, and consequently the number of particles changes during the Fokker-Planck

evolution. Fig. 2.2 shows a sample evolution of non-equilibrium distributions, ultimately approaching to equilibrium.

The formulation presented in this chapter will be used to compute spectral densities and simulate the jet-medium response in the following two chapters.

Chapter 3

Spectral Densities

3.1 Introduction

Phenomenologically, the Quark-Gluon Plasma (QGP) is believed to behave like nearly perfect fluid [28]. To investigate the properties of the plasma, lattice QCD solves the theory non-perturbatively from first principles. The main goal of lattice QCD simulations is to compute correlation functions which are related to spectral densities. Many properties of the QGP dynamics are reflected in spectral densities. For instance, spectral densities are important to study the spectrum of photons and dileptons, and their slopes at zero frequency give information about transport coefficients.

Specifically, lattice QCD simulations estimate Euclidean correlators of conserved currents, $\langle J(\tau, \boldsymbol{x}) J(0, \boldsymbol{0})\rangle$. The relation between these correlators and the spectral densities of the corresponding operators is given by the following integral transformation [29]:

$$\int \mathrm{d}^3\boldsymbol{x}\, e^{i\boldsymbol{k}\cdot\boldsymbol{x}} \,\langle J(\tau, \boldsymbol{x}) J(0, \boldsymbol{0})\rangle = \int \frac{\mathrm{d}\omega}{2\pi}\, \rho^{JJ}(\omega, \boldsymbol{k})\, \frac{\cosh(\omega(\tau - 1/2T))}{\sinh(\omega/2T)}\,. \tag{3.1}$$

The lattice data have been analyzed for non-perturbative information about transport [30, 31, 32, 33, 34, 35], but the information from the Euclidean measurements are limited [36, 37]. In order to characterize the properties completely, a number of lattice groups have begun to simulate the current-current correlators at finite spatial momentum [38, 39].

At zero spatial momentum, the shear, bulk modes of the $T^{\mu\nu}$ spectral densities and current spectral densities have been determined previously at leading order [40, 41]. With the Boltzmann equation formulated in the last chapter, we can compute spectral densities for finite frequency and momentum. In the presence of weak gravitational and electromagnetic fields, the spectral

densities of $T^{\mu\nu}$ and J^{μ} are determined at small frequency and momentum $\omega, \boldsymbol{k} \sim g^4 T$ [26].

In this chapter, we will discuss all possible modes of the spectral densities of $T^{\mu\nu}$ and J^{μ}. The numerical results of spectral densities exhibit a smooth transition from free-streaming quasi-particles to hydrodynamics. This transition will be analyzed with conformal, non-conformal hydrodynamics and diffusion equation up to second order in gradient expansions. To respond to the *Point I* mentioned in Chapter 1, we will determine the valid regime for the macroscopic theory as

$$\omega,\, ck \lesssim 0.35 \left[\frac{\eta}{(e_o + \mathcal{P}_o)c_s^2}\right]^{-1} \qquad \text{(first hydro)}\,, \tag{3.2}$$

$$\omega,\, ck \lesssim \ \ 0.7 \left[\frac{\eta}{(e_o + \mathcal{P}_o)c_s^2}\right]^{-1} \qquad \text{(second hydro)}\,. \tag{3.3}$$

Ultimately, these perturbative spectral densities can be compared to the lattice data and the AdS/CFT with a model for the high frequency continuum [42]. In kinetic theory, there is a clear distinction between the inverse temperature $\sim 1/T$ and the relaxation time $\sim 1/g^4 T$. In contrast, there is no such distinction in strongly coupled theories. This difference will be reflected by the fact that there is no visible transport peak in the AdS/CFT spectral densities [43, 44]. By using a simple model for the QCD spectral densities, we will compare the kinetic theory results with the AdS/CFT spectral densities in Section 3.7.

3.2 Spectral Densities of $T^{\mu\nu}$

To compute the spectral densities of $T^{\mu\nu}$, we turn on weak gravitational fields in the flat space. Then we measure the linear response to the perturbation by solving the Boltzmann equation derived in Chapter 2. This response will be analyzed with hydrodynamics and free-streaming solutions in two extreme limits.

Spectral densities of $T^{\mu\nu}$ are given by the imaginary part of the associated retarded Green's function:

$$\rho^{\mu\nu\alpha\beta}(\omega, \boldsymbol{k}) = -2\,\mathrm{Im} G_R^{\mu\nu\alpha\beta}(\omega, \boldsymbol{k})\,. \tag{3.4}$$

To compute the correlation function, we turn on weak gravitation fields. Then the metric is

$$g^{\mu\nu}(t, \boldsymbol{x}) = \eta^{\mu\nu} + h^{\mu\nu}(t, \boldsymbol{x})\,, \tag{3.5}$$

where $\eta^{\mu\nu} = \mathrm{diag}(-1, +1, +1, +1)$ is the flat metric and $h^{\mu\nu}(t, \boldsymbol{x})$ is linear

disturbance. With the perturbation, the action is linearly perturbed

$$S(g_{\mu\nu}) \simeq S_o + \frac{1}{2}\int \mathrm{d}^4X\, T^{\mu\nu}(X)\, h_{\mu\nu}(X)\,, \tag{3.6}$$

and the interaction Hamiltonian is

$$H_{\rm int}(t) = -\int \mathrm{d}^3\boldsymbol{x}\, \mathcal{L}_{\rm int} = -\frac{1}{2}\int \mathrm{d}^3\boldsymbol{x}\, T^{\alpha\beta}(X) h_{\alpha\beta}(X)\,. \tag{3.7}$$

By using the linear response theory, the averaged energy-momentum tensor is

$$\langle T^{\mu\nu}(X)\rangle_{h_{\alpha\beta}} = T^{\mu\nu}_{\rm eq}(X) - \frac{-i}{2}\int \mathrm{d}^4Y\, \theta(X^0-Y^0)\left\langle\left[T^{\mu\nu}(X), T^{\alpha\beta}(Y)\right]\right\rangle' h_{\alpha\beta}(Y)\,. \tag{3.8}$$

Here $T^{\mu\nu}_{\rm eq}(X) = [e(T)+\mathcal{P}(T)]u^\mu(X)u^\nu(X) + \mathcal{P}(T)g^{\mu\nu}(X)$, and $'$ indicates that the average is over the partition function in flat space. In Fourier space, Eq. (3.8) reads

$$\langle T^{\mu\nu}(\omega,\boldsymbol{k})\rangle_{h_{\alpha\beta}} = \left.\frac{\partial T^{\mu\nu}_{\rm eq}}{\partial h_{\alpha\beta}}\right|_{h=0} h_{\alpha\beta}(\omega,\boldsymbol{k}) - \frac{1}{2}G_R^{\mu\nu\alpha\beta}(\omega,\boldsymbol{k})\, h_{\alpha\beta}(\omega,\boldsymbol{k})\,, \tag{3.9}$$

where the associated retarded Green's function is

$$G_R^{\mu\nu\alpha\beta}(\omega,\boldsymbol{k}) = -i\int_{-\infty}^{\infty}\mathrm{d}t\int_{-\infty}^{\infty}\mathrm{d}\boldsymbol{x}\, e^{+i\omega t - i\boldsymbol{k}\cdot\boldsymbol{x}}\,\theta(t)\left\langle\left[T^{\mu\nu}(t,\boldsymbol{x}), T^{\alpha\beta}(0,\boldsymbol{0})\right]\right\rangle'\,. \tag{3.10}$$

In order to classify the relevant correlators, we choose $\boldsymbol{k}$ along z-axis. Then there are four possible modes according to their transformation properties under the rotation around z-axis:

- Shear Mode – $G_R^{zxzx}(\omega,k)$,
- Sound Mode – $G_R^{zzzz}(\omega,k)$,
- Transverse Tensor Mode – $G_R^{xyxy}(\omega,k)$,
- Bulk Mode – $\eta_{\mu\nu}\eta_{\alpha\beta}G_R^{\mu\nu\alpha\beta}(\omega,k)$.

3.2.1 Shear, Sound, and Transverse Tensor Mode

In this section, we compute the shear, sound, and transverse tensor modes of the $T^{\mu\nu}$ spectral densities by turning on spatial perturbations. Then the high frequency behaviors are analyzed with the free-streaming Boltzmann solutions.

In the curved spacetime, we need the Boltzmann equation in the covariant form:

$$\frac{1}{E_{\boldsymbol{p}}}\left(P^{\mu}\frac{\partial}{\partial X^{\mu}}-\Gamma^{\lambda}_{\mu\nu}P^{\mu}P^{\nu}\frac{\partial}{\partial P^{\lambda}}\right)f(t,\boldsymbol{x},\boldsymbol{p})=C[f,\boldsymbol{p}]\,, \tag{3.11}$$

where

$$\Gamma^{\lambda}_{\mu\nu}=\frac{1}{2}g^{\lambda\rho}\left(\partial_{\nu}g_{\rho\nu}+\partial_{\nu}g_{\mu\rho}-\partial_{\rho}g_{\mu\nu}\right)\,. \tag{3.12}$$

In Eq. (3.11), $\partial f/\partial E_p$ should be understood as zero. Except in the bulk mode, the metric is perturbed only in the spatial components:

$$g_{ij}(t,\boldsymbol{x})=\eta_{ij}+h_{ij}(t,\boldsymbol{x})\,. \tag{3.13}$$

Specifically, we turn on $h_{zx}(t,z)$, $h_{zz}(t,z)$, and $h_{xy}(t,z)$ for the shear, sound, and transverse tensor mode, respectively.

We linearize the Boltzmann equation around the equilibrium distribution which now depends on the background metric:

$$f(t,\boldsymbol{x},\boldsymbol{p})=n_p^h+\delta f(t,\boldsymbol{x},\boldsymbol{p})\,, \tag{3.14}$$

$$n_p^h=\frac{1}{\exp\left[\sqrt{\boldsymbol{p}^i(\eta_{ij}+h_{ij})\boldsymbol{p}^j}/T\right]-1}\,. \tag{3.15}$$

By substituting Eq. (3.14) into Eq. (3.11) and linearizing with respect to h_{ij}, the Boltzmann equation becomes

$$\left(\frac{\partial}{\partial t}+\boldsymbol{v}_p\cdot\frac{\partial}{\partial\boldsymbol{x}}\right)\delta f+n_p(1+n_p)\frac{p^ip^j}{2E_{\boldsymbol{p}}T}\frac{\partial h_{ij}}{\partial t}=C[\delta f,\boldsymbol{p}]\,. \tag{3.16}$$

In Fourier space, this equation reads

$$\begin{aligned}(-i\omega+i\boldsymbol{v}_p\cdot\boldsymbol{k})\delta f(\omega,\boldsymbol{k},p)-i\omega n_p(1+n_p)\frac{p^ip^j}{2E_{\boldsymbol{p}}T}h_{ij}(\omega,\boldsymbol{k})&\\ =\;T\mu_A\frac{\partial}{\partial p^i}\left(n_p(1+n_p)\frac{\partial\chi(\boldsymbol{p})}{\partial p^i}\right)+\;(\text{gain terms})\,.&\end{aligned} \tag{3.17}$$

Without the gain terms, this is a linear elliptic partial differential equation. It can be discretized to be a matrix equation, and can be solved by the matrix inversion. We use the conjugate gradient method to solve the equation in Fourier space (see Appendix B for details).

After solving for $\delta f(\omega,\boldsymbol{k})$, the energy-momentum tensor can be computed

from kinetic theory:

$$T^{ij}(\omega,\boldsymbol{k}) = \nu_g \int \frac{\mathrm{d}^3\boldsymbol{p}\sqrt{-g}}{(2\pi)^3}\frac{p^i p^j}{2E_{\boldsymbol{p}}}\left[n_p^h + \delta f(\omega,\boldsymbol{k})\right] ,$$
$$= -\mathcal{P}_o h_{ij}(\omega,\boldsymbol{k}) + \left[\nu_g \int \frac{\mathrm{d}^3\boldsymbol{p}}{(2\pi)^3}\frac{p^i p^j}{2E_{\boldsymbol{p}}}\frac{\delta f(\omega,\boldsymbol{k})}{h_{ij}(\omega,\boldsymbol{k})}\right] h_{ij}(\omega,\boldsymbol{k}) . \tag{3.18}$$

By comparing with Eq. (3.9), the square bracketed term in the second line gives the Green's function: $-G_R^{zxzx}(\omega,k)$, $-\frac{1}{2}G_R^{zzzz}(\omega,k)$, and $-G_R^{xyxy}(\omega,k)$ for the shear, sound, and transverse tensor modes, respectively.

The numerical results for the spectral densities are shown as solid lines in Fig. 3.1 (a)-(c). They exhibit a smooth transition from free-streaming quasi-particles at high momentum to hydrodynamics at small momentum. In the following, we will compare the high frequency behaviors with free-streaming solutions.

At high frequency, the spectral densities are determined by the free-streaming Boltzmann equation:

$$\left(\frac{\partial}{\partial t} + \boldsymbol{v}_p \cdot \frac{\partial}{\partial \boldsymbol{x}}\right)\delta f + n_p(1+n_p)\frac{p^i p^j}{2E_{\boldsymbol{p}}}\frac{\partial h_{ij}}{\partial t} = 0 . \tag{3.19}$$

By solving for δf, the solution is

$$\delta f(\omega,\boldsymbol{k}) = \frac{p^i p^j}{2E_{\boldsymbol{p}}}\frac{-\omega h_{ij} n_p(1+n_p)}{\omega - \boldsymbol{v}_p\cdot\boldsymbol{k} + i\epsilon} , \tag{3.20}$$

where we introduced the $+i\epsilon$ in order to specify the retarded response. With $\mathrm{Im}\,[1/(x+i\epsilon)] = -\pi\delta(x)$, we take the imaginary part of the response function to determine the spectral densities from the free theory:

$$\frac{\rho^{zxzx}(\omega,k)}{2\omega} = \frac{\nu_g\pi^3}{30}\frac{\omega^2}{k^3}\left(1-\frac{\omega^2}{k^2}\right)\theta(k-\omega) \qquad (\omega \text{ and } k \text{ large}) , \tag{3.21}$$

$$\frac{\rho^{zzzz}(\omega,k)}{2\omega} = \frac{\nu_g\pi^3}{15}\frac{1}{k}\left(\frac{\omega}{k}\right)^4\theta(k-\omega) \qquad (\omega \text{ and } k \text{ large}) , \tag{3.22}$$

$$\frac{\rho^{xyxy}(\omega,k)}{2\omega} = \frac{\nu_g\pi^3}{120}\frac{1}{k}\left[1-\left(\frac{\omega}{k}\right)^2\right]^2\theta(k-\omega) \qquad (\omega \text{ and } k \text{ large}) , \tag{3.23}$$

where $\theta(k-\omega)$ is the unit step function. The free solutions are shown as dotted lines in Fig. 3.1 (a)-(c). They are consistent with the Boltzmann results at large ω and k except near the light cone $\omega = k$.

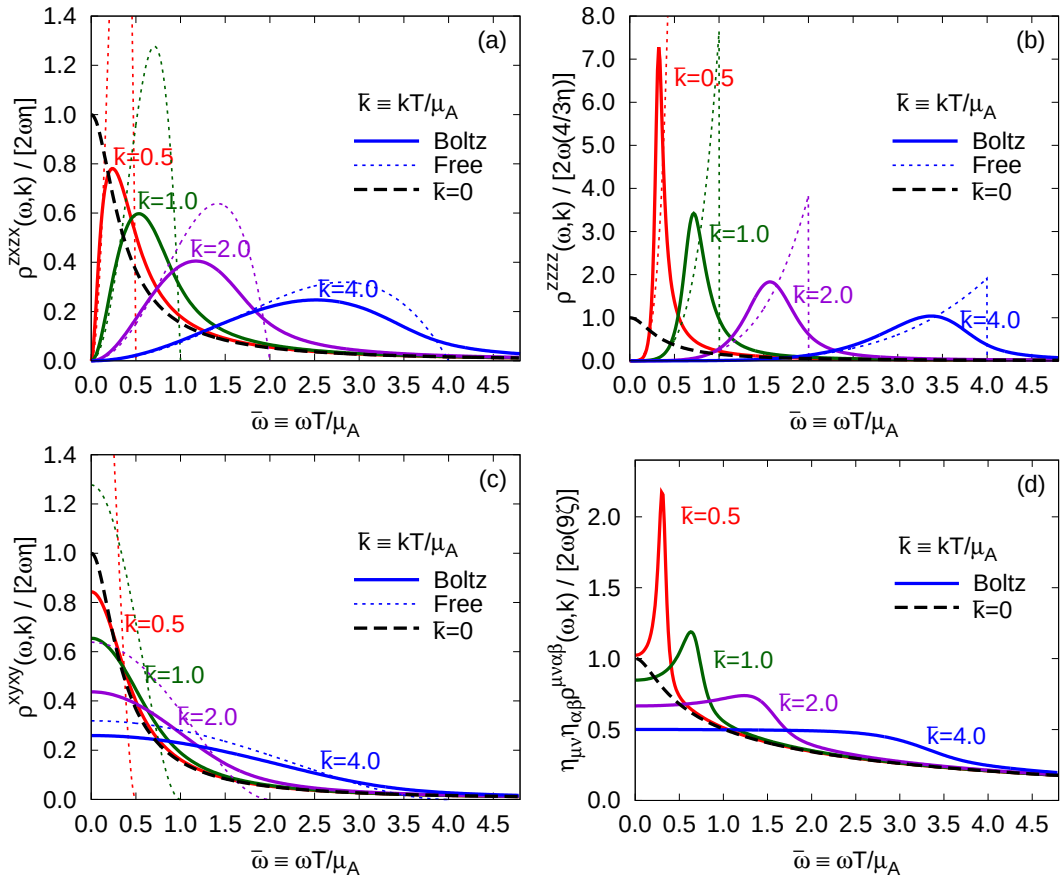

Figure 3.1: The spectral density $\rho(\omega) = -2\,\mathrm{Im}\,G_R(\omega,k)$ for (a) the shear mode $G_R^{zxzx}(\omega,k)$, (b) the sound mode $G_R^{zzzz}(\omega,k)$, (c) the transverse tensor mode $G^{xyxy}(\omega,k)$, and (d) the bulk mode $\eta_{\mu\nu}\eta_{\alpha\beta}\,G_R^{\mu\nu\alpha\beta}(\omega,k)$. The solid lines show the complete results, while the dotted lines show the expectations of the free-streaming Boltzmann equation. The variables ω and k are measured in units of μ_A/T, with $\mu_A = g^2 C_A m_D^2 \ln(T/m_D)/8\pi$. The shear viscosity is $\eta/(e_o + \mathcal{P}_o) = 0.4613\,T/\mu_A$ so that $\bar{\omega} = 0.5, 1.0, 2.0, 4.0$ corresponds to $\omega\,\eta/[(e_o + \mathcal{P}_o)c_s^2] \simeq 0.7, 1.4, 2.8, 5.6$, as chosen in Fig. 3.3.

3.2.2 Bulk Mode

In this section, we determine the bulk mode of the $T^{\mu\nu}$ spectral densities. This mode involves temporal perturbations, and needs to be treated with special care.

In the bulk mode, the metric is perturbed in the following form:

$$g_{\mu\nu}(X) = [1 + H(X)]\eta_{\mu\nu}\,. \tag{3.24}$$

If the gravitational perturbation is independent of time, hydrostatic equilibrium will be reached when $T(\boldsymbol{x})\sqrt{-g_{00}(\boldsymbol{x})} = (\text{const})$. Motivated by this observation, we assume for the time-dependent perturbation

$$T_H(X)\sqrt{-g_{00}(X)} = (\text{const}) \tag{3.25}$$

at equilibrium. Then we will show that the equilibrium distribution is given by

$$n_p^H(t, \boldsymbol{x}, \boldsymbol{p}) = \frac{1}{\exp\big[-P(X)\cdot U_H(X)/T_H(X)\big] - 1}\,, \tag{3.26}$$

where

$$T_H(X) = T_o\Big[1 - H(X)/2\Big]\,, \tag{3.27}$$

$$U_H^\mu(X) = \Big(1/\sqrt{-g_{00}(X)},\, 0,\, 0,\, 0\Big)\,. \tag{3.28}$$

Since $P^\mu P^\nu g_{\mu\nu} = -m^2[T_H(X)]$, the combination $-P(X)\cdot U_H(X)$ in the distribution function is

$$\begin{aligned} -P(X)\cdot U_H(X) &= -\frac{E_p(X)}{\sqrt{-g_{00}(X)}}\,, \\ &= \sqrt{p^i\left[\delta_{ij} + H(X)\delta_{ij}\right]p^j + m^2[T_H(X)]}\,. \end{aligned} \tag{3.29}$$

With a non-trivial dispersion relation, the Boltzmann equation is given by [45]

$$\frac{1}{E_{\boldsymbol{p}}}\left(P^\mu\frac{\partial}{\partial X^\mu} - \frac{1}{2}\frac{\partial m^2(X)}{\partial X^\mu}\frac{\partial}{\partial P_\mu} - \Gamma^\lambda_{\mu\nu}P^\mu P^\nu\frac{\partial}{\partial P^\lambda}\right) f(t, \boldsymbol{x}, \boldsymbol{p}) = C[f, \boldsymbol{p}]\,, \tag{3.30}$$

where the mass term can be understood as a force term

$$-\frac{1}{2E_{\boldsymbol{p}}}\frac{\partial m^2(X)}{\partial X^\mu}\frac{\partial f}{\partial P_\mu} = -\frac{\partial E_{\boldsymbol{p}}}{\partial \boldsymbol{x}}\frac{\partial f}{\partial \boldsymbol{p}}\,. \tag{3.31}$$

The mass depends on the distribution function [16]

$$m^2(X) = \frac{2\nu_g}{d_A} g^2 C_A \int \frac{\mathrm{d}^4 P^\mu \sqrt{-g}}{(2\pi)^4}\, \theta(E_p)\, 2\pi\delta(-P^2) f_{\boldsymbol{p}}\,. \tag{3.32}$$

In equilibrium, $m^2 = g^2 C_A T^2/6$.

We linearize the distribution around the equilibrium Eq. (3.26)

$$f(t,\boldsymbol{x},\boldsymbol{p}) = n_p^H(t,\boldsymbol{x},\boldsymbol{p}) + \delta f(t,\boldsymbol{x},\boldsymbol{p})\,, \tag{3.33}$$

where δf will be verified to be of order $(c_s^2 - 1/3) \sim g^4$. Therefore, δf is neglected when determining the gluon mass at leading order. The mass is then simply the time-dependent equilibrium mass

$$m^2[T_H(X)] \simeq m^2(T_0) - T^2 \frac{\partial m^2}{\partial T^2}\bigg|_{T_o} H(X)\,. \tag{3.34}$$

With this observation, we substitute Eq. (3.33) into Eq. (3.30). After careful algebra, the Boltzmann equation becomes

$$(\partial_t + \boldsymbol{v}_p \cdot \partial_{\boldsymbol{x}})\, \delta f - n_p(1+n_p) \frac{\tilde{m}^2}{2E_{\boldsymbol{p}} T} \partial_t H = C[\delta f, \boldsymbol{p}]\,, \tag{3.35}$$

where

$$\tilde{m}^2 \equiv m^2 - T^2 \frac{\partial m^2}{\partial T^2}\bigg|_{T=T_o} = -C_A \beta(g) \frac{T_o^2}{6}\,. \tag{3.36}$$

Here we used the definition of the beta function

$$\beta(g) \equiv \mu^2 \frac{\partial g^2(\mu^2)}{\partial \mu^2} = -\frac{g^4}{16\pi^2}\left(\frac{11 C_A}{3} - \frac{4}{3} N_f T_F\right)\,. \tag{3.37}$$

Since the source term in Eq. (3.35) is proportional to the beta function, the equilibrium distribution $n_p^H(t,\boldsymbol{x},\boldsymbol{p})$ is an exact solution of the Boltzmann equation in a conformal theory. In the presence of weak conformal breaking, δf is of order $(c_s^2 - 1/3) \sim g^4$, and we can solve Eq. (3.35) for $\delta f/g^4 H$.

Once δf is determined, the stress tensor can be computed [16, 45, 46]

$$T^\mu{}_\mu(X) = -e(T_H(X)) + 3\mathcal{P}(T_H(X)) - \nu_g \int \frac{\mathrm{d}^3\boldsymbol{p}}{(2\pi)^3} \frac{\tilde{m}^2}{E_{\boldsymbol{p}}} \delta f(X) \tag{3.38}$$

In Fourier space, the stress tensor is

$$T^{\mu}{}_{\mu}(\omega,k) = -\frac{1}{2}T\frac{\partial}{\partial T}(-e+3\mathcal{P})\Big|_{T_o} H(\omega,k) - \frac{1}{2}\left[\nu_g \int \frac{\mathrm{d}^3\boldsymbol{p}}{(2\pi)^3}\frac{\tilde{m}^2}{E_{\boldsymbol{p}}}\frac{\delta f(\omega,k)}{H(\omega,k)/2}\right] H(\omega,k)\,, \quad (3.39)$$

where the term in square brackets is $\eta_{\mu\nu}\eta_{\alpha\beta}G_R^{\mu\nu\alpha\beta}(\omega,k)$. Due to the factor $\tilde{m}^2$, the correlator is of order $(c_s^2-1/3)^2$. Fig. 3.1 (d) shows the numerical results of the bulk spectral densities.

Since the bulk mode is sensitive to the soft momenta, the free-streaming Boltzmann equation does not provide a good description at large ω and k. If we neglect the collision term in Eq. (3.35), the free-streaming solution is

$$\delta f(\omega,k) = \frac{\tilde{m}^2}{2E_pT}\frac{\omega H n_p(1+n_p)}{\omega-\boldsymbol{v}_p\cdot\boldsymbol{k}+i\epsilon}\,. \quad (3.40)$$

This solution does not obey the boundary condition $\chi(\boldsymbol{p})\big|_{\boldsymbol{p}\to 0}=0$ in Eq. (2.18), and $T^{\mu}{}_{\mu}$ is infrared divergent. Thus the free solution is not shown in Fig. 3.1 (d).

3.3 Linearized Hydrodynamics

Fig. 3.1 shows rich hydrodynamic structures at low frequency and momentum limit. In this section, we will construct the linearized hydrodynamics and determine all the transport coefficients up to second order. To analyze the hydrodynamic limit, the spectral densities of the sound mode will be compared with hydrodynamic solutions. For the bulk mode, non-conformal hydrodynamics will be also discussed.

Hydrodynamics is an effective theory at long distances compared to mean free path. In the absence of external force, it is given by a conservation law

$$\nabla_\mu T^{\mu\nu}_{\mathrm{hydro}} = 0\,, \quad (3.41)$$

with a constituent relation

$$T^{\mu\nu}_{\mathrm{hydro}} = T^{\mu\nu}_{\mathrm{ideal}} + \pi^{\mu\nu} + \Pi\Delta^{\mu\nu}\,. \quad (3.42)$$

Here $\pi^{\mu\nu}$ is the traceless part for the conformal limit, whereas Π is the non-conformal part with the projector $\Delta^{\mu\nu}=g^{\mu\nu}+u^\mu u^\nu$. In the ideal hydrody-

namics, we have only equilibrium energy-momentum tensor:

$$T^{\mu\nu}_{\rm ideal} = \big[e(T) + \mathcal{P}(T)\big] g^{\mu\nu} + \mathcal{P}(T) g^{\mu\nu} \,, \tag{3.43}$$

where $e(T)$ is energy density and $\mathcal{P}(T)$ is pressure at temperature T. In the presence of perturbation, energy density and flow velocity are disturbed away from equilibrium

$$e(t, \boldsymbol{x}) \simeq e_o + \epsilon(t, \boldsymbol{x}) \qquad \text{and} \qquad u^\mu(t, \boldsymbol{x}) \simeq (1, \boldsymbol{u}(t, \boldsymbol{x})) \,, \tag{3.44}$$

where $\epsilon(t, \boldsymbol{x})$ and $\boldsymbol{u}(t, \boldsymbol{x})$ are the linearized disturbance. The strains are expanded as derivatives of ϵ (or equivalently δT) and $\boldsymbol{u}$

$$\pi^{\mu\nu} = \pi^{\mu\nu}_1 + \pi^{\mu\nu}_2 + \cdots \,, \tag{3.45}$$

$$\Pi = \Pi_1 + \Pi_2 + \cdots \,. \tag{3.46}$$

Depending on the order, we will provide the explicit expressions of the strains in the following.

In the first order hydrodynamics, the gradient expansion yields

$$\pi^{\mu\nu}_1 = -\eta \langle \nabla^\mu u^\nu \rangle \qquad \text{and} \qquad \Pi_1 = -\zeta \nabla_\mu u^\mu \,. \tag{3.47}$$

Here η is the shear viscosity and ζ is the bulk viscosity. The angle brackets denote the symmetric, traceless, and spatial component of the tensor

$$\langle A_{\mu\nu} \rangle = \frac{1}{2} \Delta^{\mu\alpha} \Delta^{\nu\beta} \left(A_{\alpha\beta} + A_{\beta\alpha} - \frac{2}{3} g_{\alpha\beta} A_\gamma{}^\gamma \right) \,. \tag{3.48}$$

The dissipative part of the stress tensor, which is conformally invariant and the second order in derivatives, is given by [47]

$$\pi^{\mu\nu}_2 = \eta\tau_\pi \left[2u_\alpha R^{\alpha\langle\mu\nu\rangle\beta} u_\beta - 2 \left\langle \nabla^\mu \nabla^\nu \ln T \right\rangle \right] + \kappa \left[R^{\langle\mu\nu\rangle} - 2u_\alpha R^{\alpha\langle\mu\nu\rangle\beta} u_\beta \right] \,, \tag{3.49}$$

where $R^{\alpha\mu\nu\beta}$ ($R^{\mu\nu}$) is the Riemann (Ricci) tensor. τ_π and κ are the second order transport coefficients which will be determined numerically in the formulation of the Boltzmann equation. The equation of motion Eq. (3.41) with the constituent relation Eq. (3.49) gives the "static" hydrodynamic solutions. By using the lowest order equations of motion, Eq. (3.49) can be rewritten as a dynamic equation for $\pi^{\mu\nu}$:

$$\pi^{\mu\nu} = \pi^{\mu\nu}_1 - \tau_\pi \left\langle D\pi^{\mu\nu} \right\rangle + \kappa \left[R^{\langle\mu\nu\rangle} - 2u_\alpha R^{\alpha\langle\mu\nu\rangle\beta} u_\beta \right] \,. \tag{3.50}$$

This equation is similar to the phenomenological model of Israel and Stewart

[48, 49]. The non-linear generalization of these equations are used to simulate heavy ion collisions. The "dynamic" hydrodynamics consists of the equation of motion Eq. (3.41) and the constituent relation Eq. (3.50).

In non-conformal limit, the strains up to the second order can be written [50]

$$\pi^{\mu\nu} = \pi_1^{\mu\nu} + \eta\tau_\pi \left\langle D\sigma^{\mu\nu} \right\rangle + \kappa \left[R^{\langle\mu\nu\rangle} - 2u_\alpha R^{\alpha\langle\mu\nu\rangle\beta} u_\beta \right] + \kappa^* 2u_\alpha R^{\alpha\langle\mu\nu\rangle\beta} u^\beta \,, \tag{3.51}$$

$$\Pi = \Pi_1 + \zeta\tau_\Pi D(\nabla \cdot u) + \xi_5 R + \xi_6 u_\alpha u_\beta R^{\alpha\beta} \,, \tag{3.52}$$

where $\sigma^{\mu\nu} = 2\left\langle \nabla^\mu u^\nu \right\rangle$. τ_Π, κ^*, ξ_5, and ξ_6 are the non-conformal second order hydrodynamic coefficients and will be determined numerically. In the linearized hydrodynamics, we can neglect terms in the second order of u in Eqs. (3.49)-(3.52).

3.3.1 First Order Hydrodynamics

At low frequency, spectral densities are described by hydrodynamics. In the shear, sound, and transverse tensor modes, there are only spatial metric perturbations, $g_{ij} = \eta_{ij} + h_{ij}$. In the first order disturbance, the constituent relation is

$$T^{ij} = \mathcal{P}_o \left(\delta^{ij} - h_{ij}\right) + c_s^2 \, \epsilon\delta^{ij} - 2\eta \left\langle \partial^i u^j \right\rangle - \zeta\delta^{ij}\partial_l u^l - \eta\partial_t \left\langle h_{ij} \right\rangle - \frac{3}{2}\zeta\delta^{ij}\partial_t h \,, \tag{3.53}$$

where $h = h_{ll}/3$. From Eq. (3.41), the linearized equations of motion are

$$\partial_t \epsilon + (e_o + \mathcal{P}_o)\partial_i u^i = -\frac{3}{2}(e_o + \mathcal{P}_o)\partial_t h \,, \tag{3.54}$$

$$(e_o + \mathcal{P}_o)\partial_t u^i + \partial_j T^{ji} = -\mathcal{P}_o \, \partial_j h_{ji} \,. \tag{3.55}$$

For the shear mode, the only non-zero component of the metric perturbation is $h_{zx}(t, z)$. The equations of motion are easily solved in Fourier space, yielding

$$\epsilon(\omega, k) = 0, \tag{3.56}$$

$$u^z(\omega, k) = 0, \tag{3.57}$$

$$(e_o + \mathcal{P}_o)u^x(\omega, k) = \frac{\omega k \eta}{-i\omega + \frac{\eta k^2}{e_o + \mathcal{P}_o}} \,. \tag{3.58}$$

By substituting these solutions into the constituent relation Eq. (3.53), we determine the retarded Green's function in the first order hydrodynamic ap-

proximation:

$$T^{zx}(\omega,k) = -\mathcal{P}_o h_{zx}(\omega,k) - G_R^{zxzx}(\omega,k) h_{zx}(\omega,k)\,, \tag{3.59}$$

$$G_R^{zxzx}(\omega,k) = \frac{-\eta\omega^2}{-i\omega + \frac{\eta k^2}{e_o+\mathcal{P}_o}}\,. \tag{3.60}$$

The imaginary part of this retarded Green's function describes the behavior at small ω and k in Fig. 3.1 (a):

$$\frac{\rho^{zxzx}(\omega,k)}{2\omega} = \frac{\omega^2\eta}{\omega^2 + \left(\frac{\eta k^2}{e_o+\mathcal{P}_o}\right)^2} \qquad (\omega \text{ and } k \text{ small})\,. \tag{3.61}$$

The similar procedure applies to the sound and transverse tensor modes to determine the hydrodynamic solutions. In the sound mode, we have the non-zero metric perturbation $h_{zz}(\omega,k)$ in Fourier space. The hydrodynamic prediction is

$$T^{zz}(\omega,k) = -\mathcal{P}_o h_{zz}(\omega,k) - \frac{1}{2} G^{zzzz}(\omega,k) h_{zz}(\omega,k)\,, \tag{3.62}$$

$$G_R^{zzzz}(\omega,k) = (e_o+\mathcal{P}_o)\,\frac{c_s^2\omega^2 - i\Gamma_s\omega^3}{\omega^2 - c_s^2 k^2 + i\Gamma_s k^2\omega}\,, \tag{3.63}$$

where $\Gamma_s = (\frac{4}{3}\eta+\zeta)/(e_o+\mathcal{P}_o)$. In the transverse tensor mode, the non-zero metric perturbation is $h_{xy}(\omega,k)$ and the solution is

$$T^{xy}(\omega,k) = -\mathcal{P}_o\, h_{xy}(\omega,k) - G_R^{xyxy}(\omega,k) h_{xy}(\omega,k)\,, \tag{3.64}$$

$$G_R^{xyxy}(\omega,k) = -i\omega\eta\,. \tag{3.65}$$

In the bulk mode, the hydrodynamic solution is found as follows. Around the equilibrium, there are small disturbances ϵ and $\boldsymbol{u}$:

$$e(t,\boldsymbol{x}) = e(T_H(X)) + \epsilon(t,\boldsymbol{x}) \simeq e_o - \frac{1}{2} T c_V\, H(t,\boldsymbol{x}) + \epsilon(t,\boldsymbol{x})\,, \tag{3.66}$$

$$U^\mu(X) = U_H^\mu(X) + \delta U^\mu(X) \simeq \left(1 - \frac{1}{2}H(t,\boldsymbol{x}), u^i(t,\boldsymbol{x})\right)\,. \tag{3.67}$$

The stress tensor is given by the equilibrium tensor plus a small correction

$$T^{\mu\nu}(X) = \Big[e(T_H(X)) + \mathcal{P}(T_H(X))\Big] U_H^\mu U_H^\nu + \mathcal{P}(T_H(X)) g^{\mu\nu}(X) + \delta T^{\mu\nu}\,, \tag{3.68}$$

where

$$\delta T^{\mu\nu} = \int_{\boldsymbol{p}} \frac{p^\mu p^\nu}{E_{\boldsymbol{p}}} \delta f \,. \tag{3.69}$$

Substituting these expressions into the conservation law Eq. (3.41) yields the linearized equations of motion:

$$\partial_t \epsilon + (e_o + \mathcal{P}_o)\partial_i u^i = \frac{1}{2} T c_v \, \partial_t H \left(1 - 3c_s^2\right), \tag{3.70}$$

$$(e_o + \mathcal{P}_o)\partial_t u^i + \partial_j \tau^{ji} = 0. \tag{3.71}$$

Here the tensor τ^{ij} is

$$\tau^{ij} = c_s^2 \, \epsilon \delta^{ij} - 2\eta \left\langle \partial^i u^j \right\rangle - \zeta \delta^{ij} \, \partial_l u^l - \frac{3}{2} \zeta \partial_t H \, \delta^{ij} \,, \tag{3.72}$$

and we used the relation $c_s^2 = (e_o + \mathcal{P}_o)/T c_v$. In solving these equations, we can work to lowest order in the deviation from conformality, $(c_s^2 - 1/3)$. By noting $\zeta \sim (c_s^2 - 1/3)^2$ [18], while ϵ and $\boldsymbol{u}$ are of order $(c_s^2 - 1/3)$, we determine $T^\mu{}_\mu$ to leading order in $(c_s^2 - 1/3)$:

$$T^\mu{}_\mu(\omega, k) = -\frac{1}{2} T \frac{\partial}{\partial T}(-e + 3\mathcal{P})\bigg|_{T_o} H(\omega, k) + (-1 + 3c_s^2)\epsilon(\omega, k) + \frac{9}{2} i\omega\zeta H(\omega, k). \tag{3.73}$$

Then we solve for $\epsilon(t, \boldsymbol{x})$ from Eqs. (3.70) and (3.71), substitute the solution into $T^\mu{}_\mu$, and compare with Eq. (3.39) to determine the hydrodynamic prediction:

$$\eta_{\mu\nu}\eta_{\alpha\beta} G_R^{\mu\nu\alpha\beta}(\omega, k) = (1 - 3c_s^2)^2 \, T c_v \frac{-\omega^2 - i\Gamma_s \omega k^2}{\omega^2 - (c_s k)^2 + i\Gamma_s \omega k^2} - 9i\omega\zeta \,. \tag{3.74}$$

By using the thermodynamic result

$$(1 - 3c_s^2)^2 \, T c_v = \left(3s \frac{\partial}{\partial s} - T \frac{\partial}{\partial T}\right)(-e + 3\mathcal{P}) \,, \tag{3.75}$$

the imaginary part can be written

$$\eta_{\mu\nu}\eta_{\alpha\beta} \frac{\rho^{\mu\nu\alpha\beta}(\omega, k)}{2\omega} = \left(3s \frac{\partial}{\partial s} - T \frac{\partial}{\partial T}\right)(-e + 3\mathcal{P}) \frac{(c_s k)^2 \Gamma_s k^2}{(\omega^2 - c_s^2 k^2)^2 + (\omega \Gamma_s^2 k^2)^2} + 9\zeta \,. \tag{3.76}$$

As $k \to 0$, the first term approaches to a delta function [51]:

$$\eta_{\mu\nu}\eta_{\alpha\beta}\frac{\rho^{\mu\nu\alpha\beta}(\omega,k)}{2\omega} = \left(3s\frac{\partial}{\partial s} - T\frac{\partial}{\partial T}\right)(-e+3\mathcal{P})\left[\frac{\pi}{2}\delta(\omega-c_s k)+\frac{\pi}{2}\delta(\omega+c_s k)\right] + 9\zeta\,. \quad (3.77)$$

This explains the sharp sound pole seen in Fig. 3.1 (d).

3.3.2 Conformal Second Order Hydrodynamics in Sound Mode

At leading order in the coupling, the microscopic dynamics described by kinetic theory is conformal. Thus the conformal hydrodynamics can be used to describe the correlators in the long wavelength limit [47, 52]. In this section, we focus on the second order hydrodynamics in the conformal limit to analyze the sound mode.

By following the similar procedure in the first order hydrodynamics, we solve the equation of motion with the conformal constituent relation (up to second order in gradient expansions) to determine the hydrodynamic prediction. With the external field $h_{xy}(t,z)$, the Green's function of the transverse tensor mode is given by [47]

$$G_R^{xyxy}(\omega,k) = -i\eta\omega + \tau_\pi\eta\omega^2 - \frac{1}{2}\kappa(\omega^2+k^2)\,. \quad (3.78)$$

When $\omega = 0$, the source term of the Boltzmann equation in Eq. (3.17) is zero, while $G^{xyxy}(0,k) = -\kappa k^2/2$. Therefore, $\kappa = 0$ in a theory based on the conformal Boltzmann equation to this order [52]. Indeed, κ is determined by the k dependence of the static susceptibility:

$$G_R^{xyxy}(0,k) = -i\int \mathrm{d}^4X\, e^{i\boldsymbol{k}\cdot\boldsymbol{x}}\theta(t)\,\langle[T^{xy}(t,\boldsymbol{x}),T^{xy}(0,\boldsymbol{0})]\rangle' = -\frac{1}{2}\kappa k^2\,. \quad (3.79)$$

For pure glue theory, $\kappa = d_A T^2/18$ [51]. However, κ is of order T^2, and is significantly smaller than the other second order transport coefficient, $\eta\tau_\pi \sim T^2/g^8$, which can be determined by the linearized Boltzmann equation at a leading-log order. Specifically, we extract $\eta\tau_\pi$ by examining the real part of the response function in the limit $\omega \to 0$ at $k = 0$. For $N_c = 3$ and various numbers of flavors, the coefficient is numerically determined:

N_f	0	2	3
$\tau_\pi/(\eta/sT)$	6.32	6.65	6.46

.

τ_π has been determined previously in a complete leading order calculation in Ref. [52].

With the coefficients κ and τ_π known, we can calculate the retarded Green's function of the sound mode in two different ways: static hydrodynamics and dynamic hydrodynamics. With the external field $h_{zz}(t,z)$, the conservation law in Eq. (3.41) yields

$$\partial_t \epsilon + (e_o + \mathcal{P}_o)\partial_z u^z = -\frac{1}{2}(e_o + \mathcal{P}_o)\partial_t h_{zz}\,, \tag{3.80}$$

$$(e_o + \mathcal{P}_o)\partial_t u^z + c_s^2 \partial_z \epsilon + \partial_z \pi^{zz} = 0\,. \tag{3.81}$$

In the static hydrodynamics, the constituent relation in Eq. (3.49) gives

$$\pi^{zz} = -\frac{4}{3}\eta\partial_z u^z - \frac{2}{3}\eta\partial_t h_{zz} + \frac{2}{3}\eta\tau_\pi\partial_t^2 h_{zz} - \frac{4}{3}\eta\tau_\pi\frac{c_s^2}{(e_o+\mathcal{P}_o)}\partial_z^2\epsilon - \frac{1}{3}\kappa\partial_t^2 h_{zz}\,. \tag{3.82}$$

With the relation, we solve Eqs. (3.80) and (3.81) to determine the static solution:

$$G_R^{zzzz}(\omega,k) = (e_o+\mathcal{P}_o)\frac{c_s^2\omega^2 - i\Gamma_s\omega^3 + \tau_\pi\Gamma_s\omega^4 + \tau_\pi\Gamma_s c_s^2 k^2\omega^2 - \frac{2}{3}\kappa/(e_o+\mathcal{P}_o)\omega^4}{\omega^2 - c_s^2k^2 + i\Gamma_s\omega k^2 - \tau_\pi\Gamma_s c_s^2 k^4} \quad \text{(static)}\,. \tag{3.83}$$

The dynamic theory has the constituent relation in Eq. (3.50):

$$\tau_\pi\partial_t\pi^{zz} + \pi^{zz} = -\frac{2}{3}\eta\partial_t h_{zz} - \frac{4}{3}\eta\partial_z u^z - \frac{1}{3}\kappa\partial_t^2 h_{zz}\,, \tag{3.84}$$

and solving the equations of motion gives

$$G_R^{zzzz}(\omega,k) = (e_o+\mathcal{P}_o)\frac{c_s^2\omega^2 - i\Gamma_s\omega^3 - i\tau_\pi c_s^2\omega^3 - \frac{2}{3}\kappa/(e_o+\mathcal{P}_o)\omega^4}{\omega^2 - c_s^2k^2 + i\Gamma_s\omega k^2 + i\tau_\pi c_s^2\omega k^2 - i\tau_\pi\omega^3} \quad \text{(dynamic)}\,. \tag{3.85}$$

The dispersion relations for the static and the dynamic theories are

$$\omega^2 - c_s^2k^2 + i\Gamma_s\omega k^2 - \tau_\pi\Gamma_s c_s^2 k^4 = 0 \qquad \text{(static)}\,, \tag{3.86}$$

$$\omega^2 - c_s^2k^2 + i\Gamma_s\omega k^2 + i\tau_\pi c_s^2\omega k^2 - i\tau_\pi\omega^3 = 0 \qquad \text{(dynamic)}\,. \tag{3.87}$$

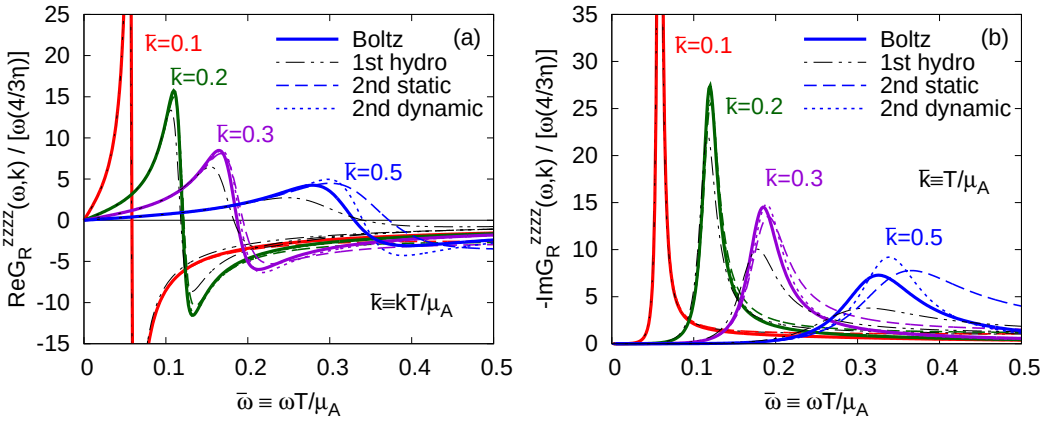

Figure 3.2: The (a) real and (b) imaginary parts of the retarded Green's function in the sound mode, $G_R^{zzzz}(\omega, k)$. The thick solid lines show the full numerical results from the Boltzmann equation, the thin dashed-dotted lines show the prediction of the first order hydrodynamics, the dashed lines show the prediction of the second order static theory (where $\pi^{\mu\nu}$ is determined by the constituent relation Eq. (3.49)), and the dotted lines show the prediction of the second order dynamic theory (where $\pi^{\mu\nu}$ is determined by a relaxation equation Eq. (3.50)). The shear viscosity is $\eta/(e_o+\mathcal{P}_o) = 0.4613\,T/\mu_A$ so that $\bar{\omega} = 0.1, 0.2, 0.3, 0.5$ corresponds to $\omega\,\eta/[(e_o+\mathcal{P}_o)c_s^2] \simeq 0.14, 0.28, 0.42, 0.7$.

In the static theory, the dispersion relation has only two solutions

$$\omega = \pm c_s k - \frac{i}{2}\Gamma_s k^2 \mp \frac{\Gamma_s}{2}\left(\frac{\Gamma_s}{4c_s} - \tau_\pi c_s\right) k^3 + \mathcal{O}(k^4)\,. \tag{3.88}$$

On the other hand, the dispersion relation in the dynamic theory has the two physical solutions of Eq. (3.88) and an extra solution

$$\omega = -\frac{i}{\tau_\pi} + \mathcal{O}(k^2)\,. \tag{3.89}$$

Since ω remains constant as $k \to 0$, this extra solution lies beyond the hydrodynamic approximation [47].

Fig. 3.2 compares the full spectral density of the sound mode with the first and the second order hydrodynamics. Roughly, at low frequencies and momentum of

$$\omega,\, ck \lesssim 0.35\,\left[\frac{\eta}{(e_o+\mathcal{P}_o)c_s^2}\right]^{-1} \qquad \text{(first hydro)}\,, \tag{3.90}$$

the first order hydrodynamics does a reasonable job in capturing the dynamics. The second order theory describes the Boltzmann results better until

$$\omega,\, ck \lesssim 0.7 \left[\frac{\eta}{(e_o+\mathcal{P}_o)c_s^2}\right]^{-1} \qquad \text{(second hydro)}\,. \tag{3.91}$$

For larger k, the second order dynamic theory becomes too reactive, whereas the static theory becomes too diffusive. Nevertheless, the dynamic theory seems to capture some aspects of the high frequency response better than the static theory. In heavy ion collisions, all hydrodynamic simulations so far have been based on the dynamical theory, which is hyperbolic and causal [11].

3.3.3 Non-conformal Second Order Hydrodynamics in Bulk Mode

Beyond the leading order in the coupling, there are corrections to the kinetic theory which break the scale invariance. Thus a non-conformal hydrodynamics must be used to describe the long wavelength response [50]. In the bulk mode, we determined the subleading non-conformal corrections to kinetic theory due to the scale dependence of gluon mass, and used this result to compute the bulk spectral function. In this section, we analyze the bulk mode to determine the non-conformal transport coefficients through the second order in gradient expansions.

Similar to the conformal coefficient κ, the non-conformal hydrodynamic coefficients κ^*, ξ_5, and ξ_6 in Eqs. (3.51) and (3.52) are determined by static susceptibilities. We turn on a static gravitational field of the following form:

$$g_{\mu\nu}(\boldsymbol{x}) = [1+H(\boldsymbol{x})]\eta_{\mu\nu} + \mathrm{diag}(0, h(\boldsymbol{x}), h(\boldsymbol{x}), h(\boldsymbol{x}))\,. \tag{3.92}$$

By substituting this form into the hydrodynamic equations, we compute a particular combination of the stress-energy tensor components

$$\langle 2T^{zz}(k) - [T^{xx}(k)+T^{yy}(k)]\rangle = 2\kappa^* k^2 H(k) + \kappa k^2 h(k)\,. \tag{3.93}$$

Similarly, we define (following Ref. [45])

$$\mathcal{O}_{\text{bulk}}(t,\boldsymbol{x}) \equiv 3c_s^2 T^0{}_0(t,\boldsymbol{x}) + T^i{}_i(t,\boldsymbol{x})\,, \tag{3.94}$$

and note that in the static gravitational field of Eq. (3.92)

$$\langle \mathcal{O}_{\text{bulk}}(k)\rangle = \left(9\,\xi_5 k^2 - \frac{3}{2}\,\xi_6 k^2\right) H(k) + 6\,\xi_5 k^2 h(k)\,. \tag{3.95}$$

Then all the coefficients are related to the static susceptibilities:

$$-i\int \mathrm{d}^4X\, e^{i\boldsymbol{k}\cdot\boldsymbol{x}}\theta(t)\,\langle[2T^{zz}(t,\boldsymbol{x})-T^{xx}(t,\boldsymbol{x})-\ T^{yy}(t,\boldsymbol{x})\,,\,T^{\mu}_{\ \mu}(0,\boldsymbol{0})]\rangle' = 2\,\kappa^* k^2\,, \tag{3.96}$$

$$-i\int \mathrm{d}^4X\, e^{i\boldsymbol{k}\cdot\boldsymbol{x}}\,\theta(t)\,\big\langle\big[\mathcal{O}_{\rm bulk}(t,\boldsymbol{x})\,,\,T^{\mu}_{\ \mu}(0,\boldsymbol{0})\big]\big\rangle' = 9\,\xi_5 k^2-\frac{3}{2}\,\xi_6 k^2\,, \tag{3.97}$$

$$-i\int \mathrm{d}^4X\, e^{i\boldsymbol{k}\cdot\boldsymbol{x}}\,\theta(t)\,\big\langle\big[\mathcal{O}_{\rm bulk}(t,\boldsymbol{x})\,,\,T^{i}_{\ i}(0,\boldsymbol{0})\big]\big\rangle' = 6\,\xi_5 k^2\,. \tag{3.98}$$

Since $T^{\mu}_{\ \mu}=\frac{\beta(g)}{2g^2}G_{\mu\nu}G^{\mu\nu}$ [53], every insertion of $T^{\mu}_{\ \mu}$ brings at least two powers of g. Thus we estimate that

$$\kappa^*=\xi_5=\xi_6=0+O(g^2) \tag{3.99}$$

In the Boltzmann equation, this must be considered as zero to the order we are working. Indeed, from Eqs. (3.16) and (3.35) the sources of δf induced by $H(\boldsymbol{x})$ and $h(\boldsymbol{x})$,

$$-\,n_p(1+n_p)\frac{\tilde{m}^2}{2E_{\boldsymbol{p}}T}\partial_t H \qquad \text{and} \qquad n_p(1+n_p)\frac{p^2}{2E_{\boldsymbol{p}}T}\partial_t h\,, \tag{3.100}$$

vanish for static gravitational fields.

To determine the coefficient τ_Π, we turn on a gravitational field $g_{\mu\nu}=[1+H(t,\boldsymbol{x})]\eta_{\mu\nu}$ and compute

$$\langle\mathcal{O}_{\rm bulk}(\omega,k)\rangle=-\frac{1}{2}\eta_{\mu\nu}G_R^{\mathcal{O}\mu\nu}(\omega,k)H(\omega,k)\,, \tag{3.101}$$

where

$$\eta_{\mu\nu}G_R^{\mathcal{O}\mu\nu}(\omega,k)=-i\int \mathrm{d}^4X\, e^{i\omega t-i\boldsymbol{k}\cdot\boldsymbol{x}}\theta(t)\,\big\langle\big[\mathcal{O}_{\rm bulk}(t,\boldsymbol{x}),T^{\mu}_{\ \mu}(0,\boldsymbol{0})\big]\big\rangle\ . \tag{3.102}$$

At $\boldsymbol{k}=0$, we substitute $g_{\mu\nu}=[1+H(t)]\eta_{\mu\nu}$ into the second order non-conformal hydrodynamic equations. Then

$$\langle\mathcal{O}_{\rm bulk}(\omega,0)\rangle=-\frac{1}{2}\Big[-9i\zeta\omega+9\zeta\tau_\Pi\omega^2\Big]H(\omega,0)\,, \tag{3.103}$$

where we used $\xi_5=\xi_6=0$. The quantity in square brackets is the hydrodynamic prediction for the response function. In kinetic theory, we turn on $g_{\mu\nu}=[1+H(t,\boldsymbol{x})]\eta_{\mu\nu}$ and measure the response $\mathcal{O}_{\rm bulk}(\omega,\boldsymbol{k})$ as described in

Section 3.2.2:

$$\mathcal{O}_{\text{bulk}}(\omega,k) = -\frac{1}{2}\left[\nu_g \int \frac{\mathrm{d}^3\boldsymbol{p}}{(2\pi)^3}\frac{3c_s^2\tilde{m}^2-(1-3c_s^2)p^2}{E_{\boldsymbol{p}}}\frac{\delta f(\omega,k)}{H(\omega,k)/2}\right]H(\omega,k)\,. \tag{3.104}$$

By comparing the functional form of our numerical results from kinetic theory to the hydrodynamic form at $\boldsymbol{k}=0$, we determine τ_Π:

N_f	0	2	3
τ_Π/τ_π	0.510	0.548	0.554

. (3.105)

Here we see that the relaxation time of bulk perturbations is similar to that of shear perturbations.

3.4 Extension to Multi-component Plasmas

So far, we computed the spectral densities of $T^{\mu\nu}$ for the pure glue theory. In this section, we extend the discussion to multi-component plasmas.

In Section 2.3, we formulated the Boltzmann equation in the presence of fermions. The spectral densities in multi-component plasmas can be computed by solving Eqs. (2.47)-(2.49) (see Appendix B for details). When the response functions are expressed in terms of appropriately scaled kinematic variables,

$$\bar{\omega} = \omega\frac{\eta}{(e_o+\mathcal{P}_o)c_s^2} \qquad \text{and} \qquad \bar{k} = ck\frac{\eta}{(e_o+\mathcal{P}_o)c_s^2}\,, \tag{3.106}$$

the spectral densities are essentially unchanged in all modes. Fig. 3.3 (a) shows the bulk spectral density in terms of these scaled variables for pure glue and three flavors. The relative agreement between these curves indicates the dominance of the Fokker-Planck evolution.

In the next section, we will discuss the spectral densities of J^μ, where a similar scaling is observed in all modes. In Fig. 3.3 (b), we plot the longitudinal spectral density for pure glue and $N_f=3$. With the scaled variables,

$$\bar{\omega} = \omega\frac{D}{c^2} \qquad \text{and} \qquad \bar{k} = k\frac{D}{c}\,, \tag{3.107}$$

the spectral density does not change.

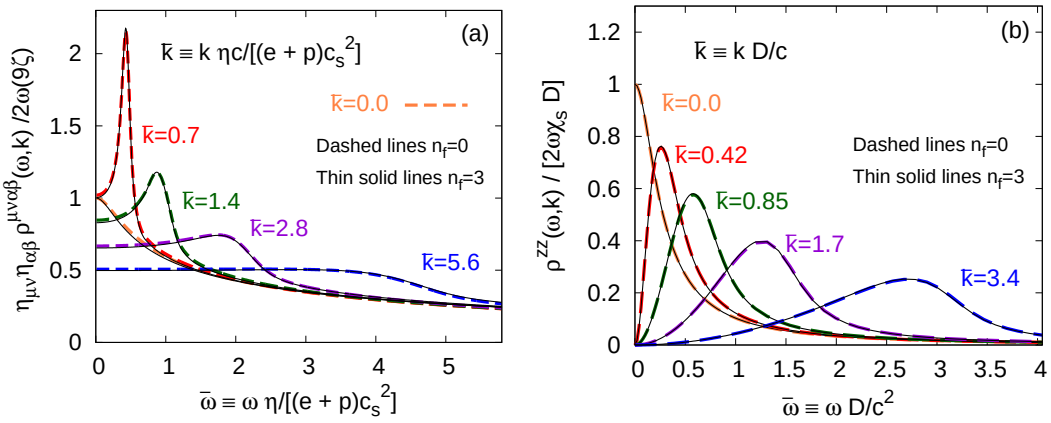

Figure 3.3: (a) The bulk spectral function for three flavors compared to the pure glue theory. In this figure, $\eta/(e_o + \mathcal{P}_o)$ is $0.917\,T/\mu_A$ for $N_f = 3$ and $0.461\,T/\mu_A$ for $N_f = 0$, so that the k values for $N_f = 0$ coincide with Fig. 3.1. (b) The longitudinal current-current spectral function for three flavors and the quenched approximation. In this figure $D = 0.944T/\mu_F$ for $N_f = 3$, while $D = 0.852T/\mu_F$ for $N_f = 0$, so that the k values for $N_f = 0$ coincide with Fig. 3.4. The results are similar in the other modes.

3.5 Spectral Densities of J^μ

In this section, we compute the spectral densities of J^μ by turning on weak gauge fields. The spectral densities exhibit a smooth transition from free-streaming solutions at high frequency to diffusion equation at low frequency. This transition will be analyzed with the second order diffusion equation.

For simplicity, we compute the current-current correlator of net strangeness. Since in a leading-log approximation the susceptibilities and correlators are diagonal in flavor space, the flavor and electromagnetic spectral densities are trivially related to this result. To determine the strangeness response function, we turn on gauge fields $A^\mu = (0, \boldsymbol{A})$. Then the interaction Hamiltonian and the current are

$$H_{\rm int} = -\int d^3\boldsymbol{x}\, J^\mu A_\mu \qquad \text{and} \qquad J^\mu(X) = \frac{\delta S}{\delta A^\mu(X)}\,. \tag{3.108}$$

By using the linear response, the average current is

$$\langle J^\mu(X)\rangle_A = +i\int \mathrm{d}^4Y\,\theta(X^0 - Y^0)\,\langle[J^\mu(X), J^\nu(Y)]\rangle\,A_\nu(Y)\,. \tag{3.109}$$

In Fourier space, it reads

$$\langle J^\mu(\omega,\boldsymbol{k})\rangle_A = -G_R^{\mu\nu}(\omega,\boldsymbol{k})A_\nu(\omega,\boldsymbol{k})\,, \tag{3.110}$$

where the corresponding retarded Green's function is

$$G_R^{\mu\nu}(\omega,\boldsymbol{k}) = -i\int \mathrm{d}^4X\, e^{i\omega t - i\boldsymbol{k}\cdot\boldsymbol{x}}\theta(t)\,\langle[J^\mu(t,\boldsymbol{x}),J^\nu(0,0)]\rangle\ . \tag{3.111}$$

By taking $\boldsymbol{k}$ along the z-direction, there are two independent correlators:

- Longitudinal Mode – $G_R^{zz}(\omega,k)$,
- Transverse Mode – $G_R^{xx}(\omega,k)$.

In the presence of the gauge fields coupled to the current, there is the Lorentz force acting on a charged particle:

$$\mathcal{F}^i = Q_a F^i{}_\mu v^\mu\,, \tag{3.112}$$

where Q_s is one for strange quarks, minus one for anti-strange quarks, and zero for all other species. Then the Boltzmann equation with the force term for the strangeness excess is given by

$$\frac{1}{E_{\boldsymbol{p}}}\left(p^\mu\partial_\mu + Q_a F^{\mu\nu}p_\nu\frac{\partial}{\partial p^\mu}\right)f^a = C^a[f,\boldsymbol{p}]\,. \tag{3.113}$$

In Fourier space, the equation becomes

$$(-i\omega + i\boldsymbol{v}_p\cdot\boldsymbol{k})\delta f^a(\omega,\boldsymbol{k}) - i\omega n_p(1\pm n_p)\,Q_aA_i\frac{p^i}{E_{\boldsymbol{p}}} = C^a[\delta f,\boldsymbol{p}]\,. \tag{3.114}$$

The gauge field does not disturb the fermion sum $\delta f^{q+\bar{q}}$, and only disturbs the fermion difference:

$$(-i\omega + i\boldsymbol{v}_p\cdot\boldsymbol{k})\delta f^{s-\bar{s}}(\omega,\boldsymbol{k}) - i\omega n_p(1-n_p)\,2Q_sA_i\frac{p^i}{E_{\boldsymbol{p}}} = C^{s-\bar{s}}[\delta f,\boldsymbol{p}]\,, \tag{3.115}$$

where $C^{s-\bar{s}}$ is given by Eq. (2.46). The numerical procedure to solve for $\delta f^{s-\bar{s}}$ is explained in Appendix B. After solving for δf, the current can be computed by

$$J^i = Q_s\,\nu_s\int\frac{\mathrm{d}^3\boldsymbol{p}}{(2\pi)^3}\frac{p^i}{E_{\boldsymbol{p}}}\delta f^{s-\bar{s}}\,. \tag{3.116}$$

By comparing with Eq. (3.110), the current-current response function is determined (see Fig. 3.4).

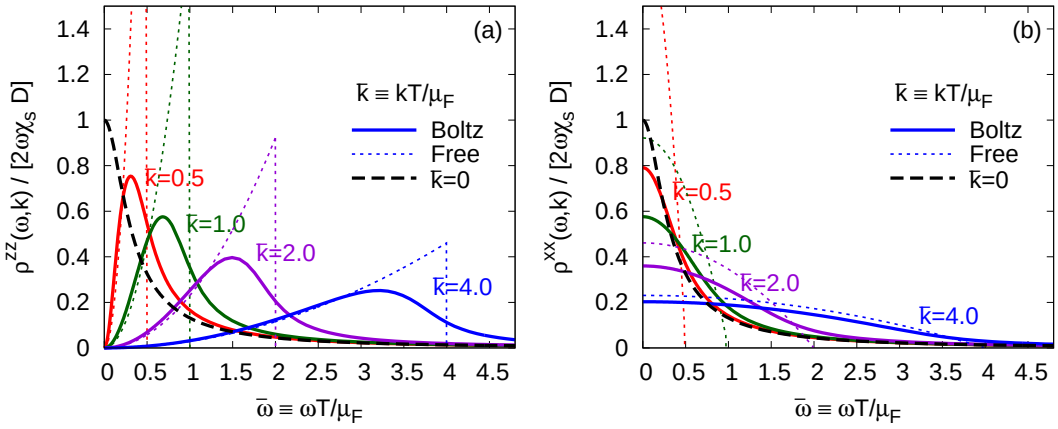

Figure 3.4: The current-current correlator for $N_c = 3$ and $N_f = 0$ in the (a) longitudinal and (b) transverse modes. $N_f = 0$ corresponds to the quenched approximation. $\mu_F \equiv g^2 C_F m_D^2 \ln(T/m_D)/8\pi$ is the drag coefficient of a quark in a leading-log approximation. The diffusion coefficient is $D = 0.852\, T/\mu_F$, so $\bar{\omega} = 0.5, 1.0, 2.0, 4.0$ corresponds to $\omega D/c^2 \simeq 0.42, 0.85, 1.7, 3.4$, as chosen in Fig. 3.3. The thin dotted lines show the results from the free-streaming Boltzmann equation.

The free-streaming solution of the Boltzmann equation describes the response at large ω and k. By following the procedure presented in Section 3.2.1, we find:

$$\frac{\rho^{zz}(\omega,k)}{2\omega} = \frac{\pi Q_s^2 \nu_s}{12}\frac{\omega^2}{k^3}\theta(k-\omega) \qquad (\omega \text{ and } k \text{ large})\,, \tag{3.117}$$

$$\frac{\rho^{xx}(\omega,k)}{2\omega} = \frac{\pi Q_s^2 \nu_s}{24}\frac{1}{k}\left(1-\frac{\omega^2}{k^2}\right)\theta(k-\omega) \qquad (\omega \text{ and } k \text{ large})\,. \tag{3.118}$$

These free solutions are shown as dotted lines in Fig. 3.4.

3.6 Second Order Diffusion Equation

In the long wavelength limit, the current-current correlator is described by the diffusion equation. The current is expressed in terms of gradients of the net strangeness $n_s(t,\boldsymbol{x})$ and the gauge field $\boldsymbol{A}(t,\boldsymbol{x})$. For a linearized theory invariant under parity, the current to the second order in the derivative expansion must have the following form:

$$J_s^i = -D\,\partial^i n_s + \sigma E^i - (\sigma\tau_J)\,\partial_t E^i + \kappa_B\,(\nabla\times\boldsymbol{B})^i\,. \tag{3.119}$$

Here D is the diffusion coefficient, σ is the conductivity, and τ_J and κ_B are new transport coefficients which will be determined numerically in the Boltzmann equation. In writing this expression, we neglected $\epsilon^{ijk}u^j B^k$ and $\mu\,\partial^i T$ which would appear in the magneto-hydrodynamics [54] (where B^i is not small) or at finite background chemical potential (where μ is not small). Similarly, we neglected the non-linear term $n_s u^i$, where $n_s(t,\boldsymbol{x})$ and $u^i(t,\boldsymbol{x})$ are small fluctuations. We also used lower order equations of motion to recognize that $\partial_t\partial^i n$ is actually third order in the derivative expansion.

The diffusion coefficient and the conductivity are related to each other. To see this, we first rewrite the constituent relation in terms of the chemical potential, and include one higher order term

$$J_s^i = -D\chi_s\,\partial^i\mu + \sigma E^i - (\sigma\tau_J)\,\partial_t E^i + \kappa_B\,(\nabla\times\boldsymbol{B})^i \\ + \left[\, c_1\chi_s\partial_t\partial^i\mu + \text{other higher order terms}\,\right]\,,$$

where χ_s is the static susceptibility

$$\chi_s = \frac{\mathrm{d}n_s}{\mathrm{d}\mu_s} = 2Q_s^2\nu_s\frac{1}{T}\int_{\boldsymbol{p}} n_p(1-n_p) = Q_s^2\nu_s\frac{T^2}{6}\,. \tag{3.120}$$

Then we note that a perturbation of the form

$$\mu(X) + A_0(X) = (\text{const}) \tag{3.121}$$

does not disturb the system away from equilibrium, *i.e.* $e^{-\beta(H-\mu N)}$ is constant. Thus all gradients in the constituent relation should involve the combination $\partial^i(\mu + A_0)$. This requirement forces a relation between the conductivity and the number diffusion coefficient

$$\chi_s D = \sigma\,, \tag{3.122}$$

and specifies the coefficient of one higher order term, $c_1 = D\tau_J$.

Since the constituent relation is specified, the conservation law $\partial_\mu J^\mu = 0$ can be solved for $J^0(\omega,k)$. By comparing the constituent relation Eq. (3.119) and linear response Eq. (3.110), the solution determines the current-current correlator at small momenta:

$$G^{zz}(\omega,k) = \frac{-\sigma\omega^2 - i\,(\sigma\tau_J)\,\omega^3}{-i\omega + Dk^2}\,, \tag{3.123}$$

$$G^{xx}(\omega,k) = -\,i\omega\sigma + (\sigma\tau_J)\,\omega^2 - \kappa_B k^2\,. \tag{3.124}$$

When $\omega = 0$, the source term in Eq. (3.115) is zero, while $G^{xx}(0,k) = -\kappa_B k^2$.

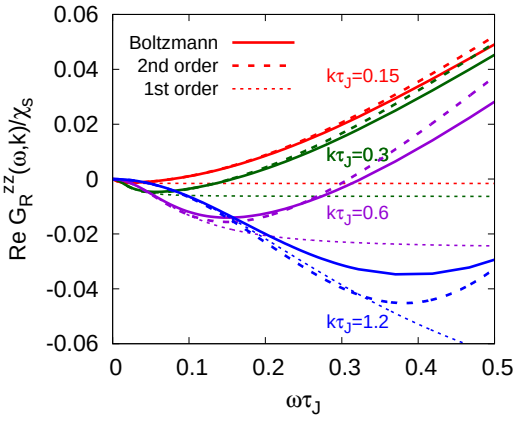

Figure 3.5: The real part of the retarded current-current correlator for $N_c = 3$ and $N_f = 0$. The thin dotted lines show the predictions of the first order diffusion equation, while the thick dashed lines show the prediction of the second order theory, Eq. (3.123). Both are compared to the full Boltzmann equation. ω and ck are in units of $\tau_J^{-1} = 0.312\,\mu_F/T$. Thus $k\tau_J = 0.15, 0.3, 0.6, 1.2$ corresponds to $\omega T/\mu_F \simeq 0.045, 0.09, 0.18, 0.36$ in Fig. 3.4, *i.e.* smaller than the first value in Fig. 3.4.

Therefore, $\kappa_B = 0$ in a theory based on the Boltzmann equation. This coefficient may be non-zero at higher order. In the limit of $\omega \to 0$ and $k = 0$, the real part of the Green's function gives the value of τ_J. For $N_c = 3$ and various numbers of flavors, we tabulate this transport coefficient in a leading-log approximation:

N_f	0	2	3
τ_J/D	3.776	3.756	3.748

.

The real part of the full Boltzmann result is compared with the first and the second order diffusion equation in Fig. 3.5. The second order solution captures some aspects of the high frequency behavior.

Eq. (3.119) is the "static" version of the second order diffusion equation. By using the first order expression $J_s^i = \sigma E^i - D\partial^i n_s$, the equation can be rewritten as the "dynamic" form:

$$J_s^i = -D\,\partial^i n_s + \sigma E^i - \tau_J\,\partial_t J_s^i\,. \tag{3.125}$$

This is the canonical form of the telegraph equation [55, 56]. In principle, we can use this relation to make the dynamic prediction, but this prediction will not be discussed in this thesis.

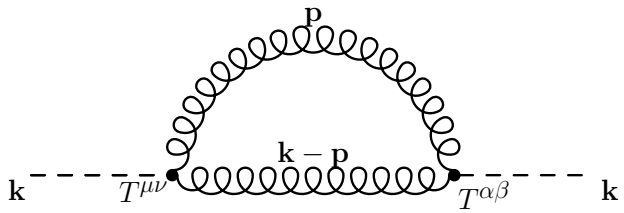

Figure 3.6: One-loop diagram contributing to the free spectral density of $T^{\mu\nu}$ for high frequency $\omega \sim T$ in pure glue theory. Curly lines denote gluons and dashed lines denote gravitons.

3.7 Comparison with AdS/CFT

So far, we calculated the spectral densities at small frequency and momentum, $\omega, k \sim g^4 T \ln(1/g)$. At weak coupling, there is scale difference between the relevant time scale $\sim 1/g^4 T \ln(1/g)$ and the inverse temperature $\sim 1/T$ [15, 57]. In contrast, in the AdS/CFT correspondence at strong coupling, there is no such distinction in the time scales. This difference is reflected by the fact that there is no visible transport peak in strongly coupled spectral densities [43, 44].

To compute the free spectral densities at high frequency $\sim T$ in QCD, we need to consider one-loop diagram shown in Fig. 3.6. After the frequency sum, the spectral densities consist of two parts, low frequency contribution and high frequency contribution [37]:

$$\rho(\omega, k) = \rho(\omega, k)\Big|_{\text{low}} + \rho(\omega, k)\Big|_{\text{high}} . \tag{3.126}$$

In particular, these free spectral densities have been computed in Ref. [58]. For example, the shear mode at $k = 0$ is given by

$$\frac{\rho^{zxzx(\omega)}}{2\omega} = \frac{4\pi^3}{225} d_A T^4 \delta(\omega) + \frac{d_A}{160\pi} \frac{\omega^3}{\tanh(\omega/4T)} . \tag{3.127}$$

Here the $\delta(\omega)$ part corresponds to the transport peak at the low frequency and the second term is the high frequency contribution. The free spectral densities in the shear mode are shown in Fig. 3.1 (a) as dotted lines, and they become a delta function at $k = 0$ limit. In the presence of interactions, this delta function is smeared and becomes the Boltzmann result shown as the dashed line[1]. In order to compare the QCD spectral densities at weak coupling with

[1]Solving the Boltzmann equation is equivalent to summing ladder diagrams [59].

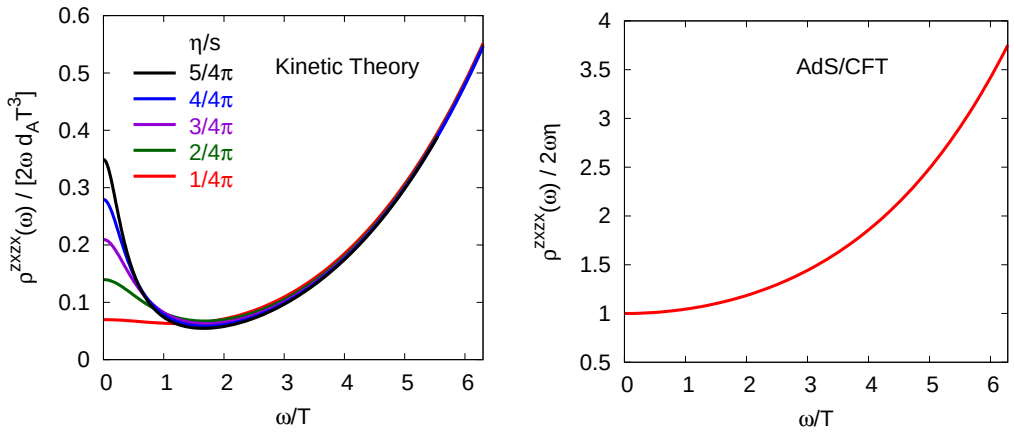

Figure 3.7: (a) The shear spectral density given by the QCD model in Eq. (3.128) as a function of η/s. The transport peak is visible for $\eta/s \gtrsim 3/4\pi$. (b) The shear spectral density given by the AdS/CFT at strong coupling ($\eta/s = 1/4\pi$). There is no transport peak. The numerical result is from Ref. [44].

the AdS/CFT results at strong coupling, we make a model for full spectral densities in QCD [60]:

$$(\text{QCD spectral density}) = (\text{Boltzmann}) + (\text{continuum})\,. \tag{3.128}$$

Here the Boltzmann numerical results are used as a function of T/μ_A (or η/sT), and the continuum part is given by the high frequency contribution (for the shear mode, the second term of Eq. (3.127)). For several values of η/s, the numerical results of the QCD model are shown in Fig. 3.7 (a). According to this model, we can estimate that kinetic theory is valid for $\eta/s \gtrsim 3/4\pi$, where the transport peak is visible. Fig. 3.7 (b) shows the corresponding spectral density given by the AdS/CFT at strong coupling. In the AdS/CFT, $\eta/s = 1/4\pi$ and there is no transport peak[2] [44].

3.8 Summary and Discussions

By solving the Boltzmann equation with weak gravitational and electromagnetic fields, we computed the spectral densities of $T^{\mu\nu}$ and J^μ shown in Fig. 3.1 and Fig. 3.4, respectively. The spectral densities exhibit a smooth

[2]Spectral densities in the weak coupling $\mathcal{N} = 4$ SYM are similar to those in the weak coupling QCD [61].

transition from free-streaming quasi-particles to hydrodynamics (or diffusion equation). The pure glue results are extended to including fermions in Fig. 3.3. With the appropriately scaled ω and k, the spectral densities do not change, indicating the dominance of the Fokker-Planck evolution.

Hydrodynamics describes the low frequency behaviors of spectral densities. From the slope of spectral densities at $\omega = 0$, we extracted all the first and second order transport coefficients which characterize the linear response in the hydrodynamic regime. With the shear viscosity η and a second order coefficient τ_π, the hydrodynamic solutions are determined up to second order. In Fig. 3.2, the sound spectral density is compared with hydrodynamics to analyze the valid limit of the macroscopic theory. The first and second order hydrodynamics are valid roughly up to

$$\omega,\, ck \lesssim 0.35 \left[\frac{\eta}{(e_o + \mathcal{P}_o)c_s^2}\right]^{-1} \qquad \text{(first hydro)}\,, \tag{3.129}$$

$$\omega,\, ck \lesssim \;\; 0.7 \left[\frac{\eta}{(e_o + \mathcal{P}_o)c_s^2}\right]^{-1} \qquad \text{(second hydro)}\,. \tag{3.130}$$

For higher momentum, the second order static solutions are too diffusive, whereas the dynamic theory becomes too reactive.

At high frequency, the spectral densities are compared with free-streaming solutions which are shown as dotted lines in Fig. 3.1 and Fig. 3.4. Near the light cone $\omega = k$, the free solutions have the sharp structure, but smeared shapes describe the Boltzmann results fairly well. When frequency and momentum are higher $\sim T$, we can calculate continuum result from one-loop diagram. In Section 3.7, we made a model for QCD spectral density by combining the continuum and the Boltzmann numerical result as a function of η/s. Roughly for $\eta/s \gtrsim 3/4\pi$, we can see a transport peak which is characteristic of kinetic theory. On the other hand, there is no visible peak in the spectral density given by the AdS/CFT, where the quasi-particle description is not applicable. This difference between kinetic theory and the AdS/CFT can be important to characterize the properties of the QGP in the lattice data.

The analysis and numerical work presented in this chapter will be continued to the next chapter in simulating the jet-medium response.

Chapter 4

Wake of a Heavy Quark Moving through Plasmas

4.1 Introduction

The quark-gluon plasma (QGP) is believed to be strongly coupled near the phase transition temperature $T_c \approx 160\text{MeV}$. Hydrodynamic simulations indicate that the shear viscosity to entropy density ratio is remarkably small [11, 63, 64, 65, 66, 67, 68]:

$$\frac{\eta}{s} \sim \frac{1 \leftrightarrow 5}{4\pi}\hbar\,. \tag{4.1}$$

This ratio is close to the AdS/CFT prediction, $\eta/s = \hbar/4\pi$ [69, 70]. At weak coupling, it is not easy to explain this ratio with a quasi-particle picture of plasmas. However, there is agreement of lattice data and resummed perturbation theory in pressure at somewhat high temperatures $\sim 5T_c$ [9]. This agreement suggests that a quasi-particle picture might be an appropriate theoretical tool to describe the properties of the QGP close to T_c [9, 71, 72]. The goal of this chapter is to compare the medium response to an energetic probe in the weakly coupled plasmas and strongly coupled plasmas.

Since the problem of determining spectral densities has been reformulated as a definite initial value problem in the last chapter, the resulting numerical procedure can be used to simulate jet-medium interactions. To respond to the *Point II* mentioned in Chapter 1, we investigate the steady state response of non-abelian plasmas to a heavy quark probe, at weak coupling and strong coupling [73]. When a heavy quark moves supersonically through the plasmas, the energy density and flux are redistributed. At long distances, the non-equilibrium disturbance produces sound waves and a diffusion wake, which are the so-called "Mach cone" structure. The original motivation for

investigating the Mach cone was the unusual structure of two particle correlations measured in heavy ion collisions [74, 75]. Today, these correlations are understood as the hydrodynamic response to fluctuations in the initial geometry [76, 77, 78, 79, 80]. Nevertheless, the interaction of a heavy quark with equilibrium plasma is the simplest way to analyze the plasma response to an energetic probe [81, 82, 83, 84, 85, 86, 87]. The goal of this study is not to explain current measurements, but rather to examine the differences between weak coupling and strong coupling, and to investigate the approach to hydrodynamics in both cases. The medium response to energetic partons is currently being studied by all the experimental collaborations in various ways [88]. Thus, this calculation, which analyzes the "jet" medium interaction precisely and determines a hydrodynamic source through second order in gradient expansions, may be useful for phenomenology in further studies.

In the strongly coupled theory, the stress tensor induced by a heavy quark was computed using the AdS/CFT correspondence [83, 85]. The approach to hydrodynamics and the short distance behavior were analyzed [84, 86, 89]. In particular, we will follow the hydrodynamic analysis of Ref. [86] to determine a hydrodynamic source through second order for weakly coupled and strongly coupled theories. In the AdS/CFT calculation, the $v \to 1$ limit was not analyzed due to various technical complications. (Here and below, v is the velocity of the heavy quark in units of c.) As discussed in Appendix E, it is possible to set $v = 1$ throughout the calculation by choosing a different set of gauge invariants.

At weak coupling, the appropriate source for kinetic theory was determined in Ref. [87], and several estimates have been given for how this kinetic source is transformed through the relaxation process to hydrodynamics [90]. We have simplified the source for kinetic theory considerably and determined the plasma response at large distances by solving the linearized kinetic theory. After comparing the hydrodynamic solution at large distances to the full (leading-log) kinetic theory results, the appropriate source at each order in the hydrodynamic expansion can be computed. As a by-product of the spectral densities, we determined the first and second order transport coefficients in the last chapter. These coefficients will be used to precisely determine the hydrodynamic source through second order.

This work is limited to the analysis of the kinetics for a single heavy quark moving from past infinity. It would be interesting to follow the evolution of a parton shower initiated at time $t = 0$ and the subsequent hydrodynamic response at late times [91, 92, 93].

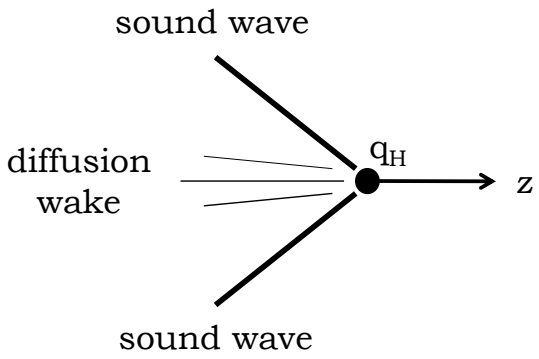

Figure 4.1: A schematic picture of a heavy quark (q_H) moving through the plasmas. There are sound waves and a diffusion wake behind the quark.

4.2 Kinetic Theory with a Heavy Quark Probe

We consider a heavy quark moving through a stationary high temperature plasmas from past infinity (see Fig. 4.1). In the presence of the heavy quark, the energy and momentum of the medium are redistributed, producing sound waves and a diffusion wake. In this section, we compute the energy density and flux distributions by solving the Boltzmann equation with the heavy quark source.

At weak coupling, kinetic theory determines the medium response to the heavy quark. For simplicity, we restrict the pure glue[1] QCD in a leading-log approximation. QCD in this limit is conformal, and the background stress tensor is

$$T_o^{\mu\nu} = \mathrm{diag}(e_o, \mathcal{P}_o, \mathcal{P}_o, \mathcal{P}_o)\,, \tag{4.2}$$

where $e_o = 3\mathcal{P}_o$. The heavy quark induces non-equilibrium response, $\delta T^{\mu\nu}$. By assuming that the quark moves in the z-direction, δT^{00} and δT^{0z} are functions of comoving transverse and longitudinal coordinates, x_T and x_L:

$$x_T = \sqrt{x^2 + y^2} \qquad \text{and} \qquad x_L = z - vt\,. \tag{4.3}$$

The rotational symmetry around the z-axis determines δT^{0x} and δT^{0y} in terms of δT^{0x_T}:

$$\delta T^{0x}(t, \boldsymbol{x}) = \delta T^{0x_T}(x_L, x_T)\cos\phi_r\,, \tag{4.4}$$
$$\delta T^{0y}(t, \boldsymbol{x}) = \delta T^{0x_T}(x_L, x_T)\sin\phi_r\,, \tag{4.5}$$

[1]Including fermions would only lead to minor changes to our results as can be seen from Fig. 3.3.

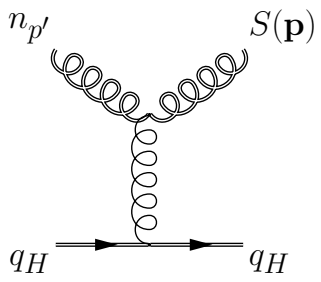

Figure 4.2: The Feynman diagram corresponding to the heavy quark source. Double curly lines denote hard gluons, a single curly line denotes a soft gluon, and a double solid line with arrows denotes a heavy quark. Time runs from left to right.

where $\phi_r = \tan^{-1}(y/x)$.

To determine the non-equilibrium response, we use the linearized Boltzmann equation:

$$\left(\frac{\partial}{\partial t} + \boldsymbol{v}_p \cdot \frac{\partial}{\partial \boldsymbol{x}}\right) \delta f(t, \boldsymbol{x}, \boldsymbol{p}) = C[f, \boldsymbol{p}] + S(t, \boldsymbol{x}, \boldsymbol{p})\,. \tag{4.6}$$

Here $S(t, \boldsymbol{x}, \boldsymbol{p})$ is the source of non-equilibrium gluons produced by the heavy quark moving through plasmas, which will be discussed in the next paragraph. In the last chapter, we determined the shear viscosity η and a second order hydrodynamic coefficient τ_π in terms of μ_A:

$$\frac{\eta}{e_o + \mathcal{P}_o} = 0.4613\,\frac{T}{\mu_A} \qquad \text{and} \qquad \frac{\tau_\pi}{\eta/(e_o + \mathcal{P}_o)} = 6.32\,. \tag{4.7}$$

These coefficients will be used in the hydrodynamic analysis. The shear viscosity that we obtained agrees with the prior results [17, 27]. The fact that τ_π is somewhat large ~ 6 compared to the viscous length is a generic result of kinetic theory [47, 52]. Finally, we note that μ_A records the transverse momentum broadening of a bath particle due to the soft scatterings. It is related to the soft part of jet-quenching parameter $\hat{q}$, $\hat{q}_{\rm soft}/2 = 2T\mu_A$ [94]. Thus, the leading-log limit provides a concrete relation between η/s and $\hat{q}$.

In the presence of a heavy quark moving at a constant velocity $\boldsymbol{v}$, the particles in equilibrium are scattered, producing the source around the quark (see Fig. 4.2):

$$S(t, \boldsymbol{x}, \boldsymbol{p}) = S(\boldsymbol{p})\delta^3(\boldsymbol{x} - \boldsymbol{v}t)\,. \tag{4.8}$$

The source term is computed in Appendix C. When $v = 1$, it is simplified at

a leading-log order:

$$S(\boldsymbol{p}) = \frac{\mu_F}{2d_A\xi_B} n_p(1+n_p)\left[-\frac{2}{p} + \frac{(1+2n_p)}{T} + \frac{(1+2n_p)}{T}\hat{\boldsymbol{p}}\cdot\hat{\boldsymbol{v}}\right] . \tag{4.9}$$

Here μ_F is the drag coefficient in a leading-log approximation

$$\begin{aligned}\mu_F(v) &= \frac{g^2 C_F m_D^2}{8\pi}\ln\left(\frac{T}{m_D}\right)\left[\frac{1}{v^2} - \frac{(1-v^2)}{2v^3}\ln\left(\frac{1+v}{1-v}\right)\right] , \\ &\Rightarrow \frac{g^2 C_F m_D^2}{8\pi}\ln\left(\frac{T}{m_D}\right) \qquad \text{for } v = 1 .\end{aligned} \tag{4.10}$$

In the last line, we implicitly took the coupling constant to zero before taking the $v \to 1$ limit, so that radiative energy loss can be neglected[2]. The leading-log energy loss of the heavy quark was computed in Refs. [96, 97]. The energy and momentum transferred to the medium per time (i.e. minus the drag force) are

$$\frac{\mathrm{d}P^\mu}{\mathrm{d}t} = \left(\frac{\mathrm{d}E}{\mathrm{d}t}, \frac{\mathrm{d}\boldsymbol{p}}{\mathrm{d}t}\right) = \mu_F(v)\left(v^2, \boldsymbol{v}\right) . \tag{4.11}$$

By multiplying the source Eq. (4.9) by p^μ and integrating over the phase space, it is straightforward to verify that the stress tensor satisfies

$$\partial_\mu \delta T^{\mu\nu} = \frac{\mathrm{d}P^\nu}{\mathrm{d}t}\delta^3(\boldsymbol{x} - \boldsymbol{v}t) . \tag{4.12}$$

Our strategy to determine the non-equilibrium stress tensor is the following. We take the Fourier transform of the Boltzmann equation in Eq. (4.6),

$$(-i\omega + i\boldsymbol{v}_p\cdot\boldsymbol{k})\delta f(\omega, \boldsymbol{k}, \boldsymbol{p}) = C[\delta f, \boldsymbol{p}] + 2\pi S(\boldsymbol{p})\delta(\omega - \boldsymbol{v}\cdot\boldsymbol{k}) , \tag{4.13}$$

and solve the equation for $\delta f(\omega, \boldsymbol{k}, \boldsymbol{p})$ in Fourier space. We use the same numerical formulation as in the previous chapter. Then we calculate the stress tensor in Fourier space using kinetic theory

$$\delta T^{0\mu}(\omega, \boldsymbol{k}) = 2d_A \int_{\boldsymbol{p}} p^\mu \delta f(\omega, \boldsymbol{k}, \boldsymbol{p}) . \tag{4.14}$$

By Fourier transforming the stress tensor back to coordinate space

$$\delta T^{0\mu}(t, \boldsymbol{x}) = \int_{\omega,\boldsymbol{k}} e^{-i\omega t + i\boldsymbol{k}\cdot\boldsymbol{x}}\delta T^{0\mu}(\omega, \boldsymbol{k}) , \tag{4.15}$$

[2]For a small but finite coupling constant, radiative energy loss is suppressed when the Lorentz factor of the heavy quark is not too large, $\gamma \lesssim \frac{m_D}{T\alpha_s} \sim 1/g$ [95].

we determine energy and momentum density distributions. Additional details about this procedure are given in Appendix D.

4.3 Comparison between Kinetic Theory and AdS/CFT

At strong coupling, we use the AdS/CFT correspondence to determine the non-equilibrium response. Roughly speaking, a heavy quark is described in the five dimensional AdS space with a trailing string (see Appendix E for details). As the heavy quark moves through the plasmas, the energy and momentum gained by the medium are again given by Eq. (4.11). However, the drag coefficient $\mu_F(v)$ is found by determining the energy and momentum flowing down the string into the black hole [98, 99, 100]:

$$\mu_F(v) = \frac{\pi}{2}\frac{\sqrt{\lambda}T^2}{\sqrt{1-v^2}}\,. \tag{4.16}$$

The stress tensor in the strongly coupled theory also satisfies Eq. (4.12) with the energy and momentum transfer given by the corresponding strong coupling formulas. The corresponding transport coefficients for the AdS/CFT are [47, 69, 70]

$$\frac{\eta}{e_o+\mathcal{P}_o} = \frac{1}{4\pi T} \qquad \text{and} \qquad \frac{\tau_\pi}{\eta/(e_o+\mathcal{P}_o)} = 4-2\ln 2\,. \tag{4.17}$$

For $v = 1$, we compare the medium response to the heavy quark probe in two asymptotic coupling limit: pure glue QCD at asymptotically weak coupling and $\mathcal{N} = 4$ SYM at asymptotically strong coupling. By noting the difference in the shear viscosities in Eqs. (4.7) and (4.17), we measure all length scales in units of the shear length:

$$L_o \equiv \frac{\frac{4}{3}\eta c}{(e_o+\mathcal{P}_o)c_s^2}\,, \tag{4.18}$$

where c_s^2 is the speed of sound squared. L_o is proportional to the mean free path in kinetic theory and equal to $1/\pi T$ for the AdS/CFT. At long distances where hydrodynamics is applicable, the amplitude of the disturbance is proportional to the strength of the energy loss. Thus, we divide the response by the corresponding drag coefficient μ_F for each theory, Eqs (4.10) and (4.16), respectively. With these rescalings, two theories produce identical stress tensors at asymptotically long distances, but differ in their approach to the hydrodynamic limit.

Fig. 4.3 and Fig. 4.4 compare the non-equilibrium stress in kinetic theory and the AdS/CFT. At long distances, both theories produce similar structures of sound waves and a diffusion wake. However, the distributions are distinguishable near the heavy quark at origin.

For the quantitative comparison, we plot angular distributions of the stress tensor in concentric circles of radius R around the head of the quark. Specifically, we define the energy density distribution

$$\frac{\mathrm{dE_R}}{\mathrm{d}\theta_\mathrm{R}} = 2\pi R^2 \sin\theta_R \, \delta T^{00}(\mathbf{R}) \,. \tag{4.19}$$

Here $\mathbf{R} = x_T \hat{\boldsymbol{x}}_T + x_L \hat{\boldsymbol{z}}$ and the polar angle is measured from the z-axis, where the heavy quark is moving along:

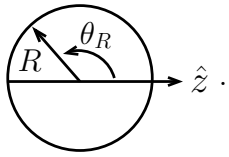

(4.20)

Similarly, the angular distribution of the energy flux is defined by

$$\begin{aligned} \frac{\mathrm{dS_R}}{\mathrm{d}\theta_\mathrm{R}} &= 2\pi R^2 \sin\theta_R \, \hat{R}^i \delta T^{0i}(\mathbf{R}) \,, \\ &= 2\pi R^2 \sin\theta_R \left[\cos\theta_R \, \delta T^{0z}(\mathbf{R}) + \sin\theta_R \, \delta T^{0x}(\mathbf{R})\right] \,. \end{aligned} \tag{4.21}$$

Numerical results for the angular distributions of the energy density and flux at several scaled distances $\mathfrak{R} \equiv R/L_o$ are shown in Fig. 4.5. There is a dramatic change in the AdS/CFT curves between $\mathfrak{R} = 5$ and $\mathfrak{R} = 1$, indicating a transition from hydrodynamic behavior to quantum dynamics. Since this quantum dynamics lies beyond the semi-classical Boltzmann approximation, no transition is seen in the kinetic theory curves.

There are limitations on the length scales that can be meaningfully studied in both theories. In kinetic theory, the resulting stress tensor is valid for distances, $R \gg 1/(g^2 T \ln g^{-1})$. For distances shorter than $1/(g^2 T \ln g^{-1})$, the collisionless non-abelian Vlasov equation should be used to describe the medium response [5, 101]. Similarly, the AdS/CFT calculation is limited to distances $x_L, x_T \gg 1/\sqrt{\gamma}\pi T$. For distances much less than $1/\sqrt{\gamma}\pi T$, the structure of stress tensor has been analyzed in detail [84, 89, 102]. In Fig. 4.5 where distances are $x_L, x_T \sim 1/\pi T$, the physics associated with these very short scales is not visible.

We are examining two extreme limits, infinitely weak and infinitely strong coupling at comparatively long distances. With this approach, some of the

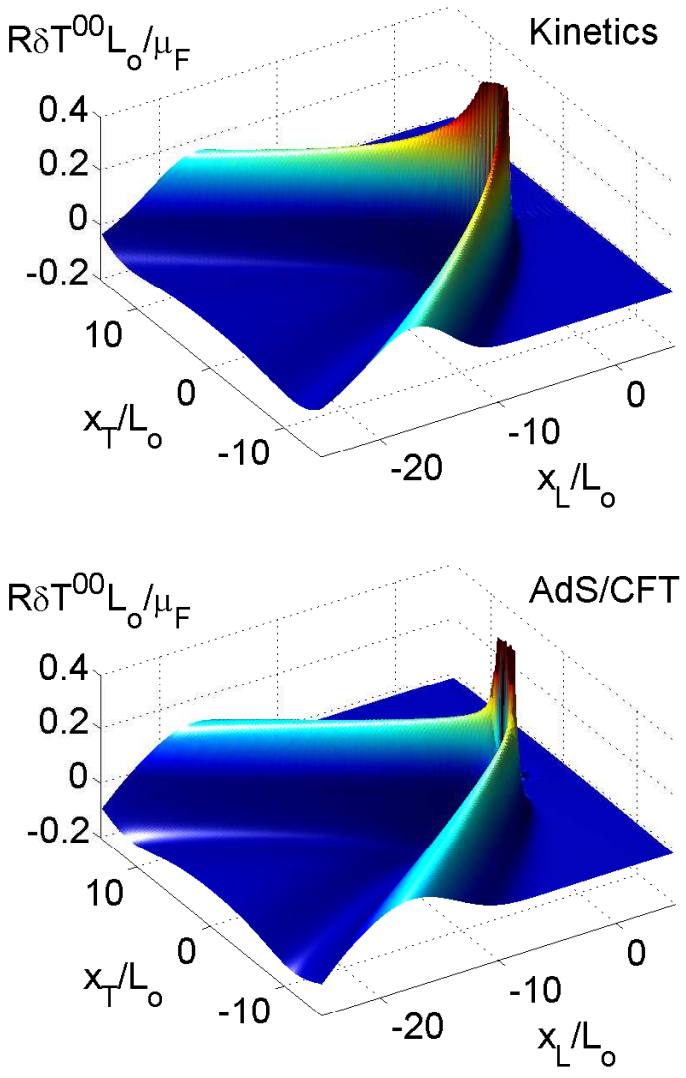

Figure 4.3: The energy density (in scaled units) times $R = \sqrt{x_T^2 + x_L^2}$ that is induced by a heavy quark probe in weakly coupled QCD and strongly coupled $\mathcal{N} = 4$ SYM. Here L_o is the shear length and μ_F is the drag coefficient for each case.

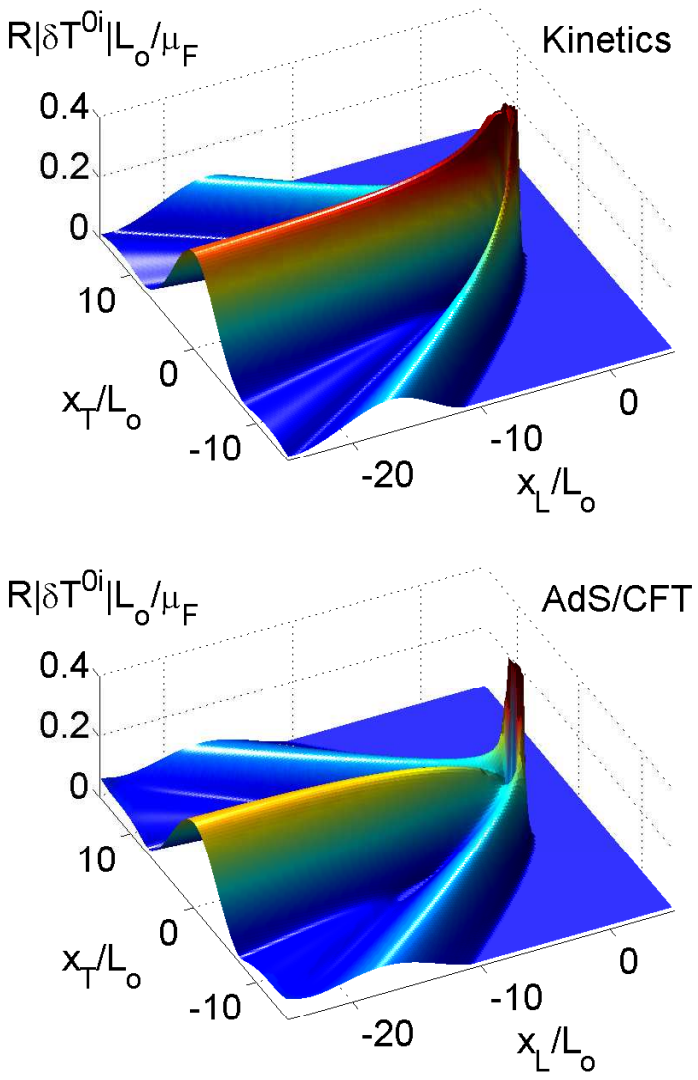

Figure 4.4: The magnitude of the Poynting vector $|T^{0i}|$ (in scaled units) times $R = \sqrt{x_T^2 + x_L^2}$ that is induced by a heavy quark probe in weakly coupled QCD and strongly coupled $\mathcal{N} = 4$ SYM. Here L_o is the shear length and μ_F is the drag coefficient for each case.

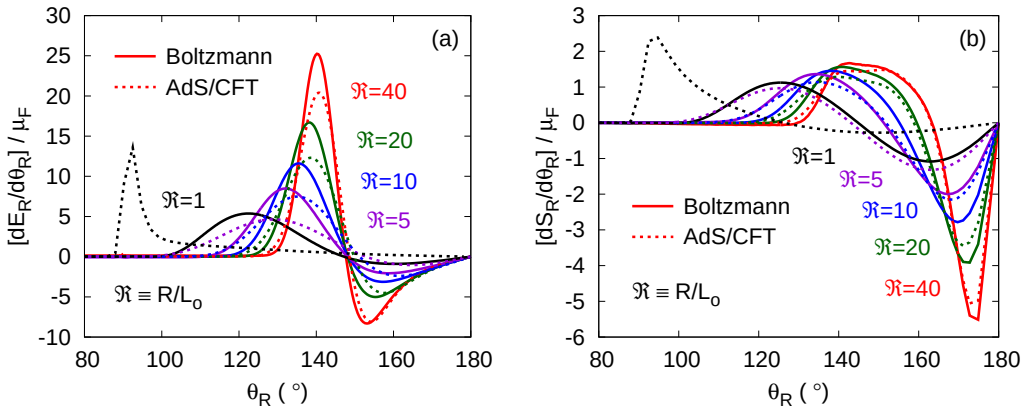

Figure 4.5: The angular distribution of (a) the energy density $[\mathrm{dE_R}/\mathrm{d}\theta_\mathrm{R}]/\mu_\mathrm{F}$ and (b) the energy flux $[\mathrm{dS_R}/\mathrm{d}\theta_\mathrm{R}]/\mu_\mathrm{F}$ given by kinetic theory and gauge gravity duality at distances $\mathfrak{R} = 1$, 5, 10, 20, and 40. Here L_o is the shear length and μ_F is the drag coefficient for each case.

marked differences between the weakly coupled QCD and the AdS/CFT correspondence at short distances are not visible [103]. However, the hydrodynamic response at long distances can be clearly compared.

4.4 Hydrodynamic Analysis

At long distances in Fig. 4.3 and Fig. 4.4, the energy density and flux distributions exhibit sound waves and a diffusion wake which are characteristic of hydrodynamics. In this section, we compare the distributions with the hydrodynamic solutions. By following Ref. [86] in part, we will determine the hydrodynamic source order by order in gradient expansions.

To determine the hydrodynamic solutions in two different ways, we consider the static and dynamic constituent relations given in Eqs. (3.49) and (3.50), respectively. Since the microscopic dynamics is conformal, linearized, and only conserves energy and momentum (and not particle number), τ_π is the only second order hydrodynamic coefficient that appears to this order. Specifically, the stress tensor in Eq. (3.42) is

$$T^{\mu\nu}_{\mathrm{hydro}} = (e + \mathcal{P})u^\mu u^\nu + \mathcal{P}g^{\mu\nu} + \pi^{\mu\nu}\,, \tag{4.22}$$

where the dissipative parts of static and dynamic theories are

$$\pi^{ij} = -2\eta \left\langle \partial^i u^j \right\rangle - 2\eta\tau_\pi \left\langle \partial^i \partial^j \ln T \right\rangle \qquad \text{(static)}\,, \tag{4.23}$$

$$\pi^{ij} = -2\eta \langle \partial^i u^j \rangle - \tau_\pi \partial_t \pi^{ij} \qquad \text{(dynamic)}\,. \tag{4.24}$$

With the constituent relations, we solve the equation of motion in Eq. (4.12).

At long distances from the heavy quark, the stress tensor is described by $T^{\mu\nu}_{\rm hydro}$ up to terms suppressed by inverse powers of the distance. Since the hydrodynamic form of the stress tensor is irregular, we express the full stress tensor as the sum of hydrodynamic term and a correction τ^{ij} which is analytic for $\omega, \boldsymbol{k} \to 0$:

$$T^{ij} = T^{ij}_{\rm hydro}[T^{00}, T^{0i}] + \tau^{ij}\,, \tag{4.25}$$

where we emphasized that $T^{ij}_{\rm hydro}$ is a functional of T^{00} and T^{0i}. Then the equation of motion in Fourier space becomes

$$-i\omega\, \delta T^{0j} + ik^i\, \delta T^{ij}_{\rm hydro} = S^j_{\rm hydro}(\omega, \boldsymbol{k})\,, \tag{4.26}$$

where

$$S^j_{\rm hydro}(\omega, \boldsymbol{k}) \equiv \frac{{\rm d}p^j}{{\rm d}t} 2\pi\delta(\omega - \boldsymbol{v}\cdot\boldsymbol{k}) - ik^i\tau^{ij}\,. \tag{4.27}$$

Here we note that $-ik^i\tau^{ij}$ acts as an additional source term for hydrodynamics.

For the steady state problem, τ^{ij} can be written with three functions proportional to the symmetric tensors consisting of $\boldsymbol{v}$ and $\boldsymbol{k}$:

$$\begin{aligned}\tau^{ij}(\omega, k^2) \equiv 2\pi\mu_F \delta(\omega - \boldsymbol{v}\cdot\boldsymbol{k}) \Bigg[& \left(v^i v^j - \tfrac{1}{3} v^2 \delta^{ij}\right) \phi_1(\omega, k^2) \\ & + \left(iv^i k^j + ik^i v^j - i\frac{2}{3} v_l k^l \delta^{ij} \right) \phi_2(\omega, k^2) + \left(k^i k^j - \tfrac{1}{3} k^2 \delta^{ij}\right) \phi_3(\omega, k^2) \Bigg]\,,\end{aligned} \tag{4.28}$$

where ϕ_1, ϕ_2 and ϕ_3 are regular for $\omega, \boldsymbol{k} \to 0$. Since τ^{ij} is localized, we can expand it for small ω and $\boldsymbol{k}$. For example, by using the Taylor's series

$$\phi_1(\omega, k^2) \simeq \phi_1^{(0,0)} + \phi_1^{(1,0)}(-i\omega) + \frac{1}{2!}\left[\phi_1^{(2,0)}\,(-i\omega)^2 + \phi_1^{(0,2)}\,(ik)^2\right] + O(k^3)\,, \tag{4.29}$$

where $\phi_1^{n,m}$ means differentiating ϕ_1 by ω, n times and by k^2, m times. The full source for hydrodynamics through second order can be expressed in terms

	$\phi_1^{(0,0)}/L_o$	$\phi_1^{(1,0)}/{L_o}^2$	$\phi_2^{(0,0)}/{L_o}^2$
Boltzmann	0	0	0.484
AdS/CFT	-1	-0.34	-0.33

Table 4.1: Hydrodynamic source coefficients. The equations of motion are given by second order hydrodynamics with a source term Eq. (4.27). The source term is expanded to second order in ω and $\boldsymbol{k}$ in Eq. (4.30) which defines these coefficients. The first coefficient $\phi_1^{(0,0)}$ was computed analytically in the AdS/CFT case [86]. Here L_o is the shear length.

of three coefficients $\phi_1^{(0,0)}$, $\phi_1^{(1,0)}$, and $\phi_2^{(0,0)}$:

$$\boldsymbol{S}_{\text{hydro}} = 2\pi\mu_F\delta(\omega - \mathbf{v}\cdot\boldsymbol{k})\Big[\underbrace{\left(1 - i\omega\phi_1^{(0,0)} - \phi_1^{(1,0)}\omega^2 + \phi_2^{(0,0)}k^2\right)}_{\equiv\phi_v}\boldsymbol{v} + \underbrace{\left(\tfrac{1}{3}v^2\phi_1^{(0,0)} - \tfrac{1}{3}v^2\phi_1^{(1,0)}i\omega - \tfrac{1}{3}\phi_2^{(0,0)}i\omega\right)}_{\equiv\phi_k} i\boldsymbol{k}\Big] + O(k^3)\,, \tag{4.30}$$

where we defined the source similarly:

$$\mathbf{S}_{\text{hydro}} \equiv 2\pi\mu_F\delta(\omega - \boldsymbol{v}\cdot\boldsymbol{k})\left[\phi_v(\omega,k^2)\boldsymbol{v} + \phi_k(\omega,k^2)i\boldsymbol{k}\right]\,. \tag{4.31}$$

τ^{ij} can be determined by comparing the full numerical solution for T^{ij} to T^{ij}_{hydro}. By fitting the forms in Eqs. (4.28) and (4.30), we can extract the three coefficients $\phi_1^{(0,0)}$, $\phi_1^{(1,0)}$, and $\phi_2^{(0,0)}$ for the Boltzmann equation and the AdS/CFT correspondence. These coefficients specify the hydrodynamic source of a heavy quark through second order. Appendix F gives sample fits to our numerical results, and the fit coefficients are collected in Table 4.1. The quality of the fits given in Appendix F indicates that τ^{ij} is well described by a polynomial at small ω and k, and justifies the analysis of this section. We notice that in the Boltzmann case the expansion coefficients proportional to ϕ_1 vanish. In fact, $\phi_1(\omega,k^2)$ vanishes to all orders in ω and $\boldsymbol{k}$. This is due to the rotational symmetry around the $\boldsymbol{k}$ axis and the special form of the kinetic theory source in Eq. (4.9) at a leading-log approximation.

With the source functions $\phi_v(\omega,k^2)$ and $\phi_k(\omega,k^2)$ as known numerically,

for $v = 1$ the hydrodynamic equation of motion reads

$$-i\omega\,\delta T^{0z'} + c^2(k)\,ik\delta T^{00} + \Gamma_s k^2\,\delta T^{0z'} = [\cos\theta\,\phi_v + ik\,\phi_k]\,2\pi\mu_F\delta(\omega - \boldsymbol{v}\cdot\boldsymbol{k})\,, \tag{4.32}$$

$$-i\omega\,\delta T^{0x'} + Dk^2\,\delta T^{0x'} = \sin\theta\,\phi_v\,2\pi\mu_F\delta(\omega - \boldsymbol{v}\cdot\boldsymbol{k})\,, \tag{4.33}$$

where z' points along the $\boldsymbol{k}$ axis and x' is perpendicular to $\boldsymbol{k}$ (see Appendix D for details). In these equations, the sound attenuation length is $\Gamma_s = (4\eta/3)/(e_o + \mathcal{P}_o)$, the diffusion constant is $D = \eta/(e_o + \mathcal{P}_o)$, and the speed of sound (squared) is $c^2(k) = c_s^2(1 + \tau_\pi\Gamma_s k^2)$. By using these approximate expressions and the exact equation,

$$-i\omega\,\delta T^{00} + ik\,\delta T^{0z'} = 2\pi\mu_F\,\delta(\omega - \boldsymbol{v}\cdot\boldsymbol{k})\,, \tag{4.34}$$

in Fourier space the second order static solutions are given by

$$\delta T^{00}(\omega,\mathbf{k}) = \frac{i\,[\omega + k\cos\theta\,\phi_v] - k^2\,[\Gamma_s + \phi_k]}{\omega^2 - c^2(k)\,k^2 + i\Gamma_s\,\omega k^2}\,2\pi\mu_F\delta(\omega - k\cos\theta)\,, \tag{4.35}$$

$$\delta T^{0x'}(\omega,\mathbf{k}) = \frac{i\sin\theta\,\phi_v}{\omega + iD\,k^2}\,2\pi\mu_F\delta(\omega - k\cos\theta)\,, \tag{4.36}$$

$$\delta T^{0z'}(\omega,\mathbf{k}) = \frac{i\,[\,\omega\cos\theta\,\phi_v + c^2(k)\,k\,] - k\omega\,\phi_k}{\omega^2 - c^2(k)\,k^2 + i\Gamma_s\,\omega k^2}\,2\pi\mu_F\delta(\omega - k\cos\theta)\,. \tag{4.37}$$

The solutions can also be used for the first order hydrodynamics provided the wave speed $c^2(k)$ and the source functions ϕ_v and ϕ_k are truncated at leading order: $c^2(k) \to c_s^2$ and $\phi_1(\omega,k^2) \simeq \phi_1^{(0,0)}$. Similarly, the hydrodynamic solutions for the dynamic theory takes the same functional forms as Eqs. (4.35)-(4.37) with the replacements:

$$c^2(k) \;\to\; c_s^2\,, \tag{4.38}$$

$$\Gamma_s \;\to\; \Gamma_s(\omega) \equiv \frac{\Gamma_s}{1 - i\tau_\pi\omega}\,, \tag{4.39}$$

$$D \;\to\; D(\omega) \equiv \frac{D}{1 - i\tau_\pi\omega}\,. \tag{4.40}$$

Given these hydrodynamic solutions and the hydrodynamic source functions tabulated in Table 4.1, the hydrodynamic stress tensor in coordinate space can be computed by using numerical Fourier transforms. The stress tensor of the first and second order (static) hydrodynamics (with the corresponding source) is compared to the full kinetic theory stress tensor in Fig. 4.6. Fig. 4.7 presents the analogous AdS/CFT results. Finally, a comparison be-

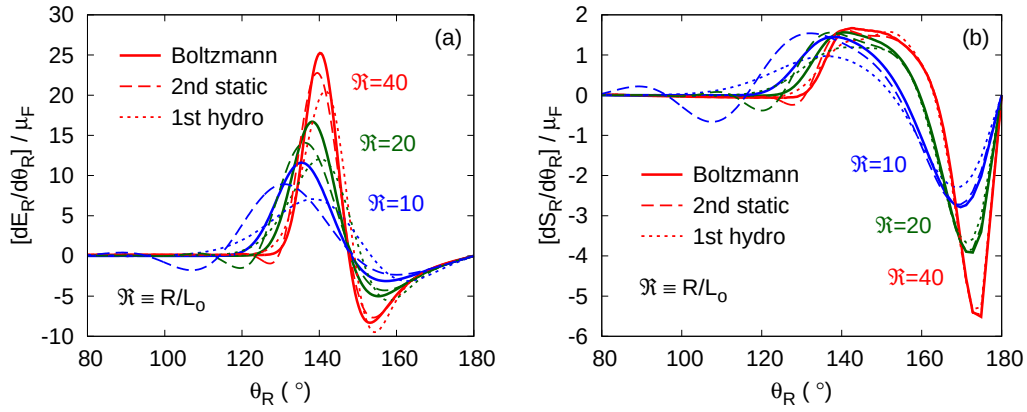

Figure 4.6: The angular distribution of (a) the energy density $[\mathrm{dE_R}/\mathrm{d}\theta_\mathrm{R}]/\mu_\mathrm{F}$ and (b) the energy flux $[\mathrm{dS_R}/\mathrm{d}\theta_\mathrm{R}]/\mu_\mathrm{F}$ given by the Boltzmann equation at distances $\mathfrak{R} = 10$, 20, and 40. The Boltzmann results are compared with the first order and second order static hydrodynamics. Here L_o is the shear length and μ_F is the heavy quark drag coefficient for kinetic theory.

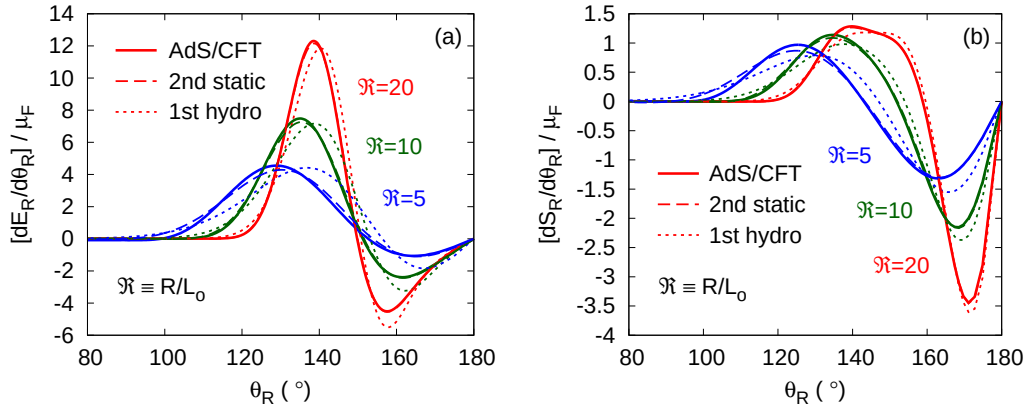

Figure 4.7: The angular distribution of (a) the energy density $[\mathrm{d}E_R/\mathrm{d}\theta_R]/\mu_F$ and (b) the energy flux $[\mathrm{d}S_R/\mathrm{d}\theta_R]/\mu_F$ given by the AdS/CFT correspondence at distances $\mathfrak{R} = 5$, 10, and 20. The AdS/CFT results are compared with the first order and the second order static hydrodynamics. Here $L_o = 1/\pi T$ is the shear length and $\mu_F = \gamma\sqrt{\lambda}\pi T^2/2$ is the heavy quark drag coefficient for the AdS/CFT.

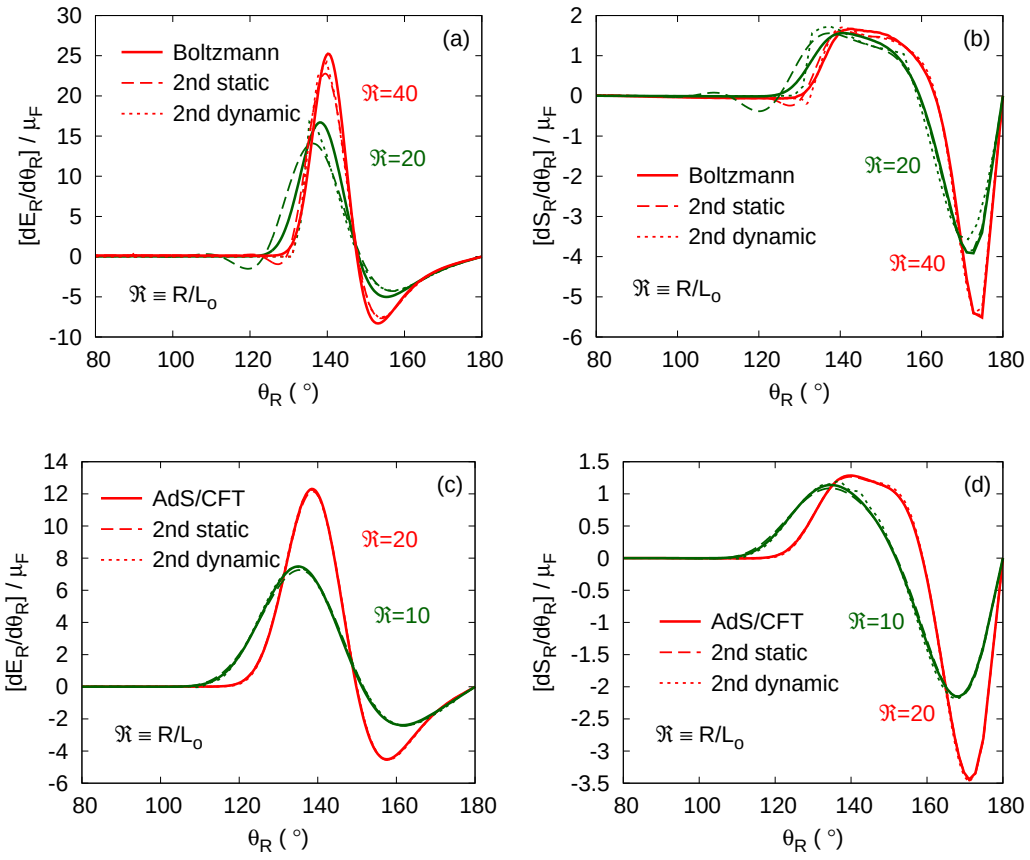

Figure 4.8: The angular distribution of (a) the energy density $[\mathrm{dE_R}/\mathrm{d}\theta_\mathrm{R}]/\mu_\mathrm{F}$ and (b) the energy flux $[\mathrm{dS_R}/\mathrm{d}\theta_\mathrm{R}]/\mu_\mathrm{F}$ in kinetic theory. The angular distribution of (c) the energy density $[\mathrm{dE_R}/\mathrm{d}\theta_\mathrm{R}]/\mu_\mathrm{F}$ and (d) the energy flux $[\mathrm{dS_R}/\mathrm{d}\theta_\mathrm{R}]/\mu_\mathrm{F}$ in AdS/CFT. The kinetic theory curves are plotted at distances $\mathfrak{R} = 20, 40$ while the AdS/CFT curves are plotted at distances $\mathfrak{R} = 10, 20$. The Boltzmann and AdS/CFT results are compared to the static and dynamic implementations of second order hydrodynamics. The differences between the static and dynamic results reflects the size of neglected third order terms. Here L_o is the shear length and μ_F is the drag coefficient for each theory.

tween the static and dynamic theories of the second order hydrodynamics is given in Fig. 4.8. The difference between the static and dynamic results provides an estimate of higher order terms in the hydrodynamic expansion.

4.5 Summary and Discussions

We simulated the wake of a heavy quark moving through the plasmas in two theories: kinetic theory based on the Boltzmann equation at weak coupling and $\mathcal{N} = 4$ SYM given by the AdS/CFT correspondence at strong coupling. At long distances, in both theories the energy density and flux distributions exhibit sound waves and a diffusion wake which are characteristic of hydrodynamics, shown in Fig. 4.3 and Fig. 4.4. However, their behaviors are distinguishable by the approach to the hydrodynamic limit. In particular, the Boltzmann results are considerably "less diffuse" than the AdS/CFT. The short distance response in kinetic theory is reactive, and the sharp band of free-streaming quasi-particles seen in kinetic theory is absent in AdS/CFT of Fig. 4.4.

To compare two different theories, we measured all distances in terms of the shear length Eq. (4.18) which is given by a combination of hydrodynamic parameters. In each theory, we divided the stress tensor by the corresponding heavy quark drag coefficient μ_F so that the rescaled stress tensors are equal at long distances where hydrodynamics is applicable. Fig. 4.5 shows the direct comparison between two theories for the angular distributions of the energy density and flux. Both theories show a smooth transition from non-equilibrium at short distances to equilibrium at long distance, except $\mathfrak{R} = 1$ for the AdS/CFT. There is a dramatic change between $\mathfrak{R} = 1$ and $\mathfrak{R} = 5$ for the AdS/CFT, indicating a transition from quantum dynamics to hydrodynamics. This transition is not visible in the semi-classical Boltzmann curves. It would be interesting to calculate the stress tensor in this region perturbatively to understand the difference of two theories at short distances.

At long distances, the energy density and flux distributions can be described by hydrodynamics. However, the appropriate source for hydrodynamics must be found by matching the numerical results to the hydrodynamic theory. By using the transport coefficients determined in the previous chapter, we compared the Boltzmann results to the hydrodynamic solutions up to second order in Fig. 4.6. In particular, we used the hydrodynamic source appropriate for the first and second order hydrodynamics. Generally, the second order static hydrodynamics provides minor improvement to the first order hydrodynamics until $\mathfrak{R} \gtrsim 40$. Indeed, the behavior of the second order theory seems rather unphysical for $\mathfrak{R} \lesssim 10$ due to the violation of causality. This

shows the limitations of second order hydrodynamics. On the other hand, the AdS/CFT results are much better described by hydrodynamics at relatively short distances in Fig. 4.7. Even the first order hydrodynamics does a fair job, and the second order hydrodynamics with the source correction works perfectly for $\mathfrak{R} = 20$.

We should mention that we used the static second order hydrodynamics in Fig. 4.6 and Fig. 4.7. With the dynamic form of the constituent relation, the stress tensor is slightly better described than the static form (see Fig. 4.8). Although the dynamic theory gives causal solutions, in kinetic theory at $\mathfrak{R} \lesssim 20$, it develops spurious shocks which are not reproduced by the full result. The difference between the static and dynamic theories gives an estimate of higher order terms, and this difference is smaller in AdS/CFT than in kinetic theory at same distance.

Clearly, the convergence to the hydrodynamic limit is significantly faster in the AdS/CFT than in kinetic theory. We note that in kinetic theory the second order hydrodynamic parameter τ_π is a factor of 2.4 greater in scaled units than the corresponding AdS/CFT parameter:

$$\frac{\tau_\pi}{\eta/(e_o + \mathcal{P}_o)} = 6.32\,, \qquad \text{(Kinetic Theory)} \tag{4.41}$$

$$\frac{\tau_\pi}{\eta/(e_o + \mathcal{P}_o)} = 4 - 2\ln 2 \simeq 2.61\,. \qquad \text{(AdS/CFT)} \tag{4.42}$$

Based on these coefficients, it is natural to expect that the convergence to the hydrodynamic limit is faster in the AdS/CFT than in kinetic theory. In theories with quasi-particles, the value of τ_π seems to be generic [52]. Therefore, due to the factor of 2.4 we expect that theories without quasi-particles approach to the hydrodynamic limit faster than theories based on quasi-particle description.

Chapter 5

Photon Emission Rate

5.1 Introduction

So far, we have worked at a leading-log approximation in the coupling constant g. At this order, typical particles have momentum $\sim T$, and only the t-channel exchange with momentum $\sim gT$ contributes. In this chapter, we will work at next-to-leading order (NLO) to compute the thermal photon emission rate in the Quark-Gluon Plasma (QGP).

In perturbative gauge theories, it is important to calculate real time quantities beyond leading order (LO). In particular, we are interested in computing transport coefficients at NLO. The only NLO dynamic quantity which has been computed so far is the heavy quark diffusion constant (which does not involve collinear bremsstrahlung) [10]. Computing the photon emission rate involves some issues including hard collisions, collinear bremsstrahlung, and screening effects. But the calculation is easier than other problems such as gluon emission rate, where gluons interact with the medium. In this sense, the NLO computation of the photon emission rate is a good warm-up problem for further research.

The photon emission rate is given by [29]

$$(2\pi)^3 \frac{\mathrm{d}\Gamma}{\mathrm{d}^3\boldsymbol{k}} = \frac{1}{2k} \sum_{a=1,2} \epsilon^{\mu *}_{(a)}(\boldsymbol{k}) \epsilon^{\nu}_{(a)}(\boldsymbol{k}) W^{<}_{\mu\nu}(K) \,. \tag{5.1}$$

Here $a = 1, 2$ correspond to the transverse polarizations and $W^{<}_{\mu\nu}(K)$ is the Wightman electromagnetic current-current correlator:

$$W^{<}_{\mu\nu}(K) = \int \mathrm{d}^4 X e^{-iK\cdot X} \left\langle J_\mu(0) J_\nu(X) \right\rangle \,. \tag{5.2}$$

At NLO, soft particles with momentum $\sim gT$ play an important role. Bare perturbation theory with only hard particles gives $\alpha_s \sim g^2$ expansions. However, in the presence of soft bosonic fields, there is the $\mathcal{O}(g)$ Bose enhancement from the occupation number

$$n_p^B \simeq \frac{T}{p^0} \sim \frac{1}{g} \qquad (p^0 \text{ small}) \,. \tag{5.3}$$

Then by using the hard-thermal-loop (HTL) effective theory, we can compute the $\mathcal{O}(g)$ correction to the LO photon emission rate.

In experiments, there are various sources of photons: hard scattering photons, fragmentation photons, jet-induced photons, and thermal photons. Some of them are thermal and others are non-thermal. It is not easy to distinguish the sources. However, in current simulations of photons with all the sources, there is a window at $p_\perp \sim 2\text{GeV} \sim 10T_c$, where thermal photons are most important.

In this chapter, we will focus on the thermal photons with hard momentum. We will start with a review on the LO photon emission rate in the QGP. Then we calculate the photon emission rate at NLO, *i.e.* at order $g^2 m_D/T$ to respond to the *Point III* mentioned in Chapter 1 [107].

5.2 LO Photon Emission Rate

The photon emission rate has been computed at leading order (LO) in Refs. [108, 109, 110]. There are three mechanisms which contribute to LO:

(i) $2 \leftrightarrow 2$ Processes – Compton Scattering, Elastic Pair Annihilation,

(ii) $1 \leftrightarrow 1$ Processes – Quark-Photon Conversion,

(iii) $1 \leftrightarrow 2$ Processes – Bremsstrahlung, Inelastic Pair Annihilation.

Let us discuss each of these mechanisms in turn.

(i) $2 \leftrightarrow 2$ *processes*: The $2 \leftrightarrow 2$ elastic collisions contribute to the LO photon emission rate [111, 112]. The quark-gluon Compton-like scattering and quark-antiquark pair annihilation correspond to this mechanism. These processes are shown in Fig. 5.1, and can be understood as the cut diagrams of two-loop diagrams shown in Fig. 5.2. By summing the four diagrams in Fig. 5.2, the emission rate from hard momentum $q_\perp^2 > \mu_\perp^2$ (where $Q \equiv P - K$

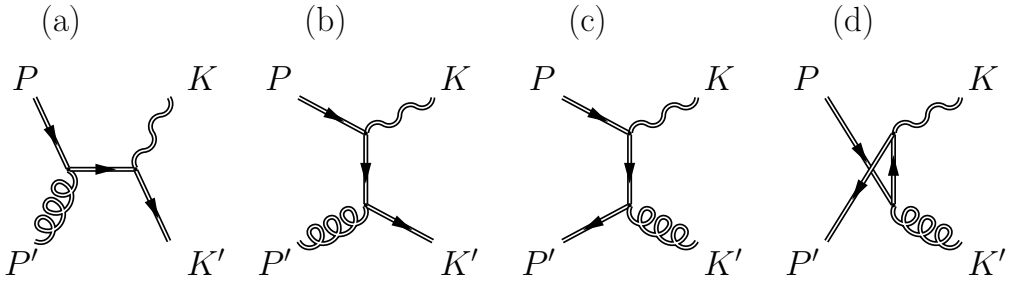

Figure 5.1: $2 \leftrightarrow 2$ processes. (a) The Compton scattering in the s-channel, (b) Compton scattering in the t-channel, (c) pair annihilation in the t-channel, and (d) pair annihilation in the u-channel. The square of these diagrams can be understood as two-loop diagrams shown in Fig. 5.2. Double solid lines denote hard quarks, double wiggly lines denote hard photons, and double curly lines denote hard gluons. Time runs from left to right.

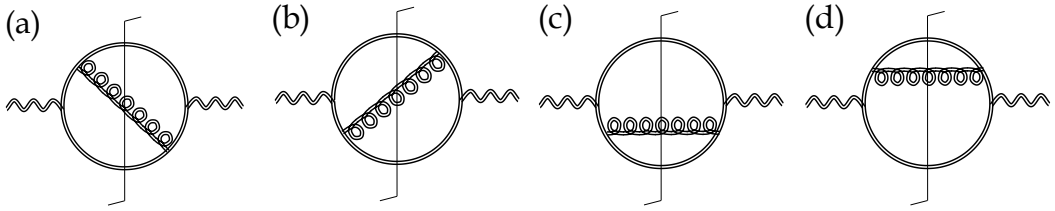

Figure 5.2: Two-loop cut diagrams contributing to the LO photon emission rate. These cut diagrams can be understood as $2 \leftrightarrow 2$ processes, the Compton scattering and pair annihilation shown in Fig. 5.1. Double solid lines denote hard quarks, double wiggly lines denote hard photons, and double curly lines denote hard gluons.

in the process $P + P' \to K + K'$) is given by [111, 112]

$$(2\pi)^3 \frac{\mathrm{d}\Gamma_{\mathrm{LO}}}{\mathrm{d}^3\boldsymbol{k}}\bigg|_{\mathrm{hard}} = \frac{1}{2k}\int_{\boldsymbol{p},\boldsymbol{p}',\boldsymbol{k}'} \frac{1}{2p2p'2k'}(2\pi)^4\delta^4(P_{tot}) \left[n_p^F n_{p'}^B(1-n_{k'}^F)|M|^2_{\mathrm{comp}} + n_p^F n_{p'}^F(1+n_{k'}^B)|M|^2_{\mathrm{pair}}\right], \\ = \mathcal{A}(k)\left[\frac{1}{2}\ln\left(\frac{T^2}{\mu_\perp^2}\right) + C_{\mathrm{hard}}\left(k/T\right)\right]. \tag{5.4}$$

Here the matrix elements are

$$|M|^2_{\mathrm{comp}} = 16e^2\sum_s q_s^2 d_F C_F g^2\left(-\frac{t}{s}-\frac{s}{t}\right), \tag{5.5}$$

$$|M|^2_{\mathrm{pair}} = 8e^2\sum_s q_s^2 d_F C_F g^2\left(\frac{u}{t}+\frac{t}{u}\right), \tag{5.6}$$

where q_s is the quark charge in units of the electric charge e and the Mandelstam variables are

$$s \equiv -(P+P')^2, \qquad t \equiv -(P-K)^2, \qquad u \equiv -(P-K')^2. \tag{5.7}$$

$\mu_\perp^2$ is an infrared cutoff which screens the soft quark exchange in Fig. 5.1 (b), (c), and (d). The dependence on $\mu_\perp^2$ will be canceled when the soft contribution is added to this rate. $C_{\mathrm{hard}}(k/T)$ is the hard contribution to the photon emission rate, as a function of k/T (the numerical LO results will be presented later). The front factor is defined by (following the notation of Ref. [109])

$$\mathcal{A}(k) \equiv \frac{1}{8\pi}e^2\sum_s q_s^2 d_F C_F g^2 T^2 \frac{n_k^F}{k}. \tag{5.8}$$

(ii) $1 \leftrightarrow 1$ *processes*: There is $1 \leftrightarrow 1$ processes, which we call "quark-photon conversion". In this process, a hard quark interacts with the medium to produce a hard photon having almost same momentum of the incoming quark, with a soft quark (see Fig. 5.3 (a)). The square of Fig. 5.3 (a) is Fig. 5.3 (b), where the soft fermion line is evaluated in HTL approximation.

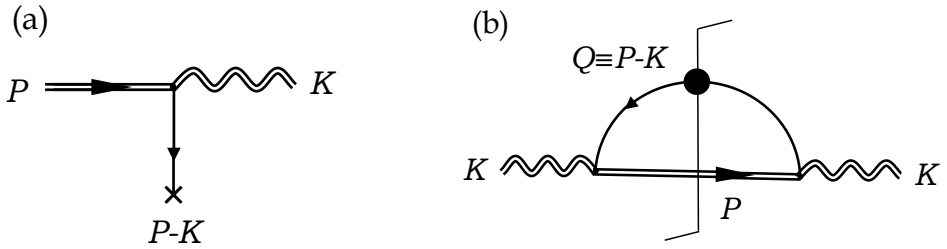

Figure 5.3: $1 \leftrightarrow 1$ processes. (a) Quark-photon conversion, where a hard quark undergoes soft momentum exchange to become a hard photon with $K \simeq P$. (b) The photon self-energy cut diagram. The square of (a). Double wiggly lines denote hard photons, double solid lines denote hard quarks, and single solid lines (with arrows) denote soft quarks. Time runs from left to right.

The LO photon emission rate from conversion is

$$\begin{aligned}(2\pi)^3 \frac{\mathrm{d}\Gamma_{\mathrm{LO}}}{\mathrm{d}^3\boldsymbol{k}}\bigg|_{\mathrm{soft}} &= \frac{\Pi^<(K)}{2k} \\ &= e^2 \sum_s q_s^2 d_F \frac{n_k^F}{k} \int \frac{\mathrm{d}q_\perp^2}{2(2\pi)} \frac{m_\infty^2}{q_\perp^2 + m_\infty^2} \\ &= \mathcal{A}(k) \frac{1}{2} \ln\left(\frac{\mu_\perp^2}{m_\infty^2}\right) , \end{aligned} \tag{5.9}$$

where in the second line we evaluated the photon self-energy shown in Fig. 5.3 (b) using a sum rule derived in Section 5.6.1. By adding this result to the hard contribution in Eq. (5.4), the emission rate is

$$(2\pi)^3 \frac{\mathrm{d}\Gamma_{\mathrm{LO}}}{\mathrm{d}^3\boldsymbol{k}}\bigg|_{\mathrm{hard+soft}} = \mathcal{A}(k) \left[\ln\left(\frac{T}{m_\infty}\right) + C_{\mathrm{hard}}\left(k/T\right)\right] . \tag{5.10}$$

Here the ultraviolet cutoff dependence on $\mu_\perp^2$ in Eq. (5.9) was canceled by the infrared cutoff dependence in Eq. (5.4). This result was thought to be the answer for the LO photon emission rate until we realized that $1 \leftrightarrow 2$ processes also contributed to LO.

(iii) $1 \leftrightarrow 2$ *processes*: The inelastic $1 \leftrightarrow 2$ processes including collinear bremsstrahlung and pair annihilation also contribute to photon emission at LO (see Fig. 5.4). These processes are seemingly higher order in perturbative expansions, but the collinear enhancement effect makes them contribute to the same order as the $2 \leftrightarrow 2$ processes. Since the formation time of photon is comparable to the time between collisions, we need to consider multiple

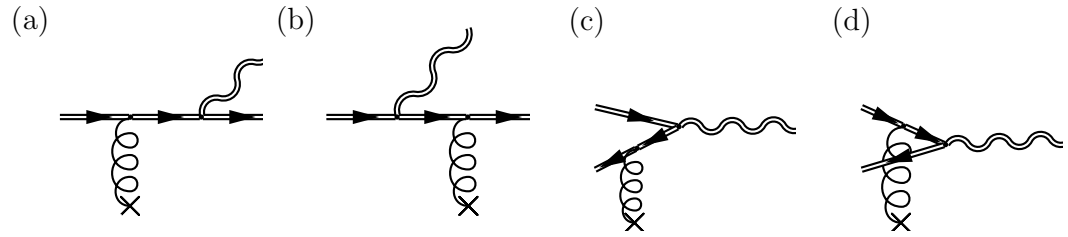

Figure 5.4: $1 \leftrightarrow 2$ processes. (a)(b) Bremsstrahlung and (c)(d) inelastic pair annihilation. Double solid lines denote hard quarks, double wiggly lines denote hard photons, and single curly lines denote soft gluons.

scatterings (see Section 5.3). Including these multiple scatterings suppresses the naive bremsstrahlung rate, which is known as the Landau-Pomeranchuk-Migdal (LPM) effect. This effect can be accounted for by summing ladder diagrams and solving an integral equation, which will be discussed in Section 5.3. At LO, the photon emission rate from these inelastic processes is given by

$$(2\pi)^3 \frac{\mathrm{d}\Gamma_{\mathrm{LO}}}{\mathrm{d}^3\boldsymbol{k}}\bigg|_{\mathrm{brem+annih}} = \mathcal{A}(k)\Big[C_{\mathrm{brem}}(k/T) + C_{\mathrm{annih}}(k/T)\Big]\,. \tag{5.11}$$

The total photon emission rate at LO is given by the sum of hard, soft, and inelastic contributions in Eqs. (5.4), (5.9), and (5.11), respectively. By following the notion of Ref. [109][1], the LO photon emission rate is

$$(2\pi)^3 \frac{\mathrm{d}\Gamma_{\mathrm{LO}}}{\mathrm{d}^3\boldsymbol{k}}\bigg|_{\mathrm{hard+soft+brem+annih}} = \mathcal{A}(k)\bigg[\ln\left(\frac{T}{m_\infty}\right) + \frac{1}{2}\ln(2k/T) + C_{2\to2}(k/T) + C_{\mathrm{brem}}(k/T) + C_{\mathrm{annih}}(k/T)\bigg]\,. \tag{5.12}$$

[1] $C_{\mathrm{hard}}(k/T) = \frac{1}{2}\ln(2k/T) + C_{2\to2}(k/T)$

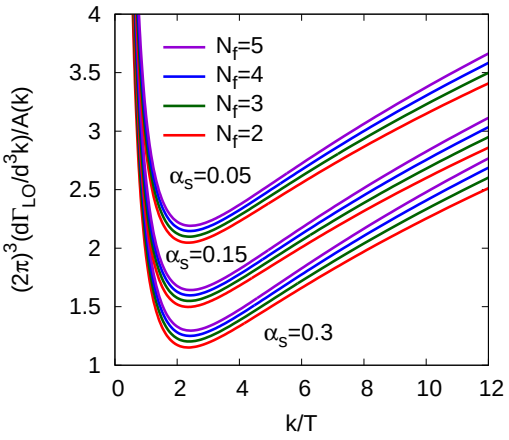

Figure 5.5: The total LO photon emission rate in Eq. (5.12) for $\alpha_s = 0.05$, 0.15, 0.3 and for $N_f = 2$, 3, 4, 5. The numerical results are from Ref. [109].

A parameterization of numerical results is given in Ref. [109]:

$$C_{2\to 2}(k/T) \simeq \frac{0.041T}{k} - 0.3615 + 1.01e^{-1.35k/T}\,, \tag{5.13}$$

$$C_{\rm brem}(k/T) + C_{\rm annih}(k/T) \simeq \sqrt{1+\frac{N_f}{6}}\left[\frac{0.548\,\ln(12.28+T/k)}{(k/T)^{3/2}} + \frac{0.133\,k/T}{\sqrt{1+k/16.27T}}\right], \tag{5.14}$$

where N_f is the number of quark flavors. Fig. 5.5 shows the total LO photon emission rate for $\alpha_s = 0.05$, 0.15, 0.3 and $N_f = 2$, 3, 4, 5.

At NLO, the three mechanisms of photon emission are not completely independent. For instance, when $gT \ll p_\perp \ll \sqrt{g}T$, it is difficult to distinguish the Compton process (with a soft gluon) from wide-angle bremsstrahlung (see Fig. 5.6 (a) and (b)). The matrix elements should be matched onto the $2 \to 3$ process to produce the finite NLO correction. Similarly, there is a matching process between bremsstrahlung and quark-photon conversion process when the photon carries most of the incoming quark momentum (see Fig. 5.6 (c) and (d)). In Section 5.5, we will do these calculations explicitly to determine the wide-angle NLO photon emission rate.

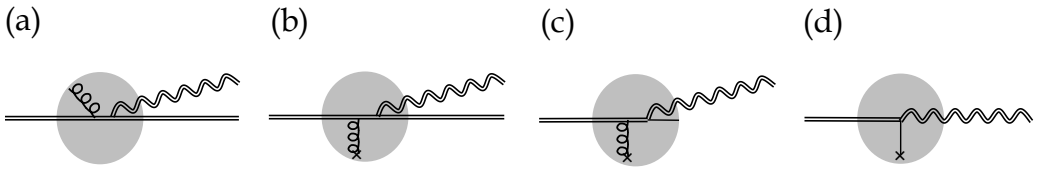

Figure 5.6: (a) The Compton scattering with a soft gluon and (b) wide-angle bremsstrahlung. When $gT \ll p_\perp \ll \sqrt{g}T$, it is difficult to distinguish the Compton scattering from wide-angle bremsstrahlung. (c) Asymmetric bremsstrahlung and (d) quark-photon conversion. When the photon carries most of the incoming quark momentum, it is difficult to distinguish bremsstrahlung from quark-photon conversion. Double solid lines denote hard quarks, double wiggly lines denote hard photons, single curly lines denote soft gluons, and single solid lines denote soft quarks.

5.3 Collinear Bremsstrahlung

As discussed in the last section, the three mechanisms of the LO photon emission are smoothly matched to determine the wide-angle NLO correction. Besides these wide-angle processes, collinear bremsstrahlung and pair annihilation also contribute to the NLO photon emission rate. Collinear processes can be accounted for by solving an integral equation which corresponds to summing ladder diagrams [108]. In this section, we will discuss the collinear photon emission rate through NLO. For completeness, we will present the numerical results from the forthcoming work [107].

Since there is coherent interaction between incoming and scattering waves, it takes some time (called the "formation" time) to complete the photon production. Therefore, it is not correct to count only single scattering in bremsstrahlung and inelastic pair annihilation as in Fig. 5.4. We need to consider multiple scatterings which are shown in Fig. 5.7. The interference of multiple scatterings can be accounted for by summing ladder diagrams shown in Fig. 5.8. This calculation can be performed by solving an integral equation, which will be discussed in this section. We will explain LO and NLO photon emission from collinear processes. When $gT \ll p_\perp \ll \sqrt{g}T$, there is an overlap region between bremsstrahlung and the Compton scattering. In this region, the integral equation will be solved perturbatively.

The formation time is the time over which quark and photon are in phase in a process. To estimate this time scale, we consider a bremsstrahlung process

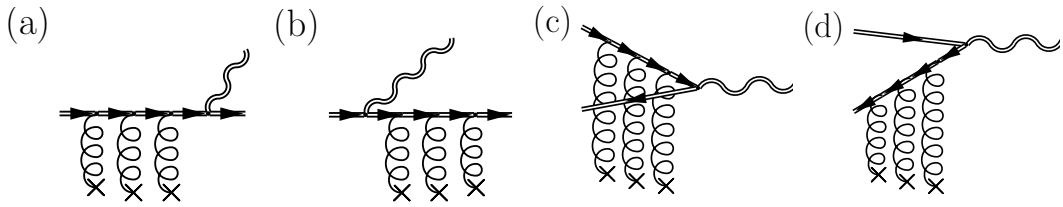

Figure 5.7: Multiple scatterings in (a)(b) bremsstrahlung and (c)(d) inelastic pair annihilation. The square of these diagrams can be understood as ladder diagrams shown in Fig. 5.8. Double solid lines denote hard quarks, double wiggly lines denote hard photons, and single curly lines denote soft gluons.

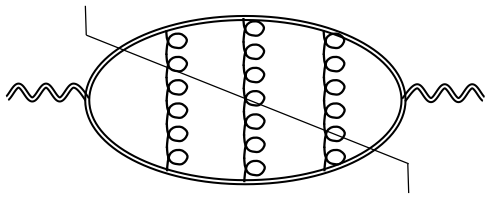

Figure 5.8: A ladder diagram including bremsstrahlung and inelastic pair annihilation with multiple scatterings. The lowest order of this ladder diagram corresponds to the two-loop diagrams shown in Fig. 5.2. Double solid lines denote hard quarks, double wiggly line denote hard photons, and single curly lines denote soft gluons.

$q \to \gamma + q$, where q is quark and γ is photon, with the following momenta:

$$P \to K + K' \,. \tag{5.15}$$

We assume the photon with momentum K is emitted in the z-direction. With the splitting constant $0 < z < 1$, the momentum splitting can be expressed in terms of the incoming quark momentum:

$$\Big[\boldsymbol{p} = (p^z, \boldsymbol{p}_\perp)\Big] \;\to\; \Big[\boldsymbol{k} = ((1-z)p^z, \boldsymbol{0})\Big] + \Big[\boldsymbol{k}' = (zp^z, \boldsymbol{p}_\perp)\Big] \,, \tag{5.16}$$

where[2] $p^z \sim T$ and $gT \lesssim p_\perp \ll \sqrt{g}T$. With this order of momentum components, the energy of the emitted quark is

$$k'^0 = \sqrt{(zp^z)^2 + \boldsymbol{p}_\perp^2 + m_\infty^2} \simeq zp^z + \frac{\boldsymbol{p}_\perp^2 + m_\infty^2}{2zp^z} \,, \tag{5.17}$$

and similarly for p^0 and k^0 formulas. Then the energy change $\delta E \equiv k^0 + k'^0 - p^0$ is

$$\begin{aligned} \delta E &\simeq (1-z)p^z + \left(zp^z + \frac{\boldsymbol{p}_\perp^2 + m_\infty^2}{2zp^z}\right) - \left(p^z + \frac{\boldsymbol{p}_\perp^2 + m_\infty^2}{2p^z}\right) \,, \\ &\simeq \frac{(1-z)(\boldsymbol{p}_\perp^2 + m_\infty^2)}{2zp^z} \,. \end{aligned} \tag{5.18}$$

By neglecting the masses of quarks, the formation time of the photon is

$$t_{\rm form} \;\sim\; \frac{1}{\delta E} \;\sim\; \frac{2zp^z}{(1-z)\boldsymbol{p}_\perp^2} \,. \tag{5.19}$$

The time between soft collisions can be estimated as follows:

$$t_{\rm coll} \;\sim\; \frac{1}{n\sigma} \;\sim\; \frac{1}{g^2 T} \,. \tag{5.20}$$

Here $n \sim T^3$ is the number density of particles, and $\sigma \sim g^2/T^2$ is the soft scattering cross-section. In computing the photon emission rate, the time between collisions should be compared to the formation time which depends on the order of $p_\perp$. When $p_\perp \sim gT$ in the collinear limit, Eq. (5.19) yields

$$t_{\rm form} \;\sim\; \frac{1}{g^2 T} \,, \tag{5.21}$$

[2]The order of momenta in light-cone coordinates will be discussed in the next section.

and the formation time is comparable to the time between collisions. Therefore, we need to consider multiple scatterings shown in Fig. 5.7. Taking the squared matrix elements of the processes in Fig. 5.7 corresponds to summing ladder diagrams shown in Fig. 5.8. By summing ladder diagrams, we obtain the following integral equation [108, 113]:

$$2\boldsymbol{p}_\perp = i\delta E(\boldsymbol{p}_\perp, p^z, \boldsymbol{k})\boldsymbol{f}(\boldsymbol{p}_\perp, p^z, \boldsymbol{k}) + \int \frac{\mathrm{d}^2\boldsymbol{p}'_\perp}{(2\pi)^2} C[\boldsymbol{p}'_\perp]\Big[\boldsymbol{f}(\boldsymbol{p}_\perp, p^z, \boldsymbol{k}) - \boldsymbol{f}(\boldsymbol{p}_\perp + \boldsymbol{p}'_\perp, p^z, \boldsymbol{k})\Big] . \quad (5.22)$$

Here the solution $\boldsymbol{f}(\boldsymbol{p}_\perp, p^z, \boldsymbol{k})$ is related to the current-current correlator in Eq. (5.41). In the above equation, the collision kernel records the soft collision rate

$$\begin{aligned} C[\boldsymbol{p}_\perp] &\equiv (2\pi)^2 \frac{\mathrm{d}\Gamma}{\mathrm{d}^2\boldsymbol{p}_\perp} , \\ &= \int \frac{\mathrm{d}p^0 \mathrm{d}p^z}{(2\pi)^2} 2\pi\delta(p^z - p^0)\frac{T}{p^0}\rho^{\mu\nu}(p^0, \boldsymbol{p}_\perp, p^z) v_\mu v_\nu , \end{aligned} \quad (5.23)$$

where $v^\mu \equiv (1, 0, 0, 1)$ is the unit vector in the z-direction.

We define the Wightman functions $iG^>_{\mu\nu}(P)$ and $iG^<_{\mu\nu}(P)$ for subsequent use:

$$\begin{aligned} iG^>_{\mu\nu}(P) &\equiv \int_P e^{-iP\cdot X} \left\langle \hat{A}_\mu(X)\hat{A}_\nu(0) \right\rangle , \\ &\equiv \langle\!\langle A_\mu(P) A_\nu \rangle\!\rangle , \end{aligned} \quad (5.24)$$

and similarly

$$\begin{aligned} iG^<_{\mu\nu}(P) &\equiv \int_P e^{-iP\cdot X} \left\langle \hat{A}_\nu(0)\hat{A}_\mu(X) \right\rangle , \\ &\equiv \langle\!\langle A_\nu A_\mu(P) \rangle\!\rangle . \end{aligned} \quad (5.25)$$

According to the fluctuation dissipation theorem, for soft P

$$iG^>_{\mu\nu}(P) = [1 + n_p^B(P)]\rho_{\mu\nu}(P) \simeq \frac{T}{p^0}\rho_{\mu\nu}(P) . \quad (5.26)$$

Here

$$\begin{aligned}\rho_{\mu\nu}(P) &= iG^{>}_{\mu\nu}(P) - iG^{<}_{\mu\nu}(P)\,, \\ &= \int_P e^{-iP\cdot X}\left\langle\left[\hat{A}_\mu(X), \hat{A}_\nu(0)\right]\right\rangle \end{aligned} \tag{5.27}$$

is the spectral density. With these definitions, the collision kernel can be written in terms of the gauge field correlation function:

$$C[\boldsymbol{p}_\perp] = \int \frac{\mathrm{d}p^0}{2\pi}\langle\!\langle A_+(P)A_+\rangle\!\rangle\Big|_{p^z=p^0}\,, \tag{5.28}$$

where we defined $A_+ \equiv -A^0 + A^z$.

There are two sources of NLO corrections in the photon emission rate from bremsstrahlung (and inelastic pair annihilation) in the strictly collinear limit, $p_\perp \sim gT$:

(i) Corrections to $C[\boldsymbol{p}_\perp]$ and δm_∞^2,

(ii) Wide-angle Bremsstrahlung and Pair Annihilation.

We discuss these sources in turn.

(i) *Corrections to* $C[\boldsymbol{p}_\perp]$ *and* δm_∞^2: There are corrections to the collision kernel, $C[\boldsymbol{p}_\perp]$ and the asymptotic mass of quarks, m_∞^2 (which will be used in the integral equation Eq. (5.22) and the emission rate Eq. (5.43)):

$$m_\infty^2 \to m_\infty^2 + \delta m_\infty^2\,, \tag{5.29}$$

$$C[p'_\perp] \simeq C[p'_\perp]_{\mathrm{LO}} + C[p'_\perp]_{\mathrm{NLO}}\,. \tag{5.30}$$

Here the fermion asymptotic mass is defined by

$$m_\infty^2 \equiv \frac{g^2 C_F}{\pi^2}\int_0^\infty \mathrm{d}p\, p(n_p^B + n_p^F) = \frac{g^2 C_F T^2}{4}\,, \tag{5.31}$$

and its $\mathcal{O}(g)$ correction is [114, 115]

$$\delta m_\infty^2 = -\frac{g^2 C_F T m_D}{2\pi}\,. \tag{5.32}$$

The LO collision kernel is known as the Aurenche-Gelis-Zaraket (AGZ) sum rule [113]

$$C[p_\perp]_{\mathrm{LO}} = \frac{g^2 C_F T m_D^2}{p_\perp^2(p_\perp^2 + m_D^2)}\,, \tag{5.33}$$

and its NLO correction was computed in Ref. [116]

$$C[p_\perp]_{\rm NLO} = g^4 T^2 C_F C_A \left[\frac{7}{32 p_\perp^3} - \frac{3m_D + \frac{2(p_\perp^2 - m_D^2)}{p_\perp} \tan^{-1}\left(\frac{p_\perp}{m_D}\right)}{4\pi (p_\perp^2 + m_D^2)^2} \right.$$
$$+ \frac{m_D - \frac{(p_\perp^2 + 4m_D^2)}{2p_\perp} \tan^{-1}\left(\frac{p_\perp}{2m_D}\right)}{8\pi p_\perp^4} - \frac{\tan^{-1}\left(\frac{p_\perp}{m_D}\right)}{2\pi p_\perp (p_\perp^2 + m_D^2)}$$
$$\left. + \frac{\tan^{-1}\left(\frac{p_\perp}{2m_D}\right)}{2\pi p_\perp^3} + \frac{m_D}{4\pi (p_\perp^2 + m_D^2)} \left(\frac{3}{p_\perp^2 + 4m_D^2} - \frac{1}{p_\perp^2} \right) \right] . \quad (5.34)$$

With these corrections, the NLO correction to the LO collinear emission rate is expanded as

$$(2\pi)^3 \frac{{\rm d}\delta\Gamma_{\rm NLO}}{{\rm d}^3 \boldsymbol{k}} \bigg|_{\rm collin} = \mathcal{A}(k) \left[\frac{\delta m_\infty^2}{m_\infty^2} C_{\rm collin}^{\delta m}(k/T) + \frac{g^2 C_A T}{m_D} C_{\rm collin}^{\delta K}(k/T) \right] . \quad (5.35)$$

Here $C_{\rm collin}^{\delta m}(k/T)$ is the correction from mass δm_∞^2, and $C_{\rm collin}^{\delta K}(k/T)$ is the correction from kernel $C[p_\perp]_{\rm NLO}$. The numerical results will be presented in Section 5.7.2 for completeness. The full discussion regarding these collinear processes will be appeared in the forthcoming paper [107].

(ii) *Wide-angle bremsstrahlung and pair annihilation*[3]: We have identified another kinematic region for bremsstrahlung and inelastic pair annihilation, which gives NLO correction (discussed in detail in the next section). In this region, the transverse momentum between photon and quark is $\sim \sqrt{g}T$. From Eq. (5.19), the formation time for bremsstrahlung with this $p_\perp$ is

$$t_{\rm form} \sim \frac{1}{gT} . \quad (5.36)$$

This is short compared to the time between collisions ($\sim 1/g^2 T$), and the LPM effect can be neglected. By noting

$$\delta E \sim \frac{1}{t_{\rm form}} \sim gT \qquad \text{and} \qquad \boldsymbol{p}_\perp'^2 C[\boldsymbol{p}_\perp'] \sim \frac{1}{t_{\rm coll}} \sim g^2 T , \quad (5.37)$$

we can solve the integral equation Eq. (5.22) perturbatively

$$\boldsymbol{f}(\boldsymbol{p}_\perp, p^z, \boldsymbol{k}) = \boldsymbol{f}^{(0)}(\boldsymbol{p}_\perp, p^z, \boldsymbol{k}) + \boldsymbol{f}^{(1)}(\boldsymbol{p}_\perp, p^z, \boldsymbol{k}) + \cdots . \quad (5.38)$$

[3]The second source of NLO corrections involves wide-angle bremsstrahlung and pair annihilation, and this is the principal result of the current chapter.

The solution without any interaction is

$$\boldsymbol{f}^{(0)}(\boldsymbol{p}_\perp, p^z, \boldsymbol{k}) = \frac{2\boldsymbol{p}_\perp}{i\delta E(\boldsymbol{p}_\perp, p^z, \boldsymbol{k})}\,, \tag{5.39}$$

and the next solution $\boldsymbol{f}^{(1)}(\boldsymbol{p}_\perp, p^z, \boldsymbol{k})$ can be obtained by solving

$$\begin{aligned} &i\delta E(\boldsymbol{p}_\perp, p^z, \boldsymbol{k})\boldsymbol{f}^{(1)}(\boldsymbol{p}_\perp, p^z, \boldsymbol{k}) \\ &\quad = -\int \frac{\mathrm{d}^2\boldsymbol{p}'_\perp}{(2\pi)^2} C[\boldsymbol{p}'_\perp] \left[\frac{2\boldsymbol{p}_\perp}{i\delta E(\boldsymbol{p}_\perp, p^z, \boldsymbol{k})} - \frac{2(\boldsymbol{p}_\perp + \boldsymbol{p}'_\perp)}{i\delta E(\boldsymbol{p}_\perp + \boldsymbol{p}'_\perp, p^z, \boldsymbol{k})}\right]. \end{aligned} \tag{5.40}$$

After solving the integral equation Eq. (5.22) for $\boldsymbol{f}(\boldsymbol{p}_\perp, p^z, \boldsymbol{k})$, the current-current correlator in Eq. (5.2) can be computed [108]

$$W^{<,\mu\nu}_{\mathrm{brem}}(K) = \int_{\boldsymbol{p}} \frac{n^F_{p+k}(1-n^F_p)}{2p^z(p^z+k)}(2P^\mu + K^\mu)\,\mathrm{Re}\, f^\nu(\boldsymbol{p}_\perp, p^z, \boldsymbol{k})\,. \tag{5.41}$$

By substituting the perturbative solution $\boldsymbol{f} \simeq \boldsymbol{f}^{(0)} + \boldsymbol{f}^{(1)}$, the correlator is

$$\begin{aligned} \sum_{a=1,2} \epsilon^{\mu *}_{(a)}(\boldsymbol{k})\epsilon^{\nu}_{(a)}(\boldsymbol{k}) W^{<}_{\mu\nu,\mathrm{brem}}(K) &\simeq \int_{\boldsymbol{p}} \frac{n^F_{p+k}(1-n^F_p)}{2p^z(p^z+k)}\,\mathrm{Re}\int_{\boldsymbol{p}'_\perp} C[\boldsymbol{p}'_\perp] \\ &\left[\frac{4\boldsymbol{p}^2_\perp}{[\delta E(\boldsymbol{p}_\perp, p^z, \boldsymbol{k})]^2} - \frac{4\boldsymbol{p}_\perp\cdot(\boldsymbol{p}_\perp+\boldsymbol{p}'_\perp)}{\delta E(\boldsymbol{p}_\perp, p^z, \boldsymbol{k})\delta E(\boldsymbol{p}_\perp+\boldsymbol{p}'_\perp, p^z, \boldsymbol{k})}\right]. \end{aligned} \tag{5.42}$$

Therefore, from Eq. (5.1) the photon emission rate is [109]

$$\begin{aligned} (2\pi)^3 \frac{\mathrm{d}\Gamma}{\mathrm{d}^3\boldsymbol{k}}\bigg|_{\mathrm{brem+annih}} &= \frac{\mathcal{A}(k)}{4m^2_\infty n^F_k}\int_{-\infty}^{\infty}\mathrm{d}p^z \frac{[(p^z)^2+(p^z+k)^2]}{(p^z)^2(p^z+k)^2} n^F_{p+k}(1-n^F_p) \\ &\qquad \int_{\boldsymbol{p}_\perp} \mathrm{Re}[2\boldsymbol{p}_\perp\cdot\boldsymbol{f}(\boldsymbol{p}_\perp, p^z, \boldsymbol{k})]\,, \\ &= \frac{\mathcal{A}(k)}{m^2_\infty n^F_k}\int_{-\infty}^{\infty}\mathrm{d}p^z \frac{[(p^z)^2+(p^z+k)^2]}{(p^z)^2(p^z+k)^2} n^F_{p+k}(1-n^F_p)\,\mathrm{Re}\int_{\boldsymbol{p}_\perp,\boldsymbol{p}'_\perp} C[\boldsymbol{p}'_\perp] \\ &\quad \left[\frac{\boldsymbol{p}^2_\perp}{[\delta E(\boldsymbol{p}_\perp, p^z, \boldsymbol{k})]^2} - \frac{\boldsymbol{p}_\perp\cdot(\boldsymbol{p}_\perp+\boldsymbol{p}'_\perp)}{\delta E(\boldsymbol{p}_\perp, p^z, \boldsymbol{k})\delta E(\boldsymbol{p}_\perp+\boldsymbol{p}'_\perp, p^z, \boldsymbol{k})}\right]. \end{aligned} \tag{5.43}$$

This perturbative emission rate is same as the rate by summing the two-loop diagrams in Fig. 5.2 with a soft gluon (see Appendix G for details). By noting that the two-loop diagrams are lowest order of ladder diagrams shown in Fig. 5.8, we can understand how the perturbative solution works. In the overlap region $gT \ll p_\perp \ll \sqrt{g}T$, the LO bremsstrahlung rate in Eq. (5.43) is

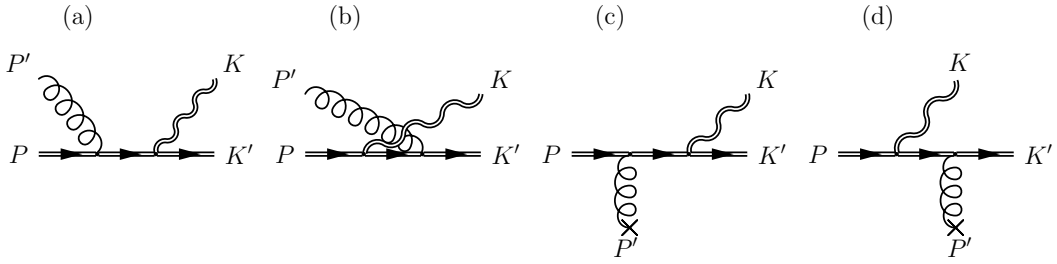

Figure 5.9: (a)(b) Plasmon scattering with time-like gluons and (c)(d) the extension to space-like gluons. It is difficult to distinguish (c)(d) from bremsstrahlung. Double solid lines denote hard quarks, double wiggly lines denote hard photons, and single curly lines denote soft gluons.

consistent with the NLO result in Section 5.5.

5.4 Plasmon[4] Scattering

To motivate wide-angle bremsstrahlung discussed in the previous section, we consider plasmon scattering shown in Fig. 5.9 (a) and (b)

$$P + P' \to K + K' \,. \tag{5.44}$$

For simplicity, the emitted photon has only hard momentum $K \sim T$. When the gluon is soft ($P' \sim gT$) and quarks are hard ($P, K' \sim T$), we expect the $\mathcal{O}(g)$ correction to the LO emission rate.

We assume that the photon is emitted in the z-direction, then it is convenient to use light-cone coordinates:

$$P^\mu = (p^+, p^-, \boldsymbol{p}_\perp) \,, \tag{5.45}$$

where $\boldsymbol{p}_\perp$ is perpendicular to the z-axis and

$$p^+ \equiv p^0 + p^z \simeq 2p^z \,, \tag{5.46}$$

$$p^- \equiv p^0 - p^z \,. \tag{5.47}$$

For hard particles, $p^+ \sim T$. The photon has $K = (k^+, k^-, \boldsymbol{k}_\perp) = (k^+, 0, \boldsymbol{0})$

[4]By "plasmon" we mean both longitudinal and transverse poles in the gluon spectral density, $\delta(p'^0 - \omega_L)$ and $\delta(p'^0 - \omega_T)$.

which is taken along the z-axis. Hard particles are almost on-shell:

$$P^2 = -p^+p^- + \boldsymbol{p}_\perp^2 = -m_\infty^2 \sim g^2T^2\,, \tag{5.48}$$

and the minus coordinate for on-shell modes is

$$p^- = \frac{\boldsymbol{p}_\perp^2 + m_\infty^2}{p^+}\,. \tag{5.49}$$

For the soft gluon, we take all four components of momentum $\sim gT$:

$$P'^\mu = (p'^+, p'^-, \boldsymbol{p}'_\perp) \sim (gT, gT, gT)\,. \tag{5.50}$$

The energy-momentum conservation yields

$$p^+ + p'^+ = k^+ + k'^+\,, \tag{5.51}$$
$$p^- + p'^- = k'^-\,, \tag{5.52}$$
$$\boldsymbol{p}_\perp + \boldsymbol{p}'_\perp = \boldsymbol{k}'_\perp\,. \tag{5.53}$$

From the minus conservation

$$p^- \sim k'^- \sim p'^- \sim gT\,, \tag{5.54}$$

which requires, since $p^- \sim p_\perp^2/p^+$, that

$$p_\perp \sim k'_\perp \sim \sqrt{g}T\,. \tag{5.55}$$

So the four components of hard particle momentum scale as

$$(p^+, p^-, \boldsymbol{p}_\perp) \sim (T, gT, \sqrt{g}T)\,. \tag{5.56}$$

With this power counting, we define the momentum fraction z as we did in bremsstrahlung:

$$k^+ \equiv (1-z)p^+ \qquad \text{and} \qquad k'^+ \equiv zp^+\,. \tag{5.57}$$

Since $\boldsymbol{p}'_\perp$ is $\mathcal{O}(\sqrt{g})$ smaller than the others in Eq. (5.53), $\boldsymbol{k}'_\perp \simeq \boldsymbol{p}_\perp$ and

$$k'^- = \frac{(\boldsymbol{k}'_\perp)^2 + m_\infty^2}{k'^+} \simeq \frac{(\boldsymbol{p}_\perp)^2 + m_\infty^2}{zp^+} = \frac{1}{z}p^-\,, \tag{5.58}$$
$$p'^- = k'^- - p^- \simeq \frac{(1-z)}{z}p^-\,. \tag{5.59}$$

In terms of the light-cone coordinates, the Mandelstam variables are

$$s \simeq p^+ p'^- \,, \qquad t \simeq -z p^+ p'^- \,, \qquad u \simeq -(1-z) p^+ p'^- \,. \tag{5.60}$$

When the gluon momentum P' is soft, it is straightforward to calculate the squared matrix elements. It has the splitting function:

$$|M|^2 \sim -\frac{s}{t} - \frac{t}{s} = \frac{1+z^2}{z} \qquad \text{(fermion splitting)} \,. \tag{5.61}$$

The photon emission rate can be obtained by integrating the squared matrix elements over the phase space. In the light-cone coordinates, the measure and the delta function are defined by

$$d^4 P \equiv \frac{dp^+}{2} dp^- d^2 \boldsymbol{p}_\perp \,, \tag{5.62}$$

$$(2\pi)^4 \delta^4(P) \equiv 2(2\pi)^4 \delta(p^+) \delta(p^-) \delta^2(\boldsymbol{p}_\perp) \,. \tag{5.63}$$

The phase space integration is

$$\begin{aligned} (2\pi)^3 \frac{\mathrm{d(PS)}}{\mathrm{d}^3 \boldsymbol{k}} &\equiv \int_{\boldsymbol{p}, P', \boldsymbol{k}'} \frac{1}{2p 2k' 2k} (2\pi)^4 \delta^4(P + P' - K - K') \,, \\ &= \int_{\boldsymbol{p}, P'} \frac{1}{2p 2k' 2k} (2\pi) \delta(p^- + p'^- - k'^-) \,, \end{aligned} \tag{5.64}$$

where in the last line we used $\delta(p^+ + p'^+ - k^+ - k'^+) \delta^2(\boldsymbol{p}_\perp + \boldsymbol{p}'_\perp - \boldsymbol{k}'_\perp)$ to integrate over $\boldsymbol{k}'$. By using Eqs. (5.47), (5.49), and (5.58), the phase space is

$$\begin{aligned} (2\pi)^3 \frac{\mathrm{d(PS)}}{\mathrm{d}^3 \boldsymbol{k}} &\simeq \int_{p^+, \boldsymbol{p}_\perp, P'} \frac{1}{p^+ k'^+ 2k} 2\pi \delta \left(p'^0 - p'^z - \frac{(1-z) p_\perp^2}{z p^+} \right) \,, \\ &= \int_{p^+, \boldsymbol{p}_\perp, \boldsymbol{p}'} \frac{1}{p^+ k'^+ 2k} \bigg|_{p'^0 = p'^z + \delta E} \,, \end{aligned} \tag{5.65}$$

where, neglecting m_∞^2, we fixed

$$p'^0 = p'^z + \delta E \qquad \text{with} \qquad \delta E \equiv \frac{(1-z) p_\perp^2}{z p^+} \,. \tag{5.66}$$

Here the energy change $\delta E = k^0 + k'^0 - p^0$ is same as the difference in the minus momenta.

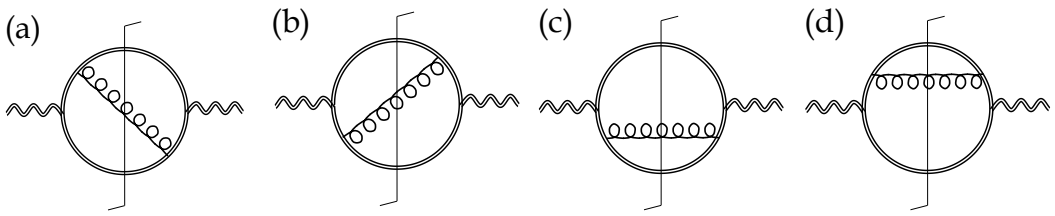

Figure 5.10: Two-loop cut diagrams contributing to the NLO photon emission rate. These cut diagrams can be understood as plasmon scattering with time-like gluons and its extension to space-like gluons shown in Fig. 5.9. Double solid lines denote hard quarks, double wiggly lines denote hard photons, and single curly lines denote soft gluons.

5.5 Wide-angle Bremsstrahlung

In the previous section, we motivated a particular kinematic region by considering plasmon scattering. In this section, we will determine the full squared matrix elements for photon emission in this kinematic window. The four relevant cut diagrams are shown in Fig. 5.10. The gluons are soft with momenta $P' = (p'^+, p'^-, p'_\perp) \sim (gT, gT, gT)$ and the quarks are hard with $P, K' \sim (T, gT, \sqrt{g}T)$. When the gluon momenta P' is time-like, these graphs correspond to plasmon scattering in Fig. 5.9 (a) and (b)[5]. For space-like momenta, these four graphs correspond to bremsstrahlung and are shown in Fig. 5.9 (c) and (d). As discussed in Section 5.2, it is difficult to distinguish these processes from bremsstrahlung. For the collinear emission discussed in Section 5.3, the angle between photon and quark is

$$\delta\theta \sim \frac{p_\perp}{p} \sim g \qquad \text{(collinear)}\,. \tag{5.67}$$

In Fig. 5.9, the angle is

$$\delta\theta \sim \frac{p_\perp}{p} \sim \sqrt{g} \qquad \text{(wide-angle)}\,. \tag{5.68}$$

Thus, we refer to this scattering mechanism as "wide-angle" bremsstrahlung. However, it must be understood that this wide-angle bremsstrahlung include plasmon scattering.

[5]There are also corresponding pair annihilation processes. For space-like momenta, it is difficult to distinguish them from inelastic pair annihilation.

5.5.1 Matrix Elements

To compute the matrix elements, we use the HTL effective theory [5, 29], and choose the Coulomb gauge for simplicity. For the soft gluon, the HTL propagators are

$$iG^R_{00}(p^0,\boldsymbol{p}) = \frac{-i\eta_{00}}{\boldsymbol{p}^2+\Pi_L(x)}\,, \tag{5.69}$$

$$iG^R_{ij}(p^0,\boldsymbol{p}) = \frac{-i(\delta^{ij}-\hat{\boldsymbol{p}}^i\hat{\boldsymbol{p}}^j)}{-(p^0)^2+\boldsymbol{p}^2+\Pi_T(x)}\,, \tag{5.70}$$

$$iG^R_{0i}(p^0,\boldsymbol{p}) = G^R_{i0}(p^0,\boldsymbol{p}) = 0\,. \tag{5.71}$$

Here $x = p^0/p$ and the HTL self-energies are[6]

$$\Pi_L(x) = m_D^2\left[1-\frac{x}{2}\ln\left(\frac{x+1}{x-1}\right)\right]\,, \tag{5.72}$$

$$\Pi_T(x) = \frac{m_D^2}{2}\left[x^2+\frac{x(1-x^2)}{2}\ln\left(\frac{x+1}{x-1}\right)\right]\,. \tag{5.73}$$

At zero frequency $p^0=0$, the self-energies are

$$\Pi_L(0,\boldsymbol{p}) = m_D^2 \qquad \text{and} \qquad \Pi_T(0,\boldsymbol{p}) = 0, \tag{5.74}$$

and the HTL propagators simplify to

$$iG^R_{00}(0,\boldsymbol{p}) = \frac{-i\eta_{00}}{\boldsymbol{p}^2+m_D^2} \qquad \text{and} \qquad iG^R_{ij}(0,\boldsymbol{p}) = \frac{-i(\delta^{ij}-\hat{\boldsymbol{p}}^i\hat{\boldsymbol{p}}^j)}{\boldsymbol{p}^2}\,, \tag{5.75}$$

which are also known as the electrostatic QCD (EQCD) propagators. The imaginary part of the retarded Green's function gives the spectral density, $\rho_{\mu\nu} \equiv iG^R_{\mu\nu} - iG^A_{\mu\nu}$. The longitudinal and transverse components are

$$\rho^L(P) = 2\pi z_L(P)\Big[\delta\big(p^0-\omega_L(p)\big)-\delta\big(p^0+\omega_L(p)\big)\Big]+\beta_L(P)\,\theta\big(p^2-(p^0)^2\big)\,, \tag{5.76}$$

$$\rho^T(P) = 2\pi z_T(P)\Big[\delta\big(p^0-\omega_T(p)\big)-\delta\big(p^0+\omega_T(p)\big)\Big]+\beta_T(P)\,\theta\big(p^2-(p^0)^2\big)\,. \tag{5.77}$$

[6]The HTL self-energies correspond to the free spectral densities of J^μ correlators, Eqs. (3.117) and (3.118).

Here $z_L(P)$ and $z_T(P)$ are the residues of the longitudinal and transverse poles, and $\beta_L(P)$ and $\beta_T(P)$ correspond to the cut contributions for space-like momentum.

The fermion propagator can be written in the form of

$$iS^R(P) = \frac{h_+(\hat{\boldsymbol{p}})}{p^0 - p - \Sigma_+(P)} + \frac{h_-(\hat{\boldsymbol{p}})}{p^0 + p - \Sigma_-(P)}\,, \tag{5.78}$$

where we defined the chiral projection

$$h_\pm(\hat{\boldsymbol{p}}) \equiv -\frac{i}{2}(-\gamma^0 \pm \gamma\cdot\hat{\boldsymbol{p}})\,. \tag{5.79}$$

The fermion self-energies are

$$\Sigma_+(x) = \frac{m_\infty^2}{2p}\left[1 + \frac{1}{2}(1-x)\ln\left|\frac{x+1}{x-1}\right|\right] - i\pi\frac{m_\infty^2}{4p}(1-x)\,\theta(1-x^2)\,, \tag{5.80}$$

$$\Sigma_-(x) = -\frac{m_\infty^2}{2p}\left[1 - \frac{1}{2}(1+x)\ln\left|\frac{x+1}{x-1}\right|\right] - i\pi\frac{m_\infty^2}{4p}(1+x)\,\theta(1-x^2)\,, \tag{5.81}$$

which can be neglected for hard momentum. We can verify that only h_+ part contributes to the matrix elements in the order we are working. With these propagators, it is straightforward to compute the squared matrix elements. In the Coulomb gauge, the longitudinal and the transverse parts are

$$|M|_L^2\rho^L(P') \simeq 16e^2\sum_s q_s^2 d_F C_F g^2 \frac{1+z^2}{z}\frac{p_\perp'^2}{2(p'^-)^2}\rho^L(P')\,, \tag{5.82}$$

$$|M|_T^2\rho^T(P') \simeq 16e^2\sum_s q_s^2 d_F C_F g^2 \frac{1+z^2}{z}\left[1 - \frac{m_g^2\sin^2\theta}{2(p'^-)^2}\right]\rho^T(P')\,, \tag{5.83}$$

where $m_g^2 = (p'^0)^2 - p'^2$ and $\sin^2\theta = p_\perp'^2/p'^2$. The LO bare contribution of the matrix elements is

$$|M|_{\rm bare}^2\,\rho^{\rm bare}(P') = 16e^2\sum_s q_s^2 d_F C_F g^2 \frac{1+z^2}{z}\rho^{\rm bare}(P')\,, \tag{5.84}$$

where

$$\rho^{\rm bare}(P') = \frac{2\pi}{2p'}\Big[\delta(p'^0 - p') + \delta(p'^0 + p')\Big]\,. \tag{5.85}$$

The matrix elements in Eqs. (5.82) and (5.83) can be understood in terms

of the Wightman correlator. We define the field strength

$$F_{a+}(P') \equiv ip'_a A_+(P') - ip'_+ A_a(P')\,, \tag{5.86}$$

where $a = x, y$ for transverse components. F_{a+} corresponds to the transverse force acting on a quark which moves and radiates in the z-direction. With this force, the matrix elements can be written[7]

$$\frac{T}{p'^0}\Big[|M|_L^2\rho^L + |M|_T^2\rho^T\Big] = 16e^2\sum_s q_s^2 d_F C_F g^2 \frac{1+z^2}{z}\frac{1}{2(p'^-)^2}\langle\!\langle F_{a+}(P')F_{a+}\rangle\!\rangle\,, \tag{5.87}$$

where we used $n_{p'}^B \simeq T/p'^0$ and the following relations:

$$p'_a p'_a\langle\!\langle A_+(P')A_+\rangle\!\rangle = p'^2_\perp\big(\langle\!\langle A^0(P')A^0\rangle\!\rangle + \langle\!\langle A^z(P')A^z\rangle\!\rangle\big) = p'^2_\perp(\rho^L + \sin^2\theta\rho^T)\,, \tag{5.88}$$

$$p'_+ p'_a\langle\!\langle A_a(P')A_+\rangle\!\rangle = p'_+ p_a\langle\!\langle A_a(P')A_z\rangle\!\rangle = -p'_z p'_+\sin^2\theta\rho^T\,, \tag{5.89}$$

$$p'_+ p'_+\langle\!\langle A_a(P')A_a\rangle\!\rangle = p'^2_+(2-\sin^2\theta)\rho^T\,. \tag{5.90}$$

5.5.2 Phase Space Integration

The photon emission rate is obtained by integrating the matrix elements (with statistical factors) over the phase space Eq. (5.65):

$$(2\pi)^3\frac{\mathrm{d}\Gamma}{\mathrm{d}^3\boldsymbol{k}}\bigg|_{\text{brem}}^{\text{wide}} = \int_{p^+,\boldsymbol{p}_\perp,\boldsymbol{p}'}\frac{1}{p^+k'^+2k}n_p^F(1-n_{k'}^F)\frac{T}{p'^0}\Big[|M|_L^2\rho^L+|M|_T^2\rho^T\Big]\Big|_{p'^0=p'^z+\delta E}\,. \tag{5.91}$$

In order to get the NLO correction, we subtract the LO bare contribution:

$$(2\pi)^3\frac{\mathrm{d}\delta\Gamma_{\text{NLO}}}{\mathrm{d}^3\boldsymbol{k}}\bigg|_{\text{brem}}^{\text{wide}} = \int_{p^+,\boldsymbol{p}_\perp,\boldsymbol{p}'}\frac{1}{p^+k'^+2k}n_p^F(1-n_{k'}^F) \frac{T}{p'^0}\Big[|M|_L^2\rho^L + |M|_T^2\rho^T - |M|_{\text{bare}}^2\rho^{\text{bare}}\Big]\Big|_{p'^0=p'^z+\delta E}\,, \tag{5.92}$$

[7] In general, the force-force correlator is convoluted with the Wilson line $\Big\langle F^a_{\mu\nu}(X)W_{ab}(X)F^b_{\alpha\beta}(0)\Big\rangle$, where $W_{ab}(X) \equiv \mathcal{P}e^{ig\int A^\mu dX_\mu} \simeq \delta_{ab} + \mathcal{O}(g)$. At the order we are working, only δ_{ab} contributes. Therefore, the correlator in Eq. (5.87) is gauge-invariant.

where we used $\delta\Gamma_{\rm NLO}$ to emphasize that it is the $\mathcal{O}(g)$ correction to the LO result. By using the rotational symmetry of perpendicular momenta,

$$\int_{\boldsymbol{p}_\perp} = \frac{(2\pi)}{2(2\pi)^2}\int \mathrm{d}p_\perp^2\,, \tag{5.93}$$

the emission rate is

$$(2\pi)^3\frac{\mathrm{d}\delta\Gamma_{\rm NLO}}{\mathrm{d}^3\boldsymbol{k}}\bigg|^{\rm wide}_{\rm brem} = \int_k^\infty\frac{\mathrm{d}p^z}{2\pi}\int_0^\infty\frac{\mathrm{d}p_\perp^2}{2(2\pi)}\int_0^\infty\frac{\mathrm{d}p_\perp'^2}{2(2\pi)}\frac{1}{2p2k'2k}n_p^F(1-n_{k'}^F)$$
$$\int_{-\infty}^\infty\frac{\mathrm{d}p'^z}{2\pi}\frac{T}{p'^0}\Big[|M|^2_L\rho^L+|M|^2_T\rho^T-|M|^2_{\rm bare}\,\rho^{\rm bare}\Big]\Big|_{p'^0=p'^z+\delta E}\,. \tag{5.94}$$

The p'^z integration can be handled by contour integration. By taking the residue at $p'^0=0$ with the EQCD propagators in Eq. (5.75), the integration yields [116]

$$\int_{-\infty}^\infty\frac{\mathrm{d}p'^z}{2\pi}\frac{T}{p'^0}\Big[|M|^2_L\rho^L+|M|^2_T\rho^T\Big]\Big|_{p'^0=p'^z+\delta E}$$
$$=16e^2\sum_s q_s^2 d_F C_F g^2\frac{1+z^2}{z}T\left[\frac{p_\perp'^2}{2(\delta E)^2}\frac{-1}{p'^2+m_D^2}+\left(1+\frac{p'^2\sin^2\theta}{2(\delta E)^2}\right)\frac{1}{p'^2}\right]\Bigg|_{p'^z=-\delta E}. \tag{5.95}$$

Similarly, the bare contribution is

$$\int_{-\infty}^\infty\frac{\mathrm{d}p'^z}{2\pi}\frac{T}{p'^0}|M|^2_{\rm bare}\rho^{\rm bare}=16e^2\sum_s q_s^2 d_F C_F g^2\frac{1+z^2}{z}T\frac{1}{p'^2}\bigg|_{p'^z=-\delta E}. \tag{5.96}$$

Therefore,

$$\int_{-\infty}^\infty\frac{\mathrm{d}p'^z}{2\pi}\frac{T}{p'^0}\Big[|M|^2_L\rho^L+|M|^2_T\rho^T-|M|^2_{\rm bare}\rho^{\rm bare}\Big]\Big|_{p'^0=p'^z+\delta E}$$
$$=16e^2\sum_s q_s^2 d_F C_F g^2\frac{1+z^2}{z}\frac{T}{2(\delta E)^2}\frac{m_D^2 p_\perp'^2}{(p'^2+m_D^2)p'^2}\bigg|_{p'^z=-\delta E}. \tag{5.97}$$

Fig. 5.11 shows a sample integrand of Eq. (5.97) for $\delta E=0.5$ and $p_\perp'^2=0.7$. The integrand consists of a continuous cut part and two peaks. Wide-angle bremsstrahlung contributes to the continuous part. The peaks correspond to plasmons: the longitudinal pole $\delta\big(p'^0-\omega_L(p')\big)$ and the transverse pole $\delta\big(p'^0-\omega_T(p')\big)$. We note that in Eq. (5.97) the integrand is a complicated

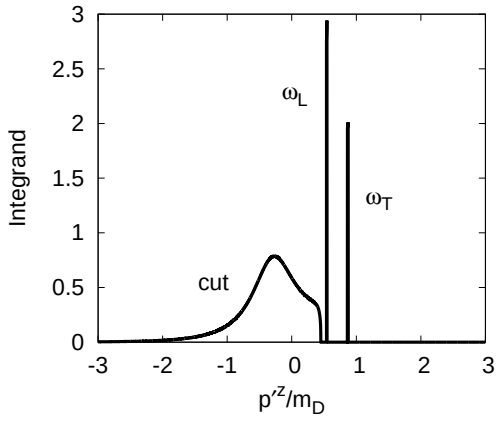

Figure 5.11: A sample integrand of Eq. (5.97) with $\delta E = 0.5$ and $p_\perp'^2 = 0.7$. The continuous part corresponds to the cut contribution and the two peaks to the longitudinal and transverse poles.

function of p'^z, but the integrated result is simple. This integration generalizes the AGZ sum rule with finite energy transfer.

In wide-angle bremsstrahlung (and plasmon collisions), we started with $\boldsymbol{p}_\perp \sim \sqrt{gT}$. When this transverse momentum becomes soft $gT \ll p_\perp \ll \sqrt{gT}$, this process reduces to the LO collinear bremsstrahlung. At wide angle, the LPM effect can be neglected since the formation time is short. By taking the limit $p_\perp \to 0$, $\delta E = p'^- \to 0$ and the matrix elements become

$$\Big[|M|_L^2\rho^L + |M|_T^2\rho^T\Big]\Big|_{p'^0=p'^z+\delta E} \to 16e^2\sum_s q_s^2 d_F C_F g^2 \frac{1+z^2}{z}\frac{p_\perp'^2}{2(\delta E)^2}\left(\rho^L + \rho^T\sin^2\theta\right) . \quad (5.98)$$

Here $\rho^L + \rho^T\sin^2\theta = \rho^{\mu\nu}v_\mu v_\nu$ is same as the LO result in Eq. (5.23) (see also Eq. (G.19) in Appendix G). In order to obtain the NLO correction, we subtract the LO bremsstrahlung contribution which is given by

$$16e^2\sum_s q_s^2 d_F C_F g^2 \int_k^\infty \frac{\mathrm{d}p^z}{2\pi}\int_0^\infty \frac{\mathrm{d}p_\perp^2}{2(2\pi)}\int_0^\infty \frac{\mathrm{d}p_\perp'^2}{2(2\pi)}\frac{1}{2p2k'2k} n_p^F(1-n_{k'}^F) \frac{1+z^2}{z}\int_{-\infty}^\infty \frac{\mathrm{d}p'^z}{2\pi}\frac{T}{p'^0}\frac{p_\perp'^2}{2(\delta E)^2}(\rho^L + \rho^T\sin^2\theta)\Big|_{p'^0=p'^z} . \quad (5.99)$$

Performing the contour integration over p'^z yields

$$\int_{-\infty}^{\infty}\frac{\mathrm{d}p'^z}{2\pi}\frac{T}{p'^0}\frac{p_\perp'^2}{2(\delta E)^2}(\rho^L+\rho^T\sin^2\theta)\Big|_{p'^0=p'^z}=\frac{T}{2(\delta E)^2}\frac{m_D^2}{(p_\perp'^2+m_D^2)}\Big|_{p'^z=0}. \quad (5.100)$$

By subtracting Eq. (5.99) from Eq. (5.94) (after integrating over p'^z), the NLO correction is

$$(2\pi)^3\frac{\mathrm{d}\delta\Gamma_{\mathrm{NLO}}}{\mathrm{d}^3\boldsymbol{k}}\Big|_{\mathrm{brem}}^{\mathrm{wide}}=16e^2\sum_s q_s^2 d_F C_F g^2\int_k^\infty\frac{\mathrm{d}p^z}{2\pi}\frac{1}{2p2k'2k}\frac{1+z^2}{z}n_p^F(1-n_{k'}^F)$$
$$\int_0^\infty\frac{\mathrm{d}p_\perp^2}{2(2\pi)}\int_0^\infty\frac{\mathrm{d}p_\perp'^2}{2(2\pi)}\frac{T}{2(\delta E)^2}\left[\frac{m_D^2p_\perp'^2}{(p'^2+m_D^2)p'^2}-\frac{m_D^2}{(p_\perp'^2+m_D^2)}\right]\Big|_{p'^z=-\delta E}. \quad (5.101)$$

The rest of the integrations can be done as follows. To get the splitting function factored out, we change the integration variable from $p_\perp^2$ to δE:

$$\int_{p_\perp^2}\to\frac{2zp^z}{(1-z)}\int_{\delta E}, \quad (5.102)$$

and integrate over δE and $p_\perp'^2$

$$\int_0^\infty\frac{\mathrm{d}(\delta E)}{2(2\pi)}\int_0^\infty\frac{\mathrm{d}p_\perp'^2}{2(2\pi)}\frac{T}{2(\delta E)^2}\left[\frac{m_D^2p_\perp'^2}{(p'^2+m_D^2)p'^2}-\frac{m_D^2}{(p_\perp'^2+m_D^2)}\right]\Big|_{p'^z=-\delta E}$$
$$=-\frac{m_DT}{16\pi}. \quad (5.103)$$

By recalling the splitting function

$$\frac{1+z^2}{z}=\frac{p^z}{p^z-k}+\frac{p^z-k}{p^z}, \quad (5.104)$$

we have

$$(2\pi)^3\frac{\mathrm{d}\delta\Gamma_{\mathrm{NLO}}}{\mathrm{d}^3\boldsymbol{k}}\Big|_{\mathrm{brem}}^{\mathrm{wide}}=\frac{2}{\pi}e^2\sum_s q_s^2d_FC_Fg^2\frac{1}{k^2}\left(-\frac{m_DT}{16\pi}\right)$$
$$\int_k^\infty\mathrm{d}p^z\left(\frac{p^z}{p^z-k}+\frac{p^z-k}{p^z}\right)n_p^F(1-n_{p-k}^F). \quad (5.105)$$

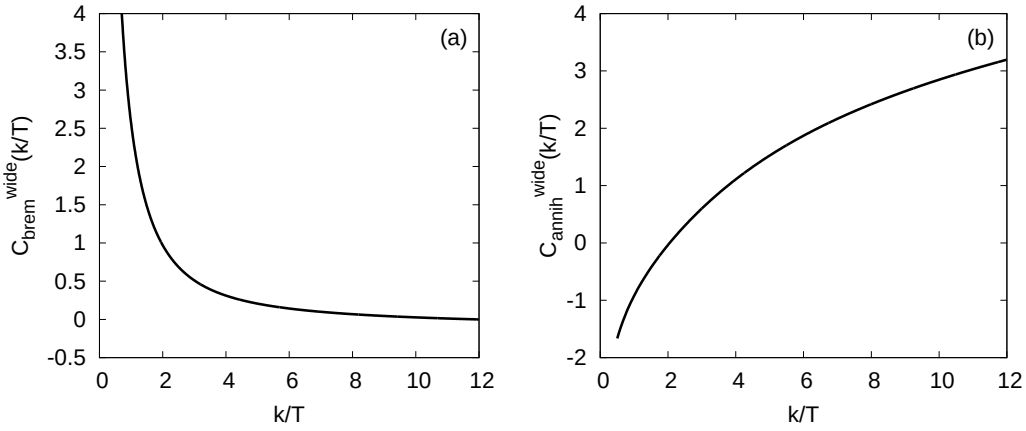

Figure 5.12: The NLO correction to the photon emission rate from (a) wide-angle bremsstrahlung, $C_{\rm brem}^{\rm wide}(k/T)$ and (b) wide-angle pair annihilation, $C_{\rm annih}^{\rm wide}(k/T)$.

We note that Eq. (5.105) is logarithmically divergent when $p^z \to k$:

$$\int_{k+\mu_z}^{\infty} {\rm d}p^z \left(\frac{p^z}{p^z-k} + \frac{p^z-k}{p^z} \right) n_p^F (1-n_{p-k}^F) = \frac{k n_k^F}{2} \ln\left(\frac{T}{\mu_z}\right) + ({\rm finite}) \,, \quad (5.106)$$

where $gT \ll \mu_z \ll T$ is a cutoff. By separating the logarithmically divergent part, we obtain a finite result for wide-angle bremsstrahlung:

$$(2\pi)^3 \frac{{\rm d}\delta\Gamma_{\rm NLO}}{{\rm d}^3\boldsymbol{k}}\bigg|_{\rm brem}^{\rm wide} = -\frac{1}{8\pi^2} e^2 \sum_s q_s^2 d_F C_F g^2 m_D T \frac{n_k^F}{2k} \left[\ln\left(\frac{T}{\mu_z}\right) + C_{\rm brem}^{\rm wide}(k/T) \right] . \quad (5.107)$$

Here $C_{\rm brem}^{\rm wide}(k/T)$ is independent of μ_z. With the notation of Ref. [109], the NLO correction to the photon emission rate from wide-angle bremsstrahlung is

$$(2\pi)^3 \frac{{\rm d}\delta\Gamma_{\rm NLO}}{{\rm d}^3\boldsymbol{k}}\bigg|_{\rm brem}^{\rm wide} = -\frac{m_D}{2\pi T} \mathcal{A}(k) \left[\ln\left(\frac{T}{\mu_z}\right) + C_{\rm brem}^{\rm wide}(k/T) \right] . \quad (5.108)$$

The numerical result of $C_{\rm brem}^{\rm wide}(k/T)$ is shown in Fig. 5.12 (a). It becomes negative for higher photon momentum $k/T > 12$.

Similarly, wide-angle pair annihilation contributes to the photon emission

rate at NLO (see Appendix H for details):

$$(2\pi)^3 \frac{\mathrm{d}\delta\Gamma_{\mathrm{NLO}}}{\mathrm{d}^3\boldsymbol{k}}\bigg|_{\mathrm{annih}}^{\mathrm{wide}} = -\frac{m_D}{2\pi T}\mathcal{A}(k)\left[\ln\left(\frac{T}{\mu_z}\right) + C_{\mathrm{annih}}^{\mathrm{wide}}(k/T)\right]. \tag{5.109}$$

The numerical result of $C_{\mathrm{annih}}^{\mathrm{wide}}(k/T)$ is shown in Fig. 5.12 (b). The infrared cutoff dependence on μ_z in Eqs. (5.108) and (5.109) will cancel the ultraviolet dependence later when adding the quark-photon conversion contribution.

5.6 Quark-Photon Conversion

In the previous section, we computed the photon emission rate from wide-angle bremsstrahlung and wide-angle pair annihilation. They are logarithmically divergent, and we regularized it with the infrared cutoff μ_z. As discussed earlier, when the photon carries most of the incoming quark momentum, bremsstrahlung reduces to quark-photon conversion. The photon emission rate from quark-photon conversion (see Fig. 5.13 (a)) can be calculated by using the HTL propagator in the t-channel exchange. The μ_z dependence in Eqs. (5.108) and (5.109) will be canceled by the ultraviolet cutoff of the quark-photon conversion contribution. In this section, we derive the "sum rule" (which generalize the AGZ result [113]) at LO and intuitively generalize it to NLO. The verification of the NLO sum rule will be given in the forthcoming work [107].

5.6.1 Sum Rule

The photon emission rate is related to the photon self-energy by [29]

$$(2\pi)^3 \frac{\mathrm{d}\Gamma}{\mathrm{d}^3\boldsymbol{k}}\bigg|_{\mathrm{convs}} = \frac{1}{2k}\Pi^<(K). \tag{5.110}$$

The cut diagram in Fig. 5.13 (b) can be calculated by using the cutting rules [5, 29]

$$\Pi^<(K) = 2e^2 \sum_s q_s^2 d_F \int_{P-K} \mathrm{Tr}\left[S^>(P-K)\,\gamma^a\,S^<_{\mathrm{bare}}(P)\,\gamma_a\right], \tag{5.111}$$

where $S^>$ is the HTL dressed fermion propagator and $S^<_{\mathrm{bare}}$ is the bare fermion propagator. For simplicity, we change the variable of the soft momentum

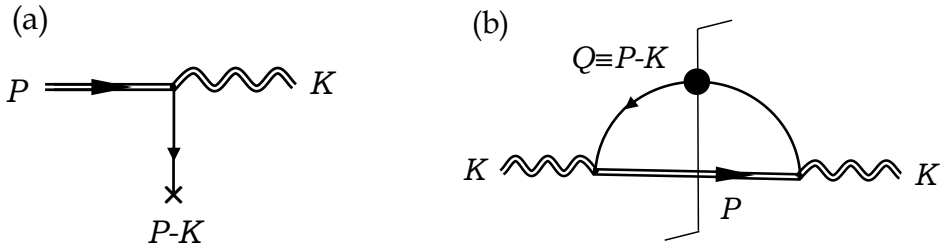

Figure 5.13: (a) Quark-photon conversion, where a hard quark undergoes soft momentum exchange to become a hard photon with $K \simeq P$. (b) The photon self-energy cut diagram. The square of (a). Double wiggly lines denote hard photons, double solid lines denote hard quarks, and single solid lines (with arrows) denote soft quarks. Time runs from left to right.

$P - K \equiv Q$, then the self-energy is[8]

$$\Pi^{<}(K) = 2e^2 \sum_s q_s^2 d_F \int_Q \mathrm{Tr}\left[S^{>}(Q)\,\gamma^a\,S^{<}_{\rm bare}(Q+K)\,\gamma_a\right]. \tag{5.112}$$

Here the dressed fermion propagator is written in terms of spectral densities:

$$iS^{>}(Q) = (1-n_q^F)\Big[h_+(\hat{\boldsymbol{q}})\,\rho^+(Q) + h_-(\hat{\boldsymbol{q}})\,\rho^-(Q)\Big]. \tag{5.113}$$

For the fermion cut line, we use the positive energy part of

$$\begin{aligned} iS^{<}_{\rm bare}(Q+K) \simeq -i\frac{2\pi}{2E_{q+k}} n^F_{q+k} k^+\gamma_+\,\delta(q^0+k^0-E_{q+k}) \\ + i\frac{2\pi}{2E_{q+k}} n^F_{-q-k} k^+\gamma_+\,\delta(q^0+k^0+E_{q+k}), \end{aligned} \tag{5.114}$$

where we used $(\not{Q}+\not{K}) \simeq k^+\gamma_+$. With $E_{q+k} \simeq q^z + k + (q_\perp^2+m_\infty^2)/2k$, the delta function can be approximated as

$$\delta(q^0+k^0-E_{q+k}) \simeq \delta\big(q^0 - q^z + \mathcal{O}(g^2)\big). \tag{5.115}$$

[8]The trace part can be also written as Tr $[\gamma_+ S^<(Q)]$, where $\gamma_+ = -\gamma^0 + \gamma^z$.

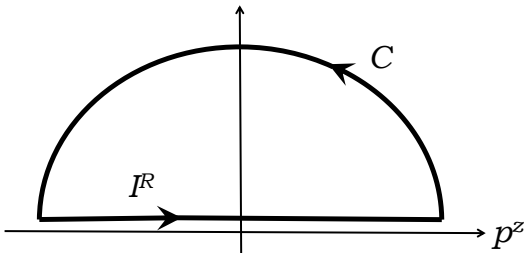

Figure 5.14: The contour for the integration of I^R in the upper-half plane. C corresponds to the counterclockwise semi-circle part.

By approximating $n_q^F \simeq 1/2$ and $n_{q+k}^F \simeq n_k^F$, the self-energy is

$$\begin{aligned}\Pi^<(K) &\simeq 2e^2 \sum_s q_s^2 d_F n_k^F \frac{2\pi}{4k} \int_Q \delta(q^0 - q^z) \\ &\qquad\qquad k^+ \Big[\mathrm{Tr}\,[h_+\gamma^a\gamma_+\gamma_a]\rho^+ + \mathrm{Tr}\,[h_-\gamma^a\gamma_+\gamma_a]\rho^- \Big], \\ &= 2e^2 \sum_s q_s^2 d_F n_k^F \int \frac{\mathrm{d}^2\boldsymbol{q}_\perp}{(2\pi)^2} \int \frac{\mathrm{d}q^z}{2\pi} \left[\left(1 - \frac{q^z}{q}\right)\rho^+ + \left(1 + \frac{q^z}{q}\right)\rho^- \right] \Big|_{q^0=q^z}.\end{aligned} \tag{5.116}$$

The integral over q^z can be handled with contour integrations. By recalling the definition of spectral densities $\rho_\pm = iS_\pm^R - iS_\pm^A$, we define

$$I^R \equiv \int \frac{\mathrm{d}q_\perp^2}{2(2\pi)} \int \frac{\mathrm{d}q^z}{2\pi} \left[\frac{i(1 - q^z/q)}{q^0 - q - \Sigma_+(Q)} + \frac{i(1 + q^z/q)}{q^0 + q - \Sigma_-(Q)} \right] \Big|_{q^0=q^z}, \tag{5.117}$$

$$I^A \equiv \int \frac{\mathrm{d}q_\perp^2}{2(2\pi)} \int \frac{\mathrm{d}q^z}{2\pi} \left[\frac{i(1 - q^z/q)}{q^0 - q - \Sigma_+^*(Q)} + \frac{i(1 + q^z/q)}{q^0 + q - \Sigma_-^*(Q)} \right] \Big|_{q^0=q^z}. \tag{5.118}$$

Then the self-energy can be written

$$\Pi^<(K) = 2e^2 \sum_s q_s^2 d_F n_k^F (I^R - I^A). \tag{5.119}$$

The integrand of I^R is analytic in the upper-half plane, and we consider the contour shown in Fig. 5.14. Since there is no pole inside the contour, we can change the real q^z integration into the contour integral at C which is the semi-circle of $q^z \to \infty$. By noticing

$$q^0 = q^z \qquad \text{and} \qquad q \simeq q^z + \frac{q_\perp^2}{2q^z}, \tag{5.120}$$

$x \to 1$ when $q^z \to \infty$. So, the fermion self-energy in Eqs. (5.80) has a simple form

$$\Sigma_+(Q) \simeq \frac{m_\infty^2}{2q}\,, \tag{5.121}$$

and $\Sigma_-(Q)$ can be neglected. Now the integral is straightforward to calculate:

$$I^R \simeq \int \frac{\mathrm{d}q_\perp^2}{2(2\pi)} \int_C \frac{\mathrm{d}q^z}{2\pi} \frac{i}{q^z} \left[\frac{q_\perp^2}{q_\perp^2 + m_\infty^2} - 1 \right], \tag{5.122}$$

$$= \frac{1}{2} \int \frac{\mathrm{d}q_\perp^2}{2(2\pi)} \frac{m_\infty^2}{q_\perp^2 + m_\infty^2}\,, \tag{5.123}$$

where we changed the integral $\int_C \mathrm{d}q^z/q^z$ into $i\int_0^\pi \mathrm{d}\theta$. Similarly, the integrand of I^A is analytic in the lower half-plane, and the integral yields

$$I^A = -\frac{1}{2} \int \frac{\mathrm{d}q_\perp^2}{2(2\pi)} \frac{m_\infty^2}{q_\perp^2 + m_\infty^2}\,. \tag{5.124}$$

Therefore, the LO photon emission rate from quark-photon conversion is given by[9]

$$(2\pi)^3 \frac{\mathrm{d}\Gamma_{\mathrm{LO}}}{\mathrm{d}^3\boldsymbol{k}}\bigg|_{\mathrm{convs}} = e^2 \sum_s q_s^2 d_F \frac{n_k^F}{k} \int \frac{\mathrm{d}q_\perp^2}{2(2\pi)} \frac{m_\infty^2}{q_\perp^2 + m_\infty^2}\,,$$

$$= e^2 \sum_s q_s^2 d_F \frac{n_k^F}{k} \frac{m_\infty^2}{4\pi} \ln\left(\frac{\mu_\perp^2}{m_\infty^2}\right), \tag{5.125}$$

where we used the ultraviolet cutoff $\mu_\perp^2$. As discussed in Section 5.2, this cutoff dependence is canceled by the infrared one in $2 \leftrightarrow 2$ scattering with a hard gluon at LO.

In deriving the sum rule in Eq. (5.125), there was no explicit use of HTL. We only used the definition of the asymptotic mass, $m_\infty^2 = 2q\,\mathrm{Re}\,\Sigma_+|_{q\to\infty}$. Although it is not obvious, the sum rule is generalized to NLO with the replacement of m_∞^2 by $m_\infty^2 + \delta m_\infty^2$ [107]. Then the NLO correction is found by

[9] By neglecting the screening, we can get the leading-log emission rate $(2\pi)^3 \frac{\mathrm{d}\Gamma_{\mathrm{LLog}}}{\mathrm{d}^3\boldsymbol{k}} = e^2 \sum_s q_s^2 d_F \frac{n_k^F}{k} \int \frac{\mathrm{d}q_\perp^2}{2(2\pi)} \frac{m_\infty^2}{q_\perp^2} = e^2 \sum_s q_s^2 d_F m_\infty^2 \frac{n_k^F}{4\pi k} \ln(1/g)$. Here the coefficient corresponds to γ in Eq. (2.43) (after changing one of gluons into photon).

taking the difference between LO and NLO:

$$(2\pi)^3 \frac{\mathrm{d}\delta\Gamma_{\mathrm{NLO}}}{\mathrm{d}^3\boldsymbol{k}}\bigg|_{\mathrm{convs}} = e^2 \sum_s q_s^2 d_F \frac{n_k^F}{k} \int \frac{\mathrm{d}q_\perp^2}{2(2\pi)} \left[\frac{m_\infty^2 + \delta m_\infty^2}{q_\perp^2 + m_\infty^2 + \delta m_\infty^2} - \frac{m_\infty^2}{q_\perp^2 + m_\infty^2}\right], \\ = \frac{1}{4\pi} e^2 \sum_s q_s^2 d_F \frac{n_k^F}{k} \delta m_\infty^2 \left[\ln\left(\frac{\mu_\perp^2}{m_\infty^2}\right) - 1\right]. \tag{5.126}$$

5.6.2 Cutoff

In wide-angle bremsstrahlung and pair annihilation process, we used the infrared cutoff μ_z for the z-component of momentum, while in the conversion process the ultraviolet divergence was regulated by cutting off the transverse momentum integrals with $\mu_\perp^2$. Therefore, we need to relate μ_z with $\mu_\perp^2$. When the photon carries most of the incoming quark momentum, wide-angle bremsstrahlung reduces to quark-photon conversion. In order to compute the contribution, we return to the integral Eq. (5.101) in the limit $p^z \to k$:

$$(2\pi)^3 \frac{\mathrm{d}\delta\Gamma_{\mathrm{NLO}}}{\mathrm{d}^3\boldsymbol{k}}\bigg|_{\mathrm{cut}} \simeq 16 e^2 \sum_s q_s^2 d_F C_F g^2 \frac{n_k^F}{k} \int_0^{\mu_z} \frac{\mathrm{d}k'^z}{2\pi} \frac{1}{16(k'^z)^2} \int_{\mu_\perp^2}^\infty \frac{\mathrm{d}p_\perp^2}{2(2\pi)} \\ \int_0^\infty \frac{\mathrm{d}p_\perp'^2}{2(2\pi)} \frac{T}{2(\delta E)^2} \left[\frac{m_D^2 p_\perp'^2}{(p'^2 + m_D^2)p'^2} - \frac{m_D^2}{(p_\perp'^2 + m_D^2)}\right]\bigg|_{p'^z = -\delta E}. \tag{5.127}$$

Here we used

$$\int_k^{k+\mu_z} \mathrm{d}p \to \int_0^{\mu_z} \mathrm{d}k', \qquad \frac{1+z^2}{z} \simeq \frac{p^z}{k'^z}, \qquad n_p^F(1 - n_{k'}^F) \simeq \frac{n_k^F}{2}. \tag{5.128}$$

By changing the integration variable from k'^z to $\delta E \simeq p_\perp^2/2k'^z$

$$\int_0^{\mu_z} \frac{dk'^z}{2\pi} \to \int_{p_\perp^2/2\mu_z}^\infty \frac{\mathrm{d}(\delta E)}{2\pi} \frac{2(k'^z)^2}{p_\perp^2}, \tag{5.129}$$

and assuming $\mu_\perp^2 \ll m_D \mu_z$, the NLO correction is given by

$$(2\pi)^3 \frac{\mathrm{d}\delta\Gamma_{\mathrm{NLO}}}{\mathrm{d}^3\boldsymbol{k}}\bigg|_{\mathrm{cut}} \simeq -\frac{m_D}{2\pi T} \mathcal{A}(k) \ln\left(\frac{2 m_D \mu_z}{\mu_\perp^2}\right). \tag{5.130}$$

We add this contribution to the wide-angle bremsstrahlung result Eq. (5.108) to relate μ_z with $\mu_\perp^2$. This addition amounts to the replacement of the logarithmic part

$$\ln\left(\frac{T}{\mu_z}\right) \to \ln\left(\frac{2m_D T}{\mu_\perp^2}\right) . \tag{5.131}$$

5.7 Summary and Discussions

5.7.1 NLO Correction at Wide Angle

The NLO correction at wide angle is given by the sum of contributions from wide-angle bremsstrahlung, wide-angle pair annihilation, and quark-photon conversion. In this section, we will focus on the wide-angle NLO correction to the LO photon emission rate. By comparing with the LO results and applying several values of the coupling constant g, we will interpret the numerical results.

By adding the soft contribution Eq. (5.130) to wide-angle bremsstrahlung rate Eq. (5.108) and pair annihilation Eq. (5.109), the NLO corrections are

$$(2\pi)^3 \frac{\mathrm{d}\delta\Gamma_{\mathrm{NLO}}}{\mathrm{d}^3\boldsymbol{k}}\bigg|^{\mathrm{wide}}_{\mathrm{brem}} = \frac{\delta m_\infty^2}{4m_\infty^2}\mathcal{A}(k)\left[\ln\left(\frac{2m_D T}{\mu_\perp^2}\right) + C^{\mathrm{wide}}_{\mathrm{brem}}(k/T)\right] , \tag{5.132}$$

$$(2\pi)^3 \frac{\mathrm{d}\delta\Gamma_{\mathrm{NLO}}}{\mathrm{d}^3\boldsymbol{k}}\bigg|^{\mathrm{wide}}_{\mathrm{annih}} = \frac{\delta m_\infty^2}{4m_\infty^2}\mathcal{A}(k)\left[\ln\left(\frac{2m_D T}{\mu_\perp^2}\right) + C^{\mathrm{wide}}_{\mathrm{annih}}(k/T)\right] . \tag{5.133}$$

From Eq. (5.126), quark-photon conversion contributes

$$(2\pi)^3 \frac{\mathrm{d}\delta\Gamma_{\mathrm{NLO}}}{\mathrm{d}^3\boldsymbol{k}}\bigg|_{\mathrm{convs}} = \frac{\delta m_\infty^2}{2m_\infty^2}\mathcal{A}(k)\left[\ln\left(\frac{\mu_\perp^2}{m_\infty^2}\right) - 1\right] . \tag{5.134}$$

The sum of three results reads

$$\begin{aligned}&(2\pi)^3 \frac{\mathrm{d}\delta\Gamma_{\mathrm{NLO}}}{\mathrm{d}^3\boldsymbol{k}}\bigg|^{\mathrm{wide}}_{\mathrm{brem+annih+convs}} \\ &= \frac{\delta m_\infty^2}{2m_\infty^2}\mathcal{A}(k)\left[\ln\left(\frac{2m_D T}{m_\infty^2}\right) + \frac{1}{2}C^{\mathrm{wide}}_{\mathrm{brem}}(k/T) + \frac{1}{2}C^{\mathrm{wide}}_{\mathrm{annih}}(k/T) - 1\right] .\end{aligned} \tag{5.135}$$

We note that the $\mu_\perp^2$ infrared dependencies in Eqs. (5.132) and (5.133) were canceled by the $\mu_\perp^2$ ultraviolet dependence in Eq. (5.134), and the rate is finite.

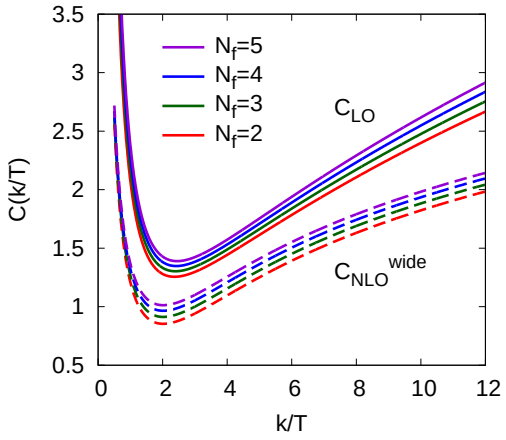

Figure 5.15: The wide-angle NLO $C^{\rm wide}_{\rm NLO}(k/T)$ in Eq. (5.136) and the LO $C_{\rm LO}(k/T)$ in Eq. (5.138) for the number of flavors $N_f = 2$, 3, 4, and 5. They are independent of the coupling constant g. Note that the NLO contribution has the factor $\delta m_\infty^2/2m_\infty^2$ relative to LO.

By defining the "wide-angle" contribution

$$C^{\rm wide}_{\rm NLO}(k/T) \equiv \ln\left(\frac{2m_D}{m_\infty}\right) + \frac{1}{2}C^{\rm wide}_{\rm brem}(k/T) + \frac{1}{2}C^{\rm wide}_{\rm annih}(k/T) - 1\,, \tag{5.136}$$

we rewrite the wide-angle NLO correction Eq. (5.135) as

$$(2\pi)^3\frac{{\rm d}\delta\Gamma_{\rm NLO}}{{\rm d}^3\boldsymbol{k}}\bigg|^{\rm wide}_{\rm brem+annih+convs} = \frac{\delta m_\infty^2}{2m_\infty^2}\mathcal{A}(k)\left[\ln\left(\frac{T}{m_\infty}\right) + C^{\rm wide}_{\rm NLO}(k/T)\right]\,, \tag{5.137}$$

Similarly, for the LO photon emission rate, we define (following the notation of Ref. [109])

$$C_{\rm LO}(k/T) \equiv \frac{1}{2}\ln(2k/T) + C_{2\to2}(k/T) + C_{\rm brem}(k/T) + C_{\rm annih}(k/T)\,, \tag{5.138}$$

and the LO result is

$$(2\pi)^3\frac{{\rm d}\Gamma_{\rm LO}}{{\rm d}^3\boldsymbol{k}}\bigg|_{\rm hard+soft+brem+annih} = \mathcal{A}(k)\left[\ln\left(\frac{T}{m_\infty}\right) + C_{\rm LO}(k/T)\right]\,. \tag{5.139}$$

$C_{\rm LO}(k/T)$ and $C^{\rm wide}_{\rm NLO}(k/T)$ are independent of the coupling constant g. Fig. 5.15 shows the comparison, and the shapes of $C_{\rm LO}(k/T)$ and $C^{\rm wide}_{\rm NLO}(k/T)$ are similar. However, we should note that the NLO emission rate has a relative factor

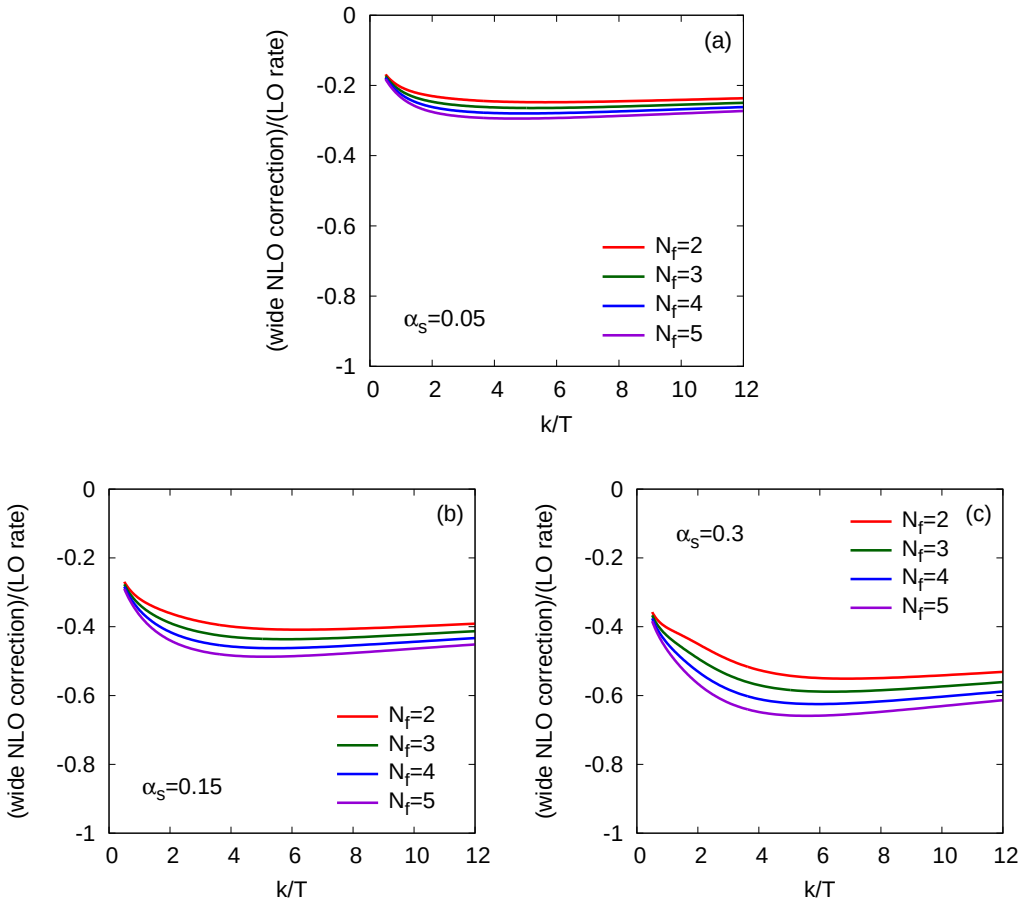

Figure 5.16: The ratio of the wide-angle NLO correction to the LO photon emission rate for $N_f = 2$, 3, 4, and 5 (see Eq. (5.140)). (a) For $\alpha_s = 0.05$, the wide-angle NLO correction is almost $25 \sim 30\%$ of LO depending on the number of flavors. (b) For $\alpha_s = 0.15$, the wide-angle NLO correction is almost $40 \sim 50\%$ of LO. (c) For $\alpha_s = 0.3$, the wide-angle NLO correction is almost $50 \sim 60\%$ of LO. The ratio decreases at low k/T and high $k/T \gg 12$ due to bremsstrahlung and inelastic pair annihilation contributions at LO, respectively.

$\delta m_\infty^2/2m_\infty^2$.

To see the size of the NLO correction, we consider the ratio of the wide-angle NLO correction to the LO emission rate:

$$\frac{(2\pi)^3\frac{\mathrm{d}\delta\Gamma^{\mathrm{wide}}_{\mathrm{NLO}}}{\mathrm{d}^3\boldsymbol{k}}}{(2\pi)^3\frac{\mathrm{d}\Gamma_{\mathrm{LO}}}{\mathrm{d}^3\boldsymbol{k}}} = \frac{\frac{\delta m_\infty^2}{2m_\infty^2}\left[\ln\left(\frac{T}{m_\infty}\right) + C^{\mathrm{wide}}_{\mathrm{NLO}}(k/T)\right]}{\left[\ln\left(\frac{T}{m_\infty}\right) + C_{\mathrm{LO}}(k/T)\right]}\,. \tag{5.140}$$

The numerical results of the ratio is shown in Fig. 5.16 for several values of the coupling constant g, specifically $\alpha_s = g^2/4\pi \simeq 0.05, 0.15,$ and 0.3. The wide-angle NLO correction is almost $25 \sim 30\%$ of LO at $\alpha_s \simeq 0.05$, and more at larger α_s.

We expect that there will be more contributions from inelastic processes. From the LO parameterization in Eqs. (5.13)and (5.14), we see $C_{\mathrm{brem}}(k/T) + C_{\mathrm{annih}}(k/T) \propto \sqrt{k/T}$ and $C_{2\to2}(k/T) \propto (\mathrm{const})$ for high k/T. So, inelastic pair annihilation is dominant for high k/T. Since we did not include these contributions at NLO, the ratio between LO and NLO approaches to zero for high k/T. Although it is not shown in the Fig. 5.16, the ratio goes to zero for $k/T \gg 12$. Indeed, the total LO result $C_{\mathrm{LO}}(k/T) \propto \sqrt{k/T}$, whereas $C^{\mathrm{wide}}_{\mathrm{NLO}}(k/T) \propto \ln(k/T)$ for high k/T. At low k/T, the collinear bremsstrahlung contribution is dominant, and the ratio also decreases.

5.7.2 Total NLO Photon Emission Rate

The total NLO correction of the photon emission rate is given by the sum of the wide-angle contribution in Eq. (5.137) and the collinear contribution in Eq. (5.35):

$$\begin{aligned}(2\pi)^3\frac{\mathrm{d}\delta\Gamma_{\mathrm{NLO}}}{\mathrm{d}^3\boldsymbol{k}}\bigg|_{\mathrm{tot}} = \mathcal{A}(k)\Bigg[&\frac{\delta m_\infty^2}{2m_\infty^2}\ln\left(\frac{T}{m_\infty}\right) + \frac{\delta m_\infty^2}{2m_\infty^2}C^{\mathrm{wide}}_{\mathrm{NLO}}(k/T) \\ &+\frac{\delta m_\infty^2}{m_\infty^2}C^{\delta m}_{\mathrm{collin}}(k/T) + \frac{g^2C_AT}{m_D}C^{\delta K}_{\mathrm{collin}}(k/T)\Bigg]\,.\end{aligned} \tag{5.141}$$

For the comparison, we present the total LO rate in Eq. (5.139)

$$(2\pi)^3\frac{\mathrm{d}\Gamma_{\mathrm{LO}}}{\mathrm{d}^3\boldsymbol{k}}\bigg|_{\mathrm{tot}} = \mathcal{A}(k)\left[\ln\left(\frac{T}{m_\infty}\right) + C_{\mathrm{LO}}(k/T)\right]\,. \tag{5.142}$$

Fig. 5.17 shows the collinear corrections $C^{\delta m}_{\mathrm{collin}}(k/T)$ and $C^{\delta K}_{\mathrm{collin}}(k/T)$ from δm_∞^2 and $C[\boldsymbol{p}_\perp]_{\mathrm{NLO}}$, respectively. In Eq. (5.141), $C^{\delta m}_{\mathrm{collin}}(k/T)$ is multiplied by $\delta m_\infty^2/m_\infty^2$, whereas $C^{\delta K}_{\mathrm{collin}}(k/T)$ is multiplied by g^2C_AT/m_D. By noting

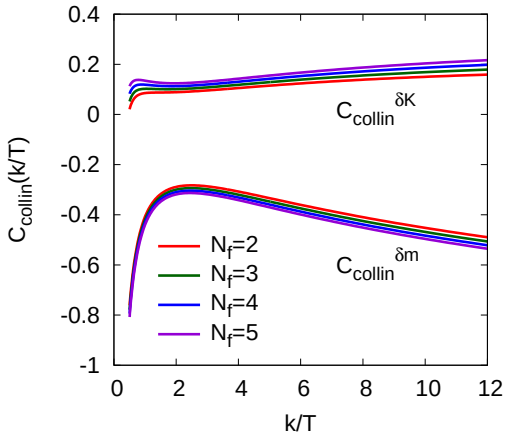

Figure 5.17: The comparison between $C^{\delta m}_{\rm collin}(k/T)$ and $C^{\delta K}_{\rm collin}(k/T)$ for $N_f =$ 2, 3, 4, and 5. They are independent of the coupling constant g. We note that $C^{\delta m}_{\rm collin}(k/T)$ is multiplied by $\delta m^2_\infty/m^2_\infty$, while $C^{\delta K}_{\rm collin}(k/T)$ is multiplied by $g^2 C_A T/m_D$ in Eq. (5.141). By noticing the numerological equality $-\delta m^2_\infty/m^2_\infty = g^2 C_A T/\pi m_D$ for $N_f = N_c = 3$, $C^{\delta m}_{\rm collin}(k/T)$ can be compared to $\pi C^{\delta K}_{\rm collin}(k/T)$.

the numerological equality $-\delta m^2_\infty/m^2_\infty = g^2 C_A T/\pi m_D$ for $N_c = N_f = 3$, $C^{\delta m}_{\rm collin}(k/T)$ should be compared to $\pi C^{\delta K}_{\rm collin}(k/T)$.

To see the size of the collinear NLO correction, in Fig. 5.18 we plot the ratio of the sum of two collinear NLO corrections to the LO photon emission rate:

$$\frac{(2\pi)^3 \frac{{\rm d}\delta\Gamma^{\rm collin}_{\rm NLO}}{{\rm d}^3\boldsymbol{k}}}{(2\pi)^3 \frac{{\rm d}\Gamma_{\rm LO}}{{\rm d}^3\boldsymbol{k}}} = \frac{\left[\frac{\delta m^2_\infty}{m^2_\infty} C^{\delta m}_{\rm collin}(k/T) + \frac{g^2 C_A T}{m_D} C^{\delta K}_{\rm collin}(k/T)\right]}{\left[\ln\left(\frac{T}{m_\infty}\right) + C_{\rm LO}(k/T)\right]} \,. \tag{5.143}$$

Depending on α_s, k/T, and the number of flavors, the collinear NLO correction is up to 80% of the LO result, which might indicate a breakdown of perturbation theory for $\alpha_s \gtrsim 0.3$.

In Fig. 5.19, the wide-angle and collinear NLO corrections scaled by $\mathcal{A}(k)$ are compared with the LO photon emission rate for $\alpha_s = 0.05$, 0.15, 0.3 and $N_f = 2$, 3, 4, 5. Since the signs of the wide-angle and collinear contributions are opposite, there is cancellation in the total NLO correction.

The size of the total NLO correction is shown in Fig. 5.20, where we plot

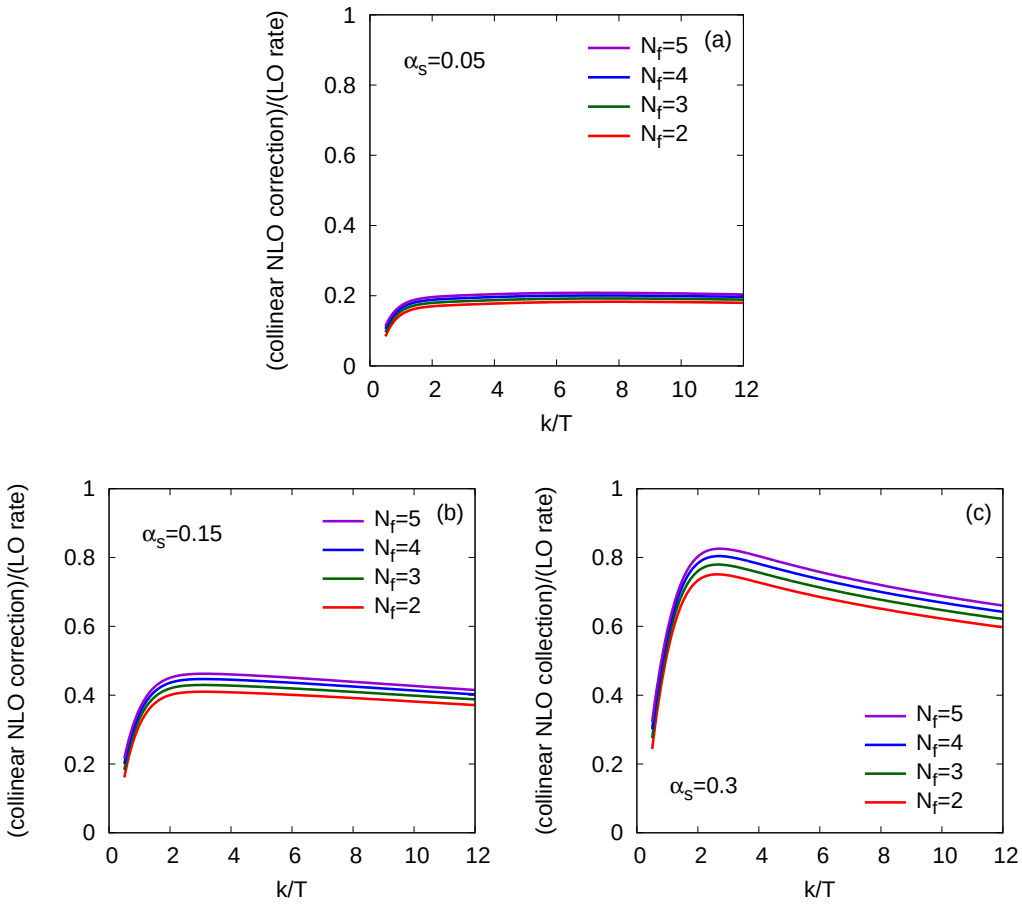

Figure 5.18: The ratio of the collinear NLO correction to the LO photon emission rate for $\alpha_s = 0.05$, 0.15, 0.3 and $N_f = 2$, 3, 4, 5 (see Eq. (5.143)). (a) For $\alpha_s = 0.05$, the collinear NLO correction is almost 20% of LO. (b) For $\alpha_s = 0.15$, the collinear NLO correction is almost 40% of LO. (c) For $\alpha_s = 0.3$, the collinear NLO correction is almost $60 \sim 80\%$ of LO depending on k/T and the number of flavors.

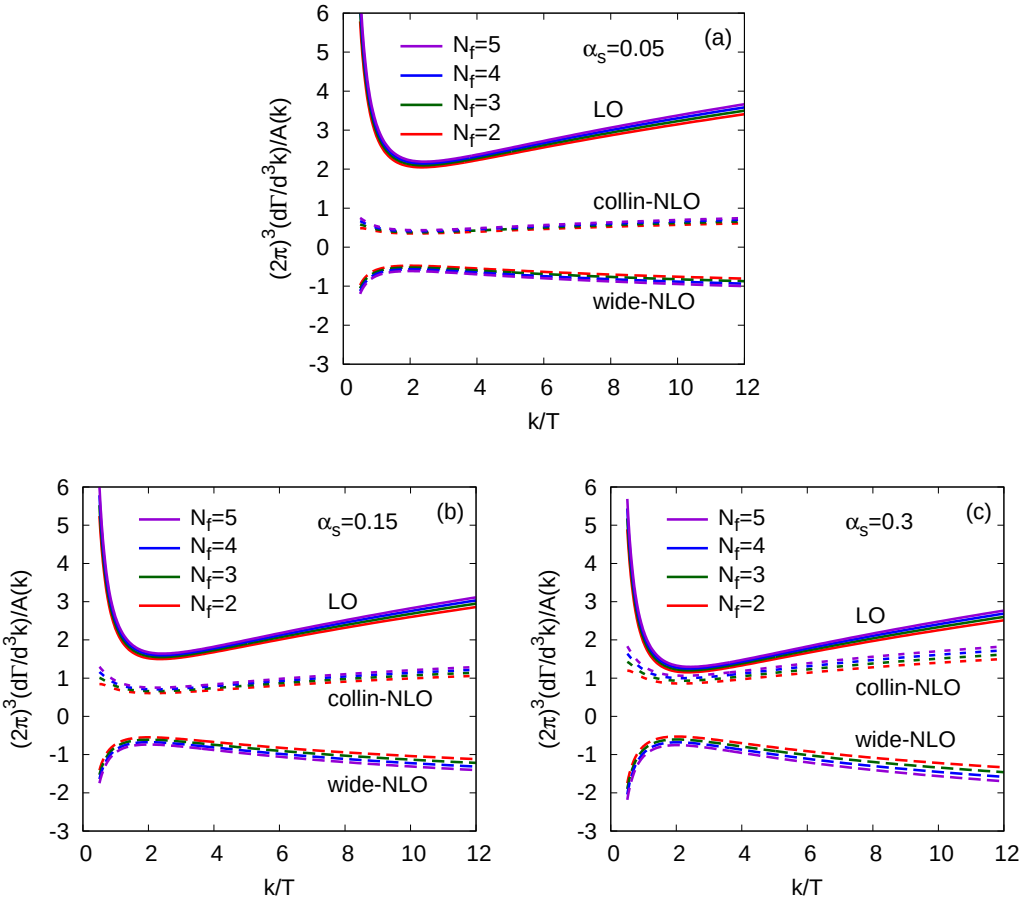

Figure 5.19: The wide-angle NLO correction (long-dashed lines), the collinear NLO correction (short-dashed lines), and the LO photon emission rate (solid lines) scaled by $\mathcal{A}(k)$ for $\alpha_s = 0.05$, 0.15, 0.3 and $N_f = 2$, 3, 4, 5. Note that the signs of the wide-angle and collinear contributions are opposite. Therefore, there is cancellation in the total NLO correction.

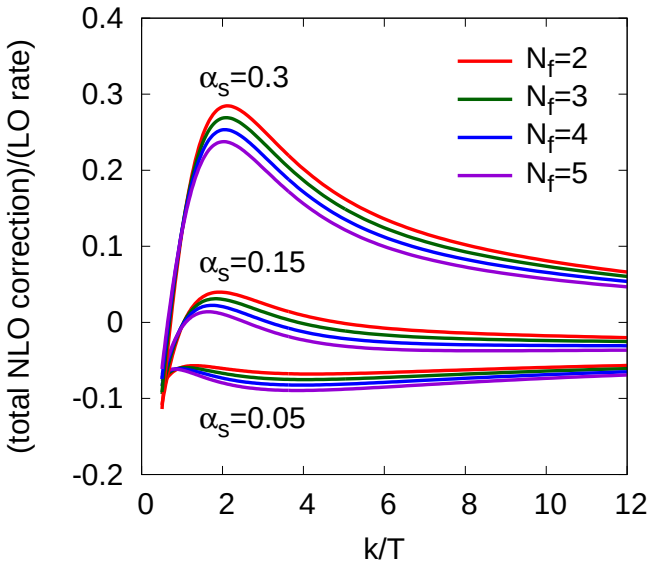

Figure 5.20: The ratio of the total NLO corrections to the LO photon emission rate for $\alpha_s = 0.05, 0.15, 0.3$ and $N_f = 2, 3, 4, 5$ (see Eq. (5.144)). Due to the cancellation between the wide-angle and collinear contributions, the NLO correction is at most 10%, 5%, and 30% of LO for $\alpha_s = 0.05$, 0.15, and 0.3, respectively.

the ratio of the total NLO correction to the LO emission rate:

$$\frac{(2\pi)^3 \frac{\mathrm{d}\delta\Gamma_{\mathrm{NLO}}}{\mathrm{d}^3\boldsymbol{k}}}{(2\pi)^3 \frac{\mathrm{d}\Gamma_{\mathrm{LO}}}{\mathrm{d}^3\boldsymbol{k}}} =$$

$$\frac{\left[\frac{\delta m_\infty^2}{2m_\infty^2} \ln\left(\frac{T}{m_\infty}\right) + \frac{\delta m_\infty^2}{2m_\infty^2} C_{\mathrm{NLO}}^{\mathrm{wide}}(k/T) + \frac{\delta m_\infty^2}{m_\infty^2} C_{\mathrm{collin}}^{\delta m}(k/T) + \frac{g^2 C_A T}{m_D} C_{\mathrm{collin}}^{\delta K}(k/T)\right]}{\left[\ln\left(\frac{T}{m_\infty}\right) + C_{\mathrm{LO}}(k/T)\right]}. \tag{5.144}$$

Due to the cancellation, the NLO correction is at most 10%, 5%, and 30% of the LO rate for $\alpha_s = 0.05$, 0.15, and 0.3, respectively. This kind of cancellation is typical of perturbative calculations, and we should be careful to interpret the numerical results. Since both of the NLO corrections from wide-angle and collinear processes are greater than the sum, the error of the total correction could be greater than what we naively expect by considering only the sum.

Finally, we plot the LO photon emission rate and the NLO photon emission rate (which is the sum of the LO rate and the total NLO correction) in Fig. 5.21. Accidentally, the NLO rate is comparable to the LO rate at $\alpha_s = 0.15$. Even at $\alpha_s = 0.3$, the convergence of the NLO result is not as bad as in the NLO heavy quark diffusion constant [10].

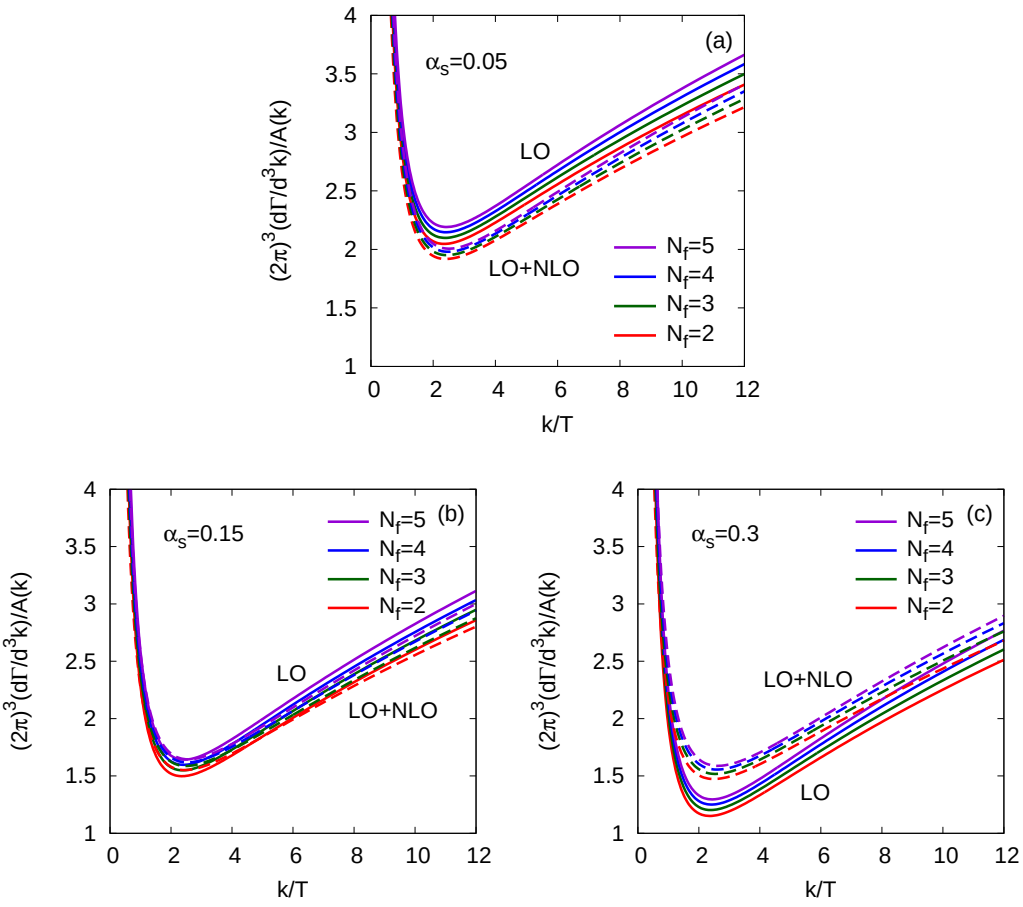

Figure 5.21: The LO and NLO photon emission rates scaled by $\mathcal{A}(k)$ for $\alpha_s = 0.05$, 0.15, 0.3 and $N_f = 2$, 3, 4, 5. Solid lines indicate the LO photon emission rate, and dashed lines indicate the sum of the LO rate and the total NLO correction.

Chapter 6

Conclusions and Outlook

In Introduction, we mentioned *Point I, II, III* that we would like to address in this thesis. By responding to the points, we summarize the topics discussed in previous chapters and suggest extensions of the studies.

In Chapter 2, the linearized Boltzmann equation was formulated in a leading-log approximation. The equation was written down as a Fokker-Planck equation to describe diffusion process. It was shown that given arbitrary perturbations, the numerical solution of the Boltzmann equation ultimately approached to equilibrium. With this setup, in Chapter 3 we computed spectral densities of $T^{\mu\nu}$ and J^{μ} in the presence of weak gravitational and electromagnetic fields. As expected, the spectral densities exhibit a smooth transition from free streaming quasi-particles to hydrodynamics. This transition was analyzed with hydrodynamics and diffusion equation to investigate the macroscopic theory limit. To respond to the *Point I*, we determined the validity regime for hydrodynamics:

$$\omega,\, ck \lesssim 0.35 \left[\frac{\eta}{(e_o+\mathcal{P}_o)c_s^2}\right]^{-1} \qquad \text{(first hydro)}\,, \tag{6.1}$$

$$\omega,\, ck \lesssim \ \ 0.7 \left[\frac{\eta}{(e_o+\mathcal{P}_o)c_s^2}\right]^{-1} \qquad \text{(second hydro)}\,. \tag{6.2}$$

In particular, in the second order diffusion equation we ignored terms related to magneto-hydrodynamics. Recently, there have been many efforts to understand the plasma response in the presence of strong magnetic fields. With non-negligible magnetic fields, it would be interesting to study the magneto-hydrodynamic response in high temperature-density plasmas.

In Chapter 4, we compared weakly coupled theories with strongly coupled theories to answer the *Point II*. With a heavy quark probe, we simulated the jet-medium interaction in high temperature QCD plasmas and $\mathcal{N}=4$ SYM

plasmas. In both cases, we compared the energy density and flux distributions with hydrodynamic solutions at long distances. In contrast to the kinetic theory results, the AdS/CFT results converged to the hydrodynamic regime much faster at relatively short distances. We argued that this difference seemed to be related to the transport coefficient τ_π which was relatively greater in theories based on quasi-particle description. At short distances, there are limitations for the comparison in both theories. In the AdS/CFT, high momentum behaviors have been studied, and new scales of order $1/\gamma^{1/2}\pi T$ and $1/\gamma^{3/2}\pi T$ appear [84, 89, 117, 118]. On the other hand, in kinetic theory this quantum physics can not be described by the semi-classical Boltzmann equation. We should compute the stress tensor at short distances by using finite temperature perturbation theory to better compare the difference between two coupling limits.

This jet-medium simulation was focused on the study of a single heavy quark moving from past infinity forever. More related to heavy ion collisions, it would be interesting to generate a parton shower which would be initiated at past finite time and thermalized after a while [91, 92, 93]. Since the Boltzmann equation has been verified that the solutions approach to hydrodynamic ones, it would be interesting to compare the numerical results to experimental data which are characterized by hydrodynamics. It would be also nice to compare simulations of the energy density and flux distributions from the heavy quark with this parton shower.

To respond to the *Point III*, in Chapter 5 we computed the photon emission rate at next-to-leading order (NLO), *i.e.* at order $g^2 m_D/T$. We discussed all the possible corrections of $\mathcal{O}(g)$ to the leading order results and how the rates were matched to obtain finite results. The final photon emission rate at NLO depends on the coupling constant g. At somewhat large value of $\alpha_s = 0.3$, the NLO correction is roughly 30% at most, depending on the number of flavors. This correction is less than we expected, considering that there is accidental cancellation between the wide-angle corrections and collinear corrections. One should be careful when comparing the NLO results with experimental data. Since both wide-angle contributions and collinear contributions are greater (with opposite signs) than the sum of two, the error might be greater than what we naively expect with the final result. There need systematic methods to analyze the data and estimate errors of the NLO photon emission rate.

The photon emission rate was a warm-up problem in order to compute transport coefficients, especially the shear viscosity at NLO. By using the HTL perturbation theory, it is desirable to compute spectral densities and extract hydrodynamic coefficients as we did in Chapter 3. Photon emission can be also studied in the basis of the Boltzmann equation [5]. At a leading-log

approximation, the Boltzmann equation has only t-channel $2 \leftrightarrow 2$ scatterings in the collision term. By including $1 \leftrightarrow 2$ processes, we can study energy loss problems in jets. There are two types of energy loss: collisional energy loss and radiative energy loss. At high momentum, we expect that radiative energy loss will be more important. In particular, at NLO we suspect that there will be similar matching processes of rates as in the photon emission computation.

In conclusion, we studied transport processes of high temperature QCD plasmas by using kinetic theory based on the Boltzmann equation and hydrodynamic analysis. This work has many phenomenological applications in heavy ion collisions. The transport coefficients determined in this thesis are useful in viscous hydrodynamic simulations, and the NLO photon emission rate can be compared with experimental data. We would like to mention that this research may be useful for further studies in other areas as well as heavy ion physics. With minor modifications, it can be applicable to any high temperature-density plasmas such as existed in the early universe.

Bibliography

[1] K. Adcox *et al.* [PHENIX Collaboration], Nucl. Phys. A **757**, 184 (2005).

[2] J. Adams *et al.* [STAR Collaboration], Nucl. Phys. A **757**, 102 (2005).

[3] see for example, J. Beringer *et al.* [Particle Data Group], Phys. Rev. D. **86**, 010001 (2012).

[4] E. Braaten and R. D. Pisarski, Nucl. Phys. B **337**, 569 (1990).

[5] see for example, J. P. Blaizot and E. Iancu, Phys. Rept. **359**, 355 (2002).

[6] E. Braaten and R. D. Pisarski, Nucl. Phys. B **339**, 310 (1990).

[7] P. Arnold, G. D. Moore and L. G. Yaffe, JHEP **0305**, 051 (2003).

[8] K. Kajantie, M. Laine, K. Rummukainen and Y. Schroder, Phys. Rev. D. **67**, 105008 (2003).

[9] J. O. Andersen, L. E. Leganger, M. Strickland and N. Su, JHEP **1108**, 053 (2011).

[10] S. Caron-Huot and G. D. Moore, Phys. Rev. Lett. **100** 052301 (2008).

[11] For an overview see, D. A. Teaney, arXiv:0905.2433 [nucl-th].

[12] M. Luzum and P. Romatschke, Phys. Rev. C **78** 034915 (2008).

[13] A. Adare *et al.* [PHENIX Collaboration], Phys. Rev. Lett. **104** 132301 (2010).

[14] S. Turbide, R. Rapp and C. Gale, Phys. Rev. C **69** 014903 (2004).

[15] J. P. Blaizot and E. Iancu, Phys. Rept. **359**, 355 (2002).

[16] P. Arnold, G. D. Moore and L. G. Yaffe, JHEP **0301**, 030 (2003).

[17] G. Baym, H. Monien, C. J. Pethick and D. G. Ravenhall, Phys. Rev. Lett. **64**, 1867 (1990).

[18] P. Arnold, C. Dogan and G. D. Moore, Phys. Rev. D **74**, 085021 (2006).

[19] R. Baier, A. H. Mueller, D. Schiff and D. T. Son, Phys. Lett. B **502**, 51 (2001).

[20] S. Mrowczynski, Phys. Lett. B **314**, 118 (1993).

[21] P. Arnold, J. Lenaghan and G. D. Moore, JHEP **0308**, 002 (2003).

[22] A. H. Mueller, A. I. Shoshi and S. M. H. Wong, Phys. Lett. B **632**, 257 (2006).

[23] A. Rebhan, P. Romatschke and M. Strickland, JHEP **0509**, 041 (2005).

[24] P. Arnold, G. D. Moore and L. G. Yaffe, Phys. Rev. D **72**, 054003 (2005).

[25] P. Romatschke and R. Venugopalan, Phys. Rev. Lett. **96**, 062302 (2006).

[26] J. Hong and D. Teaney, Phys. Rev. C **82**, 044908 (2010).

[27] P. Arnold, G. D. Moore and L. G. Yaffe, JHEP **0011**, 001 (2000).

[28] see for example, E. Shuryak, Prog. Part. Nucl. Phys. **62** 48 (2009).

[29] see for example, M. Le Bellac, *Thermal Field Theory* (Cambridge University Press, 1996).

[30] K. Huebner, F. Karsch and C. Pica, Phys. Rev. D **78**, 094501 (2008).

[31] G. Aarts, C. Allton, J. Foley, S. Hands and S. Kim, Phys. Rev. Lett. **99**, 022002 (2007).

[32] H. B. Meyer, Phys. Rev. D **76**, 101701 (2007).

[33] M. Asakawa and T. Hatsuda, Phys. Rev. Lett. **92**, 012001 (2004).

[34] A. Mocsy and P. Petreczky, Phys. Rev. Lett. **99**, 211602 (2007).

[35] A. Jakovac, P. Petreczky, K. Petrov and A. Velytsky, Phys. Rev. D **75**, 014506 (2007).

[36] G. Aarts and J. M. Martinez Resco, JHEP **0204**, 053 (2002).

[37] P. Petreczky and D. Teaney, Phys. Rev. D **73**, 014508 (2006).

[38] H. B. Meyer, Nucl. Phys. A **830**, 641C (2009).

[39] G. Aarts, C. Allton, J. Foley, S. Hands and S. Kim, PoS **LAT2006**, 134 (2006).

[40] G. D. Moore and J. M. Robert, arXiv:hep-ph/0607172.

[41] G. D. Moore and O. Saremi, JHEP **0809**, 015 (2008).

[42] S. Caron-Huot, Phys. Rev. D **79**, 125009 (2009).

[43] P. Kovtun and A. Starinets, Phys. Rev. Lett. **96**, 131601 (2006).

[44] D. Teaney, Phys. Rev. D **74**, 045025 (2006).

[45] S. Jeon and L. G. Yaffe, Phys. Rev. D **53**, 5799 (1996).

[46] J. Knoll, Yu. B. Ivanov and D. N. Voskresensky, Annals Phys. **293**, 126 (2001).

[47] R. Baier, P. Romatschke, D. T. Son, A. O. Starinets and M. A. Stephanov, JHEP **0804**, 100 (2008).

[48] Annals Phys. **100**, 310 (1976).

[49] W. Israel and J. M. Stewart, Annals Phys. **118**, 341 (1979).

[50] P. Romatschke, Class. Quant. Grav. **27**, 025006 (2010).

[51] P. Romatschke and D. T. Son, Phys. Rev. D **80**, 065021 (2009).

[52] M. A. York and G. D. Moore, Phys. Rev. D **79**, 054011 (2009).

[53] see for example, M. E. Peskin and D. V. Schroeder, *An Introduction To Quantum Field Theory* (Westview Press, 1995).

[54] S. A. Hartnoll, P. K. Kovtun, M. Muller and S. Sachdev, Phys. Rev. B **76**, 144502 (2007).

[55] see for example, P. M. Morse, H. Feshbach, *Methods of theoretical physics*, New York (McGraw-Hill, 1953).

[56] see for example, P. Roe and M. Arora, Numerical Methods for Partial Differential Equations **9**, 459 (1993).

[57] see for example, P. Arnold and L. G. Yaffe, Phys. Rev. D **57**, 1178 (1998).

[58] H. B. Meyer, JHEP **0808**, 031 (2008).

[59] S. Jeon, Phys. Rev. D **52**, 3591 (1995).

[60] H. T. Ding, A. Francis, O. Kaczmarek, F. Karsch, E. Laermann *et al.*

[61] P. M. Chesler and A. Vuorinen, JHEP **0611**, 037 (2006).

[62] see for example: W. H. Press *et al.*, *"Numerical Recipes 3rd Edition: The Art of Scientific Computing"*, (Cambride University Press, 2007).

[63] D. Molnar and M. Gyulassy, Nucl. Phys. A **697**, 495 (2002) [Erratum-ibid. A **703**, 893 (2002)].

[64] D. Teaney, Phys. Rev. C **68**, 034913 (2003).

[65] P. Romatschke and U. Romatschke, Phys. Rev. Lett. **99**, 172301 (2007).

[66] H. Song and U. W. Heinz, Phys. Rev. C **77**, 064901 (2008).

[67] K. Dusling and D. Teaney, Phys. Rev. C **77**, 034905 (2008).

[68] Z. Xu and C. Greiner, Phys. Rev. C **79**, 014904 (2009).

[69] G. Policastro, D. T. Son and A. O. Starinets, Phys. Rev. Lett. **87**, 081601 (2001).

[70] P. Kovtun, D. T. Son and A. O. Starinets Phys. Rev. Lett. **94**, 111601 (2005).

[71] J. P. Blaizot, E. Iancu and A. Rebhan, Phys. Rev. D **68**, 025011 (2003).

[72] J. O. Andersen, L. E. Leganger, M. Strickland and N. Su, Phys. Rev. D. **84**, 087703 (2011).

[73] J. Hong, D. Teaney and P. M. Chesler, Phys. Rev. C **85**, 064903 (2012).

[74] A. Adare *et al.* [PHENIX Collaboration], Phys. Rev. C **78**, 014901 (2008).

[75] B. I. Abelev *et al.* [STAR Collaboration], Phys. Rev. Lett. **102**, 052302 (2009).

[76] B. Alver and G. Roland, Phys. Rev. C **81**, 054905 (2010).

[77] J. Takahashi, B. M. Tavares, W. L. Qian, R. Andrade, F. Grassi *el al.*, Phys. Rev. Lett. **103**, 242301 (2009).

[78] P. Sorensen, J. Phys. G **37**, 094011 (2010).

[79] Z. Lin, C. M. Ko, B. Li, B. Zhang S. Pal, Phys. Rev. C **72**, 064901 (2005).

[80] G. L. Ma, S. Zhang, Y. G. Ma, H. Z. Huang, X. Z. Cai *el al.*, Phys. Lett. B **641**, 362 (2006).

[81] J. Casalderrey-Solana, E. V. Shuryak and D. Teaney, J. Phys. Conf. Ser. **27**, 22 (2005).

[82] H. Stoecker, Nucl. Phys. A **750**, 121 (2005).

[83] S. S. Gubser, S. S. Pufu and A. Yarom, Phys. Rev. Lett. **100**, 012301 (2008).

[84] A. Yarom, Phys. Rev. D **75**, 125010 (2007).

[85] P. M. Chesler and L. G. Yaffe, Phys. Rev. Lett. **99**, 152001 (2007).

[86] P. M. Chesler and L. G. Yaffe, Phys. Rev. D **78**, 045013 (2008).

[87] R. B. Neufeld, Phys. Rev. D **78**, 085015 (2008).

[88] S. Chatrchyan *el al.*, [CMS Collaboration], Phys. Rev. C **84**, 024906 (2011).

[89] S. S. Gubser and S. S. Pufu, Nucl. Phys. B **790**, 42 (2008).

[90] R. B. Neufeld, Phys. Rev. C **79**, 054909 (2009).

[91] R. B. Neufeld and B. Muller, Phys. Rev. Lett. **103**, 042301 (2009).

[92] R. B. Neufeld and I. Vitev, arXiv:1105.2607 [hep-ph].

[93] P. B. Arnold, S.Cantrell and W. Xiao, Phys. Rev. D **81**, 045017 (2010).

[94] P. B. Arnold and W. Xiao, Phys. Rev. D **78**, 125008 (2008).

[95] G. D. Moore and D. Teaney, Phys. Rev. C **71**, 064904 (2005).

[96] E. Braaten and M. H. Thoma, Phys. Rev. D **44**, 1298 (1991).

[97] E. Braaten and M. H. Thoma, Phys. Rev. D **44**, 2625 (1991).

[98] C. P. Herzog, A. Karch, P. Kovtun, C. Kozcaz and L. G. Yaffe, JHEP **0607**, 013 (2006).

[99] J. Casalderrey-Solana and D. Teaney, Phys. Rev. D **74** 085012 (2006).

[100] S. S. Gubser, Phys. Rev. D **74**, 126005 (2006).

[101] H. T. Elze, U. W. Heinz, Phys. Rept. **183**, 81 (1989).

[102] J. Noronha, M. Gyulassy and G. Torrieri, Phys. Rev. Lett. **102**, 102301 (2009).

[103] B. Betz, M. Gyulassy, J. Noronha and G. Torrieri, Phys. Lett. B **675**, 340 (2009).

[104] C. Athanasiou, P. M. Chesler, H. Liu, D. Nickel and K. Rajagopal, Phys. Rev. D **81**, 126001 (2010).

[105] J. M. Maldacena, Adv. Theor. Math. Phys. **2**, 231 (1998).

[106] A. Karch and A. Katz, Fortsch. Phys. **51**, 759 (2003).

[107] J. Ghiglieri, J. Hong, A. Kurkela, G. D. Moore and D. Teaney, in preparation (2012).

[108] P. B. Arnold, G. D. Moore and L. G. Yaffe, JHEP **0111**, 057 (2001).

[109] P. B. Arnold, G. D. Moore and L. G. Yaffe, JHEP **0112**, 009 (2001).

[110] P. B. Arnold, G. D. Moore and L. G. Yaffe, JHEP **0206**, 030 (2002).

[111] J. I. Kapusta, P. Lichard and D. Seibert, Phys. Rev. D **44**, 2774 (1991), [Erratum-ibid. D **47**, 4171 (1993)].

[112] R. Baier, H. Nakkagawa, A. Niegawa and K. Redlich, Z. Phys. C **53**, 433 (1992).

[113] P. Aurenche, F. Gelis and H. Zaraket, JHEP **0205**, 043 (2002).

[114] J. P. Blaizot, E. Iancu and A. Rebhan, Phys. Rev. D **63**, 065003 (2001).

[115] S. Caron-Huot, Phys. Rev. D **79**, 125002 (2009).

[116] S. Caron-Huot, Phys. Rev. D **79**, 065039 (2009).

[117] Y. Hatta, E. Iancu and A. H. Mueller, JHEP **0805**, 037 (2008).

[118] F. Dominguez, C. Marquet, A. H. Mueller, B. Wu and B. Xiao, Nucl. Phys. A **811**, 197 (2008).

Appendix A

Collision Integral of Boltzmann Equation

This appendix closely follows Refs. [26, 27] to derive the leading-log Boltzmann equation. We first consider the pure glue case and then extend to multi-component plasmas.

A.1 Pure Glue

In this section, we derive the collision term for pure glue.

By substituting the linearized distribution function Eq. (2.2) (with the definition Eq. (2.5)) into Eq. (2.4), the collision term is linearized[1]

$$\mathcal{C}[f,\boldsymbol{p}] = -\int_{\boldsymbol{kp'k'}} \frac{1}{2}|M|^2\,(2\pi)^4\delta^4(P_{\rm tot})\,n_p n_k(1+n_{p'})(1+n_{k'}) \Big[\chi(\boldsymbol{p})+\chi(\boldsymbol{k})-\chi(\boldsymbol{p'})-\chi(\boldsymbol{k'})\Big]\,. \quad \text{(A.1)}$$

In the pure glue theory, the only relevant diagram is $t-$channel gluon exchange, the diagram (a) of Fig. 2.1. This collision term can be written as a variational problem

$$\mathcal{C}[f,\boldsymbol{p}] = -(2\pi)^3\frac{\delta}{\delta\chi(\boldsymbol{p})}I[\chi]\,, \quad \text{(A.2)}$$

[1]The matrix elements are summed over spins and colors associated with $\boldsymbol{k},\boldsymbol{p'},\boldsymbol{k'}$ and averaged over the spins and colors associated with $\boldsymbol{p}$. The distribution function $f_{\boldsymbol{p}}$ is defined so that the total number of gluons is $2d_A\int_{\boldsymbol{p}} f_{\boldsymbol{p}}$.

where

$$I[\chi] \equiv \frac{1}{16}\int_{\boldsymbol{pkp'k'}} |M|^2\,(2\pi)^4\delta^4(P_{\rm tot})\,n_p n_k(1+n_{p'})(1+n_{k'}) \\ \Big[\chi(\boldsymbol{p})+\chi(\boldsymbol{k})-\chi(\boldsymbol{p'})-\chi(\boldsymbol{k'})\Big]^2 . \quad \text{(A.3)}$$

We classify the integral as loss and gain terms, $I[\chi] = I[\chi]_{\rm loss} + I[\chi]_{\rm gain}$, with

$$I[\chi]_{\rm loss} \equiv \frac{1}{8}\int_{\boldsymbol{pkp'k'}} |M|^2\,(2\pi)^4\delta^4(P_{\rm tot})\,n_p n_k(1+n_{p'})(1+n_{k'})\Big[\chi(\boldsymbol{p})-\chi(\boldsymbol{p'})\Big]^2 , \quad \text{(A.4)}$$

$$I[\chi]_{\rm gain} \equiv \frac{1}{8}\int_{\boldsymbol{pkp'k'}} |M|^2\,(2\pi)^4\delta^4(P_{\rm tot})\,n_p n_k(1+n_{p'})(1+n_{k'}) \\ \Big[\chi(\boldsymbol{p})-\chi(\boldsymbol{p'})\Big]\Big[\chi(\boldsymbol{k})-\chi(\boldsymbol{k'})\Big] . \quad \text{(A.5)}$$

By expanding in the momentum transfer $\boldsymbol{q} \equiv \boldsymbol{p'} - \boldsymbol{p}$, the integrals are given by[2]

$$I[\chi]_{\rm loss} = \int_{\boldsymbol{pk}} n_p(1+n_p)\frac{\partial\chi(\boldsymbol{p})}{\partial p^i}\frac{\partial\chi(\boldsymbol{p})}{\partial p^j} n_k(1+n_k) I^{ij}(\boldsymbol{p},\boldsymbol{k}) , \quad \text{(A.6)}$$

$$-I[\chi]_{\rm gain} = \int_{\boldsymbol{pk}} n_p(1+n_p)\frac{\partial\chi(\boldsymbol{p})}{\partial p^i}\frac{\partial\chi(\boldsymbol{k})}{\partial k^j} n_k(1+n_k) I^{ij}(\boldsymbol{p},\boldsymbol{k}) , \quad \text{(A.7)}$$

where

$$I^{ij}(\boldsymbol{p},\boldsymbol{k}) = \frac{1}{4}\int_{\boldsymbol{p'k'}} (2\pi)^4\delta^4(P+K-P'-K')\,|M|^2\,\boldsymbol{q}^i\boldsymbol{q}^j . \quad \text{(A.8)}$$

We note that the matrix elements are symmetric in $\boldsymbol{p}$ and $\boldsymbol{k}$, and $I^{ij}(\boldsymbol{p},\boldsymbol{k})$ must have the following form:

$$I^{ij}(\boldsymbol{p},\boldsymbol{k}) = a_1\left(\hat{\boldsymbol{p}}^i\hat{\boldsymbol{p}}^j + \hat{\boldsymbol{k}}^i\hat{\boldsymbol{k}}^j\right) + a_2\left(\hat{\boldsymbol{p}}^i\hat{\boldsymbol{k}}^j + \hat{\boldsymbol{k}}^i\hat{\boldsymbol{p}}^j\right) + a_3\delta^{ij} , \quad \text{(A.9)}$$

where $a_1, a_2,$ and a_3 are coefficients of the symmetric bases. In order to compute the coefficients, we contract I^{ij} with $\hat{\boldsymbol{p}}^i\hat{\boldsymbol{p}}^j$, $\hat{\boldsymbol{p}}^i\hat{\boldsymbol{k}}^j$ and δ_{ij}. The computation can be done as follows.

We use the three momentum delta function to perform the $\boldsymbol{k'}$ integral, and shift the integral over $\boldsymbol{p'}$ to an integral over $\boldsymbol{q}$. Then we set $\boldsymbol{p}$ along the z-axis

[2]We assumed that $t \equiv -(P-P')^2$ is small. For identical particles, there is an equal contribution from the phase space where $u \equiv -(P-K')^2$ is small. This factor of two is included in the definition of I^{ij}.

and $\boldsymbol{k}$ in the zx plane:

$$\boldsymbol{p} = (0,\, 0,\, p)\,, \tag{A.10}$$
$$\boldsymbol{k} = (k\sin\theta_{pk},\, 0,\, k\cos\theta_{pk})\,, \tag{A.11}$$
$$\boldsymbol{q} = (q\sin\theta_{qp}\cos\phi,\, q\sin\theta_{qp}\sin\phi,\, q\cos\theta_{qp})\,. \tag{A.12}$$

The energy conservation δ-function can be written

$$\delta(p+k-p'-k') = \frac{1}{q}\frac{1-\cos\theta_{pk}}{(1-\cos\theta_{pk})^2+\sin\theta_{pk}^2\cos^2\phi} \\ \delta\left(\cos\theta_{pq} - \frac{\sin\theta_{pk}\cos\phi}{\left[(1-\cos\theta_{pk})^2+\sin\theta_{pk}^2\cos^2\phi\right]^{1/2}}\right)\,, \tag{A.13}$$

where we used $p' \simeq p + q\cos\theta_{qp}$ and $k' \simeq k + k\cos\theta_{kq}$. The averaged matrix element in a leading-log approximation is

$$\frac{1}{\nu_g}\sum_{s,c}|M|^2 = \frac{1}{16p^2k^2\nu_g}\,|\mathcal{M}|^2 \quad \text{with} \quad |\mathcal{M}|^2 = \frac{4\nu_g^2 g^4 C_A^2}{d_A}\,\frac{s^2}{t^2}\,. \tag{A.14}$$

Here the Mandelstam variables are

$$s \equiv -(P+K)^2 = 2pk(1-\cos\theta_{pk})\,, \\ t \equiv -(P'-P)^2 = -q^2\frac{(1-\cos\theta_{pk})^2}{(1-\cos\theta_{pk})^2+\sin\theta_{pk}^2\cos\phi^2}\,. \tag{A.15}$$

Thus $\hat{\boldsymbol{p}}^i I^{ij}\hat{\boldsymbol{p}}^j$ is given by

$$\begin{aligned}\hat{p}^i I^{ij}(\boldsymbol{p},\boldsymbol{k})\hat{p}^j &= \frac{1}{4}\int\frac{\mathrm{d}^3q}{(2\pi)^3}|M|^2\,2\pi\delta(p+k-p'-k')\,\hat{\boldsymbol{p}}\cdot\boldsymbol{q}\,\hat{\boldsymbol{p}}\cdot\boldsymbol{q}\,, \\ &= \frac{\nu_g\,g^4C_A^2}{8\pi d_A}\int\frac{\mathrm{d}q}{q}\int\frac{\mathrm{d}\phi}{2\pi}\frac{\sin\theta_{pk}^2}{1-\cos\theta_{pk}}\cos^2\phi\,, \\ &= \frac{\nu_g\,g^4C_A^2}{16\pi d_A}\ln\left(T/m_D\right)(1+\cos\theta_{pk})\,. \end{aligned} \tag{A.16}$$

The remaining contractions $\hat{\boldsymbol{p}}^i I^{ij} \hat{\boldsymbol{k}}^j$ and I^{ii} are computed similarly, yielding

$$\hat{\boldsymbol{p}}^i I^{ij} \hat{\boldsymbol{p}}^j = \frac{T\mu_A}{2\xi_B}(1+\cos\theta_{pk}) = a_1(1+\cos^2\theta_{pk}) + 2a_2\cos\theta_{pk} + a_3\,, \tag{A.17}$$

$$\hat{\boldsymbol{p}}^i I^{ij} \hat{\boldsymbol{k}}^j = \frac{T\mu_A}{2\xi_B}(1+\cos\theta_{pk}) = 2a_1\cos\theta_{pk} + a_2(1+\cos^2\theta_{pk}) + a_3\cos\theta_{pk}\,, \tag{A.18}$$

$$I^{ii} = \frac{T\mu_A}{2\xi_B}(3-\cos\theta_{pk}) = 2a_1 + 2a_2\cos\theta_{pk} + 3a_3\,. \tag{A.19}$$

By solving for a_1, a_2, and a_3, I^{ij} is written

$$I^{ij}(\boldsymbol{p},\boldsymbol{k}) = \frac{T\mu_A}{2\xi_B}\left(\hat{\boldsymbol{p}}^i\hat{\boldsymbol{k}}^j + \hat{\boldsymbol{k}}^i\hat{\boldsymbol{p}}^j\right) + \frac{T\mu_A}{2\xi_B}(1-\hat{\boldsymbol{p}}\cdot\hat{\boldsymbol{k}})\delta^{ij}\,. \tag{A.20}$$

The loss term can be obtained by substituting I^{ij} into Eq. (A.6)

$$I[\chi]_{\text{loss}} = \frac{1}{2}T\mu_A\int_{\boldsymbol{p}} n_p(1+n_p)\frac{\partial\chi(\boldsymbol{p})}{\partial p^i}\frac{\partial\chi(\boldsymbol{p})}{\partial p^i}\,, \tag{A.21}$$

where we used the rotational invariance of $n_k(1+n_k)$ and the definition of ξ_B. Similarly, the gain term is given by

$$\begin{aligned}-I[\chi]_{\text{gain}} =& \frac{T\mu_A}{2\xi_B}\left[\int_{\boldsymbol{p}} n_p(1+n_p)\,\hat{\boldsymbol{p}}\cdot\frac{\partial\chi(\boldsymbol{p})}{\partial\boldsymbol{p}}\right]^2 + \frac{T\mu_A}{2\xi_B}\left[\int_{\boldsymbol{p}} n_p(1+n_p)\frac{\partial\chi(\boldsymbol{p})}{\partial p^i}\right]^2 \\ &+ \frac{T\mu_A}{2\xi_B}\int_{\boldsymbol{pk}} n_p n_k(1+n_p)(1+n_k) \\ &\qquad\left[\hat{p}^j\hat{k}^i\frac{\partial\chi(\boldsymbol{p})}{\partial p^i}\frac{\partial\chi(\boldsymbol{k})}{\partial k^j} - \hat{\boldsymbol{p}}\cdot\hat{\boldsymbol{k}}\left(\frac{\partial\chi(\boldsymbol{p})}{\partial p^i}\right)\left(\frac{\partial\chi(\boldsymbol{k})}{\partial k^i}\right)\right]\,,\end{aligned} \tag{A.22}$$

where the last line is in fact zero. In order to show this, we note that for the rotationally invariant $n_k(1+n_k)$, we have

$$\begin{aligned}&\int_{\boldsymbol{k}}\frac{n_k(1+n_k)}{k}\left[k^i\frac{\partial\chi(\boldsymbol{k})}{\partial k^j} - k^j\frac{\partial\chi(\boldsymbol{k})}{\partial k^i}\right] \\ &\qquad = -\int_{\boldsymbol{k}}\left[\left(k^i\frac{\partial}{\partial k^j} - k^j\frac{\partial}{\partial k^i}\right)\frac{n_k(1+n_k)}{k}\right]\chi(\boldsymbol{k}) = 0\,.\end{aligned} \tag{A.23}$$

This result can be used to interchange i and j in $k^i\partial\chi(\boldsymbol{k})/\partial k^j$ in $I[\chi]_{\text{gain}}$. By taking the variation of the loss and gain terms, the linearized Boltzmann equation can be obtained as in Eq. (2.6).

A.2 Extension to Multi-component Plasmas

In this section, we derive the collision term for multi-component plasmas. The discussion follows from the pure glue case and will be brief.

The collision term of the Boltzmann equation is written as a variational form:

$$C^a[f,\boldsymbol{p}] = -\frac{(2\pi)^3}{\nu_a}\frac{\delta}{\delta\chi^a(\boldsymbol{p})}I[\chi]\,, \tag{A.24}$$

where[3]

$$I[\chi] \equiv \sum_{abcd}\frac{1}{16}\int_{\boldsymbol{pkp'k'}}|M^{cd}_{ab}|^2\,(2\pi)^4\delta^4(P_{\rm tot})\,n^a_p n^b_k(1\pm n^c_{p'})(1\pm n^d_{k'}) \\ \left[\chi^a(\boldsymbol{p})+\chi^b(\boldsymbol{k})-\chi^c(\boldsymbol{p'})-\chi^d(\boldsymbol{k'})\right]^2. \tag{A.25}$$

The collision integral is classified with loss and gain terms as in the previous section. The t-channel exchange diagrams (a)-(c) in Fig. 2.1 and Fig. 2.3 yield

$$I[\chi]^{(a)-(c)}_{\rm loss} = \sum_{ab}\int_{\boldsymbol{pkp'k'}}|M|^2\,(2\pi)^4\delta^4(P_{\rm tot})\,n^a_p n^b_k(1\pm n^a_{p'})(1\pm n^b_{k'}) \\ \frac{1}{4}\left[\chi^a(\boldsymbol{p})-\chi^a(\boldsymbol{p'})\right]^2\,, \tag{A.26}$$

where the invariant matrix elements are

$$\left|\mathcal{M}^{ab}_{ab}\right|^2 = 4\nu_a\nu_b\frac{g^4 C_{R_a}C_{R_b}}{d_A}\frac{s^2}{t^2}\,. \tag{A.27}$$

Expanding the matrix elements gives

$$I[\chi]^{(a)-(c)}_{\rm loss} = \frac{Tm_D^2}{16\pi}\ln(T/m_D)\sum_a g^2 C_{R_a}\nu_a\int_{\boldsymbol{p}}n^a_p(1\pm n^a_p)\left(\frac{\partial\chi^a(\boldsymbol{p})}{\partial p^i}\right)^2\,, \tag{A.28}$$

where we used the definition of the Debye mass Eq. (2.40). The gain terms

[3] In the last section, the matrix elements were averaged over the spins and colors of the particle a. Here the matrix elements are summed over the spins and colors of particle a.

are handled as in the previous section:

$$-I[\chi]^{(a)-(c)}_{\rm gain} = \frac{\ln(T/m_D)}{16\pi d_A}\left[\sum_a g^2 C_{R_a}\nu_a \int_{\boldsymbol{p}} n^a_p(1\pm n^a_p)\,\hat{\boldsymbol{p}}\cdot\frac{\partial\chi^a(\boldsymbol{p})}{\partial\boldsymbol{p}}\right]^2 + \frac{\ln(T/m_D)}{16\pi d_A}\left[\sum_a g^2 C_{R_a}\nu_a \int_{\boldsymbol{p}} n^a_p(1\pm n^a_p)\,\frac{\partial\chi^a(\boldsymbol{p})}{\partial p^i}\right]^2 . \quad \text{(A.29)}$$

When fermions are included, there are also pair annihilation process and a Compton-like scattering. The pair annihilation diagram (d) in Fig. 2.3 yields

$$I[\chi]^{(d)}_{\rm loss} = \sum_q^{\rm f}\frac{8}{16}\int_{\boldsymbol{pkp'k'}}\left|M^{gg}_{q\bar{q}}\right|^2(2\pi)^4\delta^4(P_{\rm tot})n^q_p n^{\bar{q}}_k(1+n^g_p)(1+n^g_k) \left[[\chi^q(\boldsymbol{p})-\chi^g(\boldsymbol{p})]^2+[\chi^{\bar{q}}(\boldsymbol{k})-\chi^g(\boldsymbol{k})]^2\right], \quad \text{(A.30)}$$

$$I[\chi]^{(d)}_{\rm gain} = \sum_q^{\rm f}\frac{8}{16}\int_{\boldsymbol{pkp'k'}}\left|M^{gg}_{q\bar{q}}\right|^2(2\pi)^4\delta^4(P_{\rm tot})n^q_p n^{\bar{q}}_k(1+n^g_p)(1+n^g_k) \left[2[\chi^q(\boldsymbol{p})-\chi^g(\boldsymbol{p})][\chi^{\bar{q}}(\boldsymbol{k})-\chi^g(\boldsymbol{k})]\right]. \quad \text{(A.31)}$$

The invariant matrix element is

$$\left|\mathcal{M}^{gg}_{q\bar{q}}\right|^2 = 4\nu_q C_F^2 g^4\left(\frac{u}{t}\right). \quad \text{(A.32)}$$

Then

$$I[\chi]^{(d)}_{\rm loss} = \frac{1}{2}\sum_a^{\rm f\bar{f}}\int_{\boldsymbol{pk}} n^F_p(1+n^B_p)n^F_k(1+n^B_k)\left[\chi^a(\boldsymbol{p})-\chi^g(\boldsymbol{p})\right]^2 I(\boldsymbol{p},\boldsymbol{k}), \quad \text{(A.33)}$$

with

$$I(\boldsymbol{p},\boldsymbol{k}) = \int_{\boldsymbol{q}}|M|^2\,2\pi\delta(P^0_{\rm tot}) = \frac{\nu_q C_F^2 g^4}{4\pi pk}\ln(T/m_D). \quad \text{(A.34)}$$

This integral is performed by using the parameterization given in the previous section. Thus

$$I[\chi]^{(d)}_{\rm loss} = \frac{1}{2}\gamma\sum_a^{\rm f\bar{f}}\nu_a\int_{\boldsymbol{p}}\frac{n^F_p(1+n^B_p)}{p}\left[\chi^a(\boldsymbol{p})-\chi^g(\boldsymbol{p})\right]^2. \quad \text{(A.35)}$$

The gain term is

$$I[\chi]^{(d)}_{\rm gain} = \sum_a^{\rm f} \frac{\nu_a \gamma}{\xi_{BF}} \int_{\boldsymbol{k}} \frac{n_k^F(1+n_k^B)}{k} \Big[\chi^{\bar{a}}(\boldsymbol{k}) - \chi^g(\boldsymbol{k})\Big] \int_{\boldsymbol{p}} \frac{n_p^F(1+n_p^B)}{p} \Big[\chi^a(\boldsymbol{p}) - \chi^g(\boldsymbol{p})\Big] \,. \quad \text{(A.36)}$$

The Compton scattering diagram (e) in Fig. 2.3 yields

$$I[\chi]^{(e)}_{\rm loss} = \sum_a^{\rm f\bar{f}} \frac{1}{2} \int_{\boldsymbol{pkp'k'}} \left|M^{ag}_{ga}\right|^2 (2\pi)^4 \delta^4(P_{\rm tot}) n_p^F n_k^B (1+n_p^B)(1-n_k^F) \Big[\chi^a(\boldsymbol{p}) - \chi^g(\boldsymbol{p})\Big]^2 , \quad \text{(A.37)}$$

$$I[\chi]^{(e)}_{\rm gain} = \sum_a^{\rm f\bar{f}} \frac{1}{2} \int_{\boldsymbol{pkp'k'}} \left|M^{ag}_{ga}\right|^2 (2\pi)^4 \delta^4(P_{\rm tot}) n_p^F n_k^B (1+n_p^B)(1-n_k^F) \Big[[\chi^a(\boldsymbol{p}) - \chi^g(\boldsymbol{p})][\chi^g(\boldsymbol{k}) - \chi^a(\boldsymbol{k})]\Big] . \quad \text{(A.38)}$$

where the matrix element is

$$\left|\mathcal{M}^{qg}_{gq}\right|^2 = -4\nu_q C_F^2 g^4 \frac{s}{t} \,. \quad \text{(A.39)}$$

The integrals are simplified to

$$I[\chi]^{(e)}_{\rm loss} = \frac{1}{2}\gamma \sum_a^{\rm f\bar{f}} \nu_a \int_{\boldsymbol{p}} \frac{n_p^F(1+n_p^B)}{p} \left[\chi^a(\boldsymbol{p}) - \chi^g(\boldsymbol{p})\right]^2 , \quad \text{(A.40)}$$

$$I[\chi]^{(e)}_{\rm gain} = -\frac{1}{2}\frac{\gamma}{\xi_{BF}} \sum_a^{\rm f\bar{f}} \nu_a \left[\int_{\boldsymbol{p}} \frac{n_p^F(1+n_p^B)}{p} \left(\chi^a(\boldsymbol{p}) - \chi^g(\boldsymbol{p})\right)\right]^2 . \quad \text{(A.41)}$$

Taking a variation of Eqs. (A.28), (A.29), (A.35), (A.36), (A.40), and (A.41) yields the collision terms given in Section 2.3.

Appendix B

Numerical Solution of Boltzmann Equation

In this appendix, we provide all the details of numerical solutions and procedures to solve the Boltzmann equation. The pure glue case will be considered first, and then the extension to including fermions will be discussed.

B.1 Pure Glue

The problems we are working in this thesis are symmetric around an azimuthal angle. Therefore, it is convenient to use a real spherical harmonic basis:

$$H_{lm}(\hat{\boldsymbol{p}}) = N_{lm} P_{l|m|}(\cos\theta_{\boldsymbol{p}}) \times \begin{cases} 1 & \text{for } m = 0 \\ \sqrt{2}\cos m\phi_{\boldsymbol{p}} & \text{for } m > 0 \\ \sqrt{2}\sin |m|\phi_{\boldsymbol{p}} & \text{for } m < 0 \end{cases} . \tag{B.1}$$

Here N_{lm} is the normalization factor

$$N_{lm} = \left[\frac{2l+1}{4\pi}\frac{(l-|m|)!}{(l+|m|)!}\right]^{1/2} , \tag{B.2}$$

and $P_{l|m|}(\cos\theta_{\boldsymbol{p}})$ is the associated Legendre polynomial. We note the equality

$$\hat{p}^x = \sqrt{\frac{4\pi}{3}} H_{11}(\hat{\boldsymbol{p}}) , \qquad \hat{p}^y = \sqrt{\frac{4\pi}{3}} H_{1,-1}(\hat{\boldsymbol{p}}) , \qquad \hat{p}^z = \sqrt{\frac{4\pi}{3}} H_{10}(\hat{\boldsymbol{p}}) . \tag{B.3}$$

In the harmonic basis, the left-hand-side (LHS) of Eq. (3.17), after multi-

plied by p^2, is

$$p^2(\text{LHS}) = (-i\omega\delta_{ll'} + ikC^m_{ll'})\, N(p)\chi_{l'm} - i\omega N(p)\mathcal{H}S_{lm}(p)\,. \tag{B.4}$$

Here we defined

$$N(p) = p^2 n_p(1 \pm n_p)\,, \tag{B.5}$$

and recorded the Clebsch Gordan coefficients

$$C^m_{ll'} = \delta_{l+1,l'}\frac{N_{lm}}{N_{l+1,m}}\left(\frac{l-|m|+1}{2l+1}\right) + \delta_{l-1,l'}\frac{N_{lm}}{N_{l-1,m}}\left(\frac{l+|m|}{2l+1}\right)\,. \tag{B.6}$$

In the source term, $\mathcal{H}$ is one of the following:

$$\mathcal{H} = h_{zx},\ \frac{h_{zz}}{2},\ h_{xy},\ C_A\beta(g)T^2\frac{H}{2}\,, \tag{B.7}$$

corresponding to the shear, sound, transverse tensor, and bulk modes, respectively. By examining the source terms in Eq. (3.17) (for the first three modes) and Eq. (3.35) (for the bulk mode), $S_{lm}(p)$'s in the harmonic basis are

$$-i\omega\frac{p^z p^z}{2E_{\boldsymbol{p}}T}N(p)h_{zz} \ \Rightarrow\ S^{zz}_{lm}(p) = \left(\delta_{l2}\delta_{m0}\,2\sqrt{\frac{4\pi}{5}} + \delta_{l0}\delta_{m0}\sqrt{4\pi}\right)\frac{p}{3T}\,, \tag{B.8}$$

$$-i\omega\frac{p^z p^x}{E_{\boldsymbol{p}}T}N(p)h_{zx} \ \Rightarrow\ S^{zx}_{lm}(p) = \delta_{l2}\delta_{m1}\sqrt{\frac{4\pi}{15}}\frac{p}{T}\,, \tag{B.9}$$

$$-i\omega\frac{p^x p^y}{E_{\boldsymbol{p}}T}N(p)h_{xy} \ \Rightarrow\ S^{xy}_{lm}(p) = \delta_{l2}\delta_{m,-2}\sqrt{\frac{4\pi}{15}}\frac{p}{T}\,, \tag{B.10}$$

$$+i\omega\frac{\tilde{m}^2}{2E_{\boldsymbol{p}}T}N(p)H \ \Rightarrow\ S^{H}_{lm}(p) = \delta_{l0}\delta_{m0}\left(-\frac{\tilde{m}^2\sqrt{4\pi}}{C_A\beta(g)Tp}\right)\,, \tag{B.11}$$

where $\tilde{m}^2/T^2C_A\beta(g)$ will be given by Eq. (B.49). Then Eq. (3.17) reads

$$\begin{aligned}
&\big(-i\omega\delta_{ll'} + ikC^m_{ll'}\big)N(p)\chi_{l'm} - i\omega N(p)\mathcal{H}S_{lm}(p) \\
&= T\mu_A\left[\frac{\partial}{\partial p}N(p)\frac{\partial}{\partial p} - \frac{l(l+1)}{p^2}N(p)\right]\chi_{lm} + \frac{\delta_{l0}\delta_{m0}}{\xi_B}\sqrt{4\pi}\left[-\frac{\partial N(p)}{\partial p}\right]\left(-\frac{\mathrm{d}E}{\mathrm{d}t}\right) \\
&\qquad + \frac{\delta_{l1}\delta_{mm'}}{\xi_B}\sqrt{\frac{4\pi}{3}}\left[-\frac{\partial N(p)}{\partial p} + \frac{2}{p}N(p)\right]\left(-\frac{\mathrm{d}P}{\mathrm{d}t}\right)_{1m'}\,.
\end{aligned} \tag{B.12}$$

We discretize the momentum space so that solving the Boltzmann equation

for $\chi_{lm}(p_n)$ reduces to solving a system of linear equations

$$A_{ij}x_j = b_i\,. \tag{B.13}$$

To this end, the radial momenta are discretized, $p_n = 0.5\,\Delta p + n\Delta p$ with $n = 0 \ldots M-1$. For numerical purposes, we define

$$F_{lm} \equiv \frac{\chi_{lm}}{-i\mathsf{w}\mathcal{H}}\,, \qquad \mathsf{w} \equiv \frac{T\omega}{\mu_A}\,, \qquad \mathsf{k} \equiv \frac{Tk}{\mu_A}\,, \tag{B.14}$$

and set $T = 1$ from now on. Then the equation of motion becomes

$$\begin{aligned}
&(-i\mathsf{w}\delta_{ll'} + i\mathsf{k}C^m_{ll'})N(p)F_{l'm} + N(p)S_{lm}(p) \\
&= \left[\frac{\partial}{\partial p}N(p)\frac{\partial}{\partial p} - \frac{l(l+1)}{p^2}N(p)\right]F_{lm} - \frac{\delta_{l0}\delta_{m0}}{\xi_{B,E}}\sqrt{4\pi}\left[-\frac{\partial N(p)}{\partial p}\right]\left(\frac{1}{-i\mathsf{w}\mathcal{H}\mu_A}\frac{\mathrm{d}E}{\mathrm{d}t}\right) \\
&\qquad - \frac{\delta_{l1}\delta_{mm'}}{\xi_{B,P}}\sqrt{\frac{4\pi}{3}}\left[-\frac{\partial N(p)}{\partial p} + \frac{2}{p}N(p)\right]\left(\frac{1}{-i\mathsf{w}\mathcal{H}\mu_A}\frac{\mathrm{d}P}{\mathrm{d}t}\right)_{1m'}\,,
\end{aligned} \tag{B.15}$$

where we use a second order difference approximation for the second derivative

$$\begin{aligned}
\frac{\partial}{\partial p}N(p)\frac{\partial F(p_n)}{\partial p} = \frac{1}{(\Delta p)^2}\Big[&N(p_{n+1/2})[F(p_{n+1}) - F(p_n)] \\
&- N(p_{n-1/2})[F(p_n) - F(p_{n-1})]\Big]\,.
\end{aligned} \tag{B.16}$$

For the gain terms, we use a midpoint rule:

$$\left(\frac{1}{-i\mathsf{w}\mathcal{H}\mu_A}\frac{\mathrm{d}E}{\mathrm{d}t}\right) = \sqrt{4\pi}\sum_n \frac{\Delta p}{(2\pi)^3}\; p_n\; \frac{\partial}{\partial p}N(p_n)\frac{\partial F_{00}(p_n)}{\partial p}\,, \tag{B.17}$$

$$\begin{aligned}
\left(\frac{1}{-i\mathsf{w}\mathcal{H}\mu_A}\frac{\mathrm{d}P}{\mathrm{d}t}\right)_{1m} = &\sqrt{\frac{4\pi}{3}}\sum_n \frac{\Delta p}{(2\pi)^3}\; p_n \\
&\left[\frac{\partial}{\partial p}N(p_n)\frac{\partial F_{1m}(p_n)}{\partial p} - \frac{2}{p_n^2}N(p_n)F_{1m}(p_n)\right]\,.
\end{aligned} \tag{B.18}$$

ξ_B's are defined so that energy and momentum are conserved:

$$\xi_{B,E} = 4\pi \sum_n \frac{\Delta p}{(2\pi)^3}\, p_n \left[-\frac{\partial N(p_n)}{\partial p}\right] \simeq \frac{1}{6}\,, \tag{B.19}$$

$$\xi_{B,P} = \frac{4\pi}{3} \sum_n \frac{\Delta p}{(2\pi)^3}\, p_n \left[-\frac{\partial N(p_n)}{\partial p} + \frac{2}{p_n} N(p_n)\right] \simeq \frac{1}{6}\,, \tag{B.20}$$

and the derivative of $N(p)$ is

$$\frac{\partial N(p_n)}{\partial p} = \frac{N(p_{n+1/2}) - N(p_{n-1/2})}{\Delta p}\,. \tag{B.21}$$

The boundary conditions of the difference operator in Eq. (B.16) need to be specified. The absorptive boundary condition $\chi(\boldsymbol{p})|_{\boldsymbol{p}=0} = 0$ in Section 2.2.1 means that we take $F_{00}(p_{-1}) = -F_{00}(p_0)$, $F_{1m} = -F_{1m}(p_0)$, and $F_{lm}(p_{-1}) = F_{lm}(p_0)$ for $l \geq 2$. At high momentum, we use the first order differential equation Eq. (2.16). In the spherical harmonic basis, this equation reads

$$\begin{aligned}(-i\mathsf{w}\delta_{ll'} + i\mathsf{k}C^m_{ll'})N(p)F_{l'm}(p) + N(p)S_{lm}(p) \\ = -N(p)\frac{\partial F_{lm}}{\partial p} - \frac{\delta_{l0}\delta_{m0}}{\xi_{B,E}}\sqrt{4\pi}N(p)\left(\frac{1}{-i\mathsf{w}\mathcal{H}\mu_A}\frac{\mathrm{d}E}{\mathrm{d}t}\right) \\ - \frac{\delta_{l1}\delta_{mm'}}{\xi_{B,P}}\sqrt{\frac{4\pi}{3}}N(p)\left(\frac{1}{-i\mathsf{w}\mathcal{H}\mu_A}\frac{\mathrm{d}P}{\mathrm{d}t}\right)_{1m'}\,.\end{aligned} \tag{B.22}$$

This first order differential equation leads to the update rule for the upper boundary:

$$\begin{aligned}F_{lm}(p_M) = F_{lm}(p_{M-1}) - \Delta p\,(-i\mathsf{w} + i\mathsf{k}C^m_{ll'})F_{l'm}(p_{M-1}) \\ - \Delta p\, S_{lm}(p_{M-1}) - \Delta p\frac{\delta_{l0}\delta_{m0}}{\xi_{B,E}}\sqrt{4\pi}\left(\frac{1}{-i\mathsf{w}\mathcal{H}\mu_A}\frac{\mathrm{d}E}{\mathrm{d}t}\right) \\ - \Delta p\frac{\delta_{l1}\delta_{mm'}}{\xi_{B,P}}\sqrt{\frac{4\pi}{3}}\left(\frac{1}{-i\mathsf{w}\mathcal{H}\mu_A}\frac{\mathrm{d}P}{\mathrm{d}t}\right)_{1m'}\,.\end{aligned} \tag{B.23}$$

We now write the discretized form as the matrix equation, $Ax = b$. By examining the discretized update rules in Eqs. (B.15) and (B.16), and the boundary condition in Eq. (B.23), we see that the appropriate vector b_{nlm} is

$$b_{nlm} = N(p_n)S_{lm}(p_n) + \delta_{n,M-1}\frac{1}{(\Delta p)}N(p_{n+1/2})S_{lm}(p_n)\,. \tag{B.24}$$

We note that the last $\delta_{n,M-1}$ piece arises because in Eq. (B.22) we specified the first derivative of the distribution function at high momentum.

In order to solve the system of linear equations, we use BiCGSTAB algorithm which generalizes the conjugate gradient algorithm to non-symmetric matrices [62]. In addition to performing the multiplication Ax, a typical BiCGSTAB implementation requires $A^T x$. In the present case, $A^T x$ involves simply the replacement $\mathsf{w} \to -\mathsf{w}$ and $\mathsf{k} \to -\mathsf{k}$ in the equations. As the preconditioner, we take the diagonal parts of the matrix elements:

$$A_{\text{precond}} = \delta_{nlm,n'l'm'} \left[-\frac{2N(p_n)}{(\Delta p)^2} - \frac{l(l+1)}{p^2} N(p_n) \right] . \tag{B.25}$$

After solving for F_{lm}, the stress tensor is easily found. For example,

$$\frac{G^{zxzx}(\omega,k)}{-i\omega} \frac{\mu_A}{d_A T^5} = \frac{\delta T^{zx}(\omega,\boldsymbol{k})}{+i\omega h_{zx}} \frac{\mu_A}{d_A T^5} , \tag{B.26}$$

$$= -2\sqrt{\frac{4\pi}{15}} \sum_n \frac{\Delta p}{(2\pi)^3} N(p_n)\ p_n\, F_{21}(p_n) , \tag{B.27}$$

$$\Rightarrow \eta \frac{\mu_A}{d_A T^5} , \tag{B.28}$$

where the overall factor of two is the spin, and the arrow ($\Rightarrow$) indicates the limit $\omega \to 0$, $k = 0$.

We record the final expressions for $iG_R(\omega)/\omega$ for the sound mode, the transverse tensor mode, and the bulk mode, respectively:

$$\frac{\delta T^{zz}(\omega,k)}{i\omega(h_{zz}/2)} \frac{\mu_A}{d_A T^5} = -2 \sum_n \frac{\Delta p}{(2\pi)^3} N(p_n) \frac{p_n}{3} \left(2\sqrt{\frac{4\pi}{5}} F_{20}(p_n) + \sqrt{4\pi} F_{00}(p_n) \right) , \tag{B.29}$$

$$\Rightarrow \frac{4}{3} \eta \frac{\mu_A}{d_A T^5} , \tag{B.30}$$

$$\frac{\delta T^{xy}(\omega,k)}{i\omega h_{xy}} \frac{\mu_A}{d_A T^5} = -2 \sum_n \frac{\Delta p}{(2\pi)^3} N(p_n) \left(p_n \sqrt{\frac{4\pi}{15}} \right) F_{2,-2}(p_n) , \tag{B.31}$$

$$\Rightarrow \eta \frac{\mu_A}{d_A T^5} , \tag{B.32}$$

$$\frac{\delta T^{\mu}_{\ \mu}(\omega,k)}{i\omega(H/2)}\,\frac{\mu_A}{d_A T^5 C_A^2\beta(g)^2} = -2\sum_n \frac{\Delta p}{(2\pi)^3} N(p_n)\left(\frac{-\tilde{m}^2\sqrt{4\pi}}{C_A\beta(g)\,p_n}\right) F_{00}(p_n)\ , \tag{B.33}$$

$$\Rightarrow 9\zeta\frac{\mu_A}{d_A T^5 C_A^2\beta(g)^2}\,. \tag{B.34}$$

B.2 Multi-component Plasmas

The discussion for the pure glue case is extended to multi-component plasmas. The current-current correlators will be considered in the next section.

For multi-component plasmas, we introduce a rescaled Debye mass:

$$\hat{m}_D^2 = \frac{m_D^2}{g^2 C_A} = \sum_a^{g,(q+\bar{q})/2} \hat{\nu}_a \hat{C}_a \int_{\boldsymbol{p}} n_p(1\pm n_p) = \frac{1}{3}\left(1+\frac{N_f T_F}{N_c}\right)\,. \tag{B.35}$$

Here we also rescaled the quadratic Casimir and the number of degrees of freedom:

$$\hat{C}_a = \frac{C_{R_a}}{C_A} \qquad \text{and} \qquad \hat{\nu}_a = \frac{\nu_a}{d_A}\,. \tag{B.36}$$

Explicitly, we have $\hat{\nu}_A = 2$, $\hat{\nu}_q = 2N_f\frac{d_F}{d_A}$, and $\hat{\nu}_{(q+\bar{q})/2} = 4N_f d_F/d_A$.

Then the total work and momentum transfer per volume are

$$\left(\frac{1}{-i\mathsf{w}\mathcal{H}\mu_A d_A}\frac{\mathrm{d}E}{\mathrm{d}t}\right) = \sum_a^{g,(q+\bar{q})/2} \hat{\nu}_a\hat{C}_a\sqrt{4\pi}\sum_n \frac{\Delta p}{(2\pi)^3}\,p_n\,\frac{\partial}{\partial p}N(p_n,s_a)\frac{\partial F_{00}^a(p_n)}{\partial p}\,, \tag{B.37}$$

$$\left(\frac{1}{-i\mathsf{w}\mathcal{H}\mu_A d_A}\frac{\mathrm{d}P}{\mathrm{d}t}\right)_{1m} = \sum_a^{g,(q+\bar{q})/2} \hat{\nu}_a\hat{C}_a\sqrt{\frac{4\pi}{3}}\sum_n \frac{\Delta p}{(2\pi)^3}\,p_n \left[\frac{\partial}{\partial p}N(p_n,s_a)\frac{\partial F_{1m}^a(p_n)}{\partial p} - \frac{2}{p_n^2}N(p_n,s_a)F_{1m}^a(p_n)\right]\,. \tag{B.38}$$

The rescaled Debye masses read

$$\hat{m}_{D,E}^2 \equiv \sum_a^{g,(q+\bar{q})/2} \hat{\nu}_a\hat{C}_a\,4\pi\sum_n \frac{\Delta p}{(2\pi)^3}\,p_n\,\left[-\frac{\partial N(p_n,s_a)}{\partial p}\right] \simeq \hat{m}_D^2\,, \tag{B.39}$$

$$\hat{m}_{D,P}^2 \equiv \sum_a^{g,(q+\bar{q})/2} \hat{\nu}_a\hat{C}_a\,\frac{4\pi}{3}\sum_n \frac{\Delta p}{(2\pi)^3}\,p_n\,\left[-\frac{\partial N(p_n,s_a)}{\partial p}+\frac{2}{p_n}N(p_n,s_a)\right] \simeq \hat{m}_D^2\,. \tag{B.40}$$

The equations of motion for $a = g$ and $a = (q+\bar{q})/2$ are

$$\begin{aligned}
&\left(-i\mathsf{w}\delta_{ll'} + i\mathsf{k}C^m_{ll'}\right) N(p,s_a)F^a_{l'm} + N(p,s_a)S^a_{lm}(p) \\
&= \hat{C}_a \left[\frac{\partial}{\partial p}N(p,s_a)\frac{\partial}{\partial p} - \frac{l(l+1)}{p^2}N(p,s_a)\right] F^a_{lm} \\
&\quad - \frac{\delta_{l0}\delta_{m0}\hat{C}_a}{\hat{m}^2_{D,E}}\sqrt{4\pi}\left[-\frac{\partial N(p,s_a)}{\partial p}\right]\left(\frac{1}{-i\mathsf{w}\mathcal{H}\mu_A d_A}\frac{\mathrm{d}E}{\mathrm{d}t}\right) \\
&\quad - \frac{\delta_{l1}\delta_{mm'}\hat{C}_a}{\hat{m}^2_{D,P}}\sqrt{\frac{4\pi}{3}}\left[-\frac{\partial N(p,s_a)}{\partial p} + \frac{2}{p}N(p,s_a)\right]\left(\frac{1}{-i\mathsf{w}\mathcal{H}\mu_A d_A}\frac{\mathrm{d}P}{\mathrm{d}t}\right)_{1m'} \\
&\quad + \frac{p^2 C^a_{qg}}{-i\mathsf{w}\mathcal{H}\mu_A}\,.
\end{aligned} \tag{B.41}$$

To specify the C^a_{qg} terms, we define

$$\hat{\gamma} \equiv \frac{\gamma}{\mu_A} = 2\left(\frac{C_F}{C_A}\right)^2 \frac{\xi_{BF}}{\hat{m}^2_D}\,, \tag{B.42}$$

$$\xi_{BF} \equiv \frac{1}{16}\,, \tag{B.43}$$

$$N_{BF} \equiv p n^F_p (1 + n^B_p)\,. \tag{B.44}$$

Then the collision terms are

$$\frac{p^2}{-i\mathsf{w}\mathcal{H}\mu_A}C^{(q+\bar{q})/2}_{qg} = -\hat{\gamma}N_{BF}(p_n)\left[2F^{(q+\bar{q})/2}_{lm}(p_n) - 2F^g_{lm}(p_n)\right]\,, \tag{B.45}$$

$$\frac{p^2}{-i\mathsf{w}\mathcal{H}\mu_A}C^g_{qg} = \frac{\hat{\nu}_{(q+\bar{q})/2}}{\hat{\nu}_g}\,\hat{\gamma}N_{BF}(p_n)\,\left[2F^{(q+\bar{q})/2}_{lm}(p_n) - 2F^g_{lm}(p_n)\right]\,. \tag{B.46}$$

Finally, the expressions for the stress tensor remain valid with the appropriate modifications. For example, Eq. (B.33) becomes

$$\begin{aligned}
&\frac{\delta T^\mu_{\ \mu}(\omega,k)}{i\omega(H/2)}\,\frac{\mu_A}{d_A T^5 C_A^2 \beta(g)^2} \\
&\qquad = -\sum_a^{g,(q+\bar{q})/2}\hat{\nu}_a \sum_n \frac{\Delta p}{(2\pi)^3}N(p_n,s_a)\left(\frac{-\tilde{m}^2_a\sqrt{4\pi}}{C_A\beta(g)\,p_n}\right)F^a_{00}(p_n)\,,
\end{aligned} \tag{B.47}$$

$$\Rightarrow 9\zeta\frac{\mu_A}{d_A T^5 C_A^2\beta(g)^2}\,, \tag{B.48}$$

where the scaled masses are

$$\frac{\tilde{m}^2_{(q+\bar{q})/2}}{C_A\beta(g)T^2} = -\frac{\hat{C}_F}{4} \quad \text{and} \quad \frac{\tilde{m}^2_g}{C_A\beta(g)T^2} = -\left(\frac{1}{6} + \frac{\hat{\nu}_{(q+\bar{q})/2}\hat{C}_{(q+\bar{q})/2}}{24}\right) . \tag{B.49}$$

In solving the equations, the transpose is also needed. When multiplying by $A^T x$, it must be realized that the matrix implied by Eqs. (B.45) and (B.46) is not symmetric, and the transpose of this equation should be used. Alternatively, Eqs. (B.45) and (B.46) can be made symmetric by rescaling F^a_{lm} with $\sqrt{\nu_a}$ and changing the formulas of this section appropriately.

B.3 Current

In this section, we discuss a numerical procedure to solve Eq. (3.115). Multiplying by p^2, the left hand side becomes

$$p^2(\text{LHS}) = (-i\omega\delta_{ll'} + ikC^m_{ll'})\, N(p)\chi_{l'm}(p) - i\omega N(p)\mathcal{A}S_{lm}(p) . \tag{B.50}$$

Here $\mathcal{A}$ is one of the following:

$$\mathcal{A} = \frac{2Q_sA_z}{T}, \quad \frac{2Q_sA_x}{T} , \tag{B.51}$$

corresponding to the longitudinal and transverse modes, respectively. In this section, $N(p) = p^2 n_p(1-n_p)$ and we dropped the $s-\bar{s}$ label on $\chi^{s-\bar{s}}_{lm}$. From Eq. (3.115), the sources in the harmonic basis are

$$-i\omega n_p(1-n_p)2Q_sA_z\frac{p^z}{E_pT} \;\Rightarrow\; S^z_{lm} = \sqrt{\frac{4\pi}{3}}\delta_{l1}\delta_{m0} , \tag{B.52}$$

$$-i\omega n_p(1-n_p)2Q_sA_x\frac{p^x}{E_pT} \;\Rightarrow\; S^x_{lm} = \sqrt{\frac{4\pi}{3}}\delta_{l1}\delta_{m1} . \tag{B.53}$$

For the net strangeness, we define $F_{lm}(p) \equiv \frac{\chi}{-i\mathsf{w}\mathcal{A}}$. Then Eq. (3.115) becomes

$$\begin{aligned}(-i\mathsf{w}\delta_{ll'} + i\mathsf{k}C^m_{ll'})\, N(p)F_{l'm}(p) + N(p)S_{lm}(p) \\ = \hat{C}_F\left[\frac{\partial}{\partial p}N(p)\frac{\partial}{\partial p} - \frac{l(l+1)}{p^2}N(p)\right]F_{lm}(p) \\ - 2\hat{\gamma}N_{BF}(p)F_{lm}(p) - \frac{\delta_{l0}\delta_{m0}}{\xi_{BF,Q}}\sqrt{4\pi}N_{BF}(p)\left(\frac{1}{-i\mathsf{w}\mathcal{A}}\frac{\mathrm{d}Q}{\mathrm{d}t}\right) ,\end{aligned} \tag{B.54}$$

where the charge transfer rate is

$$\frac{1}{-i\mathsf{w}\mathcal{A}}\frac{\mathrm{d}Q}{\mathrm{d}t} = -2\hat{\gamma}\sqrt{4\pi}\sum_n \frac{\Delta p}{(2\pi)^3} N_{BF}(p_n) F_{00}(p_n)\,. \tag{B.55}$$

We define ξ_{BF} so that the strange charge is exactly conserved:

$$\xi_{BF,Q} = 4\pi \sum_n \frac{\Delta p}{(2\pi)^3} N_{BF}(p_n)\,. \tag{B.56}$$

Finally, from Eq. (3.116) and the susceptibility in Eq. (3.120), we determine the longitudinal and transverse current-current correlators:

$$\frac{J^z}{i\omega A^z}\frac{\mu_F}{T\chi_s} = -\frac{\hat{C}_F}{\xi_F}\sum_n \frac{\Delta p}{(2\pi)^3} N(p_n)\left(\sqrt{\frac{4\pi}{3}}F_{10}(p_n)\right) \;\Rightarrow\; D\frac{\mu_F}{T}\,, \tag{B.57}$$

$$\frac{J^x}{i\omega A^x}\frac{\mu_F}{T\chi_s} = -\frac{\hat{C}_F}{\xi_F}\sum_n \frac{\Delta p}{(2\pi)^3} N(p_n)\left(\sqrt{\frac{4\pi}{3}}F_{11}(p_n)\right) \;\Rightarrow\; D\frac{\mu_F}{T}\,. \tag{B.58}$$

Appendix C

Heavy Quark Source in Kinetic Theory

To compute the heavy quark source, we consider the process $g + q_H \to g + q_H$, where g is non-equilibrium gluon and q_H is a heavy quark moving at a constant velocity $\boldsymbol{v}$ (see Fig. 4.2). The squared matrix element is

$$|\mathcal{M}|^2 = 16\frac{g^4 C_F N_c}{2d_A}\left[\frac{2(K\cdot P)^2}{Q^4} - \frac{M^2}{Q^2} + \frac{M^2}{4(K\cdot P)^2}\right]. \tag{C.1}$$

Here K is the heavy quark momentum, P is the gluon momentum, $Q = P' - P$ is the four momentum transferred to the gluon, and we averaged over the colors and spins of the external gluon. In a leading-log approximation, we keep only the first term of the right hand side in Eq. (C.1). The source term is produced around the quark, and is given by another Boltzmann collisional integral corresponding to the process:

$$\begin{aligned} S(t,\boldsymbol{x},\boldsymbol{p}) =& S(\boldsymbol{p})\delta^3(\boldsymbol{x}-\boldsymbol{v}t)\,, \\ =& -\int_{kp'k'} \frac{|\mathcal{M}|^2}{16k^0k'^0pp'}(2\pi)^4\delta^4(P_{tot})\Big[f_pf_k(1+f_{p'})(1+f_{k'}) \\ & - f_{p'}f_{k'}(1+f_p)(1+f_k)\Big]. \end{aligned} \tag{C.2}$$

Here the heavy quark distribution $f_k = (2\pi)^3\delta^3(\boldsymbol{k}-\boldsymbol{k}_H)\delta^3(\boldsymbol{x}-\boldsymbol{v}t)$ is out of equilibrium.

We expand the source in a spherical harmonic basis in the laboratory co-

ordinate system (x, y, z):

$$S(\boldsymbol{p}) = \sum_{l,m} S_{lm}(p) H_{lm}(\hat{\boldsymbol{p}}; zx) = \sqrt{\frac{2l+1}{4\pi}} \sum_{l} S_{l0}(p) P_l(\cos\theta_{\boldsymbol{pk}}) \,. \tag{C.3}$$

We note that the S_{lm} vanishes for non-zero m due to the azimuthal symmetry of the problem. By following the phase space integration with kinematic approximations in Ref. [95] and using the orthogonality of $P_l(\cos\theta_{\boldsymbol{pk}})$, the expansion coefficients can be computed:

$$S_{l0}(p) = -\sqrt{\frac{2l+1}{4\pi}} \int_0^\infty dq \int_{-vq}^{vq} \frac{d\omega}{v} \int \frac{d\phi}{2\pi} P_l(\cos\theta_{\boldsymbol{pk}}) \\ \frac{|\mathcal{M}|^2}{16p^2(k^0)^2} \left[f_p(1+f_{p+\omega}) - f_{p-\omega}(1+f_p) \right] . \tag{C.4}$$

Here ω is the energy transfer, $\boldsymbol{q} = \boldsymbol{p}' - \boldsymbol{p}$ is the three momentum transfer, and ϕ is the azimuthal angle. In this parameterization, the matrix elements are

$$\frac{|\mathcal{M}|^2}{16p^2(k^0)^2} = \frac{g^4 C_F N_c}{2d_A} \frac{2(1 - v\cos\theta_{\boldsymbol{kp}})^2}{(q^2-\omega^2)^2} \,, \tag{C.5}$$

where $\cos\theta_{\boldsymbol{kp}}$ is expressed in terms of ω, q, and ϕ [95]. Now we consistently expand the integrand to quadratic order in ω/T and q/T. This includes three types of terms: an expansion of the distribution functions to quadratic order, an expansion of the angle $\cos\theta_{pk}$ to linear order in q/T, and an expansion of the Legendre polynomial to linear order, $P_l(x+\delta x) \simeq P_l(x) + P_l'(x)\,\delta x$. With the full expansion, we explicitly integrate over the azimuthal angle ϕ and the energy ω, by observing that all harmonics vanish for $l > 1$ when $v = 1$. Further, the $l = 0$ and $l = 1$ terms can be computed analytically yielding Eq. (4.9):

$$S_{00}(p) = \frac{1}{\sqrt{4\pi}T^2} \left[\frac{g^4 C_F N_c}{2d_A} \right] \log\left(\frac{T}{m_D}\right) f_p(1+f_p) \left(-\frac{2T}{p} + 1 + 2f_p \right) \,, \tag{C.6}$$

$$S_{10}(p) = \frac{1}{\sqrt{12\pi}T^2} \left[\frac{g^4 C_F N_c}{2d_A} \right] \log\left(\frac{T}{m_D}\right) f_p(1+f_p)(1+2f_p) \,. \tag{C.7}$$

Appendix D

Numerical Details in Kinetic Theory with a Heavy Quark Probe

In this appendix, we give numerical details of how the stress tensor is computed in kinetic theory with a heavy quark probe. The linearized Boltzmann equation in Fourier space reads

$$(-i\omega + i\boldsymbol{v}_p \cdot \boldsymbol{k})\delta f(\omega, \boldsymbol{k}, \boldsymbol{p}) = C[\delta f, \boldsymbol{p}] + 2\pi S(\boldsymbol{p})\delta(\omega - \boldsymbol{v}\cdot\boldsymbol{k})\,. \tag{D.1}$$

Here $\boldsymbol{k}$ in the laboratory coordinate system is

$$\boldsymbol{k} = (k^x, k^y, k^z) = k(\sin\theta_k\cos\varphi_k,\ \sin\theta_k\sin\varphi_k,\ \cos\theta_k)\,. \tag{D.2}$$

In order to solve Eq. (D.1) in Fourier space, we introduce the Fourier coordinate system (x', y', z'):

$$\hat{x}' = \frac{k}{k_T}\hat{\boldsymbol{k}} \times (\hat{\boldsymbol{v}} \times \hat{\boldsymbol{k}})\,, \tag{D.3}$$

$$\hat{y}' = \frac{k}{k_T}\hat{\boldsymbol{v}} \times \hat{\boldsymbol{k}}\,, \tag{D.4}$$

$$\hat{z}' = \hat{\boldsymbol{k}}\,. \tag{D.5}$$

We reexpress the source and ultimately the solution δf in terms of real spherical harmonics in Fourier coordinate system. We note that the unit vector $\hat{\boldsymbol{p}}$

has the following components:

$$\hat{p}^{x'} = \sqrt{\frac{4\pi}{3}} H_{11}(\hat{\boldsymbol{p}}; z'x') \,, \tag{D.6}$$

$$\hat{p}^{y'} = \sqrt{\frac{4\pi}{3}} H_{1,-1}(\hat{\boldsymbol{p}}; z'x') \,, \tag{D.7}$$

$$\hat{p}^{z'} = \sqrt{\frac{4\pi}{3}} H_{10}(\hat{\boldsymbol{p}}; z'x') \,. \tag{D.8}$$

Since the distribution function δf is independent of the azimuthal angle of $\boldsymbol{k}$ with respect to the (x, y, z) coordinate system, we choose $\varphi_k = 0$ so that $\boldsymbol{k}$ lies in the xz plane. Then in the (x', y', z') coordinate system

$$\hat{\boldsymbol{v}} = (v^{x'}, v^{y'}, v^{z'}) = (\sin\theta, 0, \cos\theta) \,, \tag{D.9}$$

and

$$\hat{\boldsymbol{v}} \cdot \hat{\boldsymbol{p}} = \sqrt{\frac{4\pi}{3}} \Big[\cos\theta \, H_{10}(\hat{\boldsymbol{p}}; z'x') + \sin\theta \, H_{11}(\hat{\boldsymbol{p}}; z'x') \Big] \,. \tag{D.10}$$

The solution to the linearized Boltzmann equation is expanded in the real spherical harmonics:

$$\delta f(\omega, \boldsymbol{k}, \boldsymbol{p}) = \sum_{lm} 2\pi\delta(\omega - \boldsymbol{v}\cdot\boldsymbol{k}) n_p(1+n_p) \chi_{lm}(p, \boldsymbol{k}) H_{lm}(\hat{\boldsymbol{p}}; z'x') \,. \tag{D.11}$$

The Boltzmann equation for χ_{lm} is

$$(-i\omega\delta_{ll'} + ikC^m_{ll'}) \, p^2 n_p(1+n_p) \chi_{l'm} = C_{lm}[\delta f, \boldsymbol{p}] + \mathcal{H} p^2 n_p(1+n_p) \frac{\mu_A}{T} \mathcal{S}_{lm}(p, \theta) \,, \tag{D.12}$$

where the index m is not summed over. In the above equation, $C^m_{ll'}$ is a Clebsch Gordan coefficient, $C_{lm}[\delta f, \boldsymbol{p}]$ is the collision integral in this basis, the normalization coefficient is

$$\mathcal{H} = \frac{\mu_F}{T^3 d_A \mu_A} \,, \tag{D.13}$$

and the source is

$$\mathcal{S}_{lm}(p, \theta) = \frac{1}{2\xi_B/T^3} \Big[\left(\frac{-2T}{p} + 1 + 2n_p \right) \sqrt{4\pi} \delta_{l0}\delta_{m0} + \sqrt{\frac{4\pi}{3}} \left(1 + 2n_p\right) \left(\delta_{l1}\delta_{m0} \cos\theta + \delta_{l1}\delta_{m1} \sin\theta \right) \Big] \,. \tag{D.14}$$

For each value of (k_x, k_z), the linear equations are solved for $F_{lm} \equiv \chi_{lm}/\mathcal{H}$. Due to rotational symmetry of the collision term around the $\boldsymbol{k}$ axis, the matrix equation does not mix harmonics with different values of m. Thus, the collision operator is diagonal in m, and the equation is solved for $m = 0$ and $m = 1$ separately.

After solving for $\delta f(\omega, \boldsymbol{k}, \boldsymbol{p})$, we use kinetic theory to compute the energy and momentum excess:

$$\delta T^{0\mu}(\omega, \boldsymbol{k}) = 2d_A \int \frac{\mathrm{d}^3\boldsymbol{p}}{(2\pi)^3}\, p^\mu \delta f(\omega, \boldsymbol{k}, \boldsymbol{p})\,. \tag{D.15}$$

Here since $T^{0\mu}(\omega, \boldsymbol{k})$ is proportional to $2\pi\delta(\omega - \boldsymbol{v}\cdot\boldsymbol{k})$, we define

$$\delta T^{0\mu}(\omega, \boldsymbol{k}) \equiv 2\pi\delta(\omega - \boldsymbol{v}\cdot\boldsymbol{k})\tilde{T}^{0\mu}(k_z, k_T)\,. \tag{D.16}$$

The relationship between (x, y, z) and (x', y', z') coordinate systems is

$$\delta T^{0x}(\omega, \boldsymbol{k}) = \cos\theta\, \delta T^{0x'}(\omega, \boldsymbol{k}) - \sin\theta\, \delta T^{0z'}(\omega, \boldsymbol{k})\,, \tag{D.17}$$

$$\delta T^{0y}(\omega, \boldsymbol{k}) = 0\,, \tag{D.18}$$

$$\delta T^{0z}(\omega, \boldsymbol{k}) = \sin\theta\, \delta T^{0x'}(\omega, \mathbf{k}) + \cos\theta\, \delta T^{0z'}(\omega, \mathbf{k})\,. \tag{D.19}$$

δT^{0x} and δT^{0y} can be expressed in terms of δT^{0k_T}:

$$\delta\tilde{T}^{0x}(\boldsymbol{k}) = \delta\tilde{T}^{0k_T}(k_z, k_T)\cos\varphi_k\,, \tag{D.20}$$

$$\delta\tilde{T}^{0y}(\boldsymbol{k}) = \delta\tilde{T}^{0k_T}(k_z, k_T)\sin\varphi_k\,. \tag{D.21}$$

Since we chose $\varphi_k = 0$, it is sufficient to determine $T^{0k_T}(k_z, k_T)$.

Once the stress tensor is tabulated in the (k_z, k_T) plane, we take the Fourier transforms to compute the stress tensor in coordinate space:

$$\delta T^{0\mu}(t, \boldsymbol{x}) = \int_{-\infty}^{\infty} \frac{\mathrm{d}\omega}{2\pi} \int \frac{\mathrm{d}^3\boldsymbol{k}}{(2\pi)^3} e^{-i\omega t + i\boldsymbol{k}\cdot\boldsymbol{x}}\, \delta T^{0\mu}(\omega, \boldsymbol{k})\,. \tag{D.22}$$

By using the identity

$$e^{ik_T x_T \cos(\varphi_r - \varphi_k)} = J_0(k_T x_T) + 2\sum_n i^n J_n(k_T x_T)\cos(n(\varphi_r - \varphi_k))\,, \tag{D.23}$$

we can show that

$$\delta T^{00}(x_L, x_T) = \int_0^\infty \frac{k_T \mathrm{d}k_T}{2\pi} J_0(k_T x_T) \int_{-\infty}^\infty \frac{\mathrm{d}k_z}{2\pi} e^{ik_z z}\, \delta\tilde{T}^{00}(k_z, k_T)\,, \tag{D.24}$$

$$\delta T^{0x_T}(x_L, x_T) = \int_0^\infty \frac{k_T \mathrm{d}k_T}{2\pi} J_1(k_T x_T) \int_{-\infty}^\infty \frac{\mathrm{d}k_z}{2\pi} e^{ik_z z} i\, \delta\tilde{T}^{0k_T}(k_z, k_T)\,, \tag{D.25}$$

$$\delta T^{0z}(x_L, x_T) = \int_0^\infty \frac{k_T \mathrm{d}k_T}{2\pi} J_0(k_T x_T) \int_{-\infty}^\infty \frac{\mathrm{d}k_z}{2\pi} e^{ik_z z}\, \delta\tilde{T}^{0k}(k_z, k_T)\,. \tag{D.26}$$

These Fourier integrals diverge at high momentum. In order to get a convergent result, we first multiply the numerical data by a window function which eliminates the high frequency contributions. For kinetic theory, a sample window function is

$$W(k) = \frac{1}{2}\Big[1 - \mathrm{erf}\left((k - k_{\max})/\sigma\right)\Big]\,, \tag{D.27}$$

with $k_{\max} = 7.5\mu_A/T$ and $\sigma = 3.5\mu_A/T$. For the AdS/CFT, $k_{\max}$ and σ are considerably larger: for instance, $k_{\max} = 80\pi T$ and $\sigma = 60\pi T$.

Appendix E

AdS/CFT with a Heavy Quark Probe

For completeness, we provide details on the response of the $\mathcal{N} = 4$ SYM plasma to a heavy quark probe, following the notations and conventions of Refs. [85, 104]. We should mention that the calculations for $v = 1$ were done by P. Chesler in Ref. [73] as an extension of Ref. [85].

According to the AdS/CFT correspondence, the strongly coupled $\mathcal{N} = 4$ SYM is dual to the five dimensional AdS-Schwarzschild geometry [105]. The five dimensional metric is

$$ds^2 = \frac{L^2}{u^2}\left[-f(u)dt^2 + d\boldsymbol{x}^2 + \frac{du^2}{f(u)}\right] . \tag{E.1}$$

Here u is the radial coordinate of the AdS geometry with $u = 0$ corresponding to the boundary, L is the AdS curvature radius, $f(u) = 1 - u^4/u_h^4$ with $u_h = 1/\pi T$, and T is the Hawking temperature of the plasma and dual geometry. A heavy quark in the SYM plasma is dual to a string in the AdS-Schwarzschild geometry, with the string ending at $u = 0$ [106]. In the large N_c limit, the five dimensional gravitational constant $\kappa_5^2 = 4\pi L^3/N_c^2$ is small, and the equation of motion can be solved perturbatively. A heavy quark moving at constant velocity $\boldsymbol{v}$ is described by the trailing string [98, 100]:

$$\boldsymbol{x}_{\text{string}}(t, u) = \boldsymbol{v}\left[t + \frac{u_h}{2}\left(\tan^{-1}\frac{u}{u_h} + \frac{1}{2}\ln\frac{u_h - u}{u_h + u}\right)\right] . \tag{E.2}$$

The corresponding five dimensional stress tensor has the following components:

$$t_{0i} = -v_i F\,, \qquad t_{ij} = v_i v_j F\,, \qquad t_{00} = \frac{u^4 v^2 + u_h^4 f}{u_h^4} F\,,$$
$$t_{05} = -\frac{u^2 v^2}{u_h^2 f} F\,, \qquad t_{i5} = \frac{u^2 v_i}{u_h^2 f} F\,, \qquad t_{55} = \frac{v^2 - f}{f^2} F\,. \tag{E.3}$$

Here

$$F = \frac{u\sqrt{\lambda}}{2\pi L^3 \sqrt{1-v^2}} \delta^3(\boldsymbol{x} - \boldsymbol{x}_{\rm string})\,, \tag{E.4}$$

and λ is the 't Hooft coupling.

The string perturbs the background geometry linearly

$$G_{MN} \equiv G^{(0)}_{MN} + \frac{L^2}{u^2} H_{MN}\,, \tag{E.5}$$

where $G^{(0)}_{MN}$ is the background metric (E.1) and H_{MN} is the perturbation. By taking the Fourier transform

$$H_{MN}(t, \boldsymbol{x}, u) = \int \frac{\mathrm{d}\omega}{2\pi} \frac{\mathrm{d}^3\boldsymbol{k}}{(2\pi)^3} H_{MN}(\omega, \boldsymbol{k}, u) e^{-i\omega t + i\boldsymbol{k}\cdot\boldsymbol{x}}, \tag{E.6}$$

we find two convenient diffeomorphism invariant fields [86, 104]:

$$\begin{aligned} Z_0 \equiv & \frac{4f}{\omega} k^i H'_{0i} - \frac{4f'}{\omega} k^i H_{0i} - \frac{2f'}{k^2} k^i k^j H_{ij} + 4if k^i H_{i5} \\ & - \frac{(2uk^2 - f')}{k^2} \left(k^2 \delta^{ij} - k^i k^j\right) H_{ij} + \frac{4k^2 f}{i\omega} H_{05} - \frac{8\kappa_5^2 f}{i\omega} t_{05}\,, \end{aligned} \tag{E.7}$$

$$\boldsymbol{Z}_1 \equiv \left(H'_{0i} - i\omega\, H_{i5}\right) \hat{\boldsymbol{\epsilon}}_a\,. \tag{E.8}$$

Here sums over repeated indices are implied with i, j running from 1 to 3 and a running from 1 to 2, $'$ denotes differentiation with respect to u, and

$$\hat{\boldsymbol{\epsilon}}_1 = \frac{k}{k_\perp} \hat{\boldsymbol{k}} \times (\hat{\boldsymbol{v}} \times \hat{\boldsymbol{k}}) \qquad \text{and} \qquad \hat{\boldsymbol{\epsilon}}_2 = \frac{k}{k_\perp} \hat{\boldsymbol{v}} \times \hat{\boldsymbol{k}}\,. \tag{E.9}$$

The field Z_0 transforms as a scalar under rotations, and $\boldsymbol{Z}_1$ transforms as a vector under rotations[1].

The equations of motion for Z_0 and $\boldsymbol{Z}_1$ are straightforward to derive from

[1] A complete set of gauge invariants also includes a field which transforms as a traceless symmetric tensor under rotations [86]. This tensor mode is not necessary here.

the linearized Einstein equations:

$$Z_0'' + A_0 Z_0' + B_0 Z_0 = \kappa_5^2 S_0 \,, \tag{E.10}$$

where

$$A_0 \equiv -\frac{24 + 4k^2u^2 + 6f + k^2u^2 f - 30f^2}{uf\,(u^2k^2 + 6 - 6f)} \,, \tag{E.11}$$

$$B_0 \equiv \frac{\omega^2}{f^2} + \frac{k^2u^2(14{-}5f{-}k^2u^2) + 18(4{-}f{-}3f^2)}{u^2 f\,(k^2u^2 + 6 - 6f)} \,, \tag{E.12}$$

$$\begin{aligned} S_0 \equiv{}& \frac{8}{f} t_{00}' + \frac{4\,(k^2u^2{+}6{-}6f)}{3uk^2 f}(k^2\delta^{ij} {-} 3k^i k^j) t_{ij} \\ &+ \frac{8i\omega}{f} t_{05} + \frac{8u\left[k^2\,(k^2u^2{+}6) - f\,(12k^2{-}9f'')\right]}{3f^2\,(k^2u^2 - 6f + 6)} t_{00} - \frac{8k^2u}{3} t_{55} - 8ik^i t_{i5} \,, \end{aligned} \tag{E.13}$$

and

$$\boldsymbol{Z}_1'' + A_1\, \boldsymbol{Z}_1' + B_1\, \boldsymbol{Z}_1 = \kappa_5^2 \boldsymbol{S}_1 \,, \tag{E.14}$$

where

$$A_1 \equiv \frac{uf' - 3f}{uf} \,, \tag{E.15}$$

$$B_1 \equiv \frac{3f^2 - u\,(uk^2 + 3f')\,f + u^2\omega^2}{u^2 f^2} \,, \tag{E.16}$$

$$\boldsymbol{S}_1 \equiv \frac{2}{f}\left[t_{0i}' + i\omega\, t_{i5}\right]\hat{\boldsymbol{\epsilon}}_a \,. \tag{E.17}$$

Since the string stress tensor in Eq. (E.3) only depends on time through the combination $\boldsymbol{x} - \boldsymbol{v}t$, the string stress tensor in Fourier space is proportional to $2\pi\delta(\omega - \boldsymbol{v}\cdot\boldsymbol{k})$. Consequently, the fields Z_s are also proportional to $2\pi\delta(\omega - \boldsymbol{v}\cdot\boldsymbol{k})$. Moreover, because the string stress tensor in Eq. (E.3) is proportional to $1/\sqrt{1-v^2}$ and Eqs. (E.10) and (E.14) are linear, we define $Z_s = \tilde{Z}_s/\sqrt{1-v^2}$ and solve for $\tilde{Z}_s$ in the $v \to 1$ limit.

By assuming that the boundary geometry is flat, near the boundary the fields Z_s have the asymptotic expansions:

$$\tilde{Z}_s(u) = \tilde{Z}_s^{(2)} u^2 + \tilde{Z}_s^{(3)} u^3 + \tilde{Z}_s^{(4)} u^4 + \cdots \,. \tag{E.18}$$

The cubic expansion coefficients $\tilde{Z}_s^{(3)}$ determine the SYM energy density δT^{00}

and the energy flux δT^{0i} [86, 104]:

$$\delta T^{00} = -\frac{L^3}{8\kappa_5^2}\frac{1}{\sqrt{1-v^2}}\tilde{Z}_0^{(3)}\,, \tag{E.19}$$

$$\delta T^{0i} = -\frac{L^3}{2\kappa_5^2}\frac{1}{\sqrt{1-v^2}}\left[\tilde{Z}_1^{(3)i} + \frac{\omega k^i}{4k^2}\tilde{Z}_0^{(3)i}\right] - \frac{ik^i\mu_F(v)v^2}{k^2}2\pi\delta(\omega - \boldsymbol{v}\cdot\boldsymbol{k})\,. \tag{E.20}$$

Appendix F

Hydrodynamic Source in AdS/CFT and Kinetic Theory

In this appendix, we explain in detail how the coefficients given in Table 4.1 are computed for both AdS/CFT and kinetic theory. In the process, we will exhibit several fits. The quality of these fits indicates that the deviation of the stress tensor from the hydrodynamic form at small ω and $\boldsymbol{k}$ is well described by a multivariate polynomial. We will first discuss the AdS/CFT correspondence and then indicate how the analysis can be applied to kinetic theory.

F.1 AdS/CFT

After computing the exact stress tensor of the AdS/CFT correspondence, we determine the functions $\phi_v(\boldsymbol{k})$ and $\phi_k(\boldsymbol{k})$ in Eqs. (4.36) and (4.37). This would seem to be simply a reparametrization of the original numerical data on $\delta T^{0x'}$ and $\delta T^{0z'}$ with two functions $\phi_v(\boldsymbol{k})$ and $\phi_k(\boldsymbol{k})$. However, as we will see, the functions $\phi_v(\boldsymbol{k})$ and $\phi_k(\boldsymbol{k})$ are analytic functions of $\boldsymbol{k}$ while the original data have poles. Hydrodynamics describes the location of these poles in expansions of $k\ell_{\text{mfp}}$, where ℓ_{mfp} is mean free path. The first order hydrodynamics determines the pole location to the linear order in $k\ell_{\text{mfp}}$, but neglects higher order terms. The pole shift is a consequence of modifying the hydrodynamic equations of motion by powers of $k\ell_{\text{mfp}}$ rather than modifying the source. Since the ideal solution has a hydrodynamic pole at $\omega = c_s k$, modifying the equations of motion does not simply correct the solution by simple powers of $k\ell_{\text{mfp}}$ close to the pole.

We determine the source functions $\phi_v(\boldsymbol{k})$ and $\phi_k(\boldsymbol{k})$ by using the first and second order hydrodynamics[1]. Since $\phi_v(\boldsymbol{k})$ and $\phi_k(\boldsymbol{k})$ are functions of k and

[1]We note that ϕ_v is the same for the first and second order hydrodynamics. Only ϕ_k is

$\omega = k\cos\theta$, we can expand these functions in Fourier series:

$$\phi_v(k,\cos\theta) \equiv \phi_{v;0}(k) + 2\phi_{v;1}(k)\cos\theta + 2\phi_{v;2}(k)\cos 2\theta + \cdots , \tag{F.1}$$

$$\pi T\phi_k(k,\cos\theta) \equiv \phi_{k;0}(k) + 2\phi_{k;1}(k)\cos\theta + 2\phi_{k;2}(k)\cos 2\theta + \cdots . \tag{F.2}$$

In Fig. F.1 (a), we plot the terms of the Fourier series $\phi_{v;n}(k)$ and $\phi_{k;n}(k)$, and fit these functions with a simple power law, Ck^α, where C is a constant. As we see from the fit, ϕ_v is well described by a quadratic polynomial at small k:

$$\phi_{v;0}(k) = 1 - 0.1643\left(\frac{k}{\pi T}\right)^2 , \tag{F.3}$$

$$\phi_{v;1}(k) = 0.5i\left(\frac{k}{\pi T}\right) , \tag{F.4}$$

$$\phi_{v;2}(k) = 0.0870\left(\frac{k}{\pi T}\right)^2 . \tag{F.5}$$

The numerical result for $\phi_{v;1}$ is consistent with the first order analytic result in Ref. [85].

Now we examine $k\phi_k$ by using the first and second order hydrodynamics[2]. When the first order hydrodynamics is used, the source function is not well described by a polynomial (see Fig. F.1 (b)). However, we see that $k\phi_k$ decreases faster than k (as $k^{1.52}$ for $n = 1$), and therefore $k\phi_k$ can be neglected in the first order hydrodynamic analysis. When the second order hydrodynamics is used, $k\phi_k$ is well described by the quadratic polynomial (see the linear fit in Fig. F.1 (c) for $\phi_{k;1}$). Numerically, we find

$$\phi_{k;0}(k) = -\frac{1}{3} \qquad \text{and} \qquad \phi_{k;1}(k) = 0.11i\left(\frac{k}{\pi T}\right) , \tag{F.6}$$

up to non-analytic terms that fall faster than k^2. These non-analytic terms could be removed by pushing the hydrodynamic analysis to the third order. By using the fits in Eqs. (F.3)-(F.6) (with the relation between ϕ_v, ϕ_k and ϕ_1,ϕ_2 in Eq. (4.30)), we parametrize the source by three numbers to second order which are given in Table 4.1.

affected by non-zero τ_π.

[2]We discuss $k\phi_k$ instead of simply ϕ_k since the source for hydrodynamics is $\boldsymbol{k}\phi_k(k)$ in Eq. (4.31).

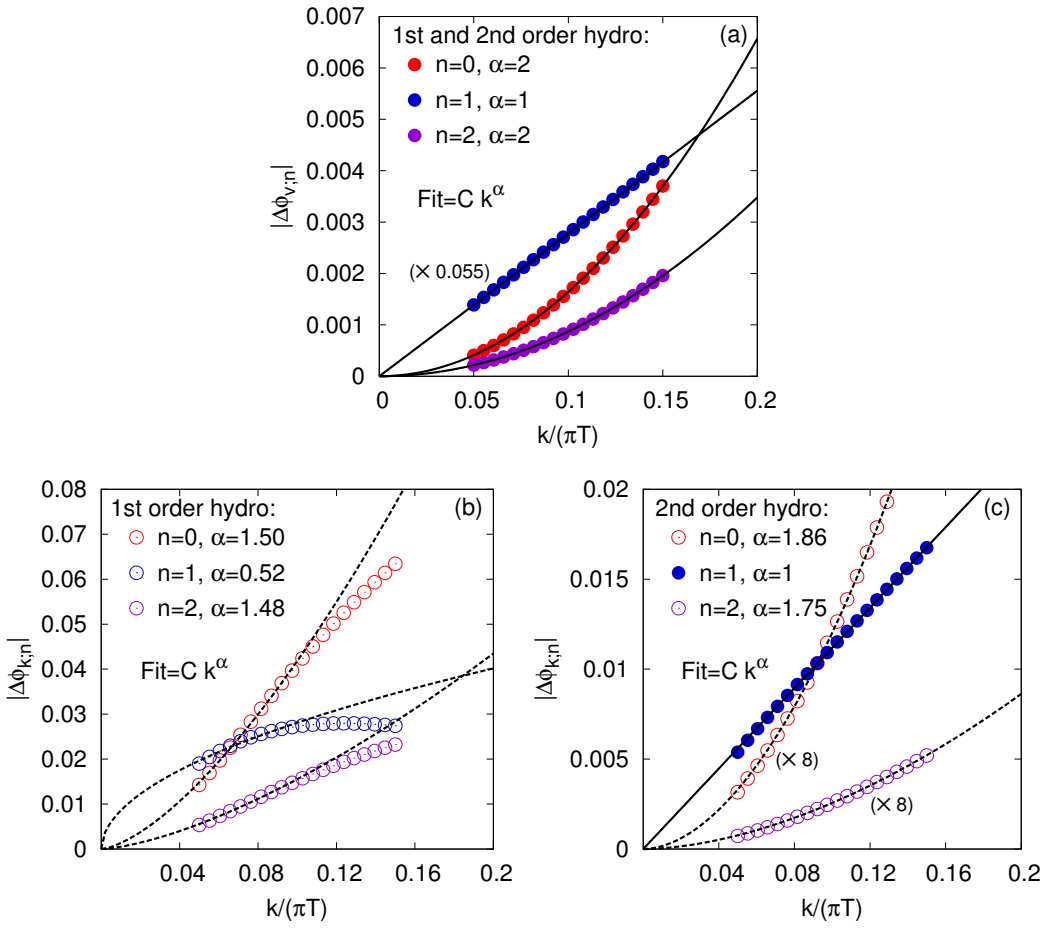

Figure F.1: Hydrodynamic fits to the AdS/CFT source functions $\phi_v \equiv 1 + \Delta\phi_v$ and $\pi T \phi_k = -\frac{1}{3} + \Delta\phi_k$ at small k. The Fourier coefficients displayed in this figure have been multiplied by a factor indicated in parentheses to increase visibility, and are fit with the functional form Ck^α. The dotted lines and open circles have non-integer fit-powers and lie beyond the description of hydrodynamics to the specified order, *i.e.* the fit is not expected to work. (a) The $n = 0$, $n = 1$, and $n = 2$ Fourier coefficients of ϕ_v. (b) The $n = 0$, $n = 1$, and $n = 2$ Fourier coefficients of ϕ_k, when ϕ_k is extracted by using the first order hydrodynamics. (c) Same as (b), but for the second order hydrodynamics.

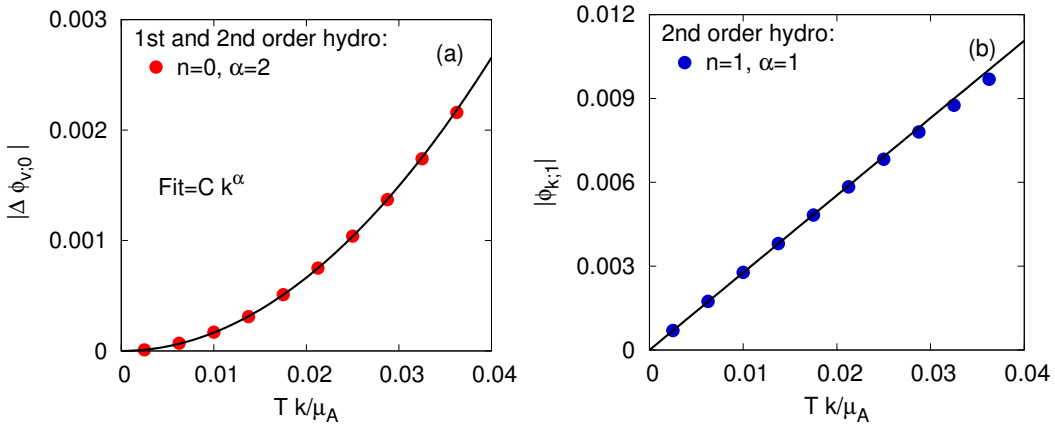

Figure F.2: (a) A polynomial fit to the kinetic theory source function $\phi_{v;0}$. The fit result is recorded in Eq. (F.7). (b) By using the fit coefficient from (a), a prediction is made for $\phi_{k;1}$ (see Eq. (F.8)).

F.2 Kinetic Theory

As in the AdS/CFT, we determine the source functions $\phi_v(\boldsymbol{k})$ and $\phi_k(\boldsymbol{k})$ from the numerical data by using Eqs. (4.36) and (4.37). Then we expand these functions in Fourier series as in Eqs. (F.1) and (F.2), but with the appropriate unit μ_A/T in place of πT. The Fourier coefficients are fit with a polynomial (see Fig. F.2):

$$\phi_{v;0}(k) = 1 + 1.66(1)\left(\frac{kT}{\mu_A}\right)^2 , \tag{F.7}$$

$$\phi_{k;1}(k) = -\frac{1}{6}1.66(1)i\left(\frac{kT}{\mu_A}\right) . \tag{F.8}$$

The other Fourier coefficients of ϕ_v and $k\phi_k$ decrease faster than k^2. The fact that $\phi_{v;0}$ and $\phi_{k;1}$ have the same fit coefficient (up to a symmetry factor of $1/6$) is a consequence of the hydrodynamic analysis in Section 4.4.

By comparing fits with Eq. (4.30), we determine the coefficients $\phi_1^{(0,0)}$, $\phi_1^{(1,0)}$, and $\phi_2^{(0,0)}$ which are recorded in Table 4.1. As discussed in Section 4.4, $\phi_1(\omega, k^2)$ vanishes to all orders in ω and $\boldsymbol{k}$, which can be understood as follows. For a given $\boldsymbol{k}$, we expect that there is a non-zero component of $T^{ij}(\omega, \boldsymbol{k})$ which transforms as a spin two tensor under rotations around the $\boldsymbol{k}$ axis. This spin two component determines the term $\left[v^i v^j - \frac{1}{3}v^2\delta^{ij}\right]\phi_1$ in Eq. (4.28). Since the kinetic theory source in Eq. (4.9) does not have $m = 2$ harmonics and

the Boltzmann equation does not mix harmonics of different spins, the spin two component of the stress tensor vanishes. Therefore, ϕ_1 vanishes. This approximate symmetry is specific to the simplified form of the source in a leading-log approximation, and is not expected to hold more generally.

Appendix G

Two-loop Diagrams

In this appendix, we compute the squared matrix elements for the two loop diagrams in Fig. 5.10. We use the following cutting rules:

- For hard quark retarded propagators,

$$\frac{-i\not{P}}{P^2+m_\infty^2-i\epsilon p^0}=\frac{i\not{v}_p}{2\big[p^- - \frac{(\boldsymbol{p}_\perp^2+m_\infty^2)}{p^+}+i\epsilon\big]}\,. \tag{G.1}$$

- For vertices with a soft gluon,

$$ig2P^\mu A_\mu(P')=igp^+v_p\cdot A(P')\,. \tag{G.2}$$

- For hard quark cut lines running through the cut, we use the positive energy part of

$$\begin{aligned} iS^<_{\rm bare}(P) &= -i\frac{2\pi}{2E_p}n_p^F\not{P}\delta(p^0-E_p)+i\frac{2\pi}{2E_p}n_{-p}^F\not{P}\delta(p^0+E_p)\,,\\ &\to -i\frac{2\pi}{2}n_p^F\not{v}_p\delta\Big(p^- - \frac{(\boldsymbol{p}_\perp^2+m_\infty^2)}{p^+}\Big)\,, \end{aligned} \tag{G.3}$$

  whereas for cut lines running against the cut,

$$iS^>_{\rm bare}(P)\to -i\frac{2\pi}{2}(1-n_p^F)\not{v}_p\delta\Big(p^- - \frac{(\boldsymbol{p}_\perp^2+m_\infty^2)}{p^+}\Big)\,. \tag{G.4}$$

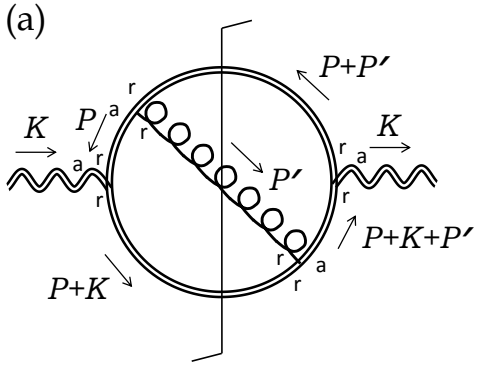

Figure G.1: A two-loop diagram with a soft gluon in Fig. 5.10 (a). Double solid lines denote hard quarks, double wiggly lines denote hard photons, and a single curly line denotes a soft gluon.

To compute the diagram (a) in Fig. 5.10, we consider the momenta drawn in Fig. G.1:

$$\begin{aligned}(\mathrm{a}) = \frac{1}{16}\int_{P,P'} & n^F_{p+k}(1-n^F_p)\,\mathrm{Tr}\,[\gamma^a \not{p}_p \gamma_\mu \not{p}_{p+p'}\gamma_a \not{p}_{p+k+p'}\gamma_\nu \not{p}_{p+k}] \\ & 2\pi\Big(p^- - \frac{(\boldsymbol{p}_\perp^2+m_\infty^2)}{(p^++k^+)}\Big)2\pi\Big(p^-+p'^- - \frac{[(\boldsymbol{p}_\perp+\boldsymbol{p}'_\perp)^2+m_\infty^2]}{p^+}\Big) \\ & \frac{1}{\Big(p^- - \frac{(\boldsymbol{p}_\perp^2+m_\infty^2)}{p^+}+i\epsilon\Big)}\frac{1}{\Big(p^-+p'^- - \frac{[(\boldsymbol{p}_\perp+\boldsymbol{p}'_\perp)^2+m_\infty^2]}{(p^++k^+)}+i\epsilon\Big)}\,. \end{aligned} \tag{G.5}$$

By using the Eikonal approximation

$$\mathbf{v}_p \simeq \mathbf{v}_{p+p'} \qquad \text{and} \qquad \mathbf{v}_{p+k} \simeq \mathbf{v}_{p+k+p'}\,, \tag{G.6}$$

and integrating over p^- and p'^- with the delta functions,

$$\begin{aligned}(\mathrm{a}) = g^2\int_{p^+,\boldsymbol{p}_\perp,p'^+,\boldsymbol{p}'_\perp} & n^F_{p+k}(1-n^F_p)[v_p\cdot A(P')][v_{p+k}\cdot A(-P')] \\ & \langle \boldsymbol{p}+\boldsymbol{p}'|J_\mu(K)|\boldsymbol{p}+\boldsymbol{k}+\boldsymbol{p}'\rangle\,\langle \boldsymbol{p}+\boldsymbol{k}|J_\nu(-K)|\boldsymbol{p}\rangle \\ & \frac{1}{[-\delta E(\boldsymbol{p}_\perp)+i\epsilon]}\frac{1}{[\delta E(\boldsymbol{p}_\perp+\boldsymbol{p}'_\perp)+i\epsilon]}\,. \end{aligned} \tag{G.7}$$

Here the energy changes are

$$\delta E(\boldsymbol{p}_\perp) = \frac{k^+(\boldsymbol{p}_\perp^2 + m_\infty^2)}{p^+(p^+ + k^+)}\,, \tag{G.8}$$

$$\delta E(\boldsymbol{p}_\perp + \boldsymbol{p}'_\perp) = \frac{k^+[(\boldsymbol{p}_\perp + \boldsymbol{p}'_\perp)^2 + m_\infty^2]}{p^+(p^+ + k^+)}\,. \tag{G.9}$$

With $v_p \simeq v_{p+k}$, the correlation of gauge fields yields the collision kernel

$$\begin{aligned} g^2 \int_{p'^+} [v_p \cdot A(P')][v_{p+k} \cdot A(-P')]\Big|_{p'^-=0} &\simeq \int_{p'^+} \frac{T}{p'^0} \rho^{\mu\nu}(P') v_\mu v_\mu \Big|_{p'^-=0}\,, \\ &= C[\boldsymbol{p}'_\perp]\,, \end{aligned} \tag{G.10}$$

and the diagram (a) is

$$\begin{aligned} \text{(a)} = -\int_{p^+,\boldsymbol{p}_\perp,\boldsymbol{p}'_\perp} & n^F_{p+k}(1-n^F_p)\frac{C[\boldsymbol{p}'_\perp]}{\delta E(\boldsymbol{p}_\perp)\delta E(\boldsymbol{p}_\perp+\boldsymbol{p}'_\perp)} \\ & \langle \boldsymbol{p}+\boldsymbol{p}'|J_\mu(K)|\boldsymbol{p}+\boldsymbol{k}+\boldsymbol{p}'\rangle \langle \boldsymbol{p}+\boldsymbol{k}|J_\nu(-K)|\boldsymbol{p}\rangle\ . \end{aligned} \tag{G.11}$$

Similarly, the diagrams (b)-(d) in Fig. 5.10 can be computed:

$$\begin{aligned} \text{(b)} = -\int_{p^+,\boldsymbol{p}_\perp,\boldsymbol{p}'_\perp} & n^F_{p+k}(1-n^F_p)\frac{C[\boldsymbol{p}'_\perp]}{\delta E(\boldsymbol{p}_\perp)\delta E(\boldsymbol{p}_\perp+\boldsymbol{p}'_\perp)} \\ & \langle \boldsymbol{p}|J_\mu(K)|\boldsymbol{p}+\boldsymbol{k}\rangle \langle \boldsymbol{p}+\boldsymbol{k}+\boldsymbol{p}'|J_\nu(-K)|\boldsymbol{p}+\boldsymbol{p}'\rangle\ , \end{aligned} \tag{G.12}$$

$$\begin{aligned} \text{(c)} = \int_{p^+,\boldsymbol{p}_\perp,\boldsymbol{p}'_\perp} & n^F_{p+k}(1-n^F_p)\frac{C[\boldsymbol{p}'_\perp]}{[\delta E(\boldsymbol{p}_\perp+\boldsymbol{p}'_\perp)]^2} \\ & \langle \boldsymbol{p}+\boldsymbol{p}'|J_\mu(K)|\boldsymbol{p}+\boldsymbol{k}+\boldsymbol{p}'\rangle \langle \boldsymbol{p}+\boldsymbol{k}+\boldsymbol{p}'|J_\nu(-K)|\boldsymbol{p}+\boldsymbol{p}'\rangle\ , \end{aligned} \tag{G.13}$$

$$\begin{aligned} \text{(d)} = \int_{p^+,\boldsymbol{p}_\perp,\boldsymbol{p}'_\perp} & n^F_{p+k}(1-n^F_p)\frac{C[\boldsymbol{p}'_\perp]}{[\delta E(\boldsymbol{p}_\perp)]^2} \\ & \langle \boldsymbol{p}|J_\mu(K)|\boldsymbol{p}+\boldsymbol{k}\rangle \langle \boldsymbol{p}+\boldsymbol{k}|J_\nu(-K)|\boldsymbol{p}\rangle\ . \end{aligned} \tag{G.14}$$

With

$$\langle \boldsymbol{p}|J_\mu(K)|\boldsymbol{p}+\boldsymbol{k}\rangle^* = \langle \boldsymbol{p}+\boldsymbol{k}|J_\mu(-K)|\boldsymbol{p}\rangle\ , \tag{G.15}$$

the diagram (b) is the complex conjugate of (a), and the sum of four diagrams is

$$\begin{aligned}(\mathrm{a})+(\mathrm{b})+(\mathrm{c})+(\mathrm{d}) = \mathrm{Re}\int_{p^+,\boldsymbol{p}_\perp,\boldsymbol{p}'_\perp} n^F_{p+k}(1-n^F_p)C[\boldsymbol{p}'_\perp] \\ \left[\frac{|\langle \boldsymbol{p}|J_\mu(K)|\boldsymbol{p}+\boldsymbol{k}\rangle|^2}{[\delta E(\boldsymbol{p}_\perp)]^2} + \frac{|\langle \boldsymbol{p}+\boldsymbol{p}'|J_\mu(K)|\boldsymbol{p}+\boldsymbol{k}+\boldsymbol{p}'\rangle|^2}{[\delta E(\boldsymbol{p}_\perp+\boldsymbol{p}'_\perp)]^2}\right. \\ \left. -\frac{2\langle \boldsymbol{p}|J_\mu(K)|\boldsymbol{p}+\boldsymbol{k}\rangle^*\langle \boldsymbol{p}+\boldsymbol{p}'|J_\nu(K)|\boldsymbol{p}+\boldsymbol{k}+\boldsymbol{p}'\rangle}{\delta E(\boldsymbol{p}_\perp)\delta E(\boldsymbol{p}_\perp+\boldsymbol{p}'_\perp)}\right]. \end{aligned} \tag{G.16}$$

By using the translation invariance $\boldsymbol{p}\to\boldsymbol{p}-\boldsymbol{p}'$,

$$\begin{aligned}(\mathrm{a})+(\mathrm{b})+(\mathrm{c})+(\mathrm{d}) \simeq 2\,\mathrm{Re}\int_{p^+,\boldsymbol{p}_\perp,\boldsymbol{p}'_\perp} n^F_{p+k}(1-n^F_p)C[\boldsymbol{p}'_\perp] \\ \left[\frac{|\langle \boldsymbol{p}|J_\mu(K)|\boldsymbol{p}+\boldsymbol{k}\rangle|^2}{[\delta E(\boldsymbol{p}_\perp)]^2} - \frac{\langle \boldsymbol{p}|J_\mu(K)|\boldsymbol{p}+\boldsymbol{k}\rangle^*\langle \boldsymbol{p}+\boldsymbol{p}'|J_\nu(K)|\boldsymbol{p}+\boldsymbol{k}+\boldsymbol{p}'\rangle}{\delta E(\boldsymbol{p}_\perp)\delta E(\boldsymbol{p}_\perp+\boldsymbol{p}'_\perp)}\right]. \end{aligned} \tag{G.17}$$

This sum yields the same photon emission rate as Eq. (5.43) which was computed by the perturbative solution, by noting

$$\langle \boldsymbol{p}|J_\mu(K)|\boldsymbol{p}+\boldsymbol{k}\rangle \;\propto\; 2\boldsymbol{p}_\perp\,\frac{\sqrt{(p^z)^2+(p^z+k)^2}}{p^z(p^z+k)}\,. \tag{G.18}$$

To see that the sum of four diagrams yields the matrix elements of the LO bremsstrahlung, we drop all masses. Then the integrand (without statistical factors) in Eq. (G.16) gives

$$\begin{aligned}C[\boldsymbol{p}'_\perp]\frac{16}{k}\frac{p^z(p^z+k)}{k}\frac{1+z^2}{z}\left[\frac{1}{\boldsymbol{p}_\perp^2}+\frac{1}{(\boldsymbol{p}_\perp+\boldsymbol{p}'_\perp)^2}-\frac{2\boldsymbol{p}_\perp\cdot(\boldsymbol{p}_\perp+\boldsymbol{p}'_\perp)}{\boldsymbol{p}_\perp^2(\boldsymbol{p}_\perp+\boldsymbol{p}'_\perp)^2}\right] \\ \simeq C[\boldsymbol{p}'_\perp]\frac{16}{k}\frac{p^z(p^z+k)}{k}\frac{1+z^2}{z}\frac{\boldsymbol{p}_\perp'^2}{\boldsymbol{p}_\perp^4}\,, \end{aligned} \tag{G.19}$$

which agrees with Eq. (5.98) up to factors.

Appendix H

Wide-angle Pair Annihilation

In this appendix, we compute the photon emission rate from the wide-angle pair annihilation process, $P + P' \to K + K'$. Now the gluon momentum is K' (not P') which is soft. The calculations are parallel to those in wide-angle bremsstrahlung, except that we have different population factors and momentum "joining" (rather than splitting).

- The momentum joining is given by

$$p^+ = (1-z)k^+ \qquad \text{and} \qquad p'^+ = zk^+ \,, \tag{H.1}$$

  where $0 < z < 1$. By using the joining factor and the conservation of the minus momenta, we express the minus coordinates in term of p^-:

$$p'^- = \frac{(1-z)}{z} p^- \qquad \text{and} \qquad k'^- = \frac{1}{z} p^- \,. \tag{H.2}$$

  The Mandelstam variables are

$$s = k^+ k'^- \,, \qquad t = -zk^+ k'^- \,, \qquad u = -(1-z)k^+ k'^- \,. \tag{H.3}$$

- The matrix elements of pair annihilation have a joining function:

$$|M|^2 \sim \frac{u}{t} + \frac{t}{u} = \frac{(1-z)^2 + z^2}{z(1-z)} \qquad \text{(fermion joining)} \,. \tag{H.4}$$

With the twice smaller degrees of freedom, they are given by

$$|M|^2_L \rho^L(K') \simeq 8e^2 \sum_s q_s^2 d_F C_F g^2 \frac{(1-z)^2+z^2}{z(1-z)} \frac{k_\perp'^2}{2(k'^-)^2} \rho^L(K')\,, \tag{H.5}$$

$$|M|^2_T \rho^T(K') \simeq 8e^2 \sum_s q_s^2 d_F C_F g^2 \frac{(1-z)^2+z^2}{z(1-z)} \left[1 - \frac{m_g^2 \sin^2\theta}{2(k'^-)^2}\right] \rho^T(K')\,, \tag{H.6}$$

$$|M|^2_{\rm bare} \rho^{\rm bare}(K') \simeq 8e^2 \sum_s q_s^2 d_F C_F g^2 \frac{(1-z)^2+z^2}{z(1-z)} \rho^{\rm bare}(K')\,. \tag{H.7}$$

- The phase space integration is defined by

$$\begin{aligned}(2\pi)^3 \frac{{\rm d}({\rm PS})}{{\rm d}^3\boldsymbol{k}} &\equiv \int_{\boldsymbol{p},\boldsymbol{p}',K'} \frac{1}{2p2p'2k} (2\pi)^4 \delta^4(P+P'-K'-K)\,, \\ &= \int_{p^+,\boldsymbol{p}_\perp,\boldsymbol{k}'} \frac{1}{p^+ p'^+ 2k}\bigg|_{k'^0 = k'^z + \delta E}\,,\end{aligned} \tag{H.8}$$

where we fixed k'^0 as

$$k'^0 = k'^z + \delta E \qquad \text{with} \qquad \delta E \equiv \frac{1}{z}\frac{p_\perp^2}{p^+}\,. \tag{H.9}$$

- After subtracting the LO result, the NLO correction is given by

$$\begin{aligned}(2\pi)^3 \frac{{\rm d}\delta\Gamma_{\rm NLO}}{{\rm d}^3\boldsymbol{k}}\bigg|^{\rm wide}_{\rm annih} &= \int_{p^+,\boldsymbol{p}_\perp,\boldsymbol{k}'} \frac{1}{p^+ p'^+ 2k} n_p^F n_{p'}^F \\ &\quad \frac{T}{k'^0}\Big[|M|^2_L \rho^L + |M|^2_T \rho^T - |M|^2_{\rm bare}\, \rho^{\rm bare}\Big]\Big|_{k'^0 = k'^z + \delta E}\,,\end{aligned} \tag{H.10}$$

where we used $1 + n^B_{k'} \simeq T/k'^0$ for soft K'. When $p_\perp^2 \to 0$, this process becomes the LO collinear pair annihilation process whose contribution must be subtracted to obtain the NLO correction. As in Section 5.5, we perform the contour integral over k'^z, change the variable from $p_\perp^2$ to δE,

and do the integrations over δE and $p_\perp'^2$ to get

$$(2\pi)^3 \frac{\mathrm{d}\delta\Gamma_{\mathrm{NLO}}}{\mathrm{d}^3\boldsymbol{k}}\bigg|_{\mathrm{annih}}^{\mathrm{wide}} = -\frac{1}{16\pi^2} e^2 \sum_s q_s^2 d_F C_F g^2 m_D T \frac{1}{k^2}\int_0^k \mathrm{d}p^z \left(\frac{p^z}{k-p^z} + \frac{k-p^z}{p^z}\right) n_p^F n_{k-p}^F \,. \quad \text{(H.11)}$$

Here we used the joining factor

$$\frac{(1-z)^2+z^2}{z(1-z)} = \frac{p^z}{k-p^z} + \frac{k-p^z}{p^z} \,. \quad \text{(H.12)}$$

- The emission rate is logarithmically divergent when $p^z \to 0$ or $p^z \to k$. After regularization, the NLO correction from wide-angle pair annihilation is

$$(2\pi)^3 \frac{\mathrm{d}\delta\Gamma_{\mathrm{NLO}}}{\mathrm{d}^3\boldsymbol{k}}\bigg|_{\mathrm{annih}}^{\mathrm{wide}} = -\frac{1}{16\pi^2} e^2 \sum_s q_s^2 d_F C_F g^2 m_D T \frac{n_k^F}{k}\left[\ln\left(\frac{T}{\mu_z}\right) + C_{\mathrm{annih}}^{\mathrm{wide}}(k/T)\right] , \quad \text{(H.13)}$$

where $C_{\mathrm{annih}}^{\mathrm{wide}}(k/T)$ is independent of the cutoff μ_z.